

The effect of tip structure in atomic manipulation: a  
combined DFT and AFM study



Samuel Paul Jarvis, MSci (Hons)

School of Physics and Astronomy  
University of Nottingham

Thesis submitted to the University of Nottingham  
for the degree of *Doctor of Philosophy*

September 2012

## Abstract

Non-contact atomic force microscopy allows us to directly probe the interactions between atoms and molecules. When operated in UHV and at low temperatures, a host of experiments, uniquely possible with the technique, can be carried out. The AFM allows us to characterise the forces present on a surface, resolve the atomic structure of molecules, measure the force required to move an atom, and even directly measure molecular pair potentials.

Generally speaking, it is the interaction between the outermost tip and surface atoms that we measure. Therefore, in each of these experiments, understanding, or controlling, the tip termination is essential. As NC-AFM experiments become increasingly sophisticated, the combination of experiment and simulation has become critical to understand, and guide the processes at play. In this thesis, I focus on semiconductor surfaces and investigate the role of tip structure in a variety of situations with both DFT simulations and NC-AFM experiments.

The clean Si(100) surface consists of rows of dimers, which can be manipulated between two different states using an NC-AFM. In order to understand the manipulation process, detailed DFT and NEB simulations were conducted to examine the energy balance of ideal and defective surfaces, with or without the presence of an AFM tip. We show that an explanation can only be reached when we consider *both* the AFM tip and variations in the PES caused by surface defects.

NC-AFM experiments were also conducted on Si(100):H. We find that on this surface we regularly cultivate chemically passivated, hydrogen-terminated, tip apices which lead to distinct inverted image contrasts in our AFM images. Following a thorough characterisation of the tip apex, we conduct preliminary experiments designed to investigate surface defect structures, and to chemically modify the tip termination. Detailed DFT simulations show that this type of tip engineering, however, critically depends on the larger tip structure, significantly complicating the chances of success.

Additionally, we investigate the structure and stability of silicon tip apices using DFT. Even with relatively simple tip structures, we observe complex behaviours, such as tip-dependent dissipation and structural development. These processes provide interesting information regarding tip stability, and commonly observed experimental behaviour. We also model an experiment in which we functionalise the tip apex with a C<sub>60</sub> molecule, revealing for the first time that submolecular resolution is possible in the attractive regime.

## Relevant publications

C. Chiutu\*, A.M. Sweetman\*, A.J Lakin\*, A. Stannard\*, **S. Jarvis\***, L. Kantorovich, J.L. Dunn and P. Moriarty

**Precise Orientation of a Single  $C_{60}$  Molecule on the Tip of a Scanning Probe Microscope**

*Phys. Rev. Lett.* **108**, 268302 (2012). \*All of these authors contributed equally

**S. Jarvis**, A. Sweetman, J. Bamidele, L. Kantorovich and P. Moriarty.

**Role of orbital overlap in atomic manipulation**

*Phys. Rev. B* **85**, 235305 (2012.)

P. Sharp, **S. Jarvis**, R. Woolley, A. Sweetman, L. Kantorovich, C. Pakes, and P. Moriarty.

**Identifying passivated dynamic force microscopy tips on H:Si(100)**

*Appl. Phys. Lett.* **100**, 233120 (2012).

A. Sweetman, **S. Jarvis**, R. Danza and P. Moriarty.

**Effect of the tip state during qPlus noncontact atomic force microscopy of Si(100) at 5 K: Probing the probe**

*Beilstein J. Nanotechnol.* **3**, 25 (2012).

A. Sweetman, **S. Jarvis**, R.Danza, J.Bamidele, L.Kantorovich and P. Moriarty.  
**Manipulating Si(100) at 5K using qPlus frequency modulated atomic force microscopy: Role of defects and dynamics in the mechanical switching of atoms**

*Phys. Rev. B* **84**, 085426 (2011).

A. Sweetman, **S. Jarvis**, R. Danza, J. Bamidele, S. Gangopadhyay, G.A. Shaw, L. Kantorovich and P. Moriarty.

**Toggling Bistable Atoms via Mechanical Switching of Bond Angle**

*Phys. Rev. Lett.* **106**, 136101 (2011).

## Other publications

J. Bamidele, Y. J. Li, **S. Jarvis**, Y. Naitoh, Y. Sugawara and L. Kantorovich.  
**Complex design of dissipation signals in non-contact atomic force microscopy**  
*Phys. Chem. Chem. Phys.*, In press (2012).

H. Alhummiany, **S. Jarvis**, R. Woolley, A. Stannard, M. Blunt and P. Moriarty.  
**Dewetting of Au nanoparticle assemblies**  
*J. Mat. Chem.* **21**, 16983 (2011).

## Acknowledgements

The completion of this thesis marks the end of a long journey, one that would not have been possible without the support and encouragement of a great many people. It gives me great pleasure to thank those who have supported me throughout my PhD and made this thesis possible.

Above all, I would like to thank my supervisor Philip Moriarty. Without his tireless enthusiasm and encouragement I would not have started a PhD. His constant advice, guidance and vision have been a continuing source of support and inspiration which has not only made this thesis possible, but has allowed me to keep sight of why I enjoy science.

I would also like to thank Lev Kantorovich, who has acted as a second supervisor for the majority of my projects. His expertise and guidance have been essential to complete the work within this thesis.

I have had the pleasure of working with many people over the last few years, in particular I would like to thank Adam Sweetman for our many distracting and even informative discussions and for maintaining an exceptionally neat working environment, Peter Sharp for the great sacrifices he made, Andrew Stannard for much advice and welcome discussion, and Josphah Bamidele for helpful conversations and the NEB code. There are numerous other people who deserve mention, including Richard Woolley, Rosanna Danza, Subhashis Gangopadhyay and all of the Nottingham nanoscience group, both past and present, who have all contributed to my time here in some way.

Many friends and family members have helped me get here today, both during this PhD and my undergraduate studies, and for that I am truly grateful.

Finally, I would like to mention my fiancée Jeanette who has been an immense source of love and support. You have been my refuge from everyday life and have always put up with late nights at work, bad moods and practice presentations. It is because of you that I am anything at all, and it is to you that I dedicate this thesis (and no, that doesn't mean you have to read it).

*“A degree... is a first step down a ruinous highway. You don’t want to waste it so you go on to graduate work and doctoral research. You end up a thoroughgoing ignoramus on everything in the world except for one subdivisional sliver of nothing.”*

Isaac Asimov

# Contents

<b>Abstract</b>	<b>i</b>
<b>List of publications</b>	<b>iii</b>
<b>Acknowledgements</b>	<b>v</b>
<b>1 Introduction</b>	<b>1</b>
1.1 Introduction . . . . .	1
1.2 Thesis outline . . . . .	4
<b>2 The atomic force microscope (AFM)</b>	<b>8</b>
2.1 Introduction . . . . .	8
2.2 The scanning tunnelling microscope STM . . . . .	9
2.3 Force interactions in AFM . . . . .	12
2.3.1 Simple measurement of force . . . . .	12
2.3.2 Forces present in AFM measurements . . . . .	13
2.3.3 Van der Waals interaction . . . . .	14
2.3.4 Separating force interactions . . . . .	18
2.3.5 Origin of ‘true’ atomic resolution . . . . .	21
2.3.6 Modelling the tip apex . . . . .	24
2.4 Frequency modulated AFM (FM-AFM) . . . . .	26
2.4.1 Basics of DFM . . . . .	28
2.4.2 Relationship between force and $\Delta f$ . . . . .	31
2.4.3 PLL controlled FM-AFM . . . . .	32
<b>3 Density Functional Theory and the SIESTA code</b>	<b>35</b>
3.1 Introduction . . . . .	35
3.2 Wave mechanics . . . . .	36
3.3 Density Functional Theory . . . . .	38
3.3.1 Kohn-Sham . . . . .	39
3.3.2 Exchange-Correlation functionals . . . . .	41
3.3.3 The local density approximation (LDA) . . . . .	41
3.3.4 The generalised gradient approximation (GGA) . . . . .	42
3.4 Implementation of DFT . . . . .	43

3.4.1	Orbitals and choice of basis set . . . . .	44
3.4.2	Pseudopotentials . . . . .	45
3.4.3	Minimising the Kohn-Sham equation . . . . .	47
3.4.4	Calculation of forces . . . . .	48
3.4.5	Calculating the minimum energy geometry . . . . .	49
3.4.6	Basis set superposition error (BSSE) . . . . .	52
3.5	SIESTA summary . . . . .	54
<b>4</b>	<b>Materials and Techniques</b>	<b>56</b>
4.1	Silicon surfaces and C <sub>60</sub> . . . . .	56
4.2	The Si(100) surface . . . . .	57
4.2.1	AFM of Si(100) . . . . .	61
4.2.2	Dimer vacancy defects . . . . .	64
4.3	Hydrogen passivated Si(100) . . . . .	66
4.3.1	Dangling bond defects on Si(100):H . . . . .	67
4.4	Si(111) surface . . . . .	73
4.5	Silicon sample preparation . . . . .	76
4.6	C <sub>60</sub> molecule . . . . .	77
4.7	Modelling methods . . . . .	84
4.7.1	Modelling and testing a surface: Si(100) example . . . . .	84
4.7.2	Simulating $F(z)$ measurements . . . . .	86
4.7.3	Nudged elastic band (NEB) basics . . . . .	88
4.8	Experimental methods . . . . .	93
4.8.1	Amplitude and force calibration . . . . .	93
4.8.2	Createc LT STM/AFM system . . . . .	97
<b>5</b>	<b>Toggling bistable atoms on the Si(100) surface</b>	<b>102</b>
5.1	Experimental manipulation of Si(100) dimers . . . . .	103
5.2	Simulated $F(z)$ spectroscopy . . . . .	110
5.2.1	Tip Clusters . . . . .	111
5.2.2	Approach-retraction $F(z)$ curves . . . . .	112
5.2.3	Simulated local variation in surface stability . . . . .	114
5.3	Potential energy surface - Nudged elastic band (NEB) calculations .	117
5.3.1	Why use NEB? . . . . .	118
5.3.2	Symmetric <i>vs.</i> asymmetric transition . . . . .	119
5.3.3	Tip induced variation in PES: Pristine surface . . . . .	122
5.3.4	Defect induced variation in PES . . . . .	125
<b>6</b>	<b>Tip engineering with hydrogen terminated probes</b>	<b>129</b>
6.1	Role of orbital overlap in atomic manipulation . . . . .	130
6.1.1	A method for characterising tip structure . . . . .	132
6.1.2	Predicting methods for vertical manipulation . . . . .	136
6.2	Tip engineering on Si(100):H . . . . .	141
6.2.1	AFM observations on the Si(100):H surface . . . . .	142

6.2.2	Identifying passivated tip structures . . . . .	148
6.2.3	Direct observation of atomic scale dispersion interaction? . . .	155
6.2.4	Surface defects: Tip engineering and defect determination . .	161
<b>7</b>	<b>Analysing tip structure and molecular functionalisation</b>	<b>170</b>
7.1	Structural development of silicon tip apices . . . . .	171
7.1.1	Energy dissipation in small apex clusters . . . . .	173
7.1.2	Enhancing tip stability via surface indentation . . . . .	175
7.2	Molecular C <sub>60</sub> tip functionalisation . . . . .	182
7.2.1	Sub-molecular resolution in the attractive regime . . . . .	183
7.2.2	Modelling the C <sub>60</sub> -Si(111)-(7 × 7) system with DFT . . . .	184
7.2.3	Origin of sub-molecular C <sub>60</sub> resolution . . . . .	187
7.2.4	C <sub>60</sub> stability and bond evolution . . . . .	191
<b>8</b>	<b>Conclusions</b>	<b>198</b>
	<b>Bibliography</b>	<b>203</b>

# Chapter 1

## Introduction

### 1.1 Introduction

Nanotechnology represents an often publicly misunderstood area of research focussed on the science of “small things”. Specifically, the small things are typically on the scale of nanometres. This includes the study of matter at the atomic and molecular scale. Individual atoms are the basic building blocks of matter, and the fundamental interactions between them determine the properties of everyday materials.

During the early conceptual beginnings of nanotechnology, many exciting and advanced ideas were put forward [1] suggesting where the technology might lead. A number of these ideas, however, were met with a great deal of scepticism resulting in a series of discussions over the past few decades [2–4]. Although the concept of nanotechnology was well established, the more mundane reality of experimental research has shown that the advancement of atomic scale technology is both challenging, and time consuming, even within highly controlled ultra-high-vacuum, low temperature, environments. As such, current experimental research, rather than focusing on building complex and somewhat fanciful structures, concentrates on examining the fundamental interactions between atoms and molecules.

Out of the many tools available to study matter at the atomic scale, perhaps the most prolific are those known as scanning probe microscopes (SPM). The basic principle of SPM takes an (ideally) atomically sharp piece of material and brings it very close to the surface layer of an atomically flat sample. The sharp probe is then scanned back and forth across the surface while measuring the variation in some local interaction between the probes tip and surface atoms. The interaction can then be plotted as a 2D image, thus ‘mapping’ the positions of the surface atoms. The first, and most successful SPM instrument is the scanning tunnelling microscope (STM).

The STM exploits the phenomenon of electron tunnelling between a tip and sample to map out the electronic structure of a surface. After the advent of the scanning tunneling microscope (STM) [5], it was quickly demonstrated that spatial information from a prepared surface could be reliably obtained on an atomic level [6, 7], a feat that was rewarded with the Nobel prize in 1986 [8]. Existing methods, such as low energy electron diffraction (LEED), could typically only reveal insights into the surface atomic structure by taking data averaged over a relatively large spatial region. Consequently, this method precludes obtaining site-specific information with atomic accuracy. Therefore, the most obvious benefit of the STM is clear; once developed it opened the floodgates to enable the study of single atoms, molecules, surface defects and many atomic scale phenomena, leading to huge advances in surface science and the understanding of physics at the smallest scale.

Far from being just an imaging tool, the phenomena driving the STM can be used for many different purposes, the most relevant to this work being atomic manipulation. A careful choice of parameters can enable atoms and molecules to be picked up onto, or deposited from, the scanning probe [9]. Moreover, they can be laterally manipulated, by either pulling, or pushing the target adsorbate across a surface with the tip [10, 11]. This allows a huge array of experiments to be carried out. For instance, rather than just studying a pre-prepared sample, molecules and

atoms can be manipulated into different configurations, and in principle allow complete customisation of the experiment. In reality, however, it is not so simple, and understanding the processes behind atomic manipulation can be just as important as its outcome.

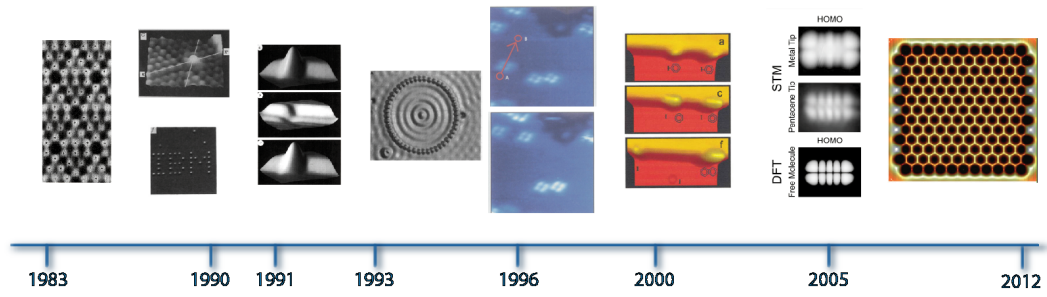


Figure 1.1: A selective history of the STM detailing some of the most important advances in atomic manipulation. Left to right. The first STM image of the 7x7 reconstruction of Si(111), putting to rest the long running debate of the surface structure [7]. STM image of the second layer of the 7x7 reconstruction of Si(111) after removal of the top layer adatoms [12]. The first demonstration of lateral atomic manipulation [10]. The first demonstration of vertical atomic manipulation used to switch an atom between two states [9]. The reproducibility of lateral manipulation is demonstrated by an elegant experiment showing electron confinement [11]. Lateral manipulation of molecules across a surface [13]. The STM is used to induce each step of a chemical reaction [14]. Sub-molecular resolution of molecular orbitals is obtained on thin insulating surfaces [15]. A graphene-like sheet is manufactured piece by piece using individual CO molecules [16].

Imaging unknown surfaces and manipulation at the single atom level with STM is now routine, allowing extraordinary experiments to be realised. To help trace some of these advances, a very selective timeline is presented in Figure 1.1. To extend the ability to observe and control matter on the smallest scale, the atomic force microscope (AFM) was developed [17]. As operated today, the AFM can be used in ultra high vacuum (UHV) to image surfaces with atomic resolution just as

the STM can. Moreover, the AFM is sensitive to the force felt between tip and sample (or, for NC-AFM, the force gradient), not the tunneling current, enabling us to ascertain a completely new subset of information from the same materials. It is even possible to operate such that both force and tunnel current information can be simultaneously acquired [18], providing complementary information that allows characterisation of materials with an unprecedented level of detail. An additional feature of the AFM is that, unlike STM, samples are not required to be electrically conducting. Although not trivial to use on insulating surfaces, AFM opens up the possibilities of carrying out experiments in systems that have erstwhile been inaccessible to the surface science community.

As with the STM, great progress in atomic manipulation with AFM has been made [19–23]. Due to the complex interaction between the scanning probe apex and surface atoms, however, atomic manipulation with AFM remains fraught with difficulties and experimental unknowns. In Figure 1.2 the timeline is expanded, selectively depicting the progress of AFM as a tool for image acquisition and atomic manipulation. Each of the AFM experiments in Figure 1.2. highlights the most formidable challenge in UHV AFM: determining the atomic structure of the tip apex. In each experiment the structure of the tip apex was paramount to the success and understanding of the experimental results, and in each case, only with the support of theoretical calculations was an explanation for the mechanisms involved obtained. The ability to understand the nature of the AFM tip apex, whilst also designing methods for its control and characterisation, forms the central focus of this thesis.

## 1.2 Thesis outline

This report focuses on the interactions involved with atomic manipulation in AFM on semiconductor surfaces. As such the next three chapters give a detailed overview of the experimental and simulated techniques implemented throughout this thesis

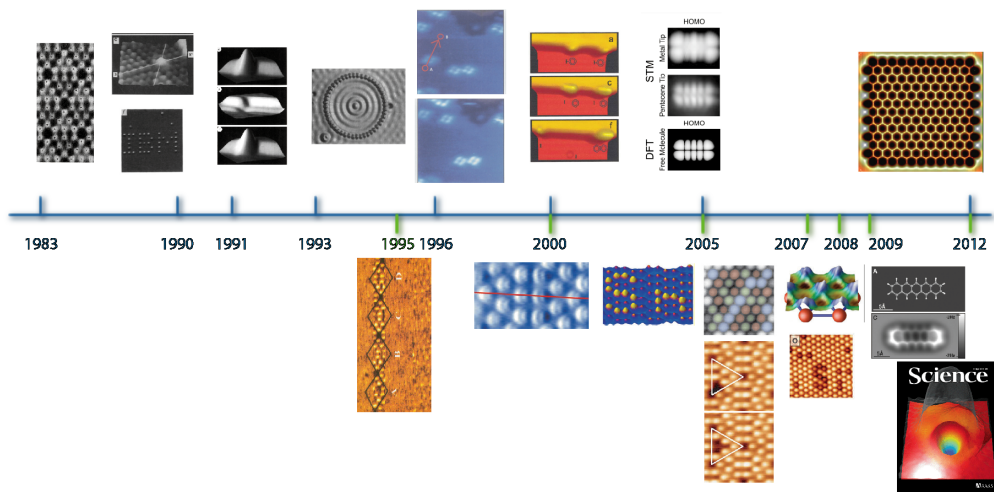


Figure 1.2: Another timeline, but with the addition of AFM results. Left to right, the first NC-AFM images with ‘true’ atomic resolution [24]. Subatomic resolution revealing the orbital structure within an atom [25]. Room temperature lateral atomic manipulation [19]. Chemical identification of atoms within an alloyed surface [26]. Lateral manipulation of adatoms on a Si(111) 7x7 surface [27]. The force required to move an atom across a surface is measured [21]. Vertical manipulation of atoms is demonstrated with a complicated exchange mechanism [20]. Submolecular resolution of molecules is shown revealing the real structure of the atoms within the molecule [28]. Subatomic resolution of the tip structure is obtained for multiple tip orientations [29].

and the various materials studied. Chapter 2 begins by explaining the basic operation of an atomic force microscope (AFM) and describes in detail the current state of the art in understanding for the force interactions responsible for atomic resolution on semiconductor surfaces and tip characterisation. Chapter 3 consists a review of the density functional theory technique (DFT) used to model many of the systems considered within this work. In the fourth chapter I review each of the sample materials included in this study, and describe many of the standard methods repeatedly implemented in the results sections.

There are three results chapters within this thesis, each of which follow a very similar theme. In chapter 5 we investigate atomic manipulation experiments carried out on the Si(100)-c( $4 \times 2$ ) surface using NC-AFM. DFT simulations allow us to examine the process of ‘dimer flipping’, where we report that the complicated interaction between the AFM tip and the surface atoms strongly affects the pathways available during manipulation. Ultimately we find that other considerations, such as surface imperfections, significantly modify the barrier heights for transition, thus suggesting a possible pathway for manipulation.

In chapter 6 I report on the simulated atomic manipulation of a single hydrogen atom within a silicon environment. Atomic transfer between the tip and surface is examined in order to establish whether variations in tip apex structure affect the outcome of manipulation. Complementary to the DFT simulations we conduct a detailed NC-AFM study of the hydrogenated Si(100) surface. We investigate the unusual appearance of the surface atoms during NC-AFM measurements, and, following a detailed study identify the unique nature of the AFM apex. The limitations to atomic manipulation are discussed within the context of the results, and alternative tip-specific experiments are suggested.

In the final results chapter, chapter 7, we examine the structure of the AFM tip apex from two perspectives. Initially we return to characterising the tip in a

silicon environment, where we report on the structure and stability of the tip apex. We find that through simple simulation, we are able to provide interesting information regarding tip stability, and commonly observed experimental dissipation. Alternatively, we examine functionalisation of the AFM probe with a C<sub>60</sub> molecule, essentially eliminating the problem of unknown tip structure. We found that by exploiting an ‘inverse imaging’ technique, we could obtain intra-molecular atomic resolution of the C<sub>60</sub> molecule. The image mechanism was found to originate from weak chemical bond formation between the reactive silicon surface and the individual carbon atoms of the C<sub>60</sub> cage.

Finally, in chapter 8, the conclusions of this study and the implications for future experiments are summarised and discussed.

## Chapter 2

# The atomic force microscope (AFM)

### 2.1 Introduction

In 1986, less than five years after the development of the STM, the atomic force microscope (AFM) was invented by G. Binnig, C.F. Quate and C. Gerber [17]. Since this time the AFM has rapidly developed into a tool regularly applied across a multitude of scientific disciplines. Fundamentally, the AFM operates via a measurement of force, or a parameter from which force can be derived, between the scanning probe tip and the sample of interest. An AFM can be designed such that it is sensitive to the forces originating between individual atoms, such as chemical bonding or Pauli repulsion, or to longer range forces such as van der Waals, electrostatic, or even magnetic forces. For this reason the AFM has the remarkable ability to operate over a range of length scales: from biological applications, resolving micron sized features, to the subatomic, imaging the individual orbitals on a single atom.

In the following section, an overview of the AFM technique will be presented, following a brief description of the STM, with particular focus on its implementation

in atomic scale study.

## 2.2 The scanning tunnelling microscope STM

The scanning tunnelling microscope (STM) exploits the phenomenon of quantum tunnelling to measure the transmittance of electrons between the tip and sample (or vice versa). Due to the exponential distance dependence of the tunnelling current ( $I_t$ ), variations in tunnelling can be detected at atomic length scales. An elementary understanding of the STM, and an appreciation of its application to atomic scale studies, can be obtained by considering the simple problem of tunnelling through a 1D barrier (see Figure 2.1) of height  $V_0$ .

Imagine a metallic tip and sample, separated in vacuum by a distance  $z_t$ . The vacuum region obviously acts as a barrier between the tip and sample, one whose width varies with tip-sample separation.

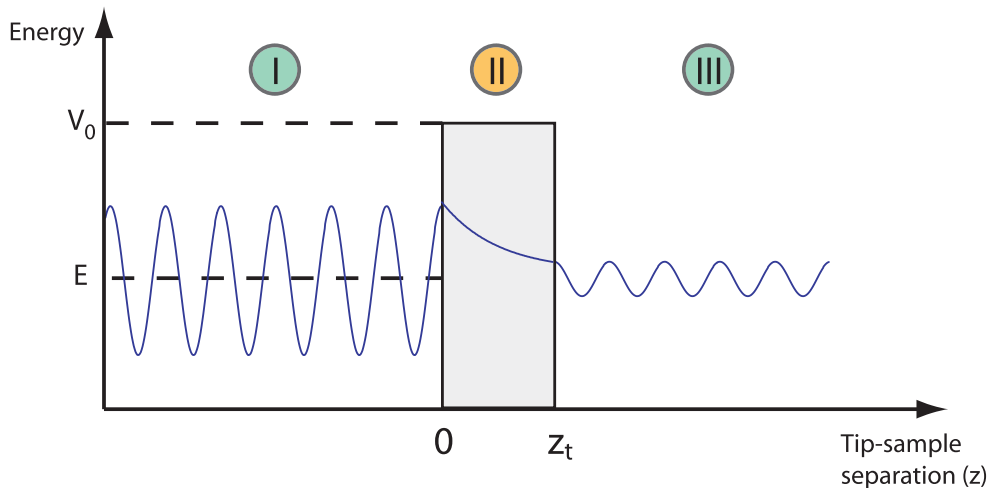


Figure 2.1: Schematic demonstrating tunnelling through a 1D barrier.

In each region the wavefunction of an incident electron can be written as:

$$\Psi_I(z) = Ae^{ikz} + Be^{-ikz} \quad (2.1)$$

$$\Psi_{II}(z) = Ce^{\mu z} + De^{-\mu z} \quad (2.2)$$

$$\Psi_{III}(z) = Fe^{ikz} \quad (2.3)$$

where  $k = \sqrt{\frac{2mE}{\hbar^2}}$  and  $\mu = \sqrt{\frac{2m}{\hbar^2}(V_0 - E)}$ .

The transmission coefficient,  $T$ , is defined as the ratio between the probability flux of the transmitted wave in region  $III$  and the incident wave in region  $I$ , i.e.  $|\frac{F}{A}|^2$ , and, as such, is related to the tunnelling current,  $I_t$ .

To obtain an expression for  $T$  we can impose matching conditions at  $z = 0$  and  $z = z_t$  for equations 2.1-2.3 and their derivatives. Combining the equations we then obtain the result,

$$T \propto I_t \propto e^{-2\mu z_t} \quad (2.4)$$

In an ideal tunnel junction between two metals,  $E$  will be close to the Fermi energy, therefore  $V_0 - E = \phi$ , where  $\phi$  is the workfunction of the tip-surface material. Using typical values for the workfunction (in the range of 4-5eV [30]) we can calculate that  $I_t$  varies by nearly an order of magnitude when the tip-sample separation (barrier width) is changed by  $\sim 1\text{\AA}$ .

As such it is clear that, providing we have a monotonic tip, and sufficient levels of vibration isolation, it is possible to resolve electronic structure at an atomic scale with STM.

The description thus far considers only a single electron. In Figure 2.2(a) a schematic for the potential barrier between a tip and sample is shown when out of electrical contact and separated by vacuum. The Fermi levels of each material are offset by the difference in  $\phi$ . When electrically connected there is a transfer of charge from the material with lower workfunction to the other and the Fermi levels

align (Figure 2.2(b)). The difference in  $\phi$  induces an electric field across the vacuum region. The Fermi level describes the electron energy, therefore, when the levels are aligned, the net tunnelling current will be zero.

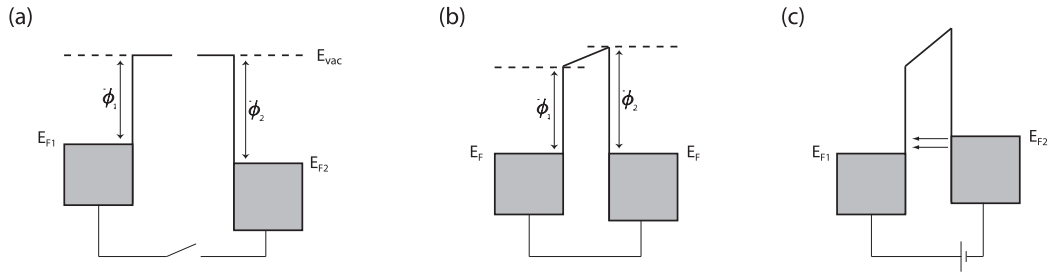


Figure 2.2: Diagrams illustrating tunnelling between a metallic tip and sample. In (a) the tip and sample are electrically isolated and the vacuum level is the common reference. In (b) the tip and sample are electrically connected and the Fermi levels align, resulting in an electric field between the two. No net tunnelling takes place. In (c) a negative bias is applied to the right hand side leading to an energy shift of  $eV$ . Electrons are now able to tunnel from the occupied (filled) states into the empty states on the left.

If a voltage is applied to the sample then its Fermi level will shift with respect to that of the tip. Therefore a net flow of tunnelling electrons will be detected. If the voltage is *positive*, electrons will tunnel from the tip into the surface (empty states), and if *negative* from the surface into the tip (filled states).

In reality, for semiconducting samples in particular, the picture isn't so simple. A semiconductor has an intrinsic band gap, such that a relatively large voltage needs to be applied for a tunnelling current to flow. Moreover, the density of states in the conduction and valence band can be complicated, and vary depending on the surface reconstruction. As such, a suitable description for these systems is more challenging. The work presented in this thesis focusses almost exclusively on NC-AFM experiments taken with zero applied sample bias. As such we will leave the topic of STM at this point and instead focus on the force interactions between the tip and sample at smaller separations.

## 2.3 Force interactions in AFM

Before explaining the experimental setup of the AFM, it is helpful to first consider the force interactions that are present between tip and sample. The AFM can be operated with relative ease such that it is sensitive to long range force interactions. Conversely, observing variations in force over atomic length scales is much more challenging, the difficulty originating from the different force interactions at play. A reasonable understanding is also essential for the purposes of simulation, and to draw meaningful conclusions from experimental data.

### 2.3.1 Simple measurement of force

The key parameter for measurement in AFM is the force between the scanning tip and sample surface. The most simple way to understand how force can be measured is to consider the set-up in Figure 2.3.

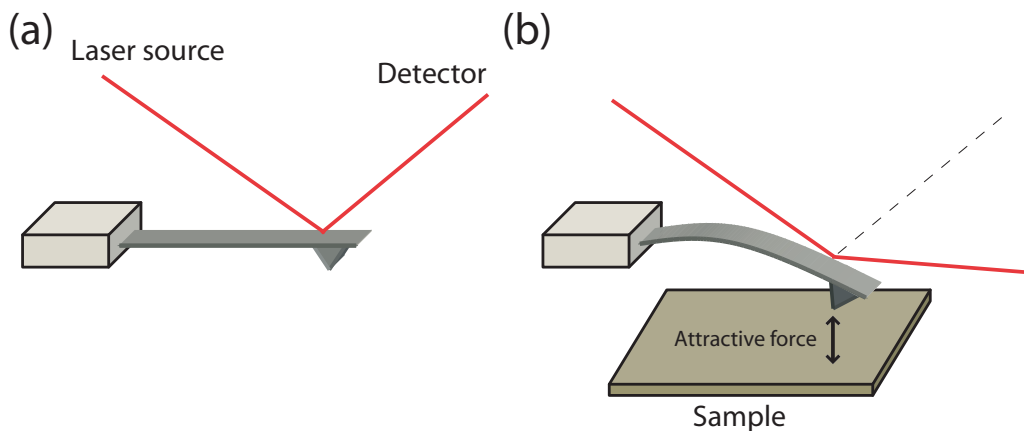


Figure 2.3: Basic diagram describing force measurement with a cantilever AFM. (a) The cantilever setup, with a laser interferometer measuring its deflection. Away from the surface no deflection is observed. (b) Close to the surface, tip-sample forces cause the cantilever to deflect by an amount measured with the laser detection setup.

The AFM probe is typically a bar of material which acts as a cantilever, such as

silicon, kept fixed at one end and with a sharp tip at the other as shown in Figure 2.3(a). The cantilever is manufactured to exhibit particular properties such that it possesses a well-defined spring constant and eigenfrequency of oscillation, and has a small radius of curvature at the tip apex.

When the cantilever is approached sufficiently close to a sample, a force will be felt between the AFM tip and the sample surface. In response to the force interaction, the cantilever will bend by an amount (defined by its stiffness) to move the tip closer to the surface (Figure 2.3(b)). If the deflection is measured, e.g. via a laser interferometer or a quadranted photo detector, the tip-sample force ( $F_{ts}$ ) can be calculated with Hooke's law (2.5).

$$F_{ts} = -kd \quad (2.5)$$

where  $k$  is the stiffness of the cantilever and  $d$  is the displacement upon deflection. Thus, a measurement of force can be made. In practice this simplistic setup has only limited usefulness. To obtain a workable signal-to-noise ratio the stiffness of the cantilever often needs to be low. As a result, the tip-sample force can often be great enough to cause a ‘snap-to-contact’, pulling the AFM tip into full contact with the surface. When in full contact, the tip-sample force is usually too high for the tip apex to remain atomically sharp, precluding atomic resolution studies. To enable routine atomic resolution measurements, the cantilever needs to be operated in the dynamic mode, by applying an oscillation (this will be discussed in more detail in Section 2.4).

### 2.3.2 Forces present in AFM measurements

The primary tip-sample forces present can be grouped into long range forces, such as van der Waals (vdW), electrostatic and magnetic interactions, and short range forces arising from chemical bonding and Pauli repulsion between atoms. Although long

range forces can be present over many nanometres, short range forces will typically occur over a length scale of only a few Angstroms.

It is the combination of these forces that contributes to all measurements taken with an AFM. It is simply a question of instrument design which determines whether a force originating from short range interactions can actually be detected, or extracted from the background of other forces. Considering how forces manifest within the tip-sample system allows us to understand how to interpret force measurements as well as to understand the origins of atomic resolution and the variations in force spectra in different systems of interest.

### **2.3.3 Van der Waals interaction**

Present and detectable in all implementations of AFM is the vdW interaction between the scanning probe tip and the sample. Magnetic forces are not always present, and often electrostatic forces can be minimised by careful choice of applied tip bias. VdW interactions, however, are unavoidable, and pose the biggest problem in extracting short range information.

The three important interactions that make up the total vdW force are the Keesom, Debye and London dispersion forces, which are all a consequence of the polarisability of atoms and molecules. The Keesom force is a dipole-dipole interaction between two permanent dipoles, whereas the Debye force is that felt between a polar molecule and an induced dipole within a non-polar molecule (dipole-induced dipole interaction). The final interaction acts between all atoms and molecules and is known as the London dispersion force. This originates from two instantaneously induced dipoles and will always be present during force measurements.

Although expressions can be derived for each interaction [31] they all share a similar form, where the non-retarded vdW interaction energy between two atoms can be written as equation 2.6.

$$U(r) = -\frac{C}{r^6} \quad (2.6)$$

where  $C$  is a constant coefficient, typically including the polarisability of the atoms and/or the dipole moment of any permanent dipoles.

This of course does not accurately reflect the geometry of the system in an AFM experiment. To do so, one must consider the vdW interaction between two larger bodies, not just atoms or small molecules. For this purpose we can again use equation 2.6 to describe the atom-atom pair potential. We then make the assumption that the net interaction energy between larger bodies of atoms or molecules is just the sum of each atom-atom interaction between one body and another. In the case of induced dipoles it is clear that a larger collection of atoms forming a single body will have a large number of interactions affecting itself and the induced dipoles on each atom. Nevertheless, the approximation is sufficient for this explanation.

In Figure 2.4(b-d) three situations are described involving interactions with a surface, shown with the original atom-atom interaction in Figure In Figure 2.4(a). Presented with the diagrams are the final results for the force obtained from the interaction energies.

The four geometries relate to four over-simplistic model cases. Figure 2.4(a) shows the simplest case of two ‘points’, such as atoms or molecules. In (b), the interaction between a single point and a flat surface is shown. Although this still does not represent a physical system, the vdW force acts over a much longer range. In (c), the AFM tip is approximated as a sphere representing a particular radius of curvature for the tip apex. In this case the interaction energy follows a  $1/r$  dependence resulting in a slower variation in the vdW force as the separation,  $D$ , is increased. Although the larger macroscopic shape of the AFM tip is not considered in (c), a sphere model is often quite successfully used to model the long range vdW component of force in AFM simulations [32,33]. Finally, a surface-surface interaction

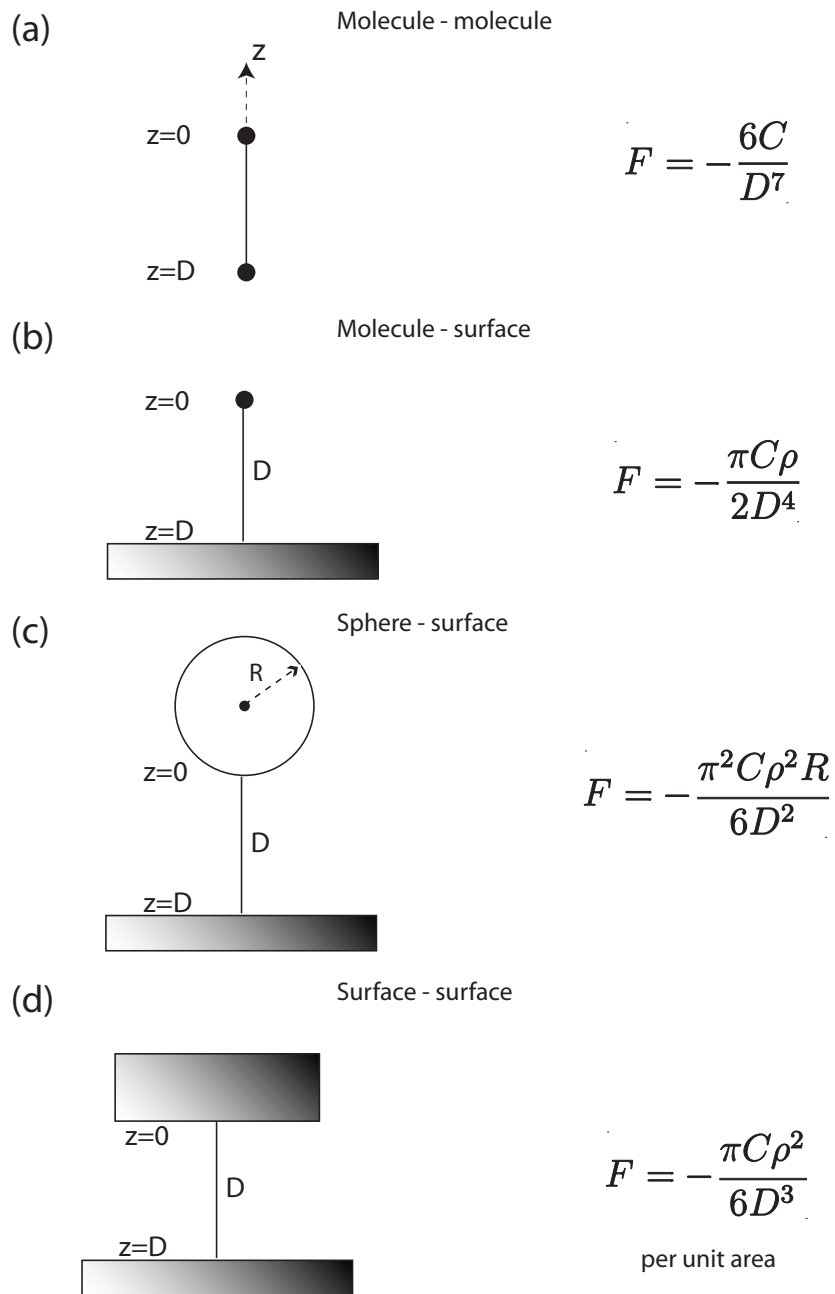


Figure 2.4: VdW interactions between bodies of different geometries. See [31] for derivation of equations.

is illustrated in (d) to model the perhaps extreme case of a blunt tip after severe treatment.

To help visualise the distance dependence of the vdW force as expressed in Figure 2.4, the four expressions for force are plotted in Figure 2.5(a). Arbitrary values are used for the constant parameters in the expressions and each curve has been normalised w.r.t. its own maximum value such that the distance dependence is clear.

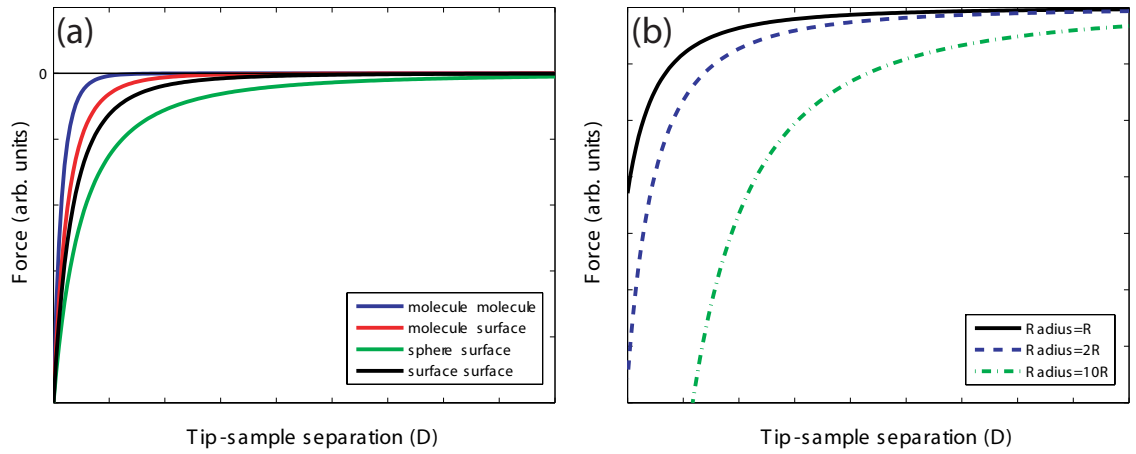


Figure 2.5: Plots of vdW force using equations in Figure 2.4. (a) Comparison of distance dependence for each geometry shown in Figure 2.4. (b) Variations in the magnitude of  $F_{vdW}$  depending on the radius of a spherical AFM tip apex.

In Figure 2.5(a) the variation between the different models is clear, highlighting the importance of a correct choice of geometry. As expected from the equation in Figure 2.4(c), the green curve (corresponding to a spherical tip apex) shows a longer tail-off in force at large tip-sample distances compared to the other geometries. A long tail in  $\Delta f$  is often observed experimentally, and to some extent can be used as a rough measure of tip sharpness.

The spherical tip approximation also has another parameter, the sphere radius,  $R$ . Figure 2.5(b) shows how larger tip radii affect the magnitude of the vdW interaction. It is clear that increasing the radius of curvature by a factor of two will double

$F_{vdW}$ . This can be problematic at small tip-sample distances where any uncertainty in the tip radius will have the largest impact on the magnitude of the force. Short range chemical forces are by nature only detected at very small tip-sample distances. Confidence in the measured radius of curvature, therefore, becomes very important. Experimentally, it can be challenging to estimate the tip apex radius of curvature without significant error bars. Consequently, uncertainties in the vdW interaction can be similar to the variations shown in Figure 2.5(b). Ultimately, for these reasons, due to the often large contribution  $F_{vdW}$  makes to  $F_{TOT}$ , uncertainties in  $F_{vdW}$  can be just as large as  $F_{chem}$  making extraction of the short range forces largely meaningless. Therefore better strategies are required to separate the force interactions.

#### 2.3.4 Separating force interactions

Although AFM is able to measure chemical forces, separating this information from the long range force contribution is a major challenge. In an approach by Guggisberg *et al* a modelling method, similar to those discussed in the previous section, was used to calculate the long range vdW force component [32, 34]. Once calculated,  $F_{vdW}$  was subtracted from  $F_{TOT}$ , in principle leaving only the short range chemical force information.

While in theory this approach can work, it relies on a good model for the vdW interaction. Due to the sometimes large contribution that  $F_{vdW}$  makes to  $F_{TOT}$ , any failures of the model could add a significant error to the extracted  $F_{chem}$ . As such, with the complicated nature of a real experimental scanning tip, a spherical tip apex with a well defined radius of curvature will struggle to completely describe the full vdW interaction.

To properly separate the long and short range interactions, ambiguity about the long range force must be eliminated. Ideally this requires direct measurement of

the long range contribution to force with exactly the same tip used to measure the short range data. This can present many problems, as the tip can become ‘blunt’ over time, changing the long range interaction between experiments. Even relatively minor controlled tip crashes, regularly implemented to atomically sharpen tips, can dramatically affect long range contributions.

Lantz *et al* [35] introduced an excellent strategy where the measurement of the long range force contributions is carried out in parallel with measurement of the short range forces. The particular system they exploit to enable use of this method is the 7x7 reconstruction of Si(111). The 7x7 surface consists of adatoms arranged into rhombus like shapes separated by ‘corner holes’. Due to the complicated nature of the reconstruction, the corner holes are two layers deep and  $\sim 9.4\text{\AA}$  wide creating a relatively large ‘null’ region on the surface.

As shown in Figure 2.6 the corner hole can be exploited as a way to directly measure the long-range contribution to force, removing the need for modelling and approximation. Initially spectra are taken over an adatom, and therefore they will contain both short and long range interactions (Figure 2.6(a)). Another spectroscopy measurement, *taken over the same z range*, is subsequently acquired over a corner hole (Figure 2.6(b)). The size and depth of the hole is large enough such that over the same  $z$  range, the tip does not come close enough to any of the surface atoms to feel any short range interactions. Therefore the two spectra can be subtracted from one another leaving only data corresponding to short range interactions, enabling the possibility of site specific measurements on an atomic scale (Figure 2.6(c)).

Although Si(111) 7x7 is a special case<sup>1</sup>, this technique can also be used on molecules and other adsorbed features. Rather than requiring a hole, we simply make use of the fact that the molecule is higher in  $z$  compared to the surface. Consequently, spectra can be taken on and off the molecule to extract the short

---

<sup>1</sup>the corner hole is an unusually large vacancy-like region

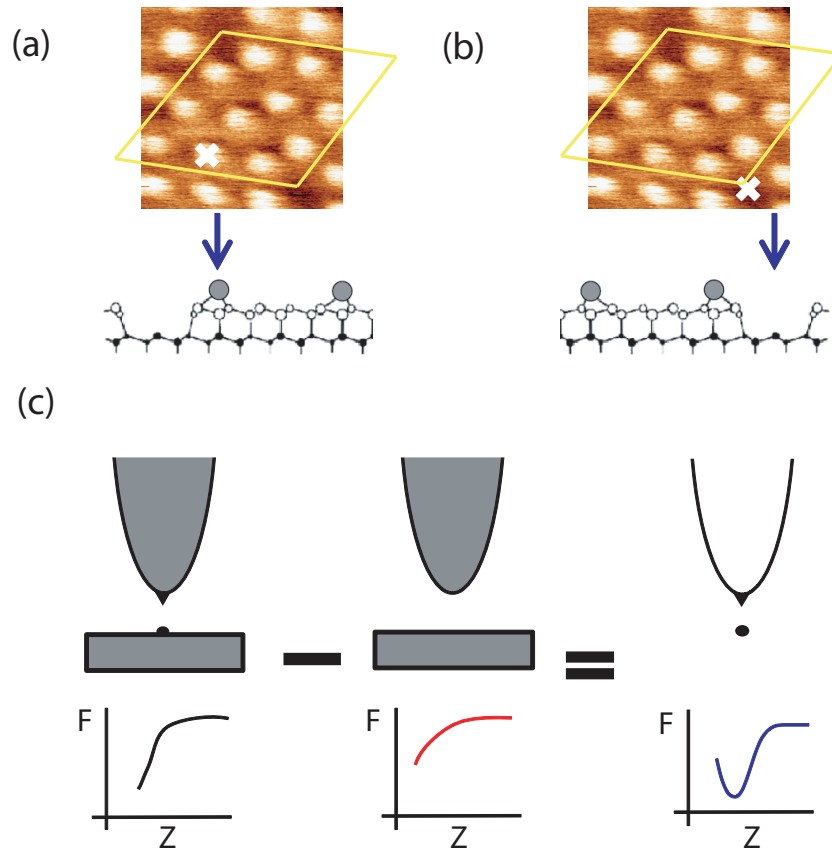


Figure 2.6: Separation of long-range and short-range forces. (a) Spectra taken over a surface atom contain both short and long range interaction forces. (b) Spectra taken over the 7x7 corner hole contain only long range force contributions. (a) and (b) show constant  $\Delta f$  images of the Si(111)-7x7 surface and partial side-on schematics of the unit cell. (c) Subtracting (b) from (a) leaves only the force contributed from short range interactions.

range tip-molecule interaction.

### 2.3.5 Origin of ‘true’ atomic resolution

During the time after the first demonstration of the AFM, considerable effort was made to ascertain whether the technique could yield atomic resolution imaging to the same standard as STM experiments. Particularly important to the AFM’s success in this field was the ability to image reactive samples such as semiconductor surfaces. The prototypical semiconductor surface is the 7x7 dimer-adatom-stacking fault (DAS) [36] reconstruction of Si(111), which was instrumental in highlighting the success of the STM. The particular problem for AFM is the high reactivity of the surface dangling bonds, and the strong interaction they have with the tip apex. Such strong interactions put a high load on the scanning tip, thought to be too much for an atomically sharp tip to withstand [37]. Furthermore, the magnitude and spatial range of these interactions relative to the dominating long-range interactions can be very small, necessitating a very good signal-to-noise ratio.

These problems were, however, overcome when ‘true’ atomic resolution was finally demonstrated by Giessibl [24] as well as Kitamura and Iwatsuri [38] in 1995 using the FM-AFM technique (see section 2.4 and [39]). Although it was assumed that short-range covalent bonding was responsible for the atomic resolution images, the exact nature of the tip-sample interaction was unknown until rigorous theoretical confirmation [40, 41] was carried out.

In the original image from Giessibl shown in Figure 2.7 three distinct regions demonstrating different image qualities are observed. In the bottom half of the figure (slow scan direction is bottom to top) is a typical ‘multi-tip’ image where although weak atomic contrast is observed, the corner holes and atomic defects are less visible. In this instance the AFM tip is likely made up of multiple tip apices, each of which make contributions to the total force gradient measured, resulting

in an unclear image. A single tip atom, closer to the surface than the others, may be responsible for the largest contribution, resulting in the faint resolution observed. Approximately half way through the scan the tip deteriorates and features are no longer observed until, for a few scan lines, the image shows very clear atomic structure. Inside the unit cell marked ‘A’, a missing adatom defect can be seen, demonstrating that this is ‘true’ atomic resolution, resulting from a single atomic apex. After only a few scan lines, however, the tip quality again deteriorates and atomic resolution is lost.

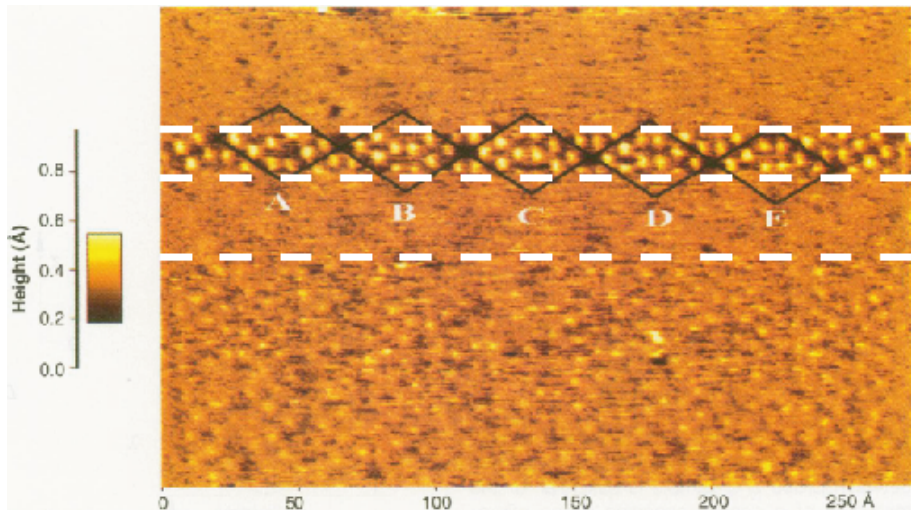


Figure 2.7: The first AFM image with ‘true’ atomic resolution. Marked by dashed lines are three regions of image quality marking lower quality regions of the image, until for a few scan lines high quality atomically resolved resolution is achieved. Adapted from [24].

Two years after Giessibl’s publication, Perez *et al* [40] published the first of two theoretical papers which attributed the experimental images to the onset of covalent bonding between a silicon tip cluster and the surface atoms. Two different tip types were studied based on the natural cleavage (111) plane of silicon, (Figure 2.8). Each tip consists of four Si atoms. One tip, however, has additional H atoms saturating the dangling bonds of the atoms in the base of the tip. The saturation results in hybridization of the apex silicon atom to a state similar to the bulk  $sp^3$ , leading to

the formation of a dangling bond [Figure 2.8(d)] which can be orientated parallel to the surface normal.

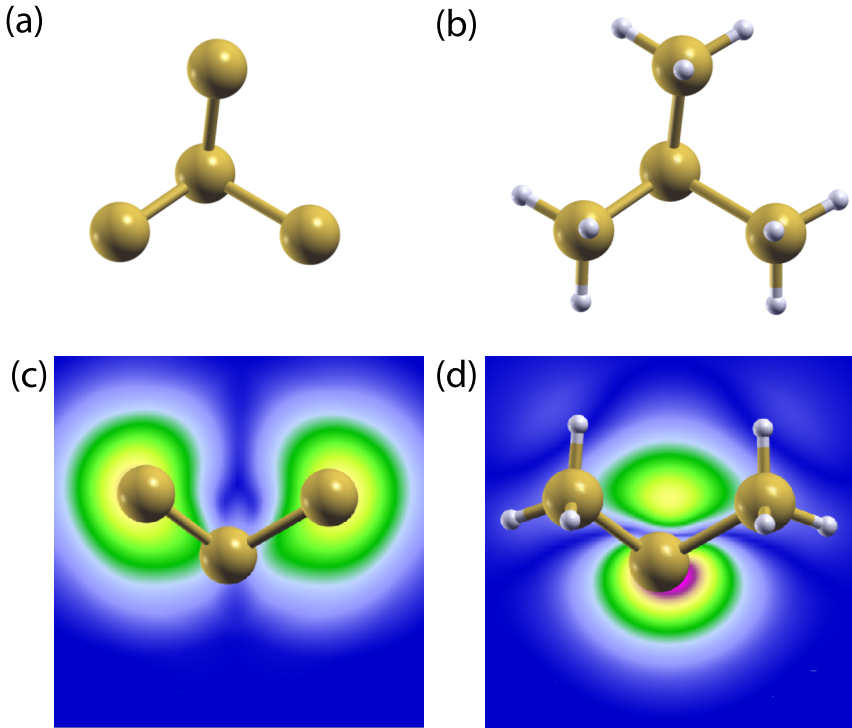


Figure 2.8: Ball-and-stick models of the tips used in [40, 41] reproduced to illustrate the differences in electronic density. (a) and (b) show top down ball-and-stick models of each of the four atom silicon tip clusters, in (b) the cluster has additional hydrogen atoms to terminate the rear three silicon atoms. (c) and (d) show electron density plots (side on) showing how the hydrogen capping of tip (b) leads to  $sp^3$  like hybridisation in the apex atom leading to a protruding dangling bond. Notice the offset in electronic density, which is an artefact of the unrealistic small tip cluster preventing further relaxation due to the hybridisation.

DFT simulations were conducted [40] to calculate the total energy and normal force of the tip-surface system at a constant tip-sample separation of 5 Å. The calculations were carried out for each tip as they were laterally displaced between adatoms<sup>2</sup>. The simulations found that the  $sp^3$  hybridised tip structure (Figure

<sup>2</sup>The surface model was a 5x5 reconstruction of the Si(111) surface to save computational time. This, however, contains the same adatom structure as 7x7

2.8(b),(d)) showed strong variations in normal force and total energy indicating the onset of covalent bonding between the tip and surface dangling bonds. Conversely, the effect is significantly less pronounced for the silicon tip in Figure 2.8(a),(c). The results suggested that only a silicon tip terminated with a dangling bond would supply a strong enough interaction with the surface to explain the corrugation in Giessibl's experimental image. Further confirmation would come when experimental  $F(z)$  spectra became available for comparison with further calculations.

In a separate paper, Perez *et al* [41] calculated the total energy, and normal force as a function of tip displacement in the  $z$  direction.  $F(z)$  spectra were simulated over various locations, including a silicon adatom, using the same  $sp^3$  hybridised tip. When Lantz *et al* [35] succeeded in making the same measurement *experimentally*<sup>3</sup>, they found that the results agreed extremely well with the simulated data from Perez *et al*, both of which observed a turnaround force value of  $\sim 2.1\text{nN}$ .

The excellent agreement between experiment and simulation confirmed that the interaction mechanism for AFM on reactive surfaces is due to weak chemical bonding between the surface adatom and tip cluster dangling bonds. The collaboration of simulated techniques and experimental observation highlights the triumph of DFT in understanding AFM at the atomic scale. The ability to build structures with known chemical species allows us to examine the tip apex in a controlled way that, currently, simply isn't possible experimentally.

### 2.3.6 Modelling the tip apex

As more surfaces were studied with AFM, collaborations between experiment and theory became more and more important. Initially, in theoretical studies designed to investigate contrast formation in AFM, silicon was regularly chosen as the tip material. This choice was motivated by the UHV-sputtered silicon cantilevers regularly

---

<sup>3</sup>via the force difference method in section 2.3.4

used throughout experiments at the time (before, for instance, the qPlus technique became more widespread). Although this approximation was suitable for silicon surfaces (see previous section), simulated results using a silicon tip often failed to agree with experimental measurements on metals or polar materials [42, 43].

It was quickly recognised, however, that silicon terminations might not always be present. During experiments, data acquisition is often optimised by first controllably crashing the tip into the surface. As such it is highly likely that surface material is transferred to the tip apex. Indeed, following this assumption, combined simulation and experiment have now helped to explain the mechanisms behind imaging not only on semiconductor surfaces, but also metals [42, 44], insulators [45, 46], polar surfaces [43, 47, 48] and graphene-like structures [49]. Furthermore, simulations can help us postulate plausible mechanisms for atomic manipulation.

Of course the real experimental termination can be complicated, and will be determined by the structure of a significant number of atoms. In *ab initio* calculations only relatively simple tip clusters can be modelled. On semiconductor surfaces in particular, a wide range of tip apex structures have been developed to explain experimental observations. These include basic silicon clusters [40, 41], oxide and carbon terminations [50], more complicated dimer terminated clusters [51–53] and very large structures designed specifically to investigate dissipation pathways [54]. Many of these tip structures are shown in Figure 2.9. Although some of these structures, for instance the H3 and dimer terminations, are modelled as over-simplistic and small apices, they have in fact been observed to terminate much larger silicon clusters following simulated annealing [52]. As such, even though the tip apices are small and simple, they should accurately reflect experimentally possible terminations.

It is clear that a large number of semiconductor tip terminations are possible, each of which comprised of a tip apex atom backbonded to a different local config-

uration. The variation in structure, therefore, significantly complicates our understanding of experimental processes. The theme of simulation supporting experiment, or experiment supporting simulation will form a central focus of this report, which will reinforce the idea that their combination is essential to understanding processes at the atomic level.

A rather elegant proposal, significantly reducing the uncertainty surrounding the tip, was demonstrated by the IBM Zurich group. By transferring an individual CO [57] molecule from the surface to the tip apex (see Figure 2.9(e)), Gross *et al.* [28] observed a dramatic increase in AFM resolution. In particular, due to the interaction between the CO and a surface adsorbed pentacene, they reported the first ever submolecular, atomic resolution images. The technique has since been used to obtain submolecular resolution for a number of molecules [55, 56].

To obtain these images, the authors exploited the passivated nature of the CO molecule to interact in the Pauli repulsion regime. As such, even though molecular-tip functionalisation enables us to obtain images with an unprecedented level of detail, manipulation experiments become significantly more complicated. Therefore, even though a diverse range of experiments are now possible with the correct tip termination, we are still far from a situation where we can fully control the tip-sample interaction in any system, for any purpose.

## 2.4 Frequency modulated AFM (FM-AFM)

As briefly mentioned in section 2.3.1, static (contact mode) AFM, whilst offering a simple interpretation of data, can only provide atomic resolution in a limited number of systems. To overcome this issue the AFM can be operated such that the cantilever is deliberately oscillated at, or near its eigenfrequency,  $f_0$ . This is generally termed dynamic force microscopy (DFM) and involves either amplitude modulation (AM) or frequency modulation (FM) techniques. The AM-AFM implementation is

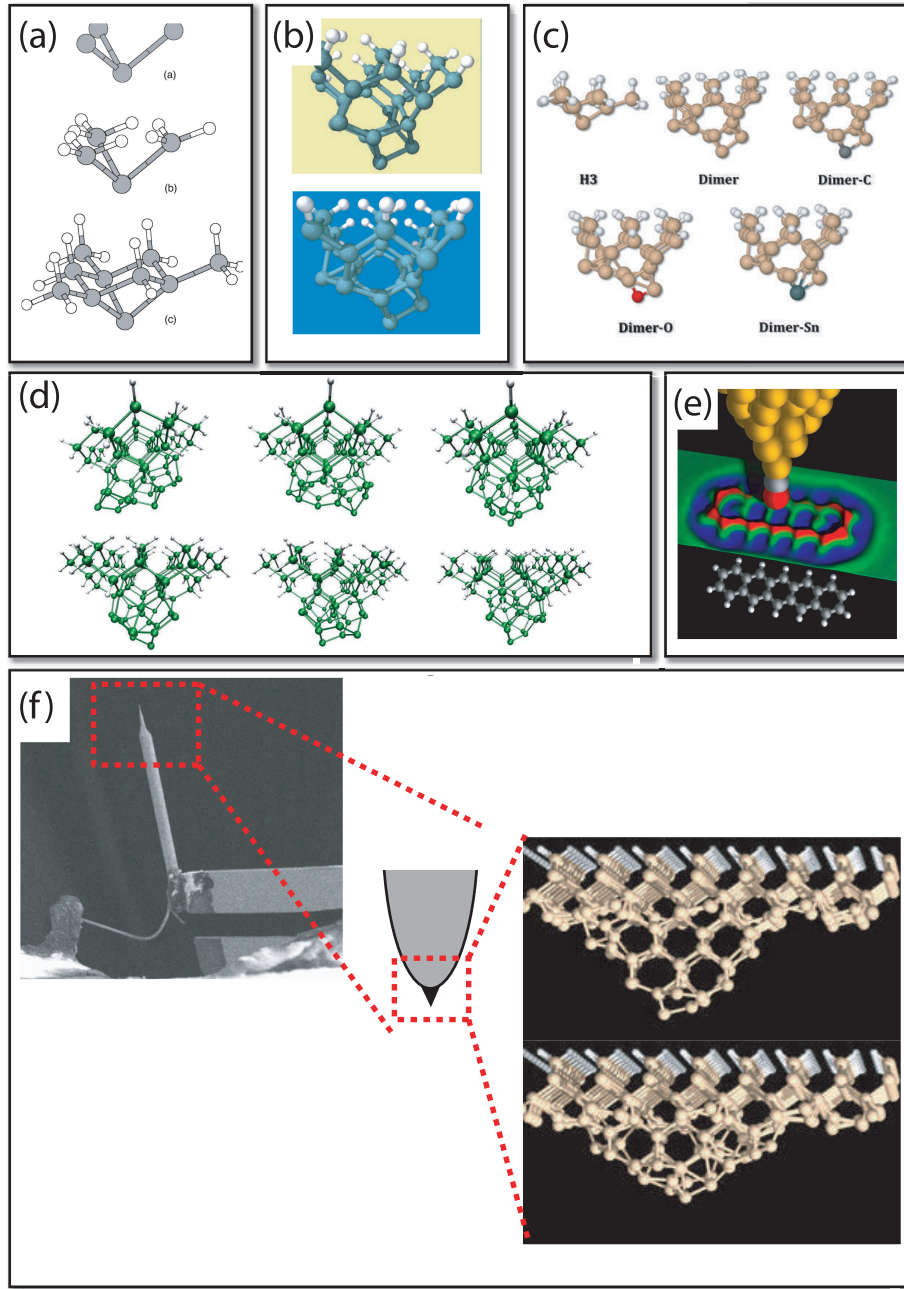


Figure 2.9: Simulated structures used to model AFM terminations on semiconductor surfaces and CO tip functionalisation. (a) simple ‘H3’ structures adapted from Perez *et al* [40, 41]. (b) Dimerised tip structures adapted from [51–53]. (c) Contaminated tip structures adapted from [50]. (d) Large, complicated tip structures adapted from [54]. (e) CO functionalisation of a Cu tip used to obtain the submolecular resolution in [28, 55, 56]. (f) Cartoon illustrating the apex of a qPlus sensor. The ball-and-stick models are adapted from Pou *et al* [52].

most widely used in ambient conditions with low Q-factors where requirements for  $z$  noise are less stringent than what is required for resolution of atomic corrugations in UHV. To resolve atomic corrugations, a high Q factor is required, which dramatically increases the integration time required for the transient change in amplitude to decay ( $\tau \sim \frac{2Q}{f_0}$ ). Consequently, operation of AM-AFM in UHV is generally impractical, however, when operated in the FM mode, the transient time no longer depends on Q and decays within a timescale of  $\tau \sim \frac{1}{f_0}$ . As the results in this report focus exclusively on atomic scale imaging with the FM-AFM technique, AM-AFM will be largely omitted from discussion.

To enable low noise measurements on a reasonable time-scale FM-AFM was developed. Originally demonstrated using magnetic force microscopy [39] FM-AFM made major improvements in image resolution [58, 59] until in 1995 true atomic resolution imaging was finally observed on a reactive surface. Although multiple problems remain to hamper atomic resolution imaging, the FM-AFM technique has been essential to overcome many obstacles enabling rapid advancement.

#### 2.4.1 Basics of DFM

To understand FM operation, it is useful to start by understanding the relationship between the frequency shift and the tip-sample force. The AFM cantilever/tuning fork, when excited in the dynamic mode, behaves as a damped, forced harmonic oscillator. The eigenfrequency of the freely oscillating cantilever is described by equation 2.7

$$f_0 = \frac{1}{2\pi} \sqrt{\frac{k}{m_{eff}}} \quad (2.7)$$

where  $k$  is the spring constant and  $m_{eff}$  the effective mass of the cantilever. When the AFM tip-sample separation is reduced such that the tip interacts with the surface, a force of  $F_{ts}$  will be present with an associated spring constant of  $k_{ts}$ .

This additional interaction modifies the effective stiffness of the cantilever, shifting its eigenfrequency by an amount  $\Delta f$  relative to its free resonance,  $f_0$ .

The expression describing  $\Delta f$  can be easily obtained if the force gradient is approximated to be constant during the oscillation cycle, i.e. when the oscillation amplitude is very small. This leads to equation 2.8 which can be substituted into 2.9.

$$k_{ts} = -\frac{\partial F_{ts}}{\partial z} = \frac{\partial^2 V_{ts}}{\partial z^2} \quad (2.8)$$

$$f_0 + \Delta f = \frac{1}{2\pi} \sqrt{\frac{k + k_{ts}}{m_{eff}}} \quad (2.9)$$

After Taylor expanding  $\sqrt{k + k_{ts}}$  we arrive at 2.10

$$\Delta f = \frac{-f_0}{2k} \frac{\partial F_{ts}}{\partial z} \quad (2.10)$$

which explains how the force gradient (not force), is simply related to the frequency shift of the cantilever. Therefore, by monitoring the frequency shift of the cantilever from its free resonance, a measure of the force gradient can be obtained.

$F_{ts}$  is made up of long and short range contributions, such as the long-range vdW and short-range chemical interactions. These contributions can be reasonably modelled with a sphere-surface vdW interaction and a Morse potential, the combination of which makes up the total tip-sample interaction force (Figure 2.10(a)). Therefore the force potential contains both attractive and repulsive regions. When operating within the attractive region of the potential, the frequency shift will be negative and largest in the region of greatest force gradient, as shown in Figure 2.10(b). If the tip-sample distance is reduced such that the force becomes dominated by repulsive interactions, then the frequency shift will be positive. Due to the non-monotonic behaviour of the force interaction, however,  $\Delta f$  feedback is generally too unstable

to operate in the repulsive part of the potential and scans are usually performed in constant height (unless only a very small attractive interaction is present, see Chapter 6).

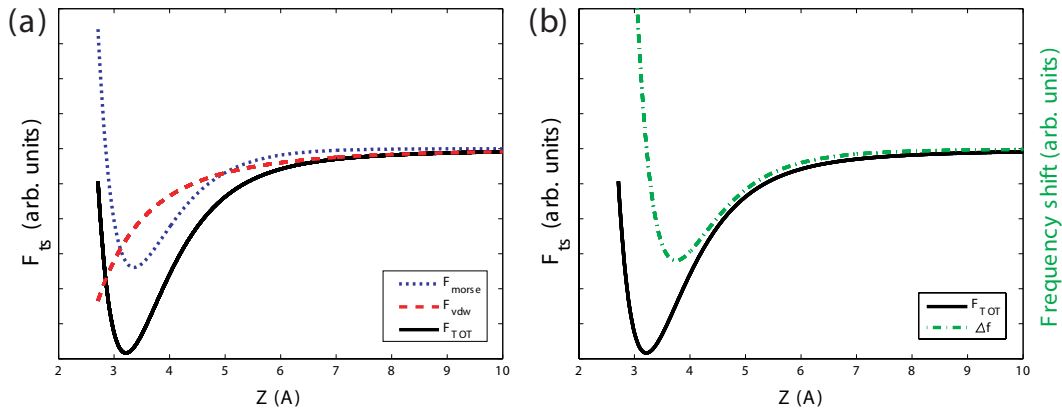


Figure 2.10: (a) Example plot of force contributions. The total force interaction (black solid curve) consists of long- and short-range contributions. The long-range contribution can be approximated as a sphere-surface vdW interaction (red dashed curve), and the short-range chemical forces by a Morse potential (blue dotted curve). (b) Plot of frequency shift calculated from  $F_{TOT}$  using equation 2.10.

In the frequency modulated mode of AFM, the cantilever is excited on resonance at a constant amplitude. As the resonant frequency shifts due to the interaction forces, so must the excitation frequency so that the cantilever continues to be excited on resonance. Therefore, the amplitude is maintained at a constant value, and it is the frequency shift,  $\Delta f$ , which is monitored and used as the feedback parameter. As such, when taking measurements, FM-AFM most generally requires two independent feedback loops to operate, one to maintain the cantilever oscillation, and another to act as a distance controller for feedback. If the PLL is also used to drive the cantilever oscillation, then a third feedback loop is required to maintain a constant phase difference between the drive signal and the cantilever response. All of the experimental data taken in this report used a phase-locked-loop (PLL) to provide the driving frequency, therefore other methods will be omitted from the following discussion.

### 2.4.2 Relationship between force and $\Delta f$

The relationship between  $\Delta f$  and the force gradient for small oscillation amplitudes is relatively simple. Typically, however, the oscillation amplitudes used in experiment are too large ( $>1\text{\AA}$ ) to be related so simply. To accurately calculate the force from  $\Delta f$  data taken at arbitrary oscillation amplitudes, Sader and Jarvis [60] derived a more complicated set of equations.

To reach each of the expressions reproduced in this section, complicated, and largely unintuitive, mathematical derivations are required. To understand the origin of these expressions the reader is directed to the original papers [60, 61] and the references therein.

To obtain the expressions for  $F(z)$  and  $U(z)$  Sader and Jarvis began with the general formula for converting force to frequency shift originally derived by Giessibl [61].

$$\frac{\Delta\omega}{\omega_{res}} = \Omega(z) = -\frac{1}{\pi ak} \int_{-1}^1 F(z + a(1+u)) \frac{u}{\sqrt{1-u^2}} du \quad (2.11)$$

where  $F$  is the force interaction,  $\omega_{res}$  is the unperturbed eigenfrequency,  $\Delta\omega$  is the frequency shift,  $a$  is the amplitude of oscillation,  $z$  is the distance of closest approach between tip and sample and  $u = \cos\phi$ .

Following a complicated mathematical derivation, they obtained a general formula for the force,

$$F(z) = 2k \int_z^\infty \left( 1 + \frac{a^{\frac{1}{2}}}{8\sqrt{\pi(t-z)}} \right) \Omega(t) - \frac{a^{\frac{3}{2}}}{\sqrt{2(t-z)}} \frac{d\Omega(t)}{dt} dt \quad (2.12)$$

and the interaction potential,

$$U(z) = 2k \int_z^\infty \Omega(t) \left( (t-z) + \frac{a^{\frac{1}{2}}}{4} \sqrt{\frac{t-z}{\pi}} + \frac{a^{\frac{3}{2}}}{\sqrt{2(t-z)}} \right) dt \quad (2.13)$$

$t$  is used as a dummy variable representing the tip-sample separation, to prevent  $z$  from being used for both the lower bound of the integral and the integration variable.

Although expressions 2.12 and 2.13 may appear unintuitive and cumbersome, they are able to provide force values with a significant degree of accuracy and are now routinely used across the field of NC-AFM. The typical method we use in this thesis to implement this approach is described in a later section (4.8.1).

### 2.4.3 PLL controlled FM-AFM

Illustrated in Figure 2.11 is a simplified flow diagram describing the most important aspects of the PLL setup. The oscillation signal is acquired from a deflection sensor, which is then passed through a bandpass filter to remove noise from unwanted frequency bands. At this point the signal is split and used for both the amplitude and the setpoint controller.

#### Amplitude controller

An RMS-to-DC converter measures the RMS noise of the oscillation and outputs a DC value corresponding to its amplitude. The measured amplitude is then sent to a PI controller to compare with, and converge to, the user determined amplitude setpoint.

To provide a clean oscillation signal to drive the amplitude at the correct frequency<sup>4</sup>, the PLL is used. The PLL detects the phase of the incoming signal using  $f_0$  as a reference. A voltage controlled oscillator (VCO) is then used to output a clean oscillation at the detected frequency. The signal is output from the PLL, and also serves as the new reference signal for the detector.

For a damped, driven oscillator, the phase of the drive amplitude,  $\phi$ , should be  $\frac{\pi}{2}$

---

<sup>4</sup>the resonant frequency will constantly change due to  $F_{ts}$ , therefore it must be measured from the oscillation signal

when driven at  $f_0$ . Therefore the output signal is phase shifted by  $90^\circ$  and input to an analogue multiplier along with the PI controller output. The resulting signal can then be used in the oscillation actuator (the excitation signal) to maintain a constant oscillation. Usually the excitation is applied mechanically using piezoelectronics.

### **$\Delta f$ setpoint controller**

With the PLL already briefly explained, the setpoint controller is much simpler to understand than the oscillation controller. The frequency of the oscillation signal is compared to the eigenfrequency of the freely oscillating cantilever, measured before the tip was approached toward the sample. If the AFM is operating with constant  $\Delta f$  feedback, then the measured  $\Delta f$  is compared to the user input setpoint. A PI controller then controls the  $Z$  extension of the scan piezo to maintain a constant  $\Delta f$ .

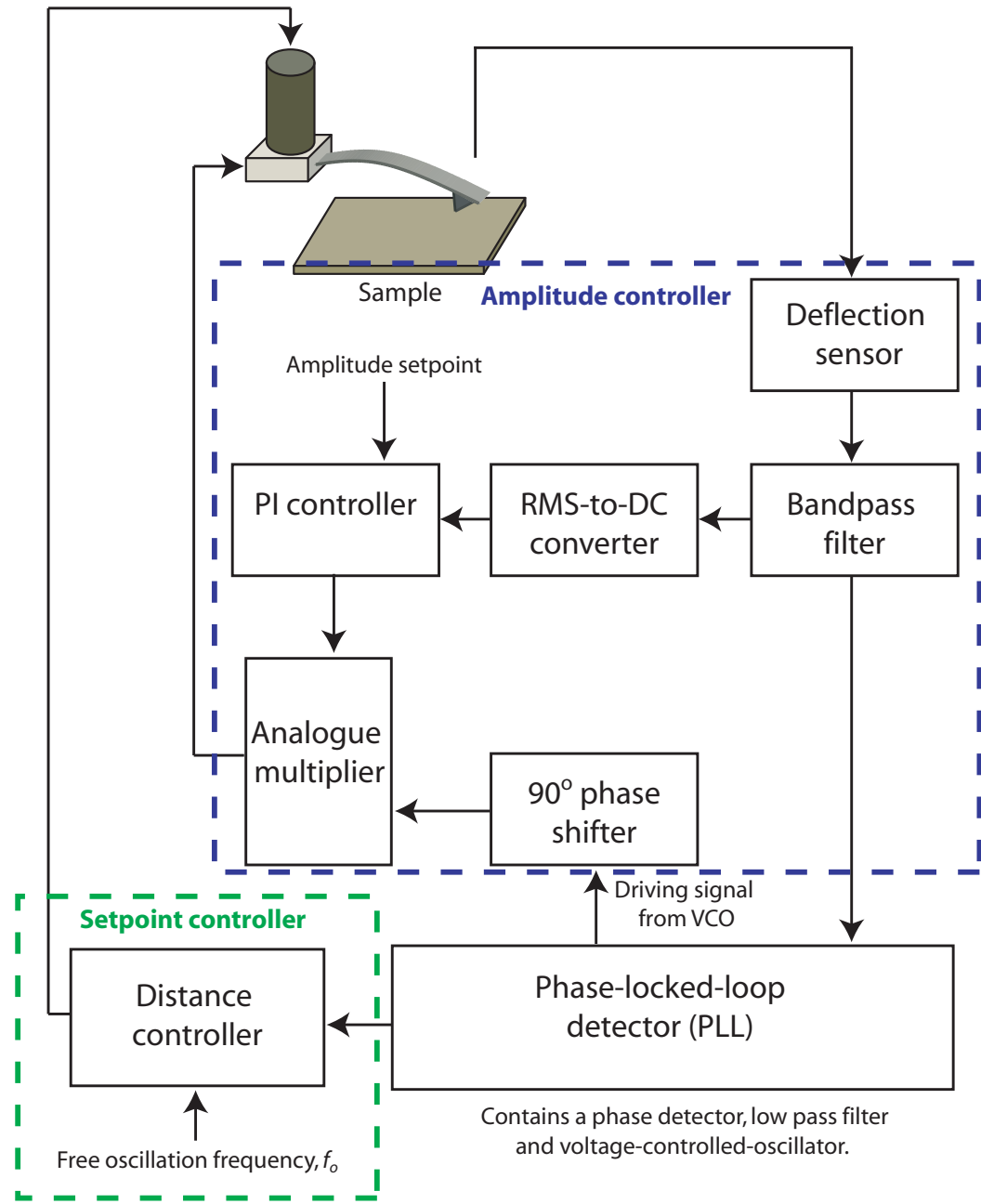


Figure 2.11: Schematic of the experimental PLL controlled FM-AFM setup.

## Chapter 3

# Density Functional Theory and the SIESTA code

### 3.1 Introduction

The necessity for theoretical modelling arises from the physical limitations of experimental techniques. That is not to say that current experimental equipment is flawed, just that theoretical modelling allows us to probe systems in a way that isn't otherwise possible. For instance, how does molecule X bond to surface Y? Or why do I obtain certain measurements with my scanning probe technique on system XY? In a theoretical simulation, many of the unknown aspects of the experimental system can be customised and tested. Calculations can be carried out and compared with experimental measurements and the simulated model can then be sensibly modified until the results agree (e.g. the correct bonding configuration can be chosen from a larger collection of equally likely candidates). With this protocol, multiple bonding configurations, system geometries or atomic arrangements can be tested until the measurements match with experiment and the understanding of the physical system can be improved. Atomic processes can then be better understood and future

experiments tailored for specific outcomes.

In this thesis, modelling is carried out with density functional theory (DFT). DFT is applied primarily to help understand experimental results, explain the mechanisms for atomic manipulation, and ultimately help motivate further experiment. In the following section an introduction to DFT will be presented. The section will finish by describing the SIESTA (Spanish Initiative for Electronic Simulations with Thousands of Atoms) simulation package used to obtain the presented results. There are several reviews and textbooks which give an extensive description of these methods and others(e.g. [62–65]).

## 3.2 Wave mechanics

The starting point for understanding electronic structure, as well as the many varied methods of study, ultimately lies with conventional wave function theory. In basic wave mechanics the state of a particle is represented by a wave function. Observable properties can then be determined by operating on the wave function with appropriate operators. Starting with this approach we can work from a single particle to a many-body system.

In most cases we are not concerned with time, therefore the time-independent Schrödinger equation may be considered, as in 3.1.

$$\hat{H}\Psi = E\Psi \tag{3.1}$$

To allow us to consider a general N-particle system of electrons and nuclei the Hamiltonian operator is expressed as shown in 3.2 where  $\hat{T}_e$  and  $\hat{T}_N$  are the kinetic energy operators for the electrons and nuclei, and where  $\hat{V}_{Ne}$ ,  $\hat{V}_{ee}$  and  $\hat{V}_{NN}$  are the electron-nucleus attraction, electron-electron repulsion and nucleus-nucleus repulsion energy operators respectively.

$$\hat{H} = \hat{T}_e + \hat{T}_N + \hat{V}_{Ne} + \hat{V}_{ee} + \hat{V}_{NN} \quad (3.2)$$

To simplify this problem a basic approximation is made: if the masses of the nuclei are much greater than that of the electrons, the electrons are able to move on a much faster time scale than the nuclei. This is the Born-Oppenheimer approximation [66]. It allows the motion of electrons and nuclei to be separated, thus greatly simplifying the Schrödinger equation. Specifically, within the timescale of electronic motion,  $\hat{T}_N$  is now zero and  $\hat{V}_{NN}$  is considered as a constant potential. Therefore the electronic Hamiltonian appears as in 3.3.

$$\hat{H} = \hat{T}_e + \hat{V}_{Ne} + \hat{V}_{ee} + \hat{V}_{NN} \quad (3.3)$$

This description of electrons in the potential field of fixed nuclei is still a complicated many-body problem. The term  $\hat{V}_{ee}$  describing electron-electron interactions does not allow for one-electron equations which would give an analytical independent electron solution. To properly explain these systems, the way in which each electron interacts with every other electron must be considered. In particular, we must consider exchange and correlation effects, which, as will be explained, are very difficult to treat. In a many-body system the electron correlation interaction originates from the interactions between fermions of parallel or opposite spin. Electrons(fermions) with parallel spin cannot occupy the same space. Additionally, we know that electrons repel each other according to Coulomb's law, through which each electron will feel a different response to each of the other electrons. This creates a complicated electron-electron correlation where one electron is influenced differently by many others. The exchange interaction is a quantum mechanical effect, originating from the Pauli exclusion principle, which describes the energy change arising from different distributions in space under exchange of spin or position.

### 3.3 Density Functional Theory

The success of DFT is that we can replace the complicated N-electron wavefunction  $\Psi(x_1, x_2, \dots, x_N)$  and its associated Schrödinger equation by something far simpler.

Although there is a much longer history, DFT as it is often now implemented (Kohn-Sham formalism - see later) begins with the work in 1964 by Hohenberg and Kohn [67] in which two deceptively simple theorems were proposed:

1. In any system of interacting particles, no two external potentials ( $\hat{V}_{Ne}$ ) differing by more than a constant will give the same ground state charge density.

Therefore the Hamiltonian will also be uniquely determined by the ground state density.

2. A functional can be defined which determines the energy  $E[n]$  in terms of the density  $n(\mathbf{r})$ . For a particular  $\hat{V}_{Ne}$  the ground state energy is then the global minimum of the functional,  $E[n]$ , where  $n_0(r)$  is the ground state density which minimises  $E[n]$ .

The consequence of these two theorems is that the ground state electronic energy is completely determined by the electron density. With this in mind, if  $n(\mathbf{r})$  is specified, the total energy can be expressed as a functional

$$\begin{aligned} E_{HK}[n] &= T[n] + V_{ee} + \int V_{Ne}(\mathbf{r})n(\mathbf{r})d^3r \\ &\equiv F_{HK}[n] + \int V_{Ne}(\mathbf{r})n(\mathbf{r})d^3r \end{aligned} \tag{3.4}$$

The functional  $F_{HK}[n]$  as defined in 3.4 therefore contains the kinetic and potential energies of the interacting electron-electron system. However these two theorems merely prove that such a functional exists. No information is given about the nature of the functional or how the ground state density may be calculated.

### 3.3.1 Kohn-Sham

In reality there is no systematic way that a density functional can be found. An explicit functional is only known for a few idealised systems such as the non-interacting uniform electron gas. The problem that remains is how to calculate  $T[n]$  along with the non-classical part of  $V_{ee}[n]$ .

Early work by Thomas [68], Fermi [69] and later by Dirac [70] attempted to deduce a functional for a many-body system based on a series of approximations. This involved treating  $V_{ee}[n]$  purely classically and used the non-interacting uniform electron gas to approximate  $T[n]$ . Dirac's contribution was the addition of the exchange energy formula for a uniform electron gas in  $V_{ee}[n]$ . This direct approach gives explicit forms for  $T[n]$  and  $V_{ee}[n]$ . They are crude approximations, however, and for instance they completely fail to predict bonding within solids and molecules.

To overcome this problem Kohn and Sham proposed introducing spin orbitals to describe the electrons, and to couple electrons suggested an approach where we map the interacting N-electron system onto an auxiliary system of N non-interacting electrons moving within a potential  $V_{KS}(\mathbf{r})$ . The Hamiltonian that describes such a system is,

$$\hat{H}_S = \sum_i^N \left( -\frac{1}{2} \nabla_i^2 \right) + \sum_i^N V_S(r_i) \quad (3.5)$$

This leads to a series of one-electron equations describing the system, known as Kohn-Sham orbitals.

$$\hat{H}_{KS} \Psi_i = \epsilon_i \Psi_i \quad (3.6)$$

where

$$\hat{H}_{KS} = -\frac{1}{2} \nabla^2 + V_{KS}(\mathbf{r}) \quad (3.7)$$

$V_{KS}(\mathbf{r})$  is a Kohn-Sham effective potential that we will go on to discuss later. In treating the system this way the non-interacting system is made up of independent-particle equations that are exactly soluble. The interacting many-body terms are then incorporated into an exchange-correlation functional of the density.

In the Kohn-Sham formalism the desire is to simplify the kinetic energy term in the total energy functional. The exact formula for the ground state density is:

$$T = \sum_i^N n_i \langle \Psi_i | -\frac{1}{2} \nabla^2 | \Psi_i \rangle \quad (3.8)$$

where  $\Psi_i$  and  $n_i$  are the natural spin orbitals and their occupation numbers.

For interacting systems of interest, this will have an infinite number of terms. Kohn and Sham showed that simpler formulae can be used,

$$T_s[n] = \sum_i^N \langle \Psi_i | -\frac{1}{2} \nabla^2 | \Psi_i \rangle \quad (3.9)$$

and

$$n(\mathbf{r}) = \sum_i^N \sum_s | \Psi_i(\mathbf{r}, s) |^2 \quad (3.10)$$

which is the particular case where  $n_i = 1$  for N orbitals and 0 for all others. This is *not* the exact kinetic energy functional  $T[n]$  for the general total energy functional in 3.4. The idea of Kohn and Sham, however, was that this *is* the exact kinetic energy component of the independent particle system. Therefore we have an auxiliary system where  $T[n]$  is exact.

The universal energy functional in the Kohn-Sham formalism is then,

$$F[n] = T_s[n] + E_H[n] + E_{xc}[n] \quad (3.11)$$

where  $T_s[n]$  is as previously defined,  $E_H[n]$  is the classical Coulomb interaction

energy of  $n(\mathbf{r})$ , and  $E_{xc}[n]$  is the additional term that encompasses all exchange and correlation effects not present in the independent particle system. Comparing this with 3.4, 3.12 is obtained.

$$E_{xc}[n] \equiv T[n] - T_s[n] + V_{ee}[n] - E_H[n] \quad (3.12)$$

The exchange correlation energy therefore includes the components of  $T[n]$  not described by  $T_s[n]$  and the non classical part of  $V_{ee}[n]$ .

### 3.3.2 Exchange-Correlation functionals

Despite all of the progress in modelling electron interactions via the Kohn-Sham method, all that has really been achieved is to replace one problem with another: what remains is that the form of  $E_{xc}$  is still not exact and is unknown for real systems. The primary task of everything up until now has been to better explain the complicated exchange and correlation terms within real interacting systems. Therefore unless we can accurately approximate  $E_{xc}$ , very little has been gained. Although this is still an approximation, the way in which the different terms in 3.11 have been separated, leaves just a single exchange-correlation functional. This makes it much easier to find a reasonable approximation.

Relatively simple approximations have had great success in describing what must be the very complicated exact functional  $E_{xc}[n]$ , and two of the most commonly used are now discussed.

### 3.3.3 The local density approximation (LDA)

The local density approximation (LDA) was proposed by Kohn and Sham [71] in the same seminal paper proposing the KS method. In the Thomas-Fermi-Dirac model the uniform-electron gas was used to locally obtain a functional for the kinetic energy and a functional for the exchange energy. In the KS method the kinetic energy term

has already been rigorously treated without approximation.

Kohn and Sham suggested that the electronic system in some solids is close to an homogeneous electron gas. These include systems with slowly varying densities such as nearly-free electron metals. In these particular systems we can use the uniform electron gas formula solely for introducing the LDA for the exchange and correlation energy.  $E_{xc}[n]$  is then just an integral over all space with the exchange-correlation energy density at each point assumed to be the same as for a homogeneous electron gas with the same density shown in Equation 3.13.

$$E_{xc}^{LDA}[n_\uparrow, n_\downarrow] = \int n(\mathbf{r}) \sigma_{xc}^{hom}[n_\uparrow(\mathbf{r}), n_\downarrow(\mathbf{r})] d^3r \quad (3.13)$$

The Kohn-Sham equation in 3.6 is then,

$$\left( -\frac{1}{2} \nabla^2 + V_{ext}(\mathbf{r}) + V_H(\mathbf{r}) + \frac{\delta E_{xc}^{LDA}}{\delta n(\mathbf{r})} \right) \Psi_i = \epsilon_i \Psi_i \quad (3.14)$$

For calculation, a function  $\epsilon_{xc}(n)$  is used which can be divided into exchange and correlation terms, an exchange part given by Dirac as in the TFD model and a correlation term from quantum Monte Carlo calculations [72]. A self consistent solution of Equation 3.14 can then be found as described earlier.

However, the assumptions made for the LDA approach are clearly unjustified for inhomogeneous systems such as individual atoms and molecules. In this case the density of electrons must smoothly converge to zero outside the radius of an atom.

### 3.3.4 The generalised gradient approximation (GGA)

To move beyond the systems LDA can handle, a non-uniform electron gas needs to be considered. GGA methods seek to do this by making  $\epsilon_c$  and  $\epsilon_x$  dependent on not just the electron density but also its derivatives.

The general form of  $E_{xc}$  is then,

$$E_{xc}^{GGA}[n_\uparrow, n_\downarrow] = \int f(n_\uparrow \mathbf{r}, n_\downarrow \mathbf{r}, \nabla n_\uparrow, \nabla n_\downarrow) d^3r \quad (3.15)$$

There are many different types of GGA which modify the behaviour of  $f$  at large gradients to preserve certain desired properties. The different functions,  $f$ , can be separated into two general categories: those whose construction starts from the uniform electron gas, or semi-empirical functionals where the parameters are fitted to a particular system to match its desired properties. This creates a situation where some GGA functionals are more suited for certain problems than others. Whilst one functional may have success in describing one system, it may completely fail for another. A good description of these problems is given by Perdew, Burke and Ernzerhof [73].

In the implementation of the SIESTA code used for the work described in this thesis, the Perdew-Burke-Ernzerhof (PBE) GGA functional is used [73]. This functional was designed to be as widely applicable as possible for both solids and atoms, addressing what are considered shortcomings of other methods.

### 3.4 Implementation of DFT

To describe an unknown function, such as a molecular orbital (MO), an expansion into a set of known functions can be made. This is called a basis set. A linear combination of these functions with different weightings, which are to be determined, forms a description of the unknown function. This can only serve as an approximation, unless an infinite set of functions are used for description, i.e. when the basis is complete.

The MO serves as the quantum mechanical description of the behaviour of one electron in the electric field due to nuclei and other electrons, i.e. it is a wavefunction. With this in mind, it is of critical importance that the basis set is complete enough

to accurately describe the MO. The usual practice is to tune the basis set to a particular system, such that at some point increasing the basis size offers no extra gain in accuracy within a specified tolerance. This allows a basis set to be used that will accurately describe the system, whilst preventing the process from becoming so computationally intensive that the calculation would take an infeasibly long time to complete. The type of basis function in use also influences the accuracy. If a single basis function is more able to reproduce the unknown function, then the calculation is more accurate and fewer basis functions are necessary for the same result.

### 3.4.1 Orbitals and choice of basis set

There are generally two ways in which the basis set can be treated: either with plane waves, or a linear combination of atomic orbitals (LCAO). The latter is the method used in this thesis. The LCAO method is considered more of an approximation than a plane wave implementation, and the choice of orbital can be very important. The most commonly applied orbital in calculations is the Gaussian type orbital (GTO) which is itself an approximation to Slater type orbitals (STO). Compared to STOs, more GTOs are required to form a complete basis, however they have serious computational savings in how they can be applied, leading to much faster calculations.

The smallest number of basis functions that can be used is the minimum basis set, usually referred to as a *single- $\zeta$*  basis. This requires one function describing each electron in each shell, e.g. Si requires three s-functions ( $1s$ ,  $2s$ ,  $3s$ ) and two sets of p-functions ( $2p$ ,  $3p$ ).

The number of orbitals for each electron can be increased such that there are two (*double- $\zeta$* ) or three (*triple- $\zeta$* ) orbitals describing each electron. This allows the true MO to be better described by combining more orbitals per electron. In complicated systems single GTO's will not be able to reproduce the shape of the real MO,

therefore at least one additional orbital is required in combination. To achieve well converged results, a polarisation is often necessary to be added to account for deformation induced by bond formation. For instance, to describe an oxygen atom, 1s, 2s and 2p atomic orbitals would suffice. To describe a oxygen molecule, however, we might add 3s, 3p and even a 3d orbital to ensure that we can describe the bonding between the two ions. In the SIESTA implementation, the *double-* $\zeta$  plus *single-* $\zeta$  polarisation *d* orbital basis set (DZP) is considered to be a standard basis, yielding high quality results. The total energy convergence compared to computational time makes DZP a useful choice. In Figure 3.1 a comparison of total energy convergence with different basis sets compared to a plane wave equivalent is shown (taken from [74]). Large gains can be seen up until the use of DZP, after which the gain in accuracy for computational cost greatly diminishes.

### 3.4.2 Pseudopotentials

When considering elements from the third row of the periodic table or higher, there are many core electrons which generally play no part in chemical interactions. The core electrons are subject to the strong coulomb potential of the nuclei making their wavefunctions very localised. Conversely, the outer valance electrons are partially screened by the core electrons which leads to a weaker interaction with the nuclei, thus making their wavefunctions more diffuse. To reduce the number of atomic orbitals required, a pseudopotential can be used to represent the core electrons. If a suitable function is used to model the electrons, good results can be achieved at a much lower cost of calculation. The SIESTA code uses ‘norm-conserving’ [75] pseudopotentials which require the integrated charge to agree with a standard complete basis set beyond some cut off radius.

The use of a basis set is an approximation that needs to be made when using a LCAO method, and the inclusion of pseudopotentials is a further approximation to

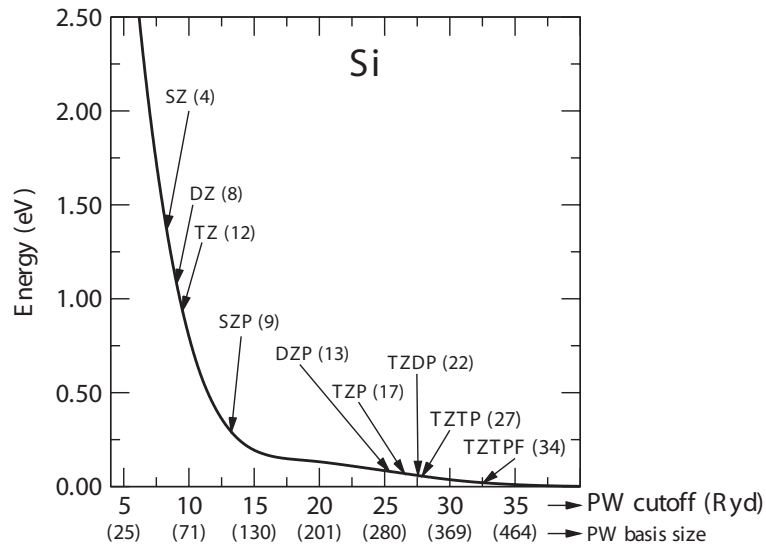


Figure 3.1: Convergence of basis sets compared to equivalent plane-wave cutoffs. Comparison is made by comparing the total energy calculated per atom in a silicon bulk material. The solid curve represents increasing PW cutoff (and hence the PW basis size), with arrows indicating the energies obtained with the different LCAO basis sets. The basis size, either the number of atomic orbitals (LCAO) or number of plane waves (PW) are given in parentheses. SZ, single- $\zeta$  ; DZ, double- $\zeta$  ; TZ, triple- $\zeta$  ; DZP, double- $\zeta$  valence orbitals plus SZ-polarization  $d$  orbitals; TZP, triple- $\zeta$  valence plus SZ polarization; TZDP, triple- $\zeta$  valence plus double- $\zeta$  polarization; TZTP, triple- $\zeta$  valence plus triple- $\zeta$  polarization; TZTPF, is the same as TZTP plus additional SZ-polarization  $f$  orbitals. Figure taken from [74]

allow larger systems to be modelled with as little sacrifice of accuracy as possible. However when using these to describe any system, the results of calculations are measured against experimental data to help guide these approximations to a point where they are considered accurate to use. Thus, even though DFT is termed an *ab initio* method of calculation, experimental data always play a significant role in guiding basis set and pseudopotential construction.

### 3.4.3 Minimising the Kohn-Sham equation

As mentioned earlier, to obtain the ground state energy of a system, the functional  $E[n]$  is minimised in terms of the density  $n(\mathbf{r})$ . This is achieved by defining an Euler-Lagrange equation for the system, which in this case appears as in 3.16.

$$\mu = V_{KS}(\mathbf{r}) + \frac{\delta T_s[n]}{\delta n(\mathbf{r})} \quad (3.16)$$

with

$$\begin{aligned} V_{KS}(\mathbf{r}) &= V_{ext}(\mathbf{r}) + \frac{\delta E_H}{\delta n(\mathbf{r}, \sigma)} + \frac{\delta E_{xc}}{\delta n(\mathbf{r}, \sigma)} \\ &\equiv V_{ext}(\mathbf{r}) + V_H(\mathbf{r}) + V_{xc}(\mathbf{r}) \end{aligned} \quad (3.17)$$

To briefly explain the minimisation of the functional let us collect the important equations from 3.6 and 3.10,

$$\left( -\frac{1}{2} \nabla^2 + V_{KS}(\mathbf{r}) \right) \Psi_i = \epsilon_i \Psi_i \quad (3.18)$$

$$n(\mathbf{r}) = \sum_i^N \sum_s |\Psi_i(\mathbf{r}, s)|^2 \quad (3.19)$$

Equation 3.16 is not directly solved. Rather, an indirect approach is taken using

the  $N$  one-electron equations from 3.18. The basic idea is that we first guess  $n(\mathbf{r})$ .  $V_{KS}(\mathbf{r})$  is then calculated and used in 3.18 to find a new  $n(\mathbf{r})$  from 3.19. This is iterated until  $n(\mathbf{r})$  converges to the ground state density thus minimising the functional.

At any point the total energy may be calculated directly from the general definition of  $E[n]$  using the KS form of  $F[n]$ . The equations 3.17, 3.19 and 3.18 are considered to be the Kohn-Sham equations. A complete explanation of how these are solved via the variational principle will not be given but can be found in the works given at the start of this chapter [62–65].

### 3.4.4 Calculation of forces

Thus far we are able to calculate the electronic structure of a system. Often, however, what we really want to know is the positions of the atoms themselves. For this we need to calculate the forces acting on each nuclei, and determine the equilibrium positions of the atoms, i.e. when  $\mathbf{F} = \mathbf{0}$ . The calculation of forces is in principle a difficult task. A typical approach would require total energy calculations for a number of different geometries. Initially, the energy of the total system would be calculated for a particular configuration. The process would subsequently be repeated with the nuclei inhabiting new positions. The force on a particular atom is then acquired by plotting energy *vs.* position.

It should be very clear that calculating  $F_x, F_y$  and  $F_z$  for many different atoms within a single system would be extremely computationally expensive. To solve this problem the Hellmann-Feynman theorem can be used. Using this method only a particular configuration of atoms, the configuration of interest, needs to be calculated. The energy, and the slope of the energy can then be independently obtained from the same calculation, saving vast amounts of computational time.

The details of the theorem are elegantly explained by Feynman himself [76].

Some of the key points will be reproduced here to serve as a simple explanation. The theorem states that<sup>1</sup> in order to calculate the derivative of the energy with respect to a parameter  $\lambda$ , we only need to calculate the derivative of the Hamiltonian, or:

$$\frac{\partial U}{\partial \lambda} = \int \Psi^* \frac{\partial \hat{H}}{\partial \lambda} \Psi d\nu \quad (3.20)$$

In order to calculate the forces on atoms we need only consider terms in the Hamiltonian which depend on the atomic positions,  $R_A$ . The important terms are  $V_{NN}$  and  $V_{Ne}$ . Without including the working to reach the result [77], it will simply be stated that the  $\alpha$  component of force acting on an atom  $A$ , can be written as in equation 3.21,

$$F_{A\alpha} = \frac{\partial V_{NN}}{\partial R_{A\alpha}} + e \int \frac{\partial V_{ion}(\mathbf{r})}{\partial R_{A\alpha}} \rho(\mathbf{r}) d\mathbf{r} \quad (3.21)$$

This implies the following conclusion; “*The force on any nucleus (considered fixed) in any system of nuclei and electrons is just the classical electrostatic attraction exerted on the nucleus in question by the other nuclei and by the electron charge density distribution for all electrons...*”.

With the possibility of simple and fast calculation of force, methods can be used to converge the atomic positions within a system to a stable state, i.e. where  $F = 0$ .

### 3.4.5 Calculating the minimum energy geometry

One of the principal tasks for atomistic simulations is to determine the optimum, or minimum energy, geometry of a system of atoms. This can be achieved after calculation of the forces acting on each atom. Typically, the atomic positions within a molecule or crystal structure will be guessed using a sensible set of initial coordinates. The energy and forces in the system can then be calculated, if the guess

---

<sup>1</sup>A steady state is assumed where each nuclei is stationary

was incorrect, then we know that the system is not in equilibrium, i.e.  $F \neq 0$ . The force can then be used to determine a vector displacement to shift the atoms. The structure calculation can be repeated and the process continued iteratively until  $F$  is small enough that it can be considered to be *zero*<sup>2</sup>.

The two most common algorithms for convergence are the steepest decent and the conjugate gradient methods.

### Steepest Descent and conjugate gradient

In the steepest descent (SD) algorithm, steps are taken proportional to the negative gradient of the energy ( $-F$ ) until a local minimum energy is reached. The basis for SD is that the fastest route to the local minimum is to go in the direction in which  $F$  decreases most rapidly. Therefore, based on the direction of the calculated force a step will be taken as in equation 3.22.

$$x_{(n)} = x_{(n-1)} + \lambda F_{(n-1)} \quad (3.22)$$

Equation 3.22 explains that to reach position  $x_{(n)}$  from position  $x_{(n-1)}$ , we travel by an amount  $\lambda F_{(n-1)}$ , where  $\lambda$  is the magnitude of the movement in the direction of  $F_{(n-1)}$ . To determine  $\lambda$  a line search is carried out along the slice  $F_{(n-1)}$  makes through the potential energy surface. The minimum energy is found (at  $F = 0$ ) and the step is taken to that position. The next step is therefore taken in an orthogonal direction, and so on, until we converge on the local minimum on the potential energy surface. The process is loosely sketched in Figure 3.2, where a fictitious steepest decent pathway is sketched on top of a theoretical potential energy surface starting at position  $x_{(0)}$ . The main drawback of SD is the very slow rate of convergence, even close to the minima. This arises because the steps can overshoot the local minimum,

---

<sup>2</sup>The tolerance for  $F$  is usually set when both the atomic displacements between steps becomes negligibly small and when  $E_{TOT}$  is converged.

undoing some of the process of the preceding steps.

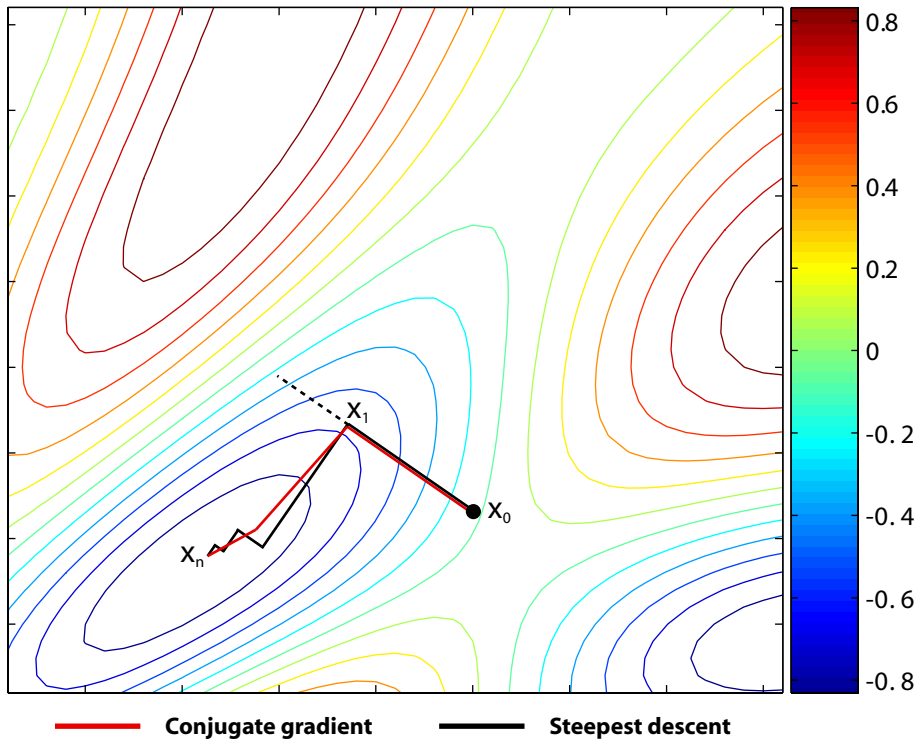


Figure 3.2: A fictitious potential energy surface generated with an equation of the form  $\sin(\alpha x^2 - \beta y^2 + c)\cos(\gamma x - e^y)$  is used to show the major differences between the steepest descent and conjugate gradient methods of geometry optimisation.

To avoid the inefficient zig-zag movement of the steepest descent method different algorithms can be used. The most common alternative is the conjugate gradient method (CG). The basic idea of the CG method is as follows. At a particular step, rather than just travel in the direction of negative energy gradient, the direction is added in a linear combination of the previous direction vectors to obtain the new direction to move. This ensures that we continuously move in a direction that brings us closer to the local minimum. Therefore, the first step in the iteration is the same as for SD, however, each subsequent step should be improved, usually reaching the local minimum much faster. A sketched example of the CG method is shown in 3.2 with the SD method to demonstrate the differences.

### 3.4.6 Basis set superposition error (BSSE)

LCAO implementations save time by defining an atomic orbital for each atom to describe the electron density. Whilst plane wave codes describe the *entire* simulation cell, including the vacuum regions, atomic orbitals only describe regions centred around the atoms. The atomic orbitals must therefore follow the position of their associated atom during geometry relaxation.

Typically, the basis set is incomplete. Furthermore, each atomic orbital has a set radius. If we consider the special case of adsorption, e.g. body A adsorbing onto another body, B, to form the composite system AB, then it is possible for the atomic orbitals of A and B to overlap. In the regions where A and B overlap, the basis is more complete (see Figure 3.3). The calculated total energy, therefore, is artificially modified for the AB system whilst not for the separate A+B system. Consequently, calculation of the binding energy will be overestimated. This is known as the basis set superposition error (BSSE), and is purely an artefact of using a finite basis set.

The level of BSSE will vary depending on the amount of bonding between A and B and will most significantly affect the calculated total energies. The work in this thesis concentrates on calculating force as a function of the separation between A and B, and only ever considers bonding between two individual atoms (rather than the multiple bonds formed during molecular surface adsorption). Assessing the effect of BSSE on the forces calculated in this thesis is a unique problem for AFM calculations, and as such, to the best of the authors knowledge, has not been considered in detail. If the basis description artificially improves when the AFM tip is approached towards the surface, then the description of any chemical bond formed may also be artificially improved. As the nature of this chemical bond determines the force exerted on the fixed AFM tip atoms, any modification can in principle affect the calculated AFM force.

The effect of BSSE can be estimated by modifying the size of the atomic orbitals

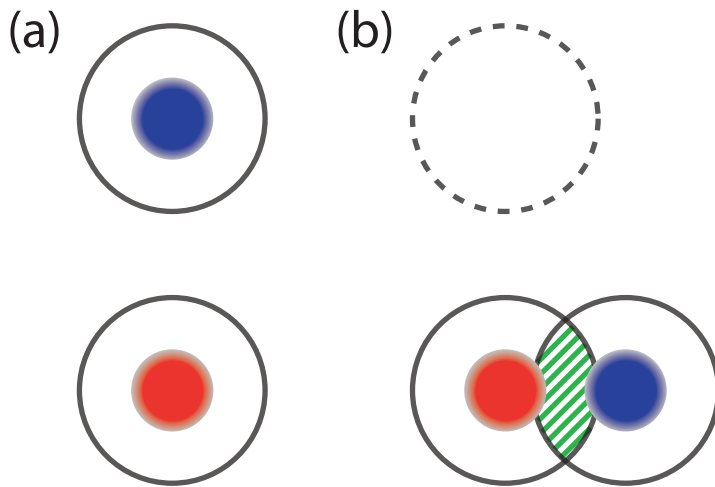


Figure 3.3: Cartoon demonstrating the origin of BSSE. (a) Two atoms are shown far from one another such that their associated atomic orbitals (black solid lines) do not overlap. (b) When the atoms come together to form a molecule, the atomic orbitals overlap, increasing the basis accuracy within the shaded region. If the original basis describing the system is incomplete, then the overlap will cause an overestimate of binding energy.

describing each atom. By reducing the “energyshift” parameter in SIESTA calculations, the atomic orbital radii are increased. Larger atomic orbitals increase the basis overlap throughout the entire calculation, improving the overall description, and reduces additional overlap when the tip-surface separation is reduced (provided the tip is small in z).

Three situations were tested, the typical radii used throughout this thesis, and two larger orbital descriptions, shown in Figure 3.4. A C<sub>60</sub>-Si  $F(z)$  calculation was then repeated with each description to test for variations in force. From Figure 3.4 it is observed that increasing the orbital radii reduces the slow ‘turn-on’ in force noticeable between 3-4 Å and slightly decreases the magnitude of the force turnaround. These variations in calculated force are small enough that a reasonable comparison with experimental data can still be made.

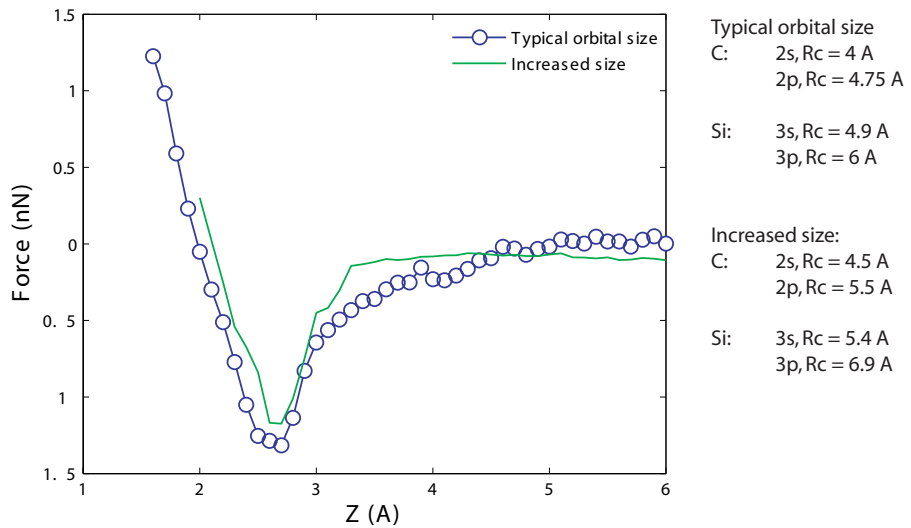


Figure 3.4: The effect of BSSE on calculated  $F(z)$  data.  $F(z)$  data for typical and increased orbital radii are compared resulting in minor deviations.

### 3.5 SIESTA summary

Many different implementations of DFT are available to numerically solve the KS equations, each with their own strengths and weaknesses. The differences are generally in the accuracy required and how this affects the time for computation. This normally involves the choice of functional (including whether to use LDA or GGA) and whether a LCAO or plane wave implementation is used.

The SIESTA code is specifically designed to handle large simulations of many atoms at a reduced computational time. Thus, a flexible LCAO method is used allowing extremely fast and accurate calculations. In the work described in this thesis DZP basis sets are used with the GGA PBE density functional and norm-conserving pseudopotentials.

The basis sizes, basis range and other precision parameters are adjusted to obtain a good convergence in calculated results, i.e. improving parameters leads to no significant changes in results. For this work the basis set is defined by an energy shift of 0.01 Ry and a mesh grid cutoff of 150Ry. The calculations are considered complete

when the forces felt by atoms are not larger than  $0.01 \text{ eV}/\text{\AA}$ , unless otherwise stated. The SIESTA method has been generally tested for various systems [78] including silicon [74] and is found to perform well. In particular, in a previous investigation of our system SIESTA results have been compared to the plane wave code VASP [79] and is found to match up very well, suggesting the fast LCAO implementation is suitable for the requirements in this work.

# Chapter 4

## Materials and Techniques

Throughout the results sections discussed within this thesis several semiconductor surfaces were studied with both simulated and experimental techniques. Consequently this chapter contains a brief review of the Si(100), Si(111) and the hydrogen terminated Si(100) surfaces, and also the C<sub>60</sub> fullerene molecule. Both DFT calculations and NC-AFM experiments are carried out to examine chemical interactions on these surfaces. Therefore, some of the experimental and theoretical methods repeatedly implemented throughout this thesis will be described in the final sections of this chapter.

### 4.1 Silicon surfaces and C<sub>60</sub>

Various crystal structures can be adopted by a material. The most important for many semiconductors is either the zinc-blende or the diamond structure. In the diamond structure, each atom is covalently bound to four nearest neighbours in a regular tetrahedral arrangement caused by an *sp*<sup>3</sup> hybridisation in the bulk structure. The diamond bulk configuration can be thought of as two inter-penetrating face centred cubic (fcc) lattices displaced from each other along the diagonal of the bulk cubic cell by  $\frac{1}{4}$  of the length of the diagonal. In Figure 4.1 a single fcc cube is

depicted shown with the additional atoms found in the diamond structure.

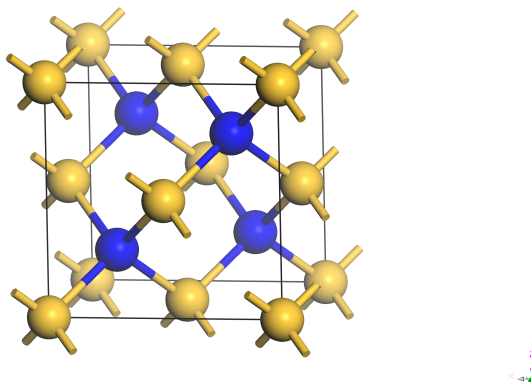


Figure 4.1: The conventional unit cell of the diamond structure. For clear distinction the fcc atoms are shaded yellow and the additional atoms of the diamond structure blue. The additional basis atoms are positioned  $\frac{1}{4}$  of the way along the cubic diagonals.

To obtain a clean silicon surface, preparation must take place under UHV conditions. Once a crystal face has been exposed, the unsaturated bonds from the bulk structure will immediately react forming oxide structures. Therefore only in UHV conditions, with pressures in the region of  $\times 10^{-10}$  mbar or better, can clean silicon be studied for any practical length of time. In the following section, an overview of some of the reconstructions possible on the exposed (100) and (111) face will be presented. Subsequently, a brief description of the C<sub>60</sub> molecule and its adsorption on the Si(111) surface will be included.

## 4.2 The Si(100) surface

A silicon wafer can be cut and polished along the (100) direction to form a macroscopically flat surface. The bulk-like termination would then result in an ‘ideal’ surface appearing as a square  $1 \times 1$  periodic grid of atoms, each with two unsaturated bonds as shown in Figure 4.2 (a). The bulk terminated surface is, however,

very unstable and undergoes a reconstruction to lower the free energy. In UHV the wafer can be prepared via flash annealing to 1200 °C to form a reconstruction consisting of buckled dimers. To explain how this is formed, we begin with the  $1 \times 1$  bulk-like termination of atoms, each with two unsaturated bonds. The balance of inter-atomic forces, however, is clearly affected and in order to reduce the number of dangling bonds present, the atoms pair together to form dimers producing rows like those shown in Figure 4.2 (b) and (f).

This model supported initial observations of the Si(100) surface measured with LEED [80] which suggested that the surface consists of symmetric dimers. Following these initial observations, many different structures for the Si(100) surface were proposed, including a buckled dimer model from Chadi *et al* [81]. In the buckling model it was observed that if the top five layers of the Si(100) structure were allowed to relax, asymmetric dimer configurations became much lower in energy than the symmetric arrangement. The structures considered were the asymmetric  $p(2 \times 1)a$  (where  $a$  denotes an asymmetric configuration, rather than the symmetric  $p(2 \times 1)$  arrangement) and the  $c(4 \times 2)$  configurations shown in Figure 4.2(c) and (e). In particular, a  $c(4 \times 2)$  arrangement produced a decrease in total energy of  $\sim 0.48$  eV/dimer. The formation of the asymmetric dimer originates from a charge transfer of  $0.36 \pm 0.02$  electrons from the lower dimer atom, to the upper dimer atom due to a Jahn-Teller like effect. Subsequent work [82, 83] confirmed Chadi's results and also showed that the  $p(2 \times 2)$  phase (shown in Figure 4.2(d)) results in a similar energy reduction to the  $c(4 \times 2)$  structure. The calculations by Inoue *et al* put the  $c(4 \times 2)$  arrangement as the ground state configuration, followed by  $p(2 \times 2)$  (1.2 meV/dimer higher),  $(2 \times 1)a$  (90.6 meV/dimer) and  $(2 \times 1)$  symmetric (260.5 meV/dimer).

After the first STM images of Si(100) were taken [84], the dimer model of the surface was confirmed. The question regarding the symmetry of the dimers, however, remained unsolved as both buckled and symmetric dimers were observed. The

question remained open until the first low-temperature study [85] (120 K) was conducted, which saw a large increase in the number of buckled dimers. These results appeared to confirm the theoretical model, as the 120 K system should have less thermal energy available ‘freezing’ the dimers into the ground state configuration. Thus it appeared that at elevated temperatures the thermal energy within the system is enough to allow the dimers to rapidly switch between buckled configurations on a timescale [79,86] faster than the feedback response of the STM. The symmetric appearance therefore arises from a time averaging effect, where the dimer rapidly flips between two states, and is not a stable state of the system. Tight-binding total energy calculations [87] predicted an order-disorder phase transition in the arrangement of the dimers, which was experimentally observed [88] to occur at  $\sim$ 200 K. Calculated [79] and experimental [89] results put the energy barrier for a dimer to switch configuration (starting from a  $c(4 \times 2)$  configuration) at  $\sim$ 100-200 meV, and much less (80 meV) for the reverse process. It has also been suggested that the energy barriers could be perturbed by the dimer’s local environment [79,81,90], leading to variations in the barrier to flip. This seems to explain why there is a mixture of apparent-symmetric and buckled dimers observed in room temperature studies.

Although the debate appeared to be settled, several studies reported low temperature observations of the symmetric dimer configuration, rather than the buckled structures which should dominate. Explanations varied. One study suggested that the  $p(2 \times 1)s$  symmetric structure was stable below 100 K [91], while others suggested that non-thermally induced dynamical dimer flipping was taking place leading to the time averaged effect previously described [92,93]. The symmetric observations appeared to occur after a phase transition at 40K [94], below which the surface once again became disordered, although the reason for this behaviour was less understood [95]. Soon after, however, observations made at 4K further complicated the

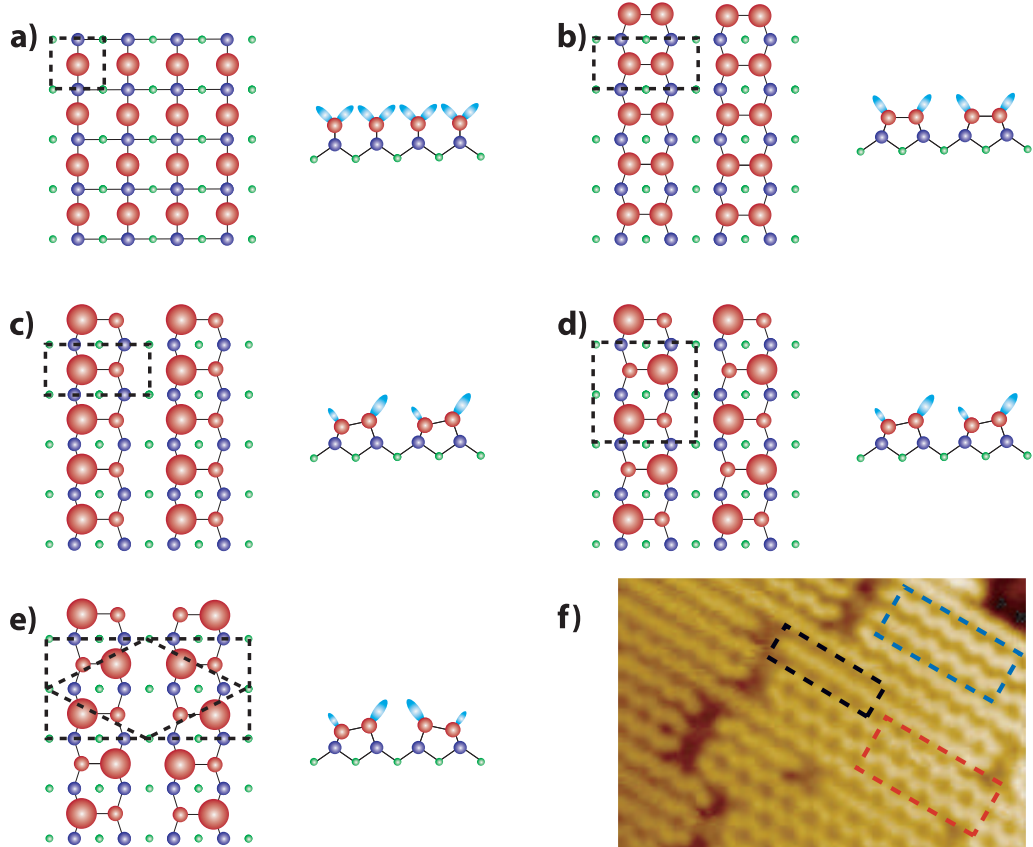


Figure 4.2: Schematics of Si(100) reconstruction and phases of dimer rows. (a) Top and side view of the polished unreconstructed 1x1 surface. Each silicon surface atom has two dangling bonds. (b) The symmetric  $p(2 \times 1)$  reconstruction of paired dimers. Now each atom has only a single dangling bond. Lower energy asymmetric dimer configurations were found to have either (c) asymmetric  $p(2 \times 1)a$ , (d)  $p(2 \times 2)$  or (e)  $c(4 \times 2)$  periodicity. (f) a typical STM image demonstrating observed  $p(2 \times 2)$  (top blue box),  $c(4 \times 2)$  (bottom red box) and apparent symmetric  $p(2 \times 1)$  regions of the surface (image taken by Adam Sweetman).

situation. Although many groups reported symmetric dimers below 40K, at 4K large areas of purely  $p(2 \times 2)$  and  $c(4 \times 2)$  structure were observed [96]. Moreover, the particular phase observed could be controlled via selection of sample bias [97]. Systematic temperature dependent studies [98] concluded that voltage-induced phase modification from  $c(4 \times 2)$  to  $p(2 \times 2)$  only occurred below 40K, the same temperature at which the phase transition was said to occur. As a result of these studies it was concluded that below 40K, inelastic tunnelling processes were in fact responsible for the appearance of the symmetric  $(2 \times 1)$  structure, seemingly explaining the controversial results reporting disordered flip-flop motion at low temperatures.

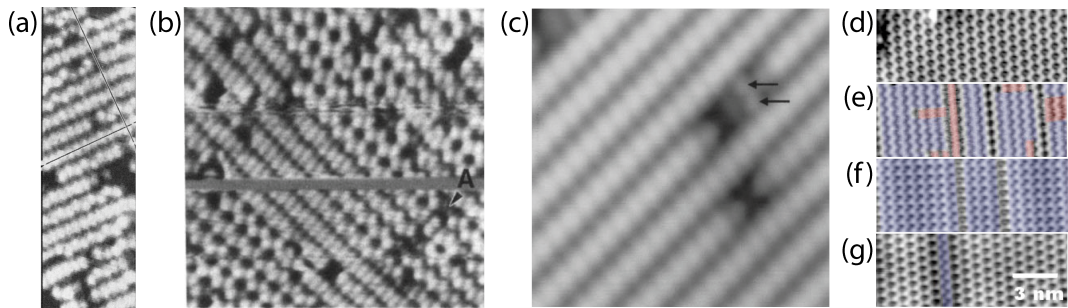


Figure 4.3: STM's contribution to the lengthy controversy surrounding Si(100). (a) The first published STM image demonstrating regions of both symmetric and buckled structure at RT [84]. (b) Images taken at 120K indicated a significant increase in the proportion of buckled dimers [85]. (c) At 20K dimers were once again observed to be symmetric, putting into question the established understanding that the ground state consists of buckled dimers. (d) STM manipulation at 4K converting regions of  $c(4 \times 2)$  phase, (e) via exciting dimers into a flickering state(red), to (f) a  $p(2 \times 2)$  configuration(blue) and subsequently (g) returning them to a  $c(4 \times 2)$  configuration(Adapted from Sagisaka *et al* [97]).

#### 4.2.1 AFM of Si(100)

It is clear that a large number of STM studies were required to gain a complete understanding of the Si(100) surface and its response to the scanning probe. The brief review in the previous section only addresses the most relevant experiments studying the ground state structure of the surface, and thus far omits any studies on

defects, adsorbed molecules or other experiments exploiting the Si(100) dimerised surface. Comparatively, there are few reports investigating Si(100) with NC-AFM.

Initial AFM experiments imaged the Si(100) surface at room temperature [99, 100] with cantilever based AFM. At such high temperatures the silicon dimers were observed to be symmetric, in line with previous STM observations. The initial report studied both the Si(100) and the Si(100):H surface (see section 4.3) with the same silicon tip, assuming that no tip changes had occurred between experiments. Under this (rather bold) assumption the images from both surfaces could be analysed and compared. It is well known that the Si(100):H surface dimers are stabilised by the presence of hydrogen, and take on a symmetric structure. Therefore, cross-sectional line profiles were taken and the distance between dimer atoms measured to check whether the clean Si(100) dimers were stable in a symmetric configuration, or flipping under the influence of thermal energy. The line profiles measured the separation between silicon atoms to be  $0.32 \pm 0.01\text{nm}$ , whereas those on Si(100):H were measured to be  $0.35 \pm 0.01\text{nm}$ . The measurement of the separation of silicon atoms in the Si(100) dimer was much larger than the actual Si-Si atomic separation, whereas the distance of  $0.35 \pm 0.01\text{nm}$  observed for the Si(100):H was in line with the separation of H atoms in the structural model. The conclusion was therefore made that only the time averaged flipping of the clean Si(100) dimer could properly explain the discrepancies in the measurements. Compared to the RT observations made in the STM studies there is one important discrepancy: whilst in the STM images there is always a mixture of buckled and apparent-symmetric dimers, in the AFM studies only symmetric dimers were observed, even around particularly defective regions of the surface. Before this observation could properly be explained [101], low temperature studies were required.

The first low temperature NC-AFM images ( $\sim 4\text{K}$ ) were obtained in 2002 [102], in which both  $c(4 \times 2)$  and  $p(2 \times 2)$  phases were observed. In a more systematic study

carried out by Li *et al* [33], the tip-sample distance dependence was investigated, revealing an interesting effect which once again appeared to show symmetric dimers at low temperatures. The effect driving this apparent imaging behaviour was, however, completely different to that noted in STM experiments. In the sequence of images shown in Figure 4.4, three images are shown at decreasing tip-sample distances showing a gradual change from  $c(4 \times 2)$  to  $p(2 \times 1)$  symmetric. From the results of theoretical calculations [33, 79] it was found that at large distances the tip-surface interaction is relatively weak, therefore a stable image is observed.

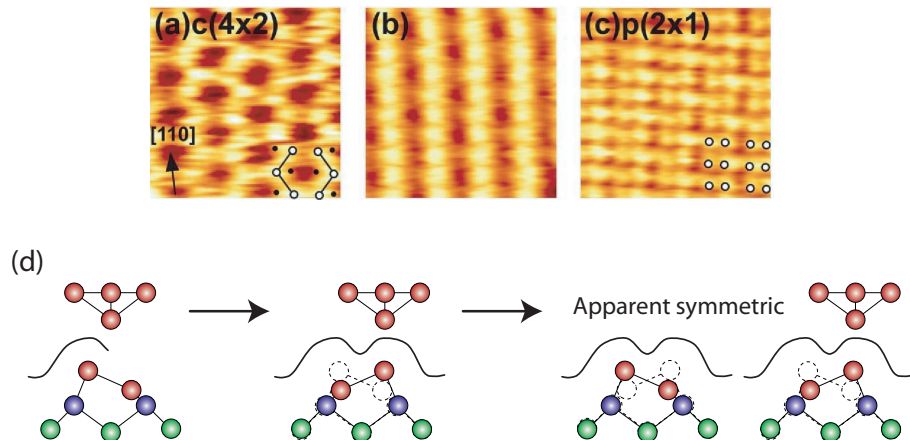


Figure 4.4: Observation of apparently symmetric dimers, at  $\sim 5\text{K}$ , with AFM. (a) Large tip-sample distance reveals an unperturbed image of the  $c(4 \times 2)$  reconstruction. (b) Tip-sample distance is reduced leading to scan induced flipping of dimers. (c) At small tip-sample distances a symmetric appearance is induced where the two atoms of each dimer are clearly visible. (d) Schematic depicting the chemical bond formation between each lower dimer atom, flipping the buckling angle of each dimer, as the tip is raster scanned across the surface. Images reproduced from [33].

Upon continued approach of the tip, however, the force interaction becomes much stronger and flips the dimers as the tip is raster scanned across them. This originates from the chemical interaction between the tip and lower dimer atom. As the tip moves above a lower dimer atom, the chemical interaction is strong enough to ‘pull’ the atom upwards, as the two silicon atoms attempt to form a stronger bond. Simultaneously, to compensate for the induced strain, the previously ‘upper’

dimer atom, trades places and moves downwards, leading to a complete switch of dimer orientation. Therefore it is always the upper atom of a dimer which is imaged. This process is schematically outlined in Figure 4.4 (d).

Although in this case the observations were scan induced, and therefore relatively uncontrolled, they pose a particularly interesting question. Is it possible to control the orientation of an individual dimer via mechanical manipulation? Moreover, using AFM can we infer the *force* required to flip a dimer? These are the questions which motivate a chapter of work presented in this thesis, and will be returned to in Chapter 5.

#### 4.2.2 Dimer vacancy defects

Several types of defect are present on Si(100). The most important for the simulations described in Chapter 5 are native dimer vacancy (DV) defects. DVs arise when a single dimer, or small cluster of dimers, are absent along a surface row. Although careful preparation of Si(100) can significantly reduce the number of DVs present, defects can never be completely eliminated and are often conveniently used as registration markers in scanning probe images. Two of the most frequently observed defects post-preparation are shown in Figure 4.5 as ball-and-stick models, adapted from Wang *et al* [103].

The most commonly observed defect is the 1DV (Figure 4.5(a)). Wang *et al.* calculated that the most stable model for the 1DV involved a reconstruction of the second layer atoms, thus terminating the four free bonds left by the missing dimer. Although this was calculated to be the most stable state, significant strain is introduced into the local area, as bond lengths are increased by up to 8%. If we consider the buckling present along the dimer row, then the calculation of the 1DV becomes more complicated. Sainoo *et al.* [104] discuss observations of 1DV defects, and group them into three categories. Two models in particular relate to the phase

of the dimer row either side of the defect which can either be  $c(4 \times 2)$  or  $p(2 \times 2)$  relative to the surrounding rows. This will of course present a problem in simulation due to the periodic repetition of the surface slab. A surface defect inducing a phase change will break the symmetry of the slab when repeated. Consequently, unless a second 1DV is included elsewhere (within a much larger simulation cell) only the 1DV structure which *does not* induce a phase change can be studied.

The buckling of a dimer affects the bond lengths, and absolute positions, of the second layer connecting atoms. Alternately buckled dimers minimise strain, leading to a long range symmetry. Therefore, the buckling arrangement of the dimers immediately adjacent to a 1DV will affect the second layer reconstruction. Sainoo *et al.* suggest a broken dimer vacancy model, where, depending on the buckling arrangement of the adjacent dimers, one, or both of the reconstructed bonds will actually be broken. In the authors experience when modelling the 1DV vacancy, buckling-induced strain at the 1DV appears to be present. In the limited number of calculations carried out thus far, however, broken bonds remain unobserved. The author also notes that a 1DV model with adjacent dimers buckled at the same angle (no phase change) appears to result in a large degree of strain, twisting the rebonding of the second layer atoms. This is in contrast to the apparent experimental observation of twisting occurring for a phase-change-inducing 1DV.

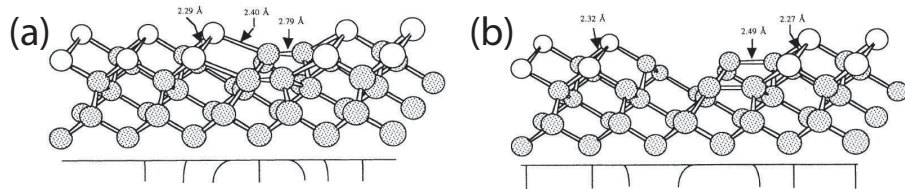


Figure 4.5: Dimer vacancy defects on Si(100). (a) Minimum energy structure for 1DV dimer defect. (b) Minimum energy structure for 2DV dimer defect. Ball-and-stick models adapted from Wang *et al* [103].

Due to the complications associated with a detailed high-level DFT study of

1DV vacancies we instead chose to model the simpler 2DV structure. Although phase changes may still be possible around a 2DV, the most widely studied stable structure of the 2DV maintains the phase, providing a simple system for simulation. Our simulations found that bond lengths were affected by a lesser extent than for the 1DV structures and support the proposed model of Wang *et al.* [103] shown in Figure 4.5(b). Additionally, the proposed structure is supported by previous experimental NC-AFM observations, which appear to show weak contrast above the second layer atoms [105].

### 4.3 Hydrogen passivated Si(100)

An interesting modification of the Si(100) surface arises after exposure to atomic hydrogen. The sample can be prepared by leaking hydrogen gas into the preparation chamber across a heated tungsten filament. The filament temperature is usually between 1800 and 2100K and serves to decompose the H<sub>2</sub> molecule into atomic hydrogen. If the Si(100) sample is elevated to a temperature of around 600 K [106], then the hydrogen atoms will react with the dangling bonds present on clean silicon, terminating the dimers, as shown in Figure 4.6. Preparation under these conditions typically results in the monohydride (2 × 1) structure shown in Figure 4.6 (b), where each dimer is now stabilised into a symmetric configuration, even at room temperature. Other preparations of Si(100):H can be followed by elevating the sample to different temperatures, such as the (3 × 1) [107, 108] and (1 × 1) [109, 110] dihydride stuctures. In the course of this thesis, however, only monohydride samples have been studied.

Several types of defects are usually present on the (2 × 1) Si(100):H surface. The number of these (see Figure 4.6(c)) can vary depending on the quality of the preparation. The first type of defect, similar to that found on the clean surface, is the vacancy type defect (blue dotted circle). These appear similar to the DV defects

on Si(100) and correspond to missing dimers in the top layer of the reconstruction. Interestingly, in some cases vacancy defects only a single atom (i.e. half a dimer) in size are observed. This is particularly clear in the AFM results presented in Chapter 6. Other defects on the surface can be difficult to distinguish without an STM tip providing clear atomic resolution, as they all appear as bright protrusions in the image. These include surface adsorbates (due to an imperfect background pressure or contaminated hydrogen line (red ellipse in Figure 4.6(c))), so called split-dimer defects (green dashed circle), and dangling bond defects (black solid circle).

Split-dimer defects usually appear as a bright bean-like protrusion in empty states STM images [111], although there is no as yet accepted explanation of their structure [112]. Original observations assigned the split-dimer defect to dihydride structures [113, 114]. Later work [112], however, used a variety of silicon samples, with different dopant atoms and a combination of filled and empty states imaging to put this model into doubt.

#### **4.3.1 Dangling bond defects on Si(100):H**

Perhaps the most interesting surface features, and certainly the most heavily studied [115], are the dangling bond (DB) defects observed due to incomplete passivation of the Si(100) surface. Incomplete passivation can lead to silicon dimers with one or more dangling bonds still present, forming isolated chemically reactive sites on an otherwise unreactive surface (see Figure 4.7(a)). The dangling bond feature typically appears as a bright protrusion in STM images as highlighted in Figure 4.6 by the black solid circle.

Dangling bond features offer a particularly interesting environment to study controlled adsorption of atoms and molecules. The hydrogen-passivated surface is extremely unreactive and, thus, individual reactive sites can be exploited. For instance, previous studies have reported directed molecular growth of styrene chains

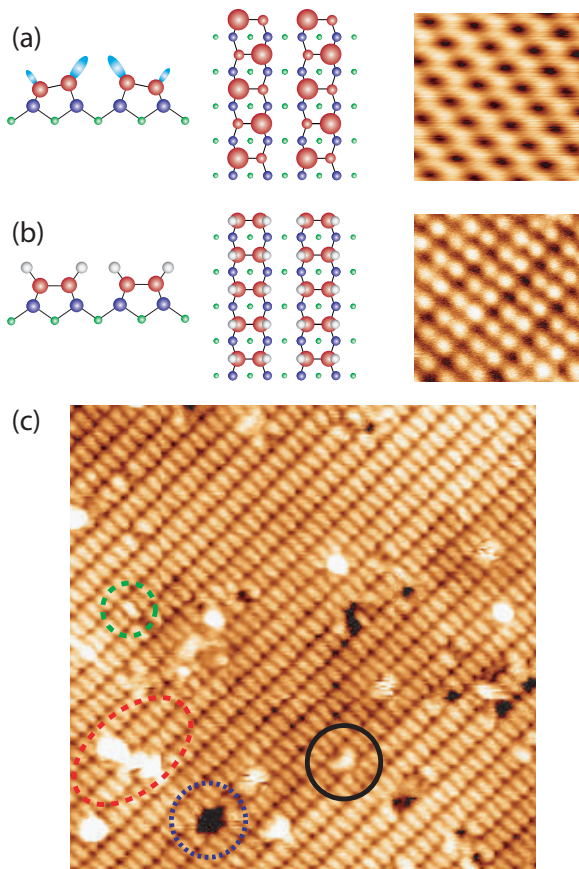


Figure 4.6: Structure of the Si(100):H surface. (a) Schematic and  $5\text{nm}^2$  constant current image of the clean Si(100) surface (-1.8V/21pA). (b) Schematic demonstrating hydrogen passivation, leading to a  $(2 \times 1)$  symmetric dimer reconstruction (+2.8V/500pA). (c)  $30 \times 30\text{nm}$  constant current image of Si(100):H highlighting typical surface defects, DV (dotted blue circle), split-dimer (dashed green circle), surface adsorbate (dashed red ellipse) and dangling bond (DB) defect (solid black circle) taken at +1.8V/30pA.

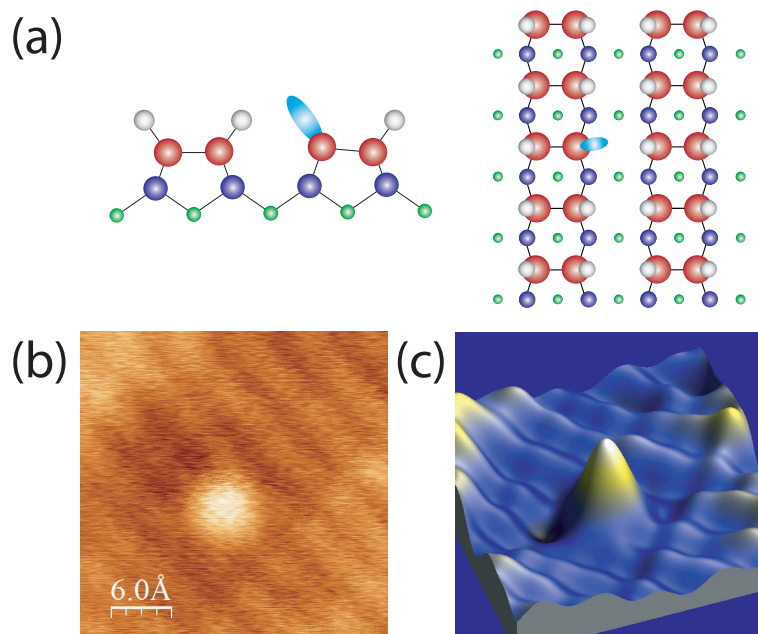


Figure 4.7: Incomplete passivation of the surface leads to formation of DB structures.  
(a) Schematic of an isolated DB defect. DB defects can be ‘highlighted’ by scanning at biases of  $\sim 2\text{V}$ , leading to dark visible halos around the defect as shown in (b).  
(c) The same image as (b) but rendered in 3D to better show the intensity of the DB relative to the surrounding dimers.

[116], where individual dangling bonds were used as nucleation points to start a chain reaction of molecular chemisorption. It is also possible to controllably remove H via the STM tip either lithographically, removing large regions of H, to form patterns of reactive surface, or with single atom precision (see later in this section). Atomically precise hydrogen desorption also makes it possible to direct the placement of individual dopants. Areas of hydrogen can be removed, exposing the surface in the desired locations whilst the remaining H acts as a masking layer [117]. This has most recently been demonstrated in an amazing sequence of experiments where an atomic wire [118], and even a single atom transistor [119] were fabricated on the Si(100):H surface.

In surfaces where there are many DB features (or where they are created via lithographic techniques, see next section), the DBs can aggregate together forming larger clusters than just the single isolated feature in Figure 4.6. Depending on the scan parameters, and the quality of the STM tip, it is possible to distinguish between cluster types and determine the individual locations of the constituent atoms with atomic precision [120]. However, in many cases, although the STM tip can provide excellent atomic resolution of the passivated surface, if the tip is not sufficiently ‘sharp’ then the DB features will be broadened, preventing clear determination of the DB cluster configuration. In these situations it can be challenging to distinguish DB clusters from surface adsorbates, often making it impossible to confidently make measurements on a DB feature. To remedy this problem it is possible to scan within a particular bias range to ‘highlight’ the DB features. On heavily doped n-type silicon samples ( $0.01 \Omega \text{ cm}$  resistivity) empty states images collected at a bias voltage of  $\sim 2\text{V}$  reveal the DB features as a bright protrusion surrounded by a dark ‘halo’ [121] as shown in Figure 4.7(b) and (c). This appears to be best explained [122] by tip and DB-induced band banding as the STM tip approaches the DB. The dominant rate of electron transfer out of the DB is the thermal emission

of electrons into the conduction band of the silicon, and as the tip approaches the DB, the electron injection rate into the DB increases exponentially. At a critical distance the injection rate becomes greater than the transfer rate out of the DB, increasing the DB's charge state, which in turn increases the band bending affecting the total current measured in the STM scan. This appears to explain the sharp appearance of the dark halo surrounding the DB site, which should in principle be even larger at lower sample temperatures.

One of the most exciting fields of study on Si(100):H involves STM H lithography. In the pioneering studies by Lyding *et al* [123] two distinct mechanisms are observed to lead to H depassivation.

1. Electronic excitation of the Si-H bond by applying a large bias between tip and sample in the field-emission regime.
2. Vibrational excitation of the Si-H bond at lower voltages. This mechanism is both voltage and current dependent.

The method of direct excitation is relatively simple to understand. It was reported [123] that the hydrogen layer can be removed, exposing the clean Si(100) surface, by increasing the the tip bias to between -5.5 and -7.5V (effective sample bias of +5.5V and +7.5V), similar to observations on the H-terminated Si(111) surface [124,125]. The process was observed to follow a step-like behaviour as the sample bias was increased, where the desorption yield rapidly increases at  $\sim +6.5V$  [126]. This suggests that once a threshold voltage has been reached, each electron emitted by the STM tip contains enough energy to break the Si-H bond, desorbing the hydrogen. Theoretical calculations [127] identifying the step with the  $\sigma(\text{Si-H})$  bonding to  $\sigma^*(\text{Si-H})$  anti-bonding transition supported the mechanism.

Low voltage desorption has been explained via a resonance excitation mechanism [126] from inelastic tunnelling, where incident electrons are temporarily trapped

within a molecular orbital causing a vibrational excitation. Due to the high current density in STM, and the relatively long vibrational lifetime of the adsorbed H, multiple ( $\sim 10$  or more) electrons are thought to impart energy to the Si-H bond through successive vibrational excitations, thus breaking the bond and causing desorption. This explanation was based on measurements of the desorption yield, which seemed to suggest  $\sim 11$  electrons were required for each H desorption event. Since these initial reports, however, a systematic study has observed that even at lower applied biases ( $V_s = +2.5V$ ) far fewer electrons are required for each desorption event [128]. This seems to indicate that higher energy dissipative inelastic electron channels are responsible for desorption [129], requiring a single electron to excite multiple vibrational quanta.

The assertion that it is only electrons that contribute the energy required to break the Si-H bond was apparently supported by the observation that only positive sample biases seem to induce desorption events [123]. Even when negative biases up to -10V are applied, no desorption was observed. Later studies [130], however, found that desorption at negative biases could occur via a hole resonance.

The resolution of the lithography methods are determined by the magnitude and extent of the electric field produced, which also depends on the tip-sample separation. In the field emission method the tip-sample separation is relatively large and the induced field can cover a large region reaching  $\sim 5\text{nm}$  at best(see Figure 4.8(a)). Additionally, if the tip is relatively blunt then the spatial resolution can be made worse. In contrast, the vibrational excitation method is able to obtain atomic scale resolution. In the first report of the technique it was already observed that atomic row precision was possible, as shown in Figure 4.8(b).

Since these initial demonstrations an explosion of interest followed, driving the technique to enable single H atom depassivation at both room and cryogenic temperatures(see Figure 4.8 (c) and [115, 117, 121, 131, 132]). Demonstrating the level

of control now possible, it has also been shown that DB features can be switched from either side of the silicon dimer via the STM tip, in principle ‘fixing’ mistakes during depassivation [133]. This surface, and the discussion relating to dangling bond features, is particularly relevant to the results presented in Chapters 6 and 7.

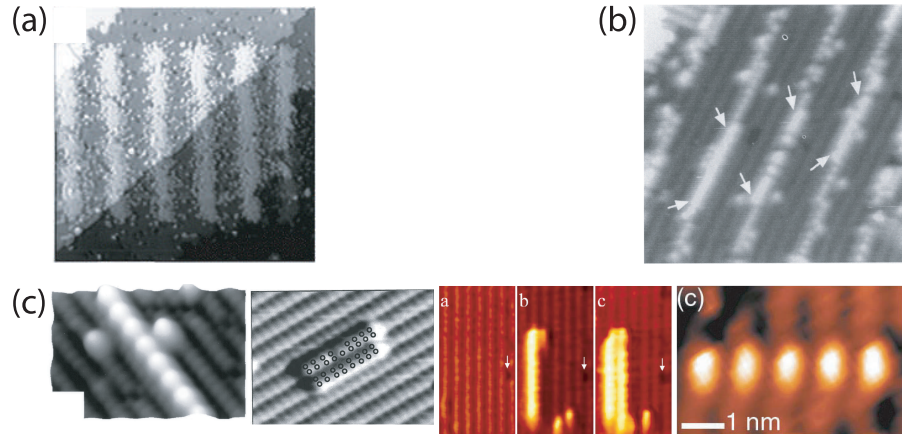


Figure 4.8: Examples of tip-induced desorption of surface H from Si(100):H. (a) and (b) show the first demonstrations of high and low voltage H desorption with an STM tip. [123, 126] (c) Images demonstrating controllable, atomic precision lithography to fabricate DB wires. Adapted from [117, 131, 132, 134]

#### 4.4 Si(111) surface

The  $(7 \times 7)$  reconstruction of the (111) face of silicon has perhaps been one of the most enigmatic surface reconstructions ever to be studied starting from the first LEED observations in 1959 [80]. It was with this surface that the true power of the STM was first demonstrated by Binnig *et al* [17], resolving individual atoms, as shown in Figure 4.9. In the years prior to the real-space STM images, the surface structure had remained relatively uncertain. The STM was able to establish that the surface consists of twelve adatoms arranged in a diamond shape, with large holes present at each corner. After these observations, the dimer-adatom-stacking (DAS) model was ascertained based on a series of TEM experiments to explain the

reconstruction [36, 135].

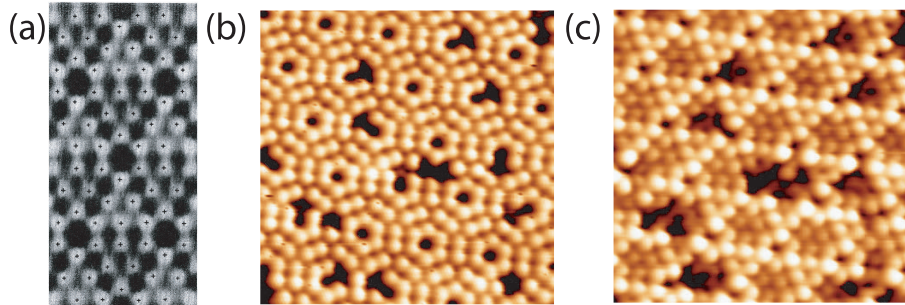


Figure 4.9: STM images of the Si(111) - (7 × 7) reconstructed surface. (a) The first real space STM image taken on the (7 × 7) surface [17]. (b) Unoccupied (+2V/40pA) and (c) occupied (-2V/40pA) states STM images taken shortly after one another with the same STM tip(taken on the Createc system). It is clear from (c) that the two halves of the unit cell appear differently due to the stacking fault.

The diamond-shaped surface unit cell is made up of a faulted and unfaulted half which are joined through dimers. The reconstruction essentially takes place over three layers. The initial third layer is the simple 1 × 1 bulk termination shown in Figure 4.10(a). The second layer then consists of the faulted and unfaulted domains, where the atomic positions of the unfaulted half in the second layer align with those of the third, rather than in the normal bulk arrangement. The faulted and unfaulted domains are joined by dimers to accommodate for the lattice mismatch (Figure 4.10(b)). At this stage there are 43 unsaturated surface bonds in the reconstruction. To minimise the number, additional silicon adatoms bond to three of the surface atoms, leaving one single unsaturated bond for every three. In the DAS model the adatoms are positioned over the second layer atoms adopting a fourfold coordination known as  $T_4$ , as shown in Figure 4.10(c). The alternative model would be that where adatoms are positioned over the third and fourth layer atoms (over hollow sites in the second layer), leading to a threefold coordination, termed  $H_3$  (this will become more relevant when modelling AFM tip clusters in the later sections).

The faulted and unfaulted halves of the unit cell can be observed in filled states

STM images where one half can appear brighter than the other (Figure 4.9 (b) and (c)). Amazingly, the DAS reconstruction model can be further confirmed in STM by removing the adatom layer following sample exposure to  $Cl_2$  [12, 136]. Shown in Figure 4.10(d) is the result of such an experiment clearly showing the 42 maxima corresponding to the unsaturated bonds (not including that present at the corner hole of the unit cell).

The particular feature of the Si(111) -  $(7 \times 7)$  surface exploited in this thesis is the relatively large separation of the adatoms<sup>1</sup> and the narrow spatial extent of their associated dangling bond orbitals. This can be particularly well observed in simultaneous STM and AFM measurements [18] where rather than the typically large features observed in STM, the true spatial extent of the dangling bond is chemically mapped out with AFM showing a marked reduction in spatial extent. Electronic structure calculations for the  $7 \times 7$  surface are computationally expensive due to the large size of the unit cell and the number of layers required to properly model the surface. In previous studies (see for e.g. [40, 41]) smaller approximations to the surface were successfully made, including the  $5 \times 5$  reconstruction and also a 10 atom approximation for a single adatom. These studies, along with more recent DFT calculations of the complete  $7 \times 7$  surface [137], all observe that the protruding dangling bond orbital is significantly localised to the adatom. This feature has been exploited in NC-AFM experiments [25] where it was thought that subatomic features, originating from the orbitals protruding from a single atom, could be resolved by reverse imaging the AFM tip with the localised  $7 \times 7$  adatom orbital. Since then, theoretical studies have concluded that rather than single orbitals, the larger structure of the AFM tip was probably responsible for the double lobed features, for instance simulated images showed that a dimerised tip consisting of C-Si apex could account for the same observations [50].

---

<sup>1</sup>~7.8 Å compared to, for instance, the 3.9 Å separation for the bulk terminated surface.

The reverse imaging technique, and the Si(111)-(7x7) surface is particularly relevant to the results presented in Chapter 7.

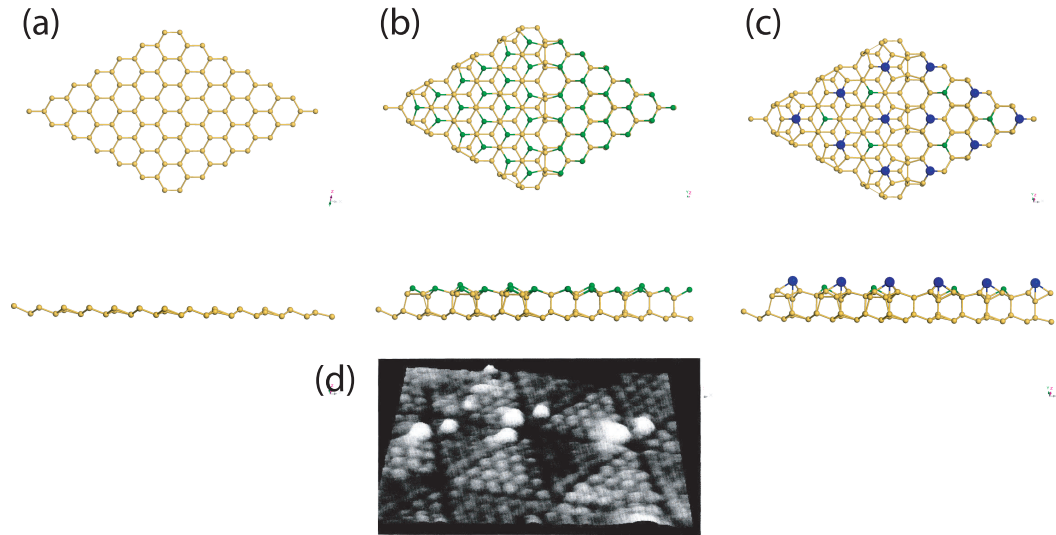


Figure 4.10: First three layers of the Si(111) - (7 × 7) DAS model shown as ball and stick diagrams. (a) Third (bottom) layer with a bulk arrangement of atoms. (b) Second layer showing the stacking fault on the right hand side of the unit cell, dangling bonds shaded in green. (c) Top adatom layer where the number of free bonds is reduced from 43 to 19. (d) A real space STM image of the second layer in the reconstruction, adapted from [136]

## 4.5 Silicon sample preparation

During the course of this thesis, experiments were primarily carried out on Si(111)-(7×7), Si(100) - (2×1) and Si(100):H (2×1) surfaces. Preparation of clean Si(111) - (7 × 7) and Si(100) follow largely the same procedure. Arsenic doped low resistivity (6 mΩcm) Si(100) and boron doped (10-20 mΩcm) Si(111) samples are used for all results. Native oxide-terminated wafers are laser cut to 3mm × 10mm in size. Samples are solvent cleaned *ex situ* before loading into the vacuum chamber. Prior to preparation, wafers are degassed at ~600°C (below the temperature required to remove the oxide) for 6-12 hours, removing contamination from the wafer. Following

this degas, samples are “flash” heated to  $\sim 1150^{\circ}\text{C}$ , after which they are gradually cooled from  $900^{\circ}\text{C}$  at a rate of  $\sim 1^{\circ}\text{C}$  per second, whilst maintaining a pressure below  $1\times 10^{-10}$  mbar.

The initial high temperature flash serves to remove the oxide layer, exposing the bare silicon, and drives carbon contamination into the bulk to leave a clean silicon surface. The slow cool from  $900^{\circ}\text{C}$  allows the surface to reconstruct into its ground state configuration. Particularly for the Si(100) samples, slow cool down rates were found to dramatically reduce surface defect densities resulting in extremely clean surfaces, similar to a suggestion by Hata *et al.* [138].

Hydrogen termination of the Si(100) surface was performed *in situ* using a Specs GmbH thermal gas cracker positioned approximately 10cm from the sample. To obtain a good  $(2 \times 1)$  reconstruction the sample was annealed at  $\sim 350^{\circ}\text{C}$  (with an associated error bar of  $\sim 50^{\circ}\text{C}$ ) during exposure to H. Hydrogen gas (99.999% purity) was introduced into the system via the gas cracker until a stable pressure of  $2\text{-}3 \times 10^{-7}$  mbar was reached, after which the sample was exposed for two minutes. At the end of the exposure time, the cracker was turned off simultaneously with a reduction in the sample temperature, after which the gas flow was quickly terminated. Prior to leaking  $\text{H}_2$ , the chamber pressure was typically  $\sim 1\text{-}2 \times 10^{-9}$  mbar due to the operation of the thermal gas cracker. To ensure a clean exposure, the  $\text{H}_2$  gas line is typically baked for 4-8 hours before flushing the line with 2 bar of gas several times. Additionally the cracker is ran at  $400^{\circ}\text{C}$  overnight, and at elevated temperatures ( $\sim 410\text{-}450^{\circ}\text{C}$ ) for 1-2 hours prior to use ( $400^{\circ}\text{C}$  relates to the capillary temperature measured via a thermocouple, corresponding to  $\sim 1800^{\circ}\text{C}$  filament temperature).

## 4.6 C<sub>60</sub> molecule

In the results presented in Chapter 7, C<sub>60</sub> molecules deposited on a Si(111) -  $(7 \times 7)$  surface serendipitously led to a series of experiments demonstrating the exciting

possibility of on-tip molecular functionalisation (see section 2.3.6). It was not the electronic structure of C<sub>60</sub>, but rather its distinct atomic structure which allowed us to demonstrate how the orientation of a tip-adsorbed molecule can be determined in AFM. Once this is known, it is possible to make orientation-specific measurements. Therefore the C<sub>60</sub>, due to its unique structure and ability to bond to the AFM tip, allowed us to demonstrate a technique which can be applied to any number of molecules. As such, rather than presenting a comprehensive review of the fullerene family of molecules and their surface interaction, this short section will instead focus on the literature surrounding AFM of C<sub>60</sub> molecules and the specific work associated with tip-adsorbed C<sub>60</sub>.

The archetypal molecule from the fullerene family is the C<sub>60</sub> molecule. Discovered in 1985 the novel ‘football’ structure (shown in Figure 4.11) of the sixty C atoms prompted a huge amount of interest. In particular, there have been a vast number of studies of C<sub>60</sub> molecules adsorbed onto atomically clean metal [139, 140] and semiconductor surfaces [141]. On semiconductor surfaces in particular, such as the (100) and (111) faces of silicon, there have been a considerable number of studies examining the bonding configurations available for the C<sub>60</sub> molecule.

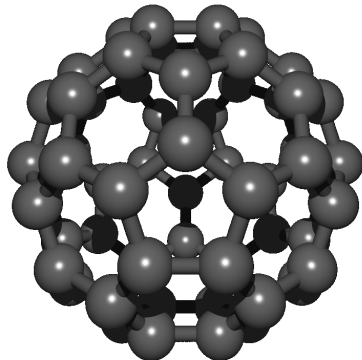


Figure 4.11: Ball and stick diagram of the C<sub>60</sub> fullerene molecule oriented with the pentagon face pointing out of the page.

An important aspect of the literature on the interaction of fullerenes with sili-

con surfaces is the long-running uncertainty over whether adsorbed C<sub>60</sub> molecules are chemi- or physisorbed onto the (7 × 7) surface [141], especially at high (i.e. monolayer) coverages. Diluting a complicated history down to only a few studies, Sakamoto *et al.*'s explanation for monolayer C<sub>60</sub> adsorption on (7 × 7) appeared to show that only a fraction of the molecules formed covalent bonds with the surface (~25%). The remaining molecules were thought to be physisorbed. A more recent combined XPS, UPS and STM study from Nottingham [142], however, finds this explanation incompatible with their results, and instead propose that *all* molecules, up to a coverage of one monolayer, are covalently bound to the surface. The results presented in this thesis were taken with very low surface coverages, in order to isolate individual C<sub>60</sub> molecules, therefore in each case the C<sub>60</sub> molecule is certainly covalently bonded to the surface. Theoretical combined DFT and molecular dynamics studies [143] have calculated the most stable adsorption sites of the C<sub>60</sub> molecule on the (7 × 7) unit cell, the most stable of which being the corner hole site where four C-Si bonds are formed. The next most stable site locates the C<sub>60</sub> molecule directly above one of the rest atoms closest to the centre of the unit cell, on the unfaulted side. In this configuration the C<sub>60</sub> makes six C-Si bonds and is significantly deformed. It is therefore important to note that multiple C-Si bonds are required to break when manipulating the molecule.

As a prelude to the AFM experiments reported in Chapter 7 it is necessary to understand some of the key features of room temperature STM manipulation experiments on both Si(111)-(7 × 7) and Si(100) surfaces. The strong covalent interaction described above makes the C<sub>60</sub> molecule bonding site particularly stable at room temperature, allowing stable manipulation experiments to be conducted. This is in contrast to the low temperature (~4K) requirements for the seminal experiments carried out by Eigler *et al* [10, 11]. The explanation for the manipulation of C<sub>60</sub> is particularly relevant to understanding how the molecule can be picked up by the

tip and attached to the end of the scanning probe. In work carried out on Si(111)-(7 × 7) it was demonstrated that individual molecules could be moved to pre-defined positions, via lateral STM manipulation, building up simple patterns [144,145]. Due to the particular bonding configurations of C<sub>60</sub> on the (7 × 7) reconstruction it was sometimes difficult to manipulate the molecule in a straight line, as the minimum energy pathway of the molecule will not necessarily follow the trajectory of the tip. On the anisotropic Si(100) surface, however, this can be avoided to a large extent by performing manipulations along the direction of the dimer rows. The success rate for manipulation then rose from 10 - 50% on (7 × 7) to ~95% along the rows, and ~15% perpendicular to them [146].

Similar to the Si(111) surface, C<sub>60</sub> forms multiple bonds on Si(100), the most stable of which are configurations where the molecule makes either two, or four Si-C bonds, when positioned within the dimer row ‘trench’. Therefore, an understanding of manipulation on (100) will also have significant relevance to (111). Further studies found that C<sub>60</sub> molecules can be either pushed or pulled [147] along the surface. The pushing mechanism corresponds to rolling the C<sub>60</sub> caused by a repulsive force and the pulling mechanism originates from an attractive tip-molecule interaction causing the molecule to ‘hop’ along the surface. The attractive mechanism in particular gives us important information about the system. Due to the size and symmetry of the molecule with respect to the scanning probe, a significant proportion of the molecule’s surface area will be exposed to the tip, making available the possibility of multiple tip-molecule bonding sites. Indeed, a comprehensive theoretical DFT study [148] which models the repulsive ‘pushing’ of the molecule shows the formation of strong C<sub>60</sub>-tip bonds. Therefore, in principle, a similar behaviour should exist for the pulling mechanism, where the C<sub>60</sub>-tip bonds are strong enough to break those between the C<sub>60</sub> and the surface, causing the molecule to hop from one position to another. In another study by Martsinovich *et al* [149], focusing on

the prediction of NC-AFM manipulation types, it was shown that it is possible to vertically remove a C<sub>60</sub> molecule from the Si(100) surface using exactly this mechanism. In this scheme the tip comes into contact with the C<sub>60</sub> forming chemical bonds. The C<sub>60</sub> is subsequently rolled from its stable bonding configuration into a metastable configuration, at which point the C<sub>60</sub>-tip bonds are stronger than those between the C<sub>60</sub> and surface, enabling the molecule to be completely removed from the sample, attaching it to the tip apex. Although it is not certain that this process is responsible for the on-tip C<sub>60</sub> experiments presented in Chapter 7, it is certainly a plausible mechanism.

The group of Berndt *et al.* in particular have carried out a series of elegant STM experiments [150, 151] with tip-adsorbed C<sub>60</sub> molecules. In their initial publication proposing the idea (Schull *et al.* [150]) the charge flow from one C<sub>60</sub> to another was probed. As shown in Figure 4.12(b) the C<sub>60</sub> molecules were deposited onto a Au(111) surface such that it was partially covered with islands, and individual molecules. Individual Au adatoms ( $\alpha$ ) or 2-3 Au atom clusters ( $\beta$ ) were then fabricated via small tip-surface indentations. In the STM scan with an Au terminated STM tip (left hand side) one can see that no structure is observed for the Au adatoms, however, clear structure can be seen for the C<sub>60</sub> molecules on the inside of the island. Note, in particular, the two orientations of the molecules observed as three bright protrusions. The tip was then positioned over a C<sub>60</sub> molecule, and the bias varied to remove a molecule from the island (black arrow). A further scan was then taken with the C<sub>60</sub> terminated tip (right hand image) in which structure is now observed on the Au adatoms, which reveals the orientation of the C<sub>60</sub> adsorbed molecule. Note in particular that one of the two orientations of the surface molecules previously mentioned now appear differently, demonstrating the more complicated convolution of the tip and molecule.

Turning to AFM investigations of C<sub>60</sub> molecules, it is apparent that far fewer

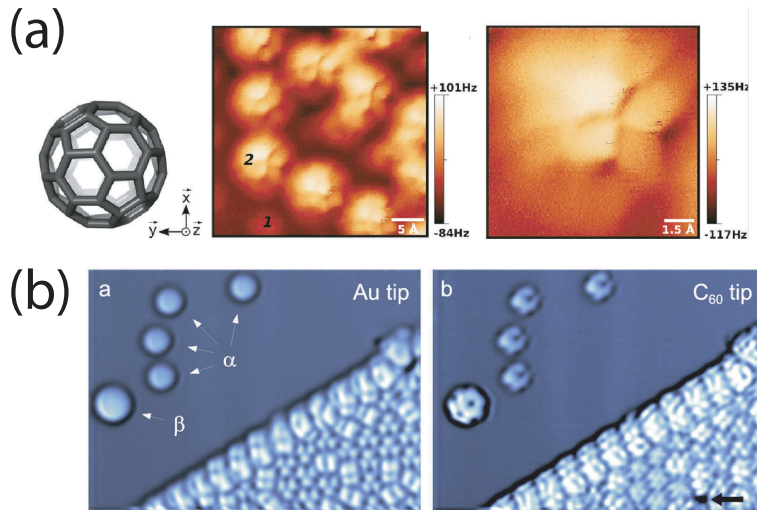


Figure 4.12: (a) NC-AFM images of resolving ‘bond’ contrast of C<sub>60</sub>s packed within a C<sub>60</sub> island. Adapted from [152]. (b) On-tip C<sub>60</sub> STM imaging. The downwards face of the molecule is determined by scanning Au clusters, reverse imaging the C<sub>60</sub> terminated tip. Adapted from [150].

studies have been conducted. Work by Kobayashi *et al.* [153,154] attempted to image both submonolayer and higher than monolayer coverages of C<sub>60</sub> on the Si(111)-(7×7) surface at room temperature. Although submolecular features were not observed, it was however possible to image the molecules as bright protrusions on the otherwise (7×7) adatom surface, or as bright spots on top of a monolayer coverage. The key problem when imaging isolated molecules with the AFM is the instability caused by the force interaction. The images observed clearly showed the molecules as ‘fuzzy’ features, often with dark depressions in their centre. This highlights two issues, first it suggests that the molecule is moving on a small scale during AFM imaging, either due to thermal motion, or small perturbations due to the AFM tip-molecule interaction. Due to the resolution required to obtain sub-molecular resolution any movement of the C<sub>60</sub> will cause a significant obstacle. Additionally, the C<sub>60</sub> molecule represents a significant change in topography relative to the sample surface which takes place over a very short distance. The feedback electronics have to respond

very quickly to the tip-surface variation to maintain a constant  $\Delta f$ , otherwise the force interaction will rapidly increase. This can almost certainly cause instabilities in imaging isolated molecules and can induce particular feedback artefacts leading to the apparent inversion in the centres of the molecules. Further studies were able to obtain molecular resolution within the close-packed C<sub>60</sub> layer after deposition of 2-3 monolayers onto the Au(111) surface [155]. However, sub-molecular resolution, of a quality similar to that obtained with STM [141] still proved to be elusive, as it was in further studies of C<sub>60</sub> islands on insulating surfaces [156,157].

Despite these observations, DFT simulations suggested that it should be possible to obtain sub-molecular resolution in AFM [158]. In this case the system was C<sub>60</sub> adsorbed onto the Si(100) surface, with the AFM scanning in the constant height mode, with a reactive silicon tip cluster. In the simulations it was shown that each carbon atom within the cage should appear as a bright maximum, reflecting the actual atomic positions within the molecule. However, it is clear that this is still a challenging experiment: in the simulations the C<sub>60</sub> was oriented such that the single C-C bond was pointing parallel to the surface normal. In this configuration only the topmost seven atoms of the cage could be resolved, demonstrating the rapid tail off in the force interaction due to the geometry of the cage.

Only very recently [152] has sub-molecular resolution of C<sub>60</sub> molecules been obtained at cryogenic temperatures. This was observed during investigations of C<sub>60</sub> islands on the Cu(111) surface. The features observed in the AFM images (see example in Figure 4.12(a)) contain the same ‘bond resolution’ as seen in the work by Gross *et al.* using CO terminated probes [28,55]. In this case the repulsive interaction is perhaps surprisingly thought to originate from a clean Cu tip and the C<sub>60</sub> molecule. Although sub-molecular resolution is observed, the contrast originates from a complicated, and unintuitive repulsive interaction, where the more repulsive hollow sites of the C<sub>60</sub> molecule are said to originate from the Cu tip repulsively

interacting with *all* of the surrounding C atoms. Moreover, the images are only made possible by the fact that the C<sub>60</sub> molecules are close packed within islands at low temperatures, restricting the movement of the molecules. This highlights the difficulties in obtaining AFM images of large organic molecules such that the orientation can be unambiguously identified.

## 4.7 Modelling methods

Throughout the work presented in this thesis, terminology is repeatedly used which refers specifically to the design of the simulated surfaces and the method for simulated  $F(z)$  measurements. Therefore, in the following sections, the techniques used to model the Si(100) surface and the method of simulated  $F(z)$  measurements will be outlined in some detail. A brief explanation of the nudged elastic band (NEB) method (used to calculate the minimum energy pathway between two energy minima) will also be presented.

### 4.7.1 Modelling and testing a surface: Si(100) example

The priority when modelling a surface structure is to accurately model the crystal bulk. Any deficiencies in the bulk approximation will add unphysical strain into the system, which will ultimately affect the surface structure. Typically, one of two methods are implemented: either the surface is mirrored around a bulk layer, or the bulk side of the surface slab is terminated with H atoms.

In the first case, strain caused by the surface reconstruction should be mirrored around the centre of the slab and will effectively be cancelled out in the bulk layer. The drawback, however, is that the surface reconstruction is modelled twice, a situation which becomes more problematic if surface processes are under investigation. In the second case, the bulk layers of the crystal are made sufficiently many such that the surface no longer has an effect, i.e. the bottom-most layer of silicon con-

verges to a bulk-like structure. Hydrogen atoms are then added to the underside of the slab to passivate the free Si bonds and represent the ‘infinite bulk’. This second method is used in the DFT calculations contained within this thesis.

Initially, to construct a surface, we must first simulate the bulk crystal. Two Si basis atoms are defined<sup>2</sup> and a geometry optimisation is carried out simulating the bulk, obtaining the correct bulk Si-Si distance within the framework of the DFT code. Subsequently, the number of layers in the surface slab should be chosen. Typically this is determined by a layer-by-layer increase until the system converges. For the Si(100) surface in this thesis, six layers were found to be more than sufficient for our needs. The free bonds on the underside of the slab are then terminated with H atoms, which must subsequently be allowed to relax to prevent artificial strain buildup within the system. The surface will then appear as the unrelaxed (2 × 1) bulk termination as shown in Figure 4.13(a).

Multiple reconstructions exist on the (100) face as local minima. To model one in particular, e.g.  $c(4 \times 2)$ , the atomic positions of the dimer atoms need to be ‘nudged’, pushing the system towards the required local minima. This can be achieved with shifts in the (x,y,z) co-ordinates by as little as 0.1Å (see Figure 4.13 (b)) prior to starting a geometry optimisation to obtain the actual atomic positions (Figure 4.13(d)). Once the surface has been made a number of checks can be performed, the most simple of which is to compare the relative energies of the reconstructions with previous results, or measuring the buckling angle and atomic separations to compare with experimental results ([159] and see Figure 4.13(c)). In the case of Si(100)- $c(4 \times 2)$ , the obtained values from calculation and experiment are summarised in Figure 4.13(c).

Now that the surface unit cell is completed, the cell can be extended to any desired size, such that it is large enough to include defects, adsorbed molecules, or

---

<sup>2</sup>which are periodically repeated to form the bulk crystal

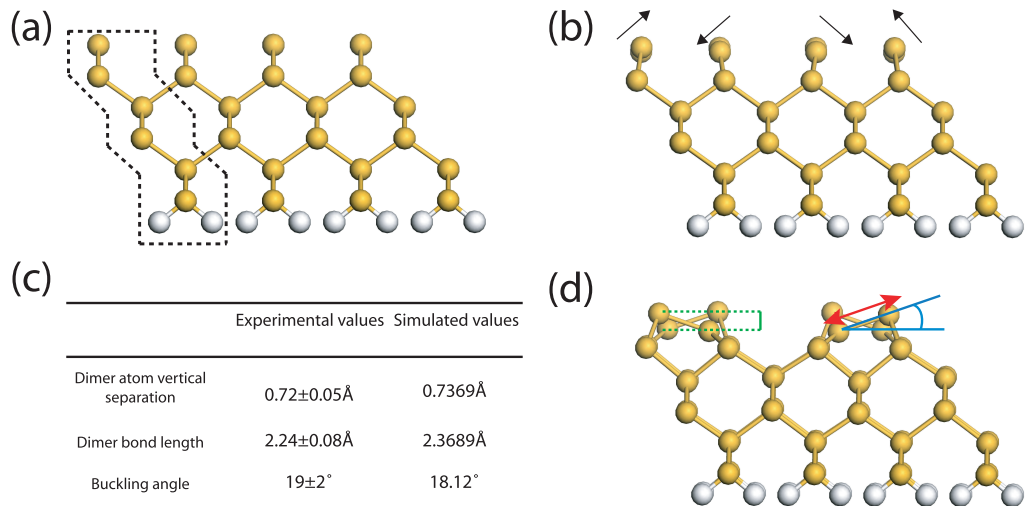


Figure 4.13: (a) The  $1 \times 1$  unreconstructed surface of the (100) face. (b) By ‘nudging’ the atomic positions in (a) by fractions of an Å the DFT geometry relaxation will converge on the  $c(4 \times 2)$  ground state shown in (d). (c) Experimental and simulated values for the dimer atom vertical separation, dimer bond length and buckling angle. Experimental data from [159]

to add a simulated tip cluster for AFM simulations. Whatever the requirement may be, the surface slab needs to be large enough such that finite size effects do not cause a problem.

#### 4.7.2 Simulating $F(z)$ measurements

Experimental  $\Delta f(z)$  measurements can be converted to  $F(z)$  via the Sader-Jarvis inversion algorithm. To properly interpret the experimental results it is often necessary to conduct DFT simulations to directly calculate  $F(z)$  curves for comparison.

To enable a plot of  $F$  vs.  $z$ , we require a full DFT geometry relaxation at a series of  $z$  (tip-sample separation) positions. Moreover, particularly when modelling the manipulation processes, the step size in  $z$  needs to be very small. If the step sizes are too large, effects such as hysteresis<sup>3</sup> will not be observed, leading to incor-

<sup>3</sup>and potentially the success of a manipulation event altogether.

rect results for comparison. In a typical simulation, we therefore use increments of  $0.15/0.1\text{\AA}$  which can require up to 110 complete geometry relaxation DFT calculations per simulated spectra. The ability to carry out such a large number of detailed calculations has been made possible by the excellent HPC facilities available within the University of Nottingham. Even so, a 110 step  $F(z)$  simulation can take up to seven days to complete, despite parallelisation across 32-64 CPU processors.

The process for simulating  $F(z)$  measurements is outlined in Figure 4.14(a). As mentioned above, ensuring a smooth evolution along the  $F(z)$  curve is paramount to accurately reflect the experimental system. As such it is important that the atomic geometry smoothly evolves with each step, thus preventing the system from jumping to alternative local minima in an unphysical way. Therefore, the initial geometry for each  $F(z)$  step is chosen to be the geometry output from its predecessor, after which the atomic positions of *all* the tip atoms are lowered, or raised, by the chosen step size. Geometry snap-shots of a typical  $F(z)$  simulation are shown in Figure 4.14(b). This perhaps helps demonstrate the quasi-static nature of the simulation, which models the  $F(z)$  curve as a single oscillation cycle, an important consideration when modelling manipulation and dissipation processes.

In an experimental  $\Delta f(z)$  measurement,  $z$  is defined by the piezo extension. Therefore, a similar definition for simulated measurements must be made to allow a proper comparison. In Figure 4.14(c) ball-and-stick models help explain the definition of  $z$ . In the initial system, the tip apex atom may be positioned  $8\text{\AA}$  above the target surface atom, defining the value of  $z$  for the starting configuration. The value for  $z$  in each subsequent step is  $8 \pm (n_a - n_r)0.1\text{\AA}$  where  $n_a$  is the number of approach steps,  $n_r$  the number of retract steps completed and  $0.1\text{\AA}$  the chosen step size. Therefore  $z$  no longer represents the tip-surface atomic separation (dashed model in Figure 4.14(c)), but instead represents the distance between the surface atom and the lowest tip apex atom *prior* to relaxation (solid model in Figure 4.14(c)),

as though the tip cluster had remained in its original configuration (without elastic deformations). Although this model is useful for experimental comparison, from a purely theoretical point of view it must be remembered that  $z$  is *not* the atomic separation of the tip-surface atoms.

#### 4.7.3 Nudged elastic band (NEB) basics

The nudged elastic band (NEB) method is used to find the minimum energy pathway (MEP) between a known initial and final configuration. In terms of atomistic calculations, a linear interpolation is typically used to obtain a set of “images” between the initial and final states. Each image corresponds to a guess at the atomic geometry along the MEP. The NEB method starts with the guessed images and minimises the energy band until it converges on the MEP.

The NEB code used to obtain the results in this thesis was written by Joseph Bamidele in King’s College London (KCL 2010). The code was used, however, on the Nottingham HPC, by the author, to obtain all of the results pertaining to minimum energy pathways in Chapters 5 and 6. Although the NEB method was implemented to some extent as a “black-box” technique, it is necessary to understand some its essential features in order to properly appreciate and critique the simulated results.

NEB [160–163] is a modification of the plain elastic band method (PES), designed to improve its major shortcomings. Both of these methods will now be explained. Figure 4.15 (adapted from [161]) demonstrates the result of the two methods applied to a simple model where an atom A can form a bond with either one of two other atoms B or C. The details of the model are not important as the figure will purely serve as a visual aid.

In the PES method, each image along the initially guessed band is subjected to a force defined as:

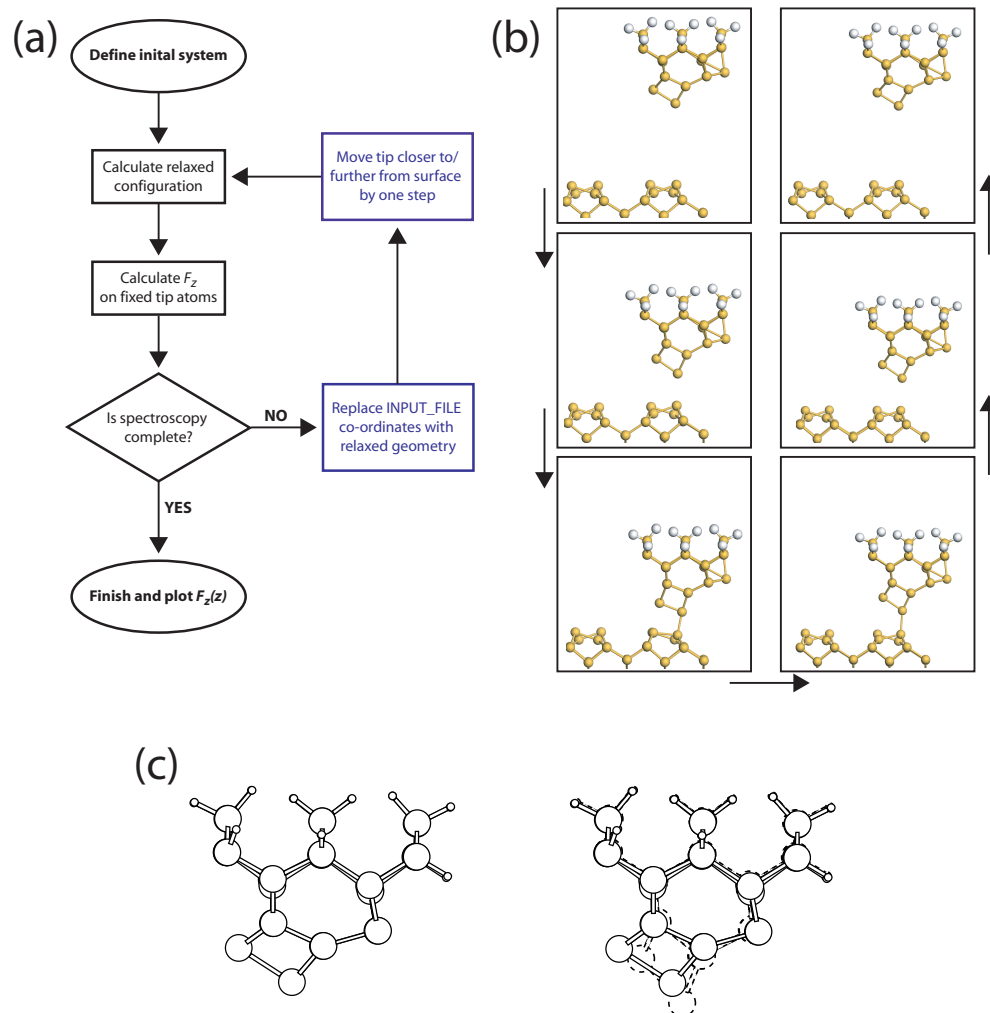


Figure 4.14: (a) Flow diagram describing the simulation process for  $F(z)$  measurements. (b) Ball-and-stick snap shots during  $F(z)$  simulation of a single oscillation cycle. (c) The tip-sample separation is defined by the distance between the surface atom and the lowest tip apex atom prior to any relaxations (top). As the tip is brought closer to the surface (bottom), the tip-sample separation no longer reflects the actual atomic separations, however, it is comparable to the experimentally known  $z$  piezo extension.

$$\mathbf{F}_i = -\nabla U(\mathbf{R}_i) + \mathbf{F}_i^s \quad (4.1)$$

where the total force acting on each atom within the system is made up of the ‘true’ atomic force ( $\nabla U(\mathbf{R}_i)$  calculated within DFT) and an artificially introduced spring force ( $\mathbf{F}_i^s$ ).  $\mathbf{F}_i^s$  is added to represent springs between each image, preventing each geometry optimisation from collapsing onto the initial or final configurations.  $\mathbf{F}_i^s$  is defined by the springs between each neighbour to  $\mathbf{R}_i$ ,  $\mathbf{R}_{i-1}$  and  $\mathbf{R}_{i+1}$ , each with an associated spring constant as shown in equation 4.2.

$$\mathbf{F}_i^s = k_{i+1} (\mathbf{R}_{i+1} - \mathbf{R}_i) - k_i (\mathbf{R}_i - \mathbf{R}_{i-1}) \quad (4.2)$$

With  $\mathbf{F}_i^s$  in this form, the spring force acting on each image has both parallel and perpendicular components relative to the direction of the path between images. Therefore, the choice of spring constant can be very important. If the spring constant is chosen to be large (see solid line with filled circles in Figure 4.15(a)) then the perpendicular component of  $\mathbf{F}_i^s$  can be large enough to push the image, and the band, away from the MEP, particularly near the saddle points. This is because  $\mathbf{F}_i^s$  overwhelms the perpendicular component of  $\nabla U(\mathbf{R}_i)$  which seeks to follow the slope into the MEP. If  $k$  is reduced, however, then although the tendency of the band to cut the corner of the true MEP will be reduced, the parallel component of  $\mathbf{F}_i^s$  is now no longer large enough to prevent the parallel component of  $\nabla U(\mathbf{R}_i)$  from pushing the images towards the initial and final states (representing the local minima  $\nabla U(\mathbf{R}_i)$  wishes to reach). As a consequence there are fewer images close to the saddle point, reducing the resolution at the area most important to obtain an estimate for the energy barrier (see Figure 4.15(b)).

To remedy this problem NEB was developed, in which only the parallel component of the spring force, and the perpendicular component of the true force are

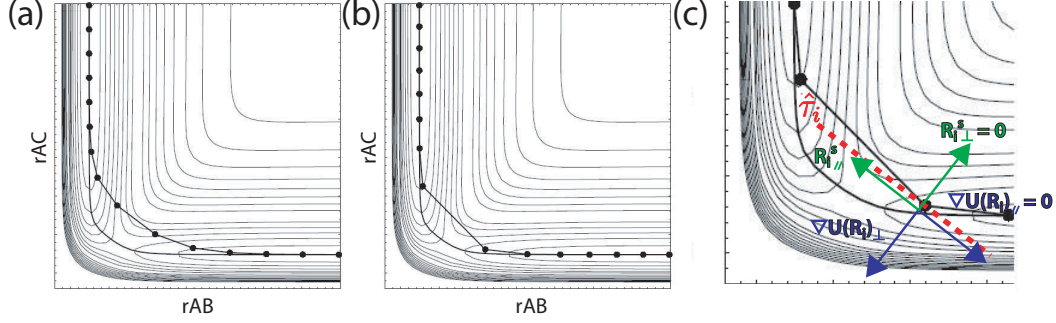


Figure 4.15: A simple potential energy surface demonstrating the elastic band methods. (a) and (b) show PES bands calculated with spring constants of  $k=1$  and  $k=0.1$  respectively, plotted as solid lines with filled circles compared with the NEB method plotted as a solid line. (c) shows a zoomed view of three images depicting the relevant forces in the NEB method. This figure is adapted from Jonsson *et al.* [161]

considered (relative to the direction of the band). Now the force on image  $i$  appears as:

$$\mathbf{F}_i = -\nabla U(\mathbf{R}_i) |_{\perp} + (\mathbf{F}_i^s \cdot \hat{\tau}_i) \hat{\tau}_i \quad (4.3)$$

where the magnitude of the parallel component of  $\mathbf{F}_i^s$  is calculated from the unit tangent to the path,  $\hat{\tau}_i$ , where,

$$\hat{\tau}_i = \frac{\mathbf{R}_i - \mathbf{R}_{i-1}}{|\mathbf{R}_i - \mathbf{R}_{i-1}|} + \frac{\mathbf{R}_{i+1} - \mathbf{R}_i}{|\mathbf{R}_{i+1} - \mathbf{R}_i|} \quad (4.4)$$

The perpendicular component of  $\nabla U(\mathbf{R}_i)$  is obtained by subtracting out the parallel component:

$$\nabla U(\mathbf{R}_i) |_{\perp} = \nabla U(\mathbf{R}_i) - (\nabla U(\mathbf{R}_i) \cdot \hat{\tau}_i) \hat{\tau}_i \quad (4.5)$$

Treating  $\mathbf{F}_i^s$  and  $\nabla U(\mathbf{R}_i)$  in this way decouples the relaxation of the band from the convergence of each image to the MEP. This is perhaps best understood by considering the sketch in Figure 4.15(c) where three images along the band are

shown. Drawn as a dashed line is  $\hat{\tau}_i$ , which is calculated at the middle image. It can be seen that if only the component of  $\nabla U(\mathbf{R}_i)$  perpendicular to  $\hat{\tau}_i$  is present, then the force pushing the image towards the final or initial local minima is 0, preventing bunching. Therefore  $\nabla U(\mathbf{R}_i)$  now serves only to converge the image to the MEP. Similarly  $\mathbf{F}_i^s$  no longer works against  $\nabla U(\mathbf{R}_i)$  (preventing the MEP from being reached), but acts solely along the direction of the band to provide a uniform separation between images. Due to the absence of  $\nabla U(\mathbf{R}_i)$  perpendicular to the band, the choice of  $k$  in  $\mathbf{F}_i^s$  no longer matters, and can take any value. The calculated band from NEB is shown as solid lines in Figure 4.15. An algorithm, such as velocity Verlet, is then used to move the images according to 4.3.

In a typical NEB calculation, the same value of  $k$  will be used for each spring connecting each image. Therefore the images will be equally separated, and a single image will not necessarily land exactly on the saddle point(s) preventing an exact measurement of the energy barrier<sup>4</sup>. The NEB method can be further modified to accommodate for this by adding a ‘climbing image’ [164]. Initially the NEB band evolves as already described until the image with the highest energy can be identified.

The force acting on image  $i_{max}$  is then changed to:

$$\mathbf{F}_{i_{max}} = -\nabla U(\mathbf{R}_{i_{max}}) |_{\perp} + (2\nabla U(\mathbf{R}_{i_{max}}) \cdot \hat{\tau}_{i_{max}}) \hat{\tau}_{i_{max}} \quad (4.6)$$

Therefore rather than modifying the image position via a spring force, an inversion of the true force acting parallel along the band is used. Thus the climbing image moves up the PES to the maximum (rather than the minimum) along the band, and moves down the PES perpendicular to the band. Because this image is moved to the saddle point without ‘seeing’ the spring forces, the spacing of the images on either side will be different. This is particularly noticeable in the results

---

<sup>4</sup>An interpolation can be made between the two closest points, however, this has a large associated uncertainty

described in Chapter 5.3.4.

Although further improvements can be made to the method, the climbing image NEB implementation allows an accurate determination of both the MEP and the energy barriers for transition. These two features are essential for understanding the results obtained on the Si(100) surface in Chapter 5.

## 4.8 Experimental methods

The majority of the experimental data presented in Chapter 6 were obtained by the author on a Createc LT STM/AFM system using qPlus sensors for FM-AFM measurements. In the following section the procedure for calibrating the qPlus sensors on the Si(111) -  $(7 \times 7)$  surface will be described. Additionally, an example experiment using the on/off and Sader-Jarvis methods for short range extraction on the  $(7 \times 7)$  surface will be discussed, demonstrating that the sensors used in Chapter 6 are calibrated correctly, and measure force interactions within the correct range. The section will finish with a brief description of the Createc system outlining the major components of the system, and some of the complications that were faced during its use.

### 4.8.1 Amplitude and force calibration

When a qPlus sensor is introduced into the system, the response of the tuning fork to the driving signal needs to be calibrated to a physical amplitude in nanometres. To do so one can use either the Giessibl [61,163] normalised  $\Delta f$ , or the Sugimoto [18] normalised time-averaged tunnel current methods.

As described in section 2.4.2, it is possible to relate the force to  $\Delta f$ , equation 2.11 is particularly useful and is reproduced below:

$$\frac{\Delta f(z, a)}{f_0} = -\frac{1}{\pi a_0 k} \int_{-1}^1 F(z + a_0(1+u)) \frac{u}{\sqrt{1-u^2}} du \quad (4.7)$$

Under the large amplitude approximation it is possible to derive equation 4.8 from 4.7 [165] shown below:

$$\frac{\Delta f(z, a)}{f_0} = \frac{1}{\pi k a_0^{\frac{3}{2}} \sqrt{2}} \int_z^{z+2a_0} \left[ \frac{F(t)}{\sqrt{t-z}} \right] dt \quad (4.8)$$

where  $z$  to  $z + 2a_0$  is the tip-sample separation range over an oscillation cycle, and  $t$  represents tip-sample separation as the integration variable. The important feature to note from equation 4.8 is that the integral is independent of  $a_0$  and only varies with  $z$ .

If we combine the integral and constant values we can see that,

$$\gamma(z) = \frac{f_0}{\pi k \sqrt{2}} \int_z^{z+2a_0} \left[ \frac{F(t)}{\sqrt{t-z}} \right] dt \quad (4.9)$$

$$\Delta f a^{\frac{3}{2}} = \gamma(z) \quad (4.10)$$

where  $\gamma(z)$  is a parameter termed the normalised frequency shift [61, 166]. It is equation 4.10 which is exploited to calibrate the amplitude. Essentially, whilst in  $\Delta f$  feedback,  $a_0$  is varied and  $\Delta f$  adjusted to maintain a constant  $\gamma(z)$ . As  $\gamma(z)$  is only dependent on  $z$ , if kept constant then the point of tip closest approach relative to the surface will also remain constant, even if  $a_0$  is varied. Therefore, to calibrate the amplitude we adopt the following procedure. At a particular, unknown amplitude<sup>5</sup> atomic resolution is obtained in  $\Delta f$  feedback.  $\gamma(z)$  can then be calculated from the current  $\Delta f$  and  $a_0$  (at this stage  $a_0$  is only known in mV). After pausing the scan, holding the tip's x-y position, we then take note of the z piezo extension required to

---

<sup>5</sup>usually chosen based on previous experience.

maintain the constant tip-sample separation.

As  $a_0$  is increased and the  $\Delta f$  setpoint adjusted to maintain a constant  $\gamma(z)$ , the z piezo extension will vary in order to maintain a constant tip-sample separation, therefore a direct measurement for  $a_0$  can be acquired. If the z piezo extension at each step is noted, then a plot of  $z$  vs.  $a_0$  can be made. The gradient of the straight part of the plot should then provide a physical calibration for the amplitude in nm/V.

The qPlus setup on the Createc system is tailored to work at small amplitudes of oscillation. The level of noise on the AFM signal is particularly high compared to our partner Omicron LT system. Therefore, at larger amplitudes, where the  $\Delta f$  setpoints required for stable feedback become smaller, the required  $\Delta f$  to maintain constant  $\gamma(z)$  can often fall below the noise level of the qPlus signal rendering it challenging, at best, to acquire suitable data points in the large amplitude region.

Alternatively, a normalised time-average  $I_t$  method can be used, proposed by Sugimoto *et al.* [18]. Similar to the  $\Delta f$  method the normalised time-average tunnelling current is independent of  $a_0$ , permitting the derivation of similar equations [18] to 4.8 and 4.10 as shown in 4.11 and 4.12.

$$\langle I_t(z) \rangle = \frac{1}{\pi\sqrt{2a_0}} \int_z^{z+2a_0} \left[ \frac{I_t(t)}{\sqrt{t-z}} \right] dt \quad (4.11)$$

$$\langle I_t(z) \rangle \sqrt{a_0} = \gamma_{I_t}(z) \quad (4.12)$$

It then follows that the same procedure can be adopted as for the  $\Delta f$  method outlined above, where the  $\langle I_t(z) \rangle$  setpoint is varied in place of  $\Delta f$ . This method can have a considerable advantage over the  $\Delta f$  method, as the tunnel currents required for feedback are easily above the noise level of the system, thus enabling a large number of accurate data points to be collected. For this method, a plot of  $\sqrt{a_0}$  vs.

$z_{ext}$  can be made. For the particular sensor used to obtain results in Chapter 6 a large difference between calibrated values obtained from the two methods was observed ( $\sim 790\text{nm/V } \Delta f$  method compared to  $\sim 212\text{nm/V } \langle I_t(z) \rangle$  method). However, this is purely due to the significant noise level in the qPlus signal affecting the  $\Delta f$  method. For the sensor in question only relatively small values for  $\Delta f$  were measured, even at small  $a_0$ , therefore the  $\Delta f$  values required for large  $a_0$  rapidly fell below the noise level of the system. The result of the  $\langle I_t(z) \rangle$  method, however, falls well within the range obtained from previous sensors where the  $\Delta f$  method could be applied.

As a check for the calibration, and of the tip-sample system in general, measurements can be made on the well understood Si(111) -  $(7 \times 7)$  surface and converted to force. Once the calibration is complete, we can optimise the choice of  $a_0$  required to obtain the best quality images and  $F(z)$  data. In Figure 4.16 on-off  $\Delta f$  measurements (see section 2.2.4) are shown, taken on the Si(111) -  $(7 \times 7)$  surface. The data are then converted to force following the methods outlined in section 2.4.2.

Initially  $\Delta f(z)$  spectra are taken above an adatom and a corner hole (Figure 4.16(a)), and the difference calculated (Figure 4.16(b)). The data in Figure 4.16(b) corresponds to the short range component of force present above a silicon adatom. Figures 4.16(c) and (d) plot the interaction potential,  $U(z)$ , and the interaction force,  $F(z)$ , obtained from the Sader-Jarvis [60] method<sup>6</sup>.

It should be noticeable that  $U(z)$  has a much smoother profile than  $F(z)$ . This is a direct consequence of one being the derivative of the other<sup>7</sup>. It does, however, demonstrate one of the major challenges faced when taking measurements on the Createc system, as the level of noise in  $F(z)$  originates from the poor noise level in the

---

<sup>6</sup>The code used to produce this data was written by Dr. Andrew Stannard (andrew.stannard@nottingham.ac.uk) in the University of Nottingham (2011), and uses an optimised procedure to carry out the required integration.

<sup>7</sup>Noise within the  $F(z)$  data can be significantly reduced if the differentiation of  $U(z)$  is made over multiple points (3-5), eliminating any artificial jumps in the  $F(z)$  curve caused by small noise-related kinks in the  $U(z)$  curve. The data density is enough such that physical features will not be present over 3-5 points (unless manipulation events occur during the measurement).

$\Delta f$  channel. To obtain a minimum acceptable noise level of  $\sim 0.2$  Hz an integration time of 150-200ms can be required, compared to  $\sim 30$ -50ms on our partner Omicron qPlus system. Consequently, individual  $\Delta f$  measurements, containing enough data points to provide a smooth  $F(z)$  curve, can take up to 2 minutes making repeat measurements, and thermal drift issues (even at liquid nitrogen temperatures) particularly challenging.

The data depicted in Figure 4.16 were taken with the same sensor used to obtain  $F(z)$  measurements in Chapter 6 of this thesis. As such it is pertinent to note that the measured turnaround force, and general profile of the data, fits well with previous observations, thus providing confidence to the previously described calibration process [18, 35, 41, 167].

#### 4.8.2 Createc LT STM/AFM system

All of the experimental results obtained by the author in this thesis (Chapter 6) were obtained using a commercial Createc GmbH LT STM-AFM system with Nanonis control electronics and software. The microscope is suspended by springs from the bottom of a cryostat which can be cooled with liquid nitrogen or helium, attaining temperatures of  $\sim 77$ K and  $\sim 5$ K respectively. We are able to maintain liquid nitrogen temperature for up to 7 days, and liquid helium for over 48 hours at a time. The scanning stage follows the beetle head (Besocke) design and contains four piezoelectric tube scanners, three outer tubes used for coarse approach,  $z$  feedback *and* for x-y scan control, and a single central tube used solely to apply the AFM oscillation excitation. The three outer tubes are each topped with a polished sapphire ball, upon which a copper ring rests. The ring is made such that it is divided into 3 parts, each of which are shaped into a ramp as shown in Figure 4.17(a).

The sample is mounted onto a transferable plate made from gold plated copper, with a raised molybdenum mount for the wafer (Figure 4.17(c)). The sample plate,

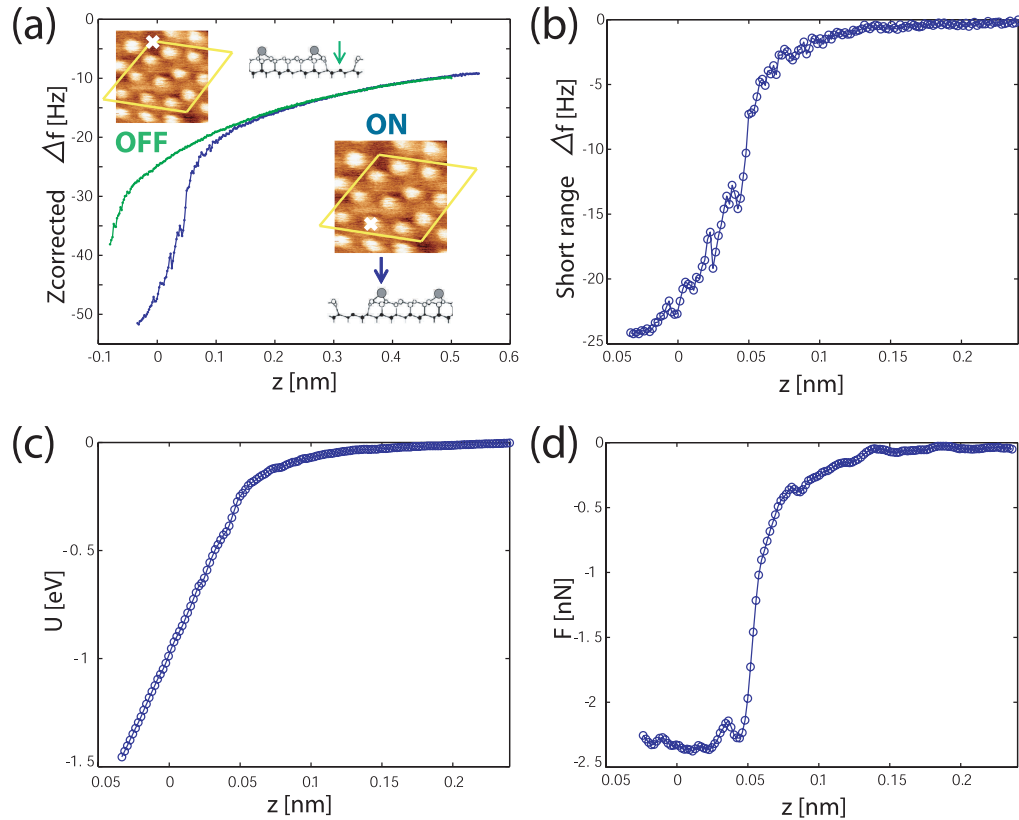


Figure 4.16: Experimental on/off data taken with a qPlus sensor on the Si(111) - (7×7) surface. (a)  $\Delta f$  measurements taken on (blue) and off(green) a silicon adatom. Note that the data curves have been shifted in  $z$  to accommodate for drift between spectra. (b)  $\Delta f$  data corresponding to short range interactions after subtraction of the two curves in (a). (c) Energy calculated from (b) using the Sader-Jarvis method. (d) Short-range force calculated from (c). The code used to convert this data was written by Andrew Stannard from the University of Nottingham.

once loaded into the scan head rests on the bottom of the suspended stage, laterally clipped into place. To coarse approach the sample the three outer piezoelectric tubes are driven in a slip-stick motion tangentially in x and y. Therefore the copper ring is made to rotate. As the ring rotates, the position of the piezo tube along the ramp varies, thus lowering the tip over a maximum range of  $600\mu m$ . The original design by Gerhard Meyer [168] is shown schematically in Figure 4.17(b). In this setup the tip is kept fixed on the bottom of the stage rather than the sample, however, the ramp design is the same. The beetle head design, whilst said to have excellent stability, works extremely well at helium temperatures. At nitrogen temperatures, however, the multiple piezo tubes used for scanning can introduce significant non-linear creep, and thus care is required when taking particularly slow measurements. Grid spectroscopy measurements at 77K are extremely challenging, even with the application of atom-tracking software to reduce thermal drift.

To obtain the results included in Chapter 6, STM and AFM measurements were obtained simultaneously. This was made possible with the qPlus [169] design AFM sensors purchased pre-made from Createc GmbH shown in Figure 4.18. The sensor is comprised of a macor block, with the tuning fork attached on one side, shaped to enable *in situ* transfer. We use  $50\mu m$  thick polycrystalline tungsten wire for the tips, attached to the end of the free tine of the tuning fork via insulating epoxy. The tunnel current signal is collected from a separate  $15\mu m$  gold wire, to decouple the AFM and STM signals. The attached W wire is etched in 2M NaOH solution and loaded into vacuum typically within a few hours. Great care needs to be taken to ensure that the wire is etched to the correct length due to the  $600\mu m$  range of the beetle head design. Typically qPlus sensors receive no further treatment once *in situ* because techniques involving heat treatment can affect the epoxy used to connect the W wire to the tuning fork, affecting the resonant frequency of the sensor.

The ability of the parent systems in IBM Zurich and the Freie Universitat Berlin,

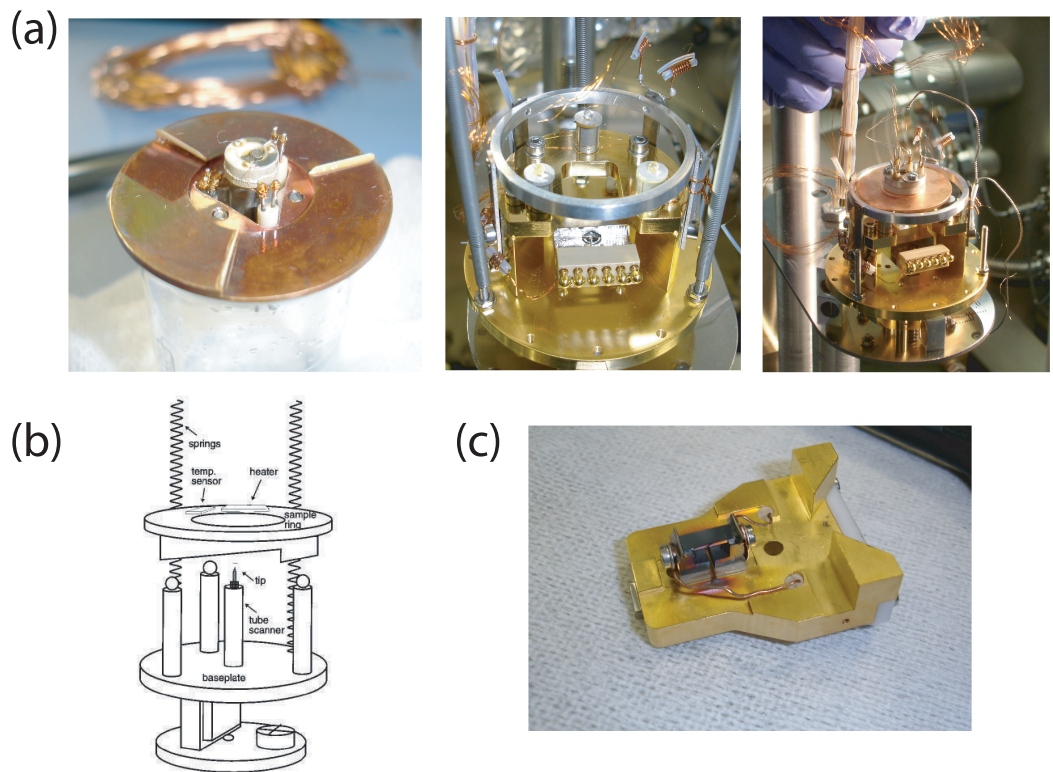


Figure 4.17: Photographs and diagram of the Createc STM/AFM stage and sample plate. (a) Photographs illustrating the beetle head ramp design, a copper disk on which the STM/AFM tip is magnetically attached sits on three piezoelectric tubes. (b) Schematic of the original prototype system build by Gerhard Meyer, adapted from Meyer 1996 [168]. (c) Photograph of the single wafer sample holder used for all silicon samples.

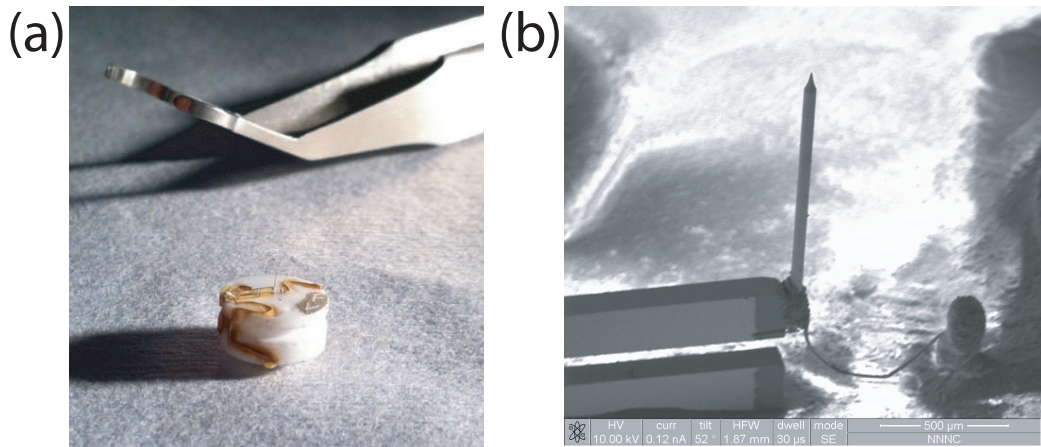


Figure 4.18: Createc GmbH qPlus sensor design. (a) The macor block, on which the tuning fork is attached, has machined ‘slots’ at each side to enable *in situ* transfer. (b) SEM close up image of the W wire attached to the end of the free tine of the tuning fork. Notice the separate wire to collect tunnel current.

on which this system is based, to produce excellent AFM data is unquestioned. Yet, the vast majority of AFM data at helium temperatures on other Createc systems is taken in the constant height mode of operation. Many of the experiments we wished to conduct required nitrogen temperatures and  $\Delta f$  feedback. With the original versions of the Createc controller software and control electronics we were unable to regularly achieve stable  $\Delta f$  feedback images in pure AFM. Therefore, a Nanonis control system was purchased including the OC4 oscillation controller to direct both AFM and STM experiments, which immediately enabled routine AFM measurements to be conducted on the Si(100) surface. The Nanonis control software includes many powerful features allowing complete control of all the feedback loops in operation, including z feedback, phase control and amplitude regulation.

## Chapter 5

# Toggling bistable atoms on the Si(100) surface

Silicon is the archetypal material for computer technology and the (nano) science of its surfaces commands a huge amount of interest in the context of scaling down components. The ultimate limit in size - and in some popular views, the limit of Moore's law - is at the single atom level. The reconstructed surface of Si(100) is particularly interesting in this respect. The ground state reconstructions are made up of pairs of atoms which can take on one of two configurations. Furthermore, the atomic pairs are organised as rows along the surface. This configuration can all too easily be thought of as rows of binary information. If only we could write the information and read it back, could we smash the limits of information storage and make usable atomic scale logic circuits? The answer of course, in a practical sense, is no. Nevertheless, Si(100) still represents an interesting model environment to test the limits of atomic manipulation. Moreover, it is a perfect system to examine how one can switch atoms between states, in a reversible non-destructive manner.

In this chapter I discuss how NC-AFM experiments were carried out to determine whether Si(100) dimers could be mechanically switched between different configu-

rations. To assist in understanding the results, a comprehensive DFT study was required. The experimental process was reproduced in simulation and the energy balance of ideal and defective surfaces was examined via the NEB method. In this section, all experimental data were collected by people other than the author. All theoretical calculations were carried out by the author unless otherwise stated. The majority of work described in this chapter has been published in *Phys. Rev. Lett.*, **106**, 136101 (2011) and *Phys. Rev. B*, **84**, 085426 (2011).

## 5.1 Experimental manipulation of Si(100) dimers

Experiments were performed on the clean Si(100) surface where individual dimers were manipulated. The aim of the experiment was to controllably manipulate the buckling angle of a Si(100) dimer back and forth between two stable states. Toggling the dimer in this way would demonstrate an atomic switch which could be mechanically activated without breaking any surface bonds, or removing or exchanging any atoms.

The original scheme for this manipulation was proposed as an explanation for the symmetric appearance of Si(100) dimers at 4K [33, 79]. In the previous work, however, the manipulation wasn't controlled, but was scan induced. Therefore, measurements were not made which could reveal the threshold force required to switch a single dimer.

The scheme for manipulation is schematically outlined in Figure 5.1. The surface dimer begins in a particular buckled configuration. The AFM tip is then positioned over the lower atom of the dimer (a) and moved towards the surface until a bond is formed between the tip and surface (b). Upon retraction of the tip, the bond is strong enough to ‘pull’ the lower dimer atom upwards, switching the buckling angle of the dimer (c). The three surface Si-Si bonds are stronger than that formed with the tip, therefore, when the tip is removed the dimer remains in its switched

configuration. The right hand side of Figure 5.1 shows how changing the state of the dimer can be thought of as changing the binary value of a row of bits.

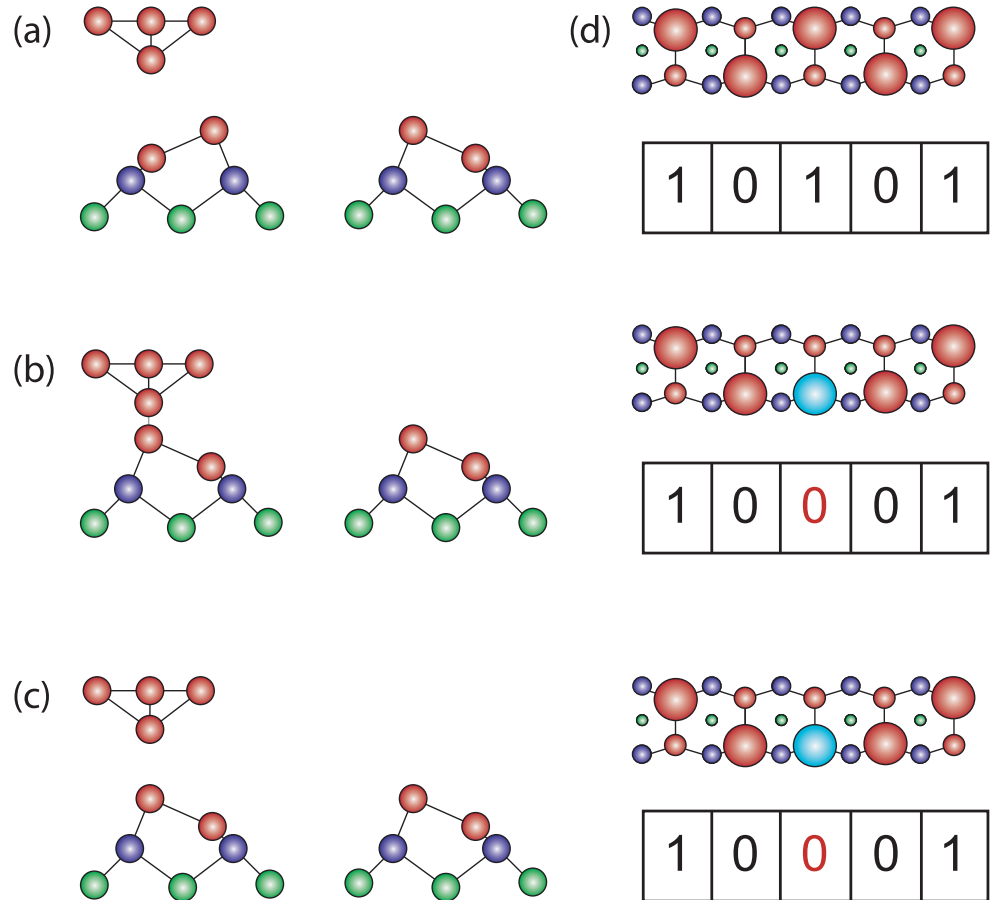


Figure 5.1: Proposed mechanism for switching the configuration of a Si(100) dimer. (a) The tip starts far away from the dimer where it does not interact. (b) The AFM tip approaches the surface and bonds to the lower dimer atom. (c) Upon retraction of the tip the lower dimer atom is ‘pulled’ upwards flipping the dimer. (d) Schematic demonstrating how this can be thought of as switching binary bits.

Experiments were carried out with a commercial (Omicron Nanotechnology GmbH) combined qPlus NC-AFM/STM operating at a base pressure of  $5 \times 10^{-11}$ mbar or lower. The Si(100) sample was kept at 5K in the scanning head unless otherwise stated after preparation. Boron doped( $1\text{m}\Omega\text{cm}$ ) Si(100) surfaces were prepared in UHV by standard methods, flash heating to  $\sim 1200^\circ\text{C}$ ; then rapidly

cooling to  $\sim 900^{\circ}\text{C}$ ; after which the sample was slowly cooled to room temperature before being introduced into the scan head.

In Figure 5.2 two typical AFM images of the Si(100) surface are presented, taken at zero applied bias, in  $\Delta f$  feedback operation. In the majority of images taken, which demonstrate “conventional” resolution [170], the upper dimer atoms are visible as bright protrusions whereas the lower dimer atoms either show a much weaker contrast or none at all, Figure 5.2(a) and(b) respectively. This observation is a consequence of the higher topography of the upper dimer atoms relative to the lower dimer atoms. Typically, to improve the contrast of the AFM image the  $\Delta f$  setpoint can be increased, thus decreasing the tip-sample interaction. The vertical distance between dimer atoms is  $\sim 0.8 \text{ \AA}$ , therefore, in principle we should be able to scan close enough to the surface such that an interaction is felt between the AFM tip and the lower dimer atom without “crashing” into the upper dimer atoms. In this case, however, imaging with a lower  $\Delta f$  setpoint leads to uncontrolled manipulation of the Si(100) dimers, as shown by the small discontinuity in the bottom of Figure 5.2(b), indicating a dimer has changed orientation.

Similar ‘slices’ during imaging were often observed when the tip-sample separation was decreased. In some cases the tip-sample separation could be gradually reduced and the number of observed uncontrolled manipulation events would be seen to increase. This was the initial indication that controlled manipulation is possible. This observation also hints at a more subtle feature of the surface. If the tip-sample distance, and therefore the strength of interaction, affects the number of dimers observed to switch, then it would appear that some dimers are ‘easier’ to flip than others. We will return to this line of thought towards the end of the chapter when we consider the energy barriers present in this system. To allow confidence in controlled manipulation of the Si(100) surface a low  $\Delta f$  setpoint was used to avoid perturbing the surface.

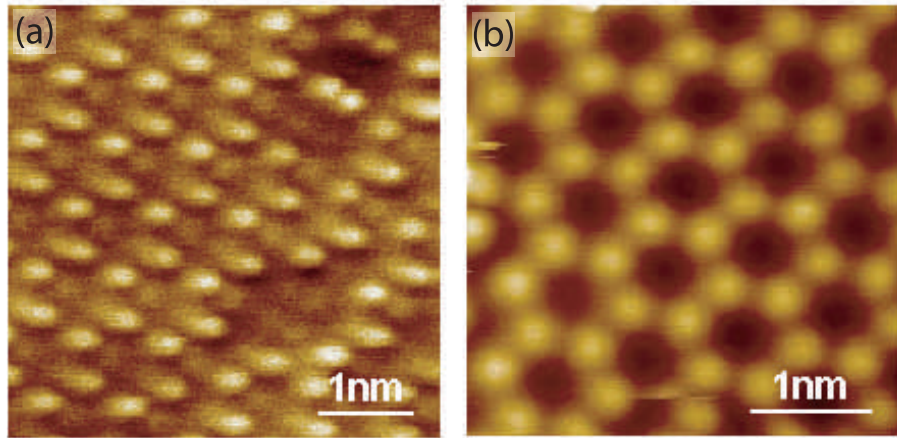


Figure 5.2: NC-AFM images of the Si(100) surface at 5K and with zero applied bias. (a) and (b) both show the  $c(4 \times 2)$  reconstruction, (a) also shows a region of  $p(2 \times 2)$  phase. In the majority of images taken, the  $\Delta f$  setpoint is chosen such that the upper dimer atoms are visible as bright protrusions whereas the lower dimer atoms show much weaker contrast, as in (a), or even none at all, (b). Images courtesy of Philip Moriarty and Adam Sweetman.

A typical experiment resulting in the individual manipulation of Si(100) dimers is shown in Figure 5.3. Initially the surface area was imaged with a low setpoint in  $\Delta f$  feedback, as previously explained. Then a  $\Delta f(z)$  measurement was carried out over the lower atom in one of the Si(100) dimers. Specifically, the scanning tip was positioned above the down atom of the dimer, then, with no active feedback loop, the tip was moved closer to the sample surface while simultaneously measuring the frequency shift of the cantilever. After a pre-determined distance the tip was retracted away from the surface and scanning resumed. In Figure 5.3 the measured  $\Delta f(z)$  curve obtained during the manipulation process is shown. A sharp change in the measured  $\Delta f$  is observed at (ii) suggesting a sudden change between the tip apex and surface has taken place. After the jump, the  $\Delta f$  curve follows a different path, (iii), on the remainder of the approach and the subsequent retract. AFM images taken after  $\Delta f(z)$  measurements show that the observed atomic resolution is unchanged, suggesting that the variations in  $\Delta f$  are not due to structural rear-

rangements of the tip. This provides compelling evidence that the process which has taken place is indeed due to chemical bond formation between the tip apex and the lower dimer atom, which provides enough force for the tip to ‘pull’ the lower dimer atom upwards, switching orientation of the Si(100) dimer. Points (i),(ii) and (iii) are expected to correspond to (a),(b) and (c) shown in Figure 5.1.

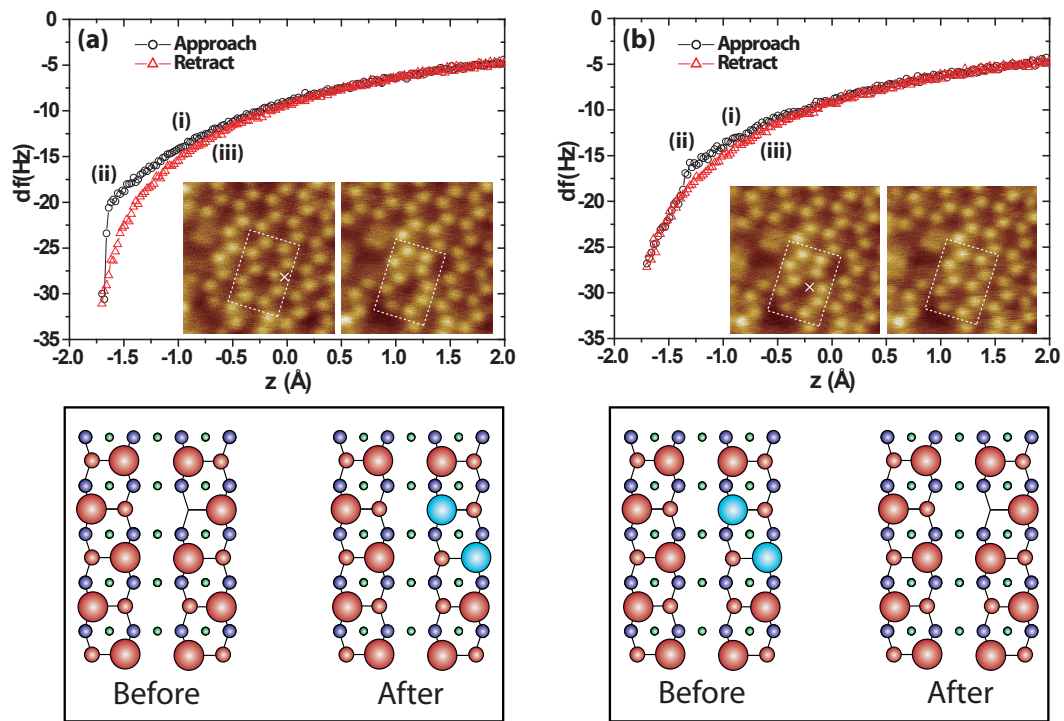


Figure 5.3: (a) Open circles: Frequency shift ( $\Delta f$ ) measured as a function of tip displacement ( $z$ ) positioned over the lower atom of a Si(100) dimer. Open triangles:  $\Delta f(z)$  measurement acquired during retraction of the tip. The insets show NC-AFM images, and illustrations of the atomic configurations, taken before and after the frequency shift measurement (acquired at the position marked with a cross). The dimer flipping event appears as a sharp jump, position (ii) in the  $\Delta f(z)$  spectra. (b) A  $\Delta f(z)$  measurement taken positioned above a lower atom of one of the dimers in the phason pair created in (a). The manipulation restores the original symmetry via a second correlated flip event. (Image parameters: tip amplitude: 250 pm;  $\Delta f$  setpoint = -9.1 Hz). Data courtesy of Adam Sweetman

The major experimental finding was that, when the initial surface configuration is the  $c(4 \times 2)$  phase, rather than flipping a single dimer, experimental measure-

ments manipulated multiple dimers in a way that appeared to be correlated. This is observed in the insets to Figure 5.3, where in this instance<sup>1</sup> what we term a ‘phason pair’ is produced. The main motivation for the simulated analysis thus became twofold.

1. How are the phason structures formed?
2. Why do we not observe single dimer flips? Is it even possible to observe a single dimer flip experimentally?

Interestingly, even with this apparent limit on the control of dimers, the process is found to be reversible and by flipping the same dimer the  $c(4 \times 2)$  surface is restored as shown in Figure 5.3 (b)<sup>2</sup>.

Shown in Figure 5.4 is an AFM image, with a schematic, explaining the term phason. As has been briefly mentioned in this chapter and previously in Section 4.2, the ground state of Si(100) is the  $c(4 \times 2)$  reconstruction, however the  $p(2 \times 2)$  structure is also very similar in energy and is commonly observed. In areas of the surface where there is a transition from one phase to another, a defect is required. In some cases this can be a vacancy defect [103, 104]. An arrangement of two adjacent dimers with the same buckling angle, called a phason defect [171, 172], will also change the phase of the reconstruction along the dimer row. Such a defect is shown in Figure 5.4 (a) (and schematically in (b)) where two distinct regions of  $c(4 \times 2)$  and  $p(2 \times 2)$  reconstruction are clearly observed. If one phason changes the phase along a row, then it is clear that a pair of phasons will maintain it (see inset to Figure 5.3).

In order to quantitatively analyse the strength of the chemical interaction required to flip dimers, force *vs.*  $z$  ( $F(z)$ ) measurements were obtained. To achieve

---

<sup>1</sup>Although the particular structure produced isn’t always the same, an individual dimer flip has never been observed on a  $c(4 \times 2)$  surface.

<sup>2</sup>Experimentally restoration wasn’t always possible. In some instances additional flipping events would occur leading to more complicated structures.

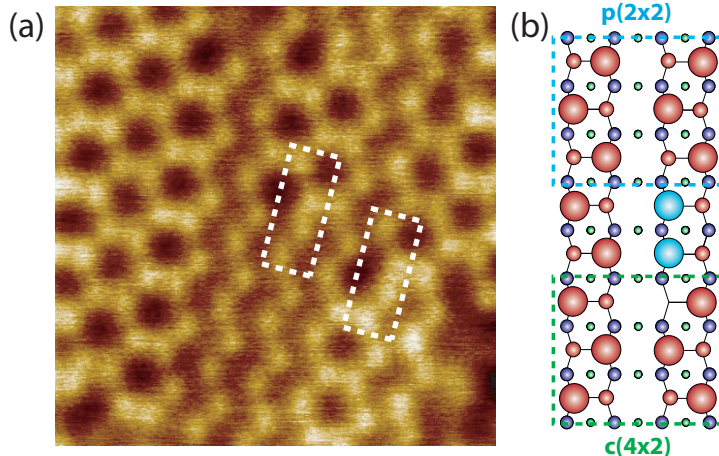


Figure 5.4: (a) AFM image of the Si(100) surface demonstrating regions of  $c(4 \times 2)$  and  $p(2 \times 2)$ . The boxed areas show individual phason defects, where the phase of one row is changed relative to its neighbours. (b) Ball and stick schematic demonstrating how a phason modifies the local reconstruction of Si(100). Data courtesy of Philip Moriarty

this, a fitting method was applied in order to remove long range contributions to the  $\Delta f$  signal not originating from the short range chemical force. The short range  $\Delta f$  data was then converted to  $F(z)$  (shown in Figure 5.5) via implementation of the Sader-Jarvis inversion algorithm( [60] and see previous chapter).

$F(z)$  data for manipulating a dimer from the  $c(4 \times 2)$  configuration to a phason pair, then returning it to its original configuration are shown in Figure 5.5 (a) and (b). Experimentally it is observed that the threshold force for flipping a dimer falls within the range of 100-600 pN. In Figure 5.5 it can be noticed that the threshold force is slightly lower to restore the dimer configuration back to the  $c(4 \times 2)$  structure. To quantitatively analyse the data and determine the processes responsible for the manipulation, DFT calculations were required and are discussed throughout the remainder of this chapter.

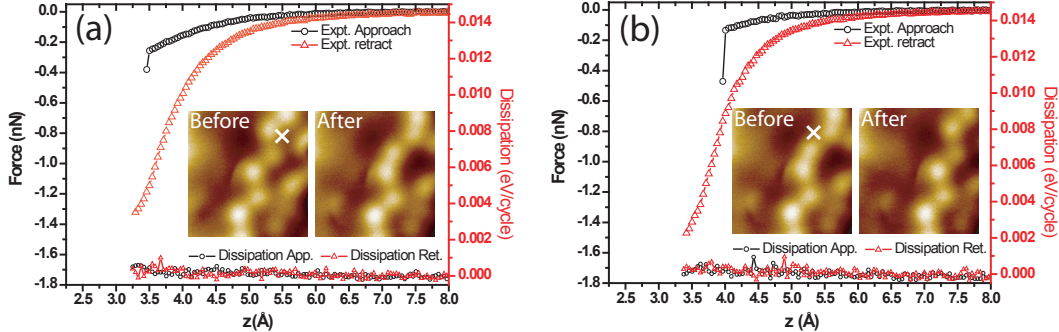


Figure 5.5: (a) Open circles (triangles): Variation of the short range force during tip approach (retraction) at the position marked with a cross in the “before” image. Also plotted is the negligible variation in dissipation observed for this particular tip. Restoring the  $c(4 \times 2)$  structure from the result of (a) is shown in (b). Data courtesy of Adam Sweetman.

## 5.2 Simulated $F(z)$ spectroscopy

To make a comparison with experimental results, theoretical calculations were carried out to model the process of  $F(z)$  measurements. The response of the Si(100)  $c(4 \times 2)$  surface was calculated in the presence of a silicon cluster, used to represent the atomically sharp AFM tip.

In our calculations we used an *ab initio* density functional theory (DFT) method as implemented in the SIESTA code (see section 3.5 and [74]). To describe the surface a 6-layer slab model (see section 4.7.1) was used with 16 surface dimers arranged as two rows, each eight dimers in length. Hydrogen atoms were used to terminate the Si bonds on the lower side of the slab, and were kept fixed, along with the bottom two layers of silicon, to simulate the missing bulk. The large size of the slab was chosen to provide reasonable isolation of the target atoms in our simulations to reduce finite size effects due to periodic boundary conditions. Atoms are only manipulated within a single row, such that when periodically repeated there is always a single unaffected dimer row separating the affected region as shown in Figure 5.6. The length of each row was chosen to be eight dimers in length to limit

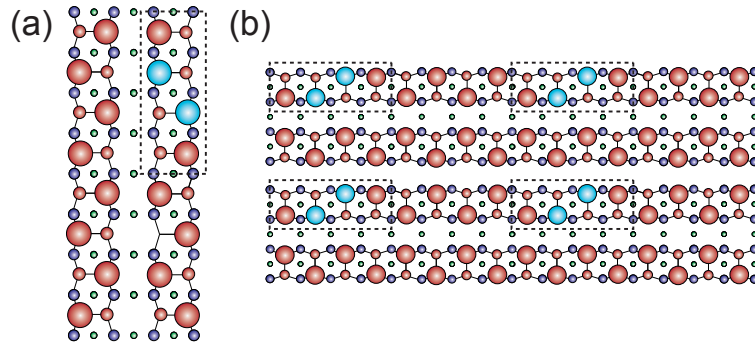


Figure 5.6: (a) The surface simulation cell used in DFT calculations. (b) The phason pair is four dimers in length, therefore when the cell is periodically repeated there are four 'normal' dimers acting as a buffer to prevent finite cell size interactions.

any effect long range surface relaxations may have along the rows. For example, when modelling a phason pair (four dimers in length), after periodically repeating the system, four other dimers, in a standard  $c(4 \times 2)/p(2 \times 2)$  buckling configuration, will be present before any repeat of the phason unit (Figure 5.6 (b)). It should be noted that this surface slab is much larger than those used in previous DFT investigations of the Si(100) surface. This large size was chosen in order to reduce finite size effects that might otherwise strongly affect investigation of phasons. Because of the cell sizes used, only the  $\Gamma$  point was employed in sampling the Brillouin zone in all of our simulations.

### 5.2.1 Tip Clusters

Two types of tip cluster were used during our theoretical investigation. The first was a standard ten atom pyramidal Si tip containing a single dangling bond at its apex pointing normal to the surface plane [41, 51] (Figure 5.7 (a)). Only four atoms at the apex are free to move in response to the interaction with the surface. This is an idealised sharp, rigid tip type, and as a possible model for the complicated structure of a real tip apex, this pyramidal tip is over-simplistic. In a more realistic large scale cluster, many more tip relaxations may occur at both short and longer range,

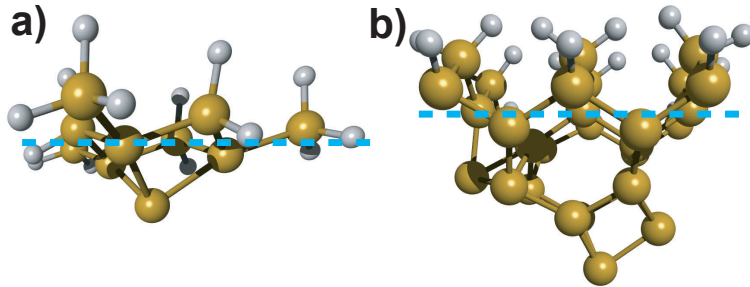


Figure 5.7: The two silicon tip clusters used during DFT investigation of tip-surface interactions. (a) A structurally rigid Si(111) type tip with 4 atoms free to respond to tip-surface interactions. (b) A larger ‘dimer terminated’ tip with 15 atoms able to respond.

affecting the tip and its response to the surface. Additionally, a pyramidal tip is perhaps unrealistically symmetric. In order to assess the role of tip structure and its ability to flip dimers and create phason structures, in our calculations we also used an asymmetric 30 atom tip cluster with 15 atoms freely able to move, terminating in a dimerised tip apex. This more complicated model provides a somewhat more realistic tip apex with respect to tip deformation and introduces an asymmetry into the system. This tip type has previously been used in [51–53] and is shown in Figure 5.7 (b). A more complete analysis of tip structure is presented in the later chapters of this thesis.

### 5.2.2 Approach-retraction $F(z)$ curves

To obtain theoretical  $F(z)$  curves a silicon tip cluster was initially positioned at a vertical distance of 8Å above the surface such that the terminating tip atom would be directly over the lower or upper atom of a surface dimer as required. The vertical distance  $z$  is defined as the distance between the surface plane measured by the vertical position of the upper dimer atom and the lowest tip apex atom *prior* to relaxation. The tip was then moved in quasi-static steps approaching the surface to just beyond the force turning point, and then retracted in the same way. At

each step the geometry of the system was optimised until the forces on the non-fixed surface and tip atoms were no larger than 0.01eV/Å (16 pN). After each step the vertical forces acting on the fixed tip atoms<sup>3</sup> were summed up to give the total force acting on the tip. The full process is explained in detail in Section 4.7.2. A direct comparison to the experimental  $F(z)$  curves can then be made, as shown in Figure 5.8. Theoretically calculated  $F(z)$  curves for the rigid “Si(111)-like” and dimer-terminated type tips are plotted with experimental data taken during manipulation of a dimer. It can be immediately seen that the experimental and calculated retract spectra agree extremely well for both tip types suggesting that the chemical bonding mechanism present in DFT calculations is in fact responsible for the experimental manipulations. A comparison of the calculated and experimental approach curves also show very good qualitative agreement. However, care has to be taken when making comparisons as the uncertainties in converting  $\Delta f$  data to force can affect the force curves to the extent that no exact comparison of simulated tip type is possible. Despite this, the calculated  $F(z)$  curves share many features, and in particular confirm that the threshold force to flip a dimer from an initial c( $4 \times 2$ ) configuration to a *phason pair* (a) is larger than for the reverse process (b). This gives compelling evidence that the chemical interaction between the tip and surface is different depending on the local environment of the dimer.

The calculated geometry of the Si(100) system is shown in Figure 5.8(c-f) before and after the manipulation for the two tip types considered. The target lower dimer atom over which the tip is positioned is shaded in green allowing the clear observation of the flipped dimer. However a disparity between calculation and experiment emerges as only a *single* dimer is flipped during simulation, rather than the *correlated* flip of *two* dimers seen in experiment. In the next two sections the reasons underlying this difference are investigated by exploring the effect of the local

---

<sup>3</sup>Which are constrained, therefore  $F \neq 0.01 \text{ eV}/\text{\AA}$ .

environment and then the energy barriers involved for the  $c(4 \times 2)$  to phason pair experimental result.

### 5.2.3 Simulated local variation in surface stability

In simulation we found that the calculated force threshold can vary strongly depending on the initial local configuration around the target dimer we wish to flip. Simulated force-distance curves were obtained for flipping a dimer in different local environments, including a *three-in-a-row* structure of dimers and a *phason pair*. We found that different dimers within a particular surface environment had different threshold forces to flip, all of which were either similar or lower in value than the force required to flip a dimer in a standard  $c(4 \times 2)$  environment. In Figure 5.9(a-e) and 5.9(f-j) we show results for the DFT-predicted force distance curves calculated above three positions around the *three-in-a-row* and *phason pair* structure respectively.

For an initial *three-in-a-row* configuration (Figure 5.9 (b)) it is clear that the central dimer ( $\gamma$ ) appears to be much less stable than a dimer in a normal  $c(4 \times 2)$  arrangement, with a calculated force threshold of 0.23nN, nearly three times smaller than the 0.64nN value calculated for the  $c(4 \times 2)$  initial configuration. Dimers adjacent to the central dimer ( $\beta$ ) have a force threshold of  $\sim$ 0.5nN, whereas the other dimers ( $\alpha$ ) show a flipping threshold of 0.64nN similar to the  $c(4 \times 2)$  initial configuration. This behaviour demonstrates that the configuration of neighbouring dimers can have a large impact on the calculated threshold force. As for the case of a  $c(4 \times 2)$  initial configuration, it is observed that in each simulation only the dimer directly underneath the tip is flipped, *irrespective of the final configuration this would result in*. In particular, when flipping dimer ( $\alpha$ ) (which relative to its nearest neighbours is initially in a  $c(4 \times 2)$  configuration) a *five-in-a-row* structure (c) of dimers would be created with the same threshold force as flipping a single

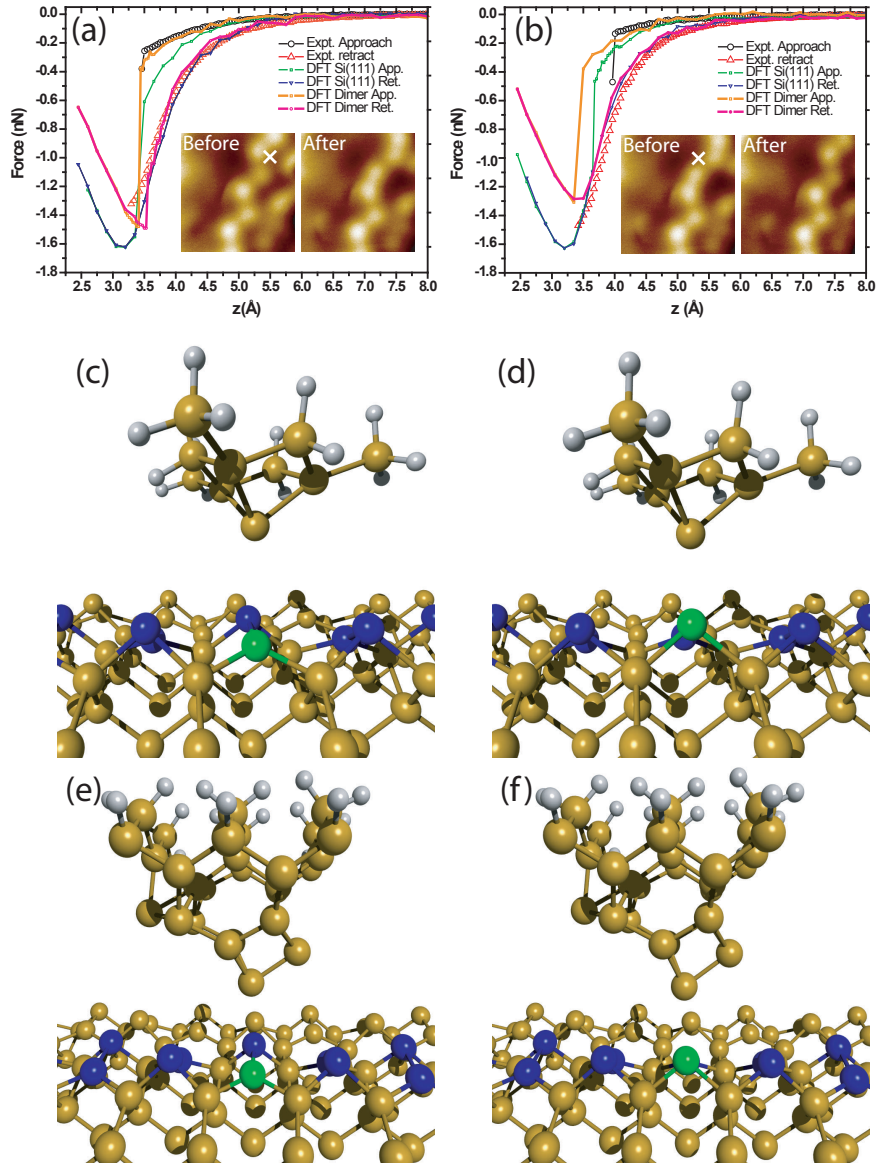


Figure 5.8: Comparison of measured and calculated force required to flip a dimer. The DFT-calculated force (solid lines), while in excellent agreement with experiment (reproduced from 5.5) for the retraction curves, show that the threshold force at which the flip occurs is critically dependent on tip structure. Frames taken from DFT simulations using a Si(111)-type (c-d) and dimer-type (e-f) terminated tip before and after the flip event is observed.

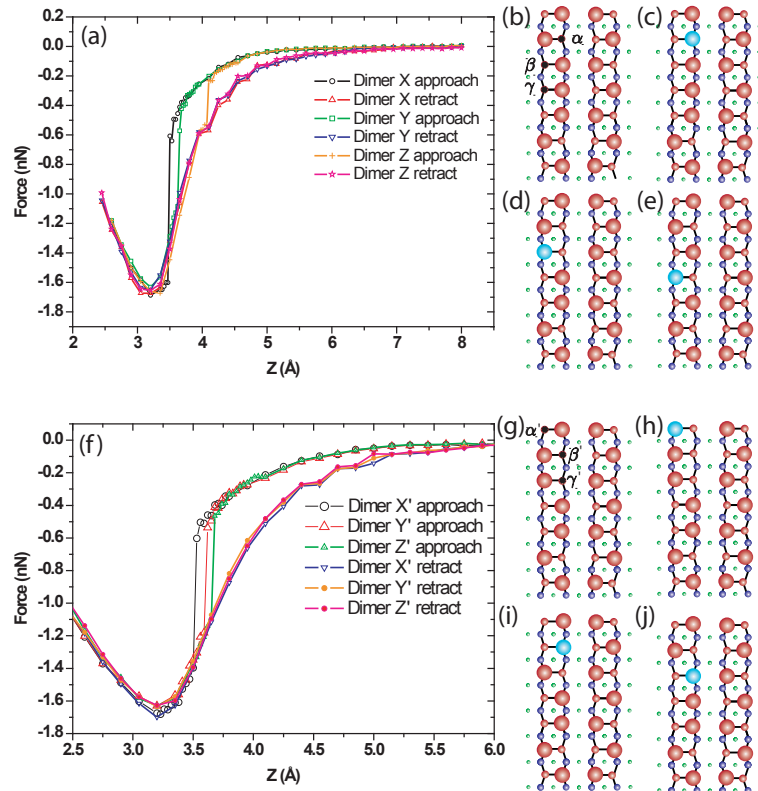


Figure 5.9: Variations in calculated approach and retract tip forces for different dimer manipulations within a *three-in-a-row*(a) and *phason pair*(f) structure. (b) Initial surface configuration (*three-in-a-row*(b),*phason pair*(g)) and locations of simulated approach and retract curves plotted in (a)and (f). (c) Final surface configuration (*five-in-a-row*) following approach and retract in position ( $\alpha$ ). (d) Final surface configuration (*phason pair*) following approach and retract in position ( $\beta$ ). (e) Final surface configuration ( $c(4 \times 2)$ ) following approach and retract in position ( $\gamma$ ). (h) Flip at ( $\alpha'$ ) leads to a *four-in-a-row* plus single phason structure. (i) Measurement at  $\beta'$  leads to two separated phasons. (j) Measurement at  $\gamma'$  leads to a *three-in-a-row* structure.

dimer in a normal initial  $c(4 \times 2)$  configuration.

Similar results are seen for dimers in a *phason pair* environment shown in Figure 5.9(f-j). In this case the differences in threshold force are less extreme. The same pattern is observed, however, and the threshold force decreases towards the centre of the phason pair. Crucially, the threshold force to flip dimer ( $\alpha'$ ) located on the outer edge of the phason pair (also in a local  $c(4 \times 2)$  initial configuration) thus forming a *four-in-a-row* plus *single phason* structure is the same as the threshold to flip a dimer in a normal  $c(4 \times 2)$  configuration. This suggests that, in our calculations, it is the initial configuration of the surface that dominates the value of the threshold force for manipulation. We therefore are confident that the calculated  $F(z)$  curves and threshold forces are valuable for making quantitative comparison with experimental results, even though the outcome for manipulation appears at odds with experiment.

It is clear that the process of dimer flipping is not well understood from simulated  $F(z)$  measurements alone. Simulations regularly appear to show experimentally unstable configurations as stable. As such, we must examine the potential energy landscape of the system to ascertain whether the energy barriers involved are what precludes certain structures and enables others.

### 5.3 Potential energy surface - Nudged elastic band (NEB) calculations

Understanding why and how correlated flipping takes place presented a significant theoretical challenge. In each DFT calculation, we observed that only a single dimer flips. In the case of an initial  $c(4 \times 2)$  structure, simulated manipulation results in a *three-in-a-row* structure, which was apparently stable. For more complicated initial configurations we observed the same behaviour, and once again only a single dimer would flip, often leading to complicated structures that should seemingly be unsta-

ble. The energy minimising calculations used to calculate the relaxed geometries at each step, however, are conducted in the absence of any thermal energy (0K). Therefore, as long as some barrier is present, no matter how small, a particular geometry will be calculated as stable. To investigate the possibility of forming a *phason pair*, and the energy barriers that must be overcome to reach such a state, nudged elastic band (NEB) calculations were performed. The advantage of this method is that it also allows the minimum energy pathway between two states to be calculated, which can assist in explaining the pathway that the surface atoms must take to form a particular structure. In the case of forming a *phason pair* from an initial c(4 × 2) surface, two dimers are required to flip, either at the same time, one after another, or some combination, each necessarily with different barriers to overcome. With multiple pathways for flipping available, the NEB method is ideal, as in principle it should calculate the minimum energy route for the manipulation.

### 5.3.1 Why use NEB?

The most basic method for calculating the energy pathway between two states is to carry out a constrained total energy calculation. In this case we assume absolute control of the atomic positions within the target dimers. We then manually guess the positions of the dimer atoms as they flip, carrying out a total energy calculation with the dimer position kept fixed at various locations between a start and finish state. The difference between the highest energy and the starting configuration energy is then assumed to be the energy barrier.

Although we will certainly obtain some answer for the energy barriers, this method is far too simplistic for the dimer flipping process. As already mentioned, to form a *phason pair* two dimers are required to flip, which could occur simultaneously, subsequently, or anywhere inbetween. Moreover, the dimers, and their backbonds are twisted in x and y, depending on their configuration, making a simple plot of

energy *vs.*  $z$  position over simplistic.

To this end we use the NEB method. In Figure 5.10 the process applied to the Si(100) surface is explained. To perform the calculation we only need to know the initial and final configuration of the process we are interested in. A linear interpolation of the geometries is then made between the two as a starting guess (Figure 5.10 (b)), which are termed ‘images’ along the NEB band.  $E_{TOT}$  is then calculated for each position as the starting guess for the energy band (Figure 5.10 (a)). The energy band then converges to a minimum by calculating the geometries corresponding to the minimum energy pathway. The evolution of a band is shown in Figure 5.10 (c), which corresponds to two dimers flipping simultaneously from the  $c(4 \times 2)$  configuration to make a *phason pair*. The energy barrier obtained from the pathway reduces by nearly half compared to the original linear interpolation. When carrying out the constrained calculation a linear interpolation will only be made in  $z$ , therefore it is clear that the energy barrier obtained from the NEB method is significantly lower due to the more accurate reflection of the real system.

### 5.3.2 Symmetric *vs.* asymmetric transition

In our NEB calculations we modelled the evolution of the energy band corresponding to the minimum energy path between the  $c(4 \times 2)$  (i) and the *phason pair* (iv) structures (see Figure 5.11 (a)) in the presence of a silicon tip cluster at different tip-sample separations. Initially, the starting (i) and ending (iv) points on the band for the highest tip position were relaxed and the atomic positions along the band (representing stages between (i) and (iv)) were obtained by a linear interpolation. To simulate each band 17 images were used in our calculations. The band was then relaxed until the energies of the images varied by less than 0.05 eV and the perpendicular component of the NEB spring force less than 0.5 eV/Å. Next, the tip-sample separation was decreased and the atomic positions in all images obtained from the

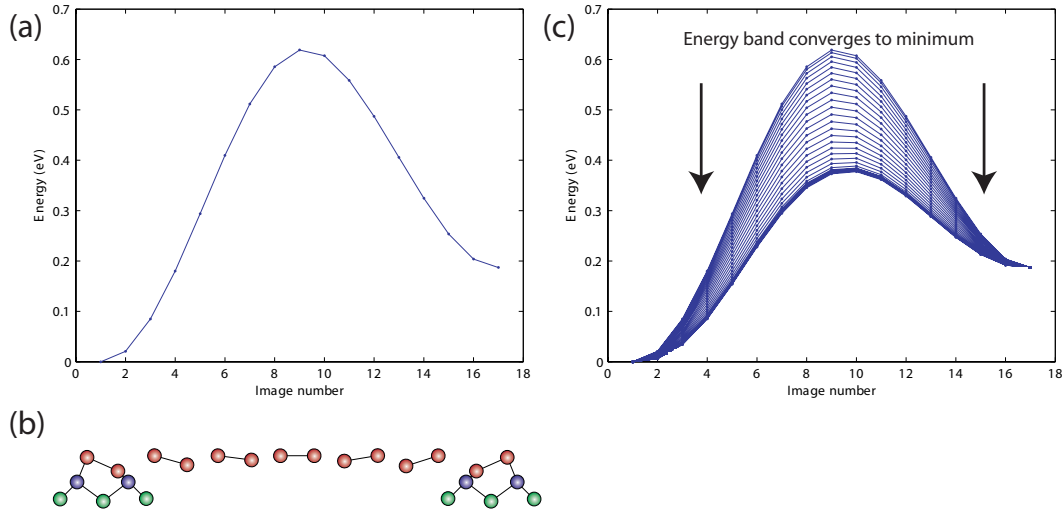


Figure 5.10: (a) The initial energy band calculated after a linear interpolation between the  $c(4 \times 2)$  and *phason pair* structures. (b) Illustration of the geometry of a single dimer aligned with the energy band in (a). (c) Convergence of the NEB band on the minimum energy pathway.

previous tip position were used as the input images for the new band calculation. This ensured smooth evolution of the band. Near the closest tip-sample separation (corresponding to just before the threshold distance to flip in our DFT calculations ( $3.47\text{\AA}$ )) small decreases in tip-sample separation steps of  $0.02\text{\AA}$  were used. This provides a clearer picture of changes around the threshold point.

Shown in Figure 5.11 (b) are the total energies for configurations i-iv in the absence of the AFM tip. From this information alone it is impossible to understand the route taken during manipulation. The only useful information appears to be that the *phason-pair* structure is more energetically favourable than the *three-in-a-row*.

Typical bands for several tip heights between  $7.0\text{\AA}$  and  $4.3\text{\AA}$  (the closest tip height we considered is  $3.47\text{\AA}$ ) are shown in Figure 5.11 (c). For convenience, relative energies are shown, i.e. all bands are plotted in such a way that their starting  $c(4 \times 2)$  structure represents the zero of the energy scale. At this distance the band between (i) and (iv) can take one of two particular forms, each related to a distinct motion of the surface dimers: a single large ( $\sim 330\text{meV}$  to  $380\text{meV}$ ) barrier

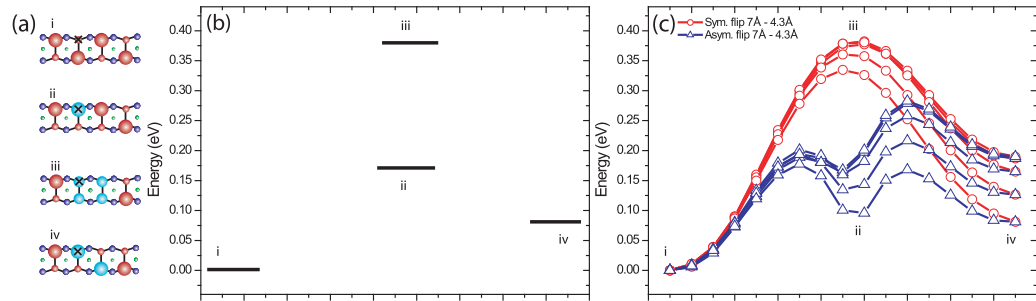


Figure 5.11: (a) Schematic of structures: (i)  $c(4 \times 2)$  buckled surface, (ii) three-in-a-row, (iii) symmetric and (iv) *phason pair* structure. The lateral position of the tip is indicated by a cross. (b) Total energies of structures i-iv. At large tip-sample separations the manipulated structures are higher in energy than the  $c(4 \times 2)$  configuration. (c) Calculated energy bands between states (i) and (iv) seeded with different starting conditions at equivalent tip-sample separations ( $7.0\text{\AA}$  -  $4.3\text{\AA}$ ). Blue (open triangles) represent sequential flipping, passing through the three-in-a-row structure. Red (open circles) represent symmetric flipping of dimers. The upper and lower bands correspond to the highest and lowest tip heights of  $7.0\text{\AA}$  and  $4.3\text{\AA}$  respectively.

corresponding to a correlated motion with both dimers flipping simultaneously (red bands), or alternatively, a band consisting of two separate barriers of different sizes (blue bands). This second situation corresponds to the dimers flipping sequentially, first forming a *three-in-a-row* structure, then a *phason pair*. These two band types correspond to different local minimum energy pathways from (i) to (iv). At larger tip-sample separations the lower energy sequential pathway was generated by seeding the NEB band with sequential flipping images taken from previously calculated closer tip-sample separations. At smaller tip-sample separations the NEB method converges on the sequential dimer flipping pathway (see next section), even when the band is initially seeded with a symmetric flipping pathway. Consequently it appears that the symmetric flipping pathway (red bands) is only a local energy minimum, and that the lowest energy pathway to transit from the  $c(4 \times 2)$  (i) to *phason pair* (iv) state is with sequential dimer flipping, both in the absence of the tip and at close tip-sample separations.

### 5.3.3 Tip induced variation in PES: Pristine surface

Calculations were performed at tip-sample separations ranging from 7 Å (tip not interacting with surface) to 3.47Å (the threshold point where  $F(z)$  simulations show the dimer flips). The aim was to address whether the presence of the tip induces complete barrier collapse, leading to formation of the *phason pair*. The full evolution of the minimum energy pathway is shown in Figure 5.12, where only the sequential global minimum route is shown.

Each band demonstrates several features:

1. They all have a distinct minimum in the middle which corresponds to the *three-in-a-row* structure (ii) (see Figure 5.11 (a)).
2. As the tip approaches the surface, the total energies of both the *three-in-a-row* and the *phason pair* structures reduce.
3. When the tip comes very close to the surface the barrier for a single dimer to flip from c(4x2) to *three-in-a-row* reduces smoothly to zero which suggests that any initial flip at 5K would occur spontaneously at the closest tip position, creating the *three-in-a-row* structure.
4. The barrier to transit to the *phason pair* configuration does not collapse at any tip height.

Hence, the NEB method predicts that for any tip height the minimum energy pathway connecting the c(4x2) dimer arrangement (i) and the *phason pair* state (iv) is via the *three-in-a-row* arrangement, i.e. by flipping the two dimers sequentially one after another. Point 3. serves to answer why we observe a dimer flip at 3.47 Å in the simulated  $F(z)$  curves. We have yet to come up with a clear explanation for the phason pair configuration, however.

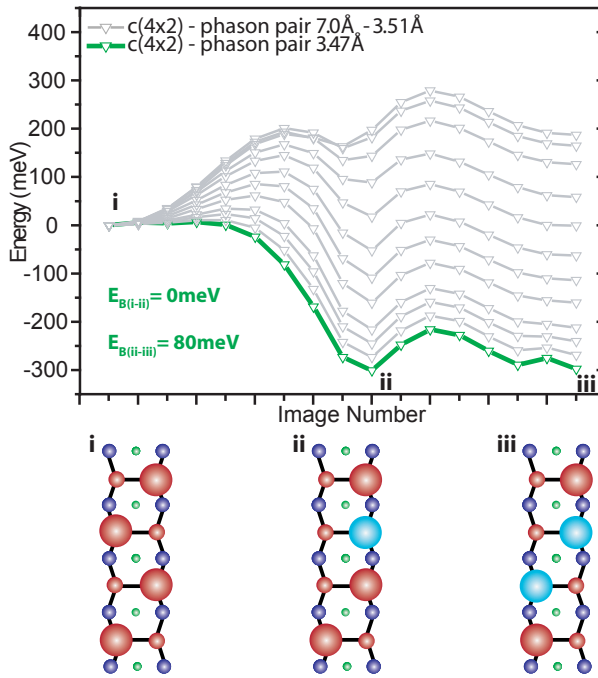


Figure 5.12: Energy profile associated with the transition from a  $c(4 \times 2)$  structure (i) to a phason pair configuration (iii) for a range of tip-sample separations. As the tip-sample separation is decreased, the barrier for the transition to an intermediate *three-in-a-row* state (ii) (never observed in experimental images) collapses.

Thus far we know that, initially, the dimer immediately underneath the tip is flipped and the system arrives into the state (ii); moreover, this happens spontaneously when the tip comes sufficiently close to the surface (no barrier). Then one of the neighbouring dimers must somehow flip, after which we observe from Figure 5.12 that the *phason pair* state (iv) is stabilised. In all calculations each individual dimer flips as a unit, its constituent atoms moving in concert rather than one atom at a time.

The results of the NEB calculations therefore pose two further questions. The first one is, why do we never observe a *three-in-a-row* structure experimentally? This may be answered by a close analysis of the NEB band at a tip-sample separation of 7 Å. If a *three-in-a-row* structure is formed at the tip positions very close to 3.47 Å, the calculated energy barrier to transit to a *phason pair* structure is always insur-

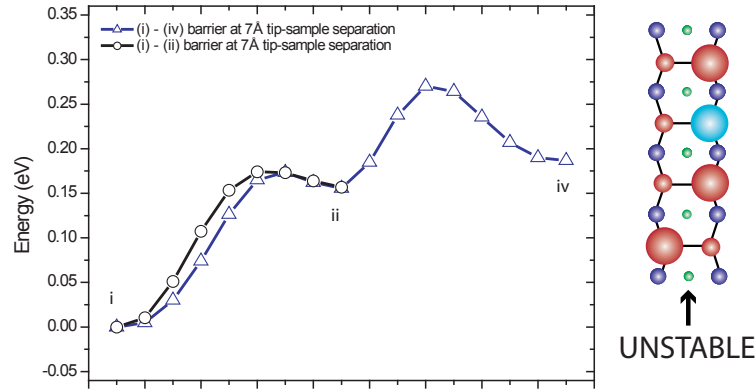


Figure 5.13: Calculated bands demonstrating barrier collapse to 17meV when transitioning from a three-in-a-row state (ii) to a c(4x2) buckled surface (i) with tip positioned as in D 7.0Å above the surface. Black band (open circles) represents transition using (i) and (ii) as fixed start and end points, blue band (open triangles) have (i) and (iv) (the phason pair) as fixed start and end points locating (ii) as in its pathway.

mountable, changing from 60-80meV at close tip-sample separations to a maximum of 110meV at the largest tip-sample separations. However, the barrier to return to a c(4x2) structure shows a smooth reduction with a minimum at tip positions far from the surface. Figure 5.13 shows the band (blue open triangles) calculated at the largest tip-sample separation (7.0Å) between the c(4x2) and *phason pair* structures. This band, which passes through the *three-in-a-row* structure, was compared to a band (black open circles) of a direct transition between the c(4x2) and *three-in-a-row* structure using a stricter force tolerance. Both calculations give a barrier of 17meV to return to the c(4x2) structure. We found this barrier was surmountable at 5K in Molecular Dynamics simulations (MD, carried out by Joseph Bamidele in King's College London), and as such we conclude that the *three-in-a-row* structure is unstable in the absence of the tip, even at 5K.

### 5.3.4 Defect induced variation in PES

The second question is about the formation of the *phason pair* structure. This question appears to be much more challenging. All our calculations clearly show that the barrier from *three-in-a-row* to the *phason pair* structure is too high to be overcome at 5K for any tip-sample separation. Initially we thought that our NEB convergence criteria were not appropriate. However, when much stricter criteria (and many more NEB steps) were applied for the tip positioned at its closest separation, the transition barrier to a *phason pair* structure was not found to reduce. Another hypothesis was that the optimisation procedure implemented in our NEB code steered the process into the wrong local minimum; specifically, that the simultaneous flipping pathway (red bands Figure 5.11 (c)) might still be possible at close tip-sample separations, possibly becoming more preferable than the sequential pathway avoiding the intermediate *three-in-a-row* structure. To check this a constrained minimisation calculation was performed at the closest tip-sample separation in which both dimers were flipped simultaneously in a correlated manner, however this produced a much larger barrier than for sequential flipping, similar in nature to the red and blue bands in Figure 5.11 (c). As such our results suggest that collapse of the energy barrier due to the presence of the tip is not solely responsible for the creation of the phason pair.

The overall conclusion which is drawn from the above calculations is that the observed formation of the phason pair structure cannot be explained for a pristine (without defects) surface at any tip position in the absence of any additional influences. Therefore, to examine the possible influence of defects, NEB calculations were repeated within the presence of a dimer vacancy defect two dimers in size (2DV).

A two dimer vacancy (2DV) was added to an extended 2 x 10 sized dimer slab. Using the NEB method, we calculated the band to create a *phason pair* configuration close to the 2DV defect. The corresponding band at the tip position just before the

threshold point was calculated and compared to the band for a perfect surface in Figure 5.14 (a). The barrier to cross from the *three-in-a-row* to the *phason pair* state is increased from 80meV to  $\sim$ 110meV, demonstrating that defects can dramatically change the energy landscape, in this case increasing the barrier to generate the phason pair by nearly 40%. The 2DV defect was chosen as an example of a defective structure which is easily accessible computationally. It is likely that other defects, particularly boron ad-dimer related structures will instead reduce the barrier for the *three-in-a-row* to *phason pair* transition. This is motivated by Figure 5.14 (b) where a double boron ad-dimer defect has a very strong visible effect on the buckling of dimers. In the centre rows, the buckling appears symmetric, indicating rapid fluctuations of dimer bond angle are taking place, whereas the neighbouring rows, as with the majority of other surrounding rows, demonstrates strong buckling of the dimers, indicating flipping is not taking place, or that there is a strong preference to remain in the observed configuration for the majority of the time. This appears to suggest that the boron derived defect is able to lower the barrier for the central row dimers to flip, resulting in these rapid fluctuations. This particular image was taken at 77K with a simultaneously measured small tunnelling current.

Based on these observations we attempted to simulate two very general cases of surface defect. Defects can perturb the local environment by affecting the bond lengths due to the strain they introduce. For instance, a subsurface dopant will have a different bond length to the Si-Si bond, perturbing the surrounding atoms as they try to compensate. Therefore, we introduced an artificial offset to the bottom two fixed layers of silicon, by either laterally compressing the simulated slab, or extending it, by 0.3 Å half way along the length of the dimer row. Thus, the distance between two of the surface dimers, *along the length of a dimer row*, would be reduced or increased by 0.3 Å. After introducing the artificial defect, the simulated slab was allowed to relax, attempting to compensate for the offset,

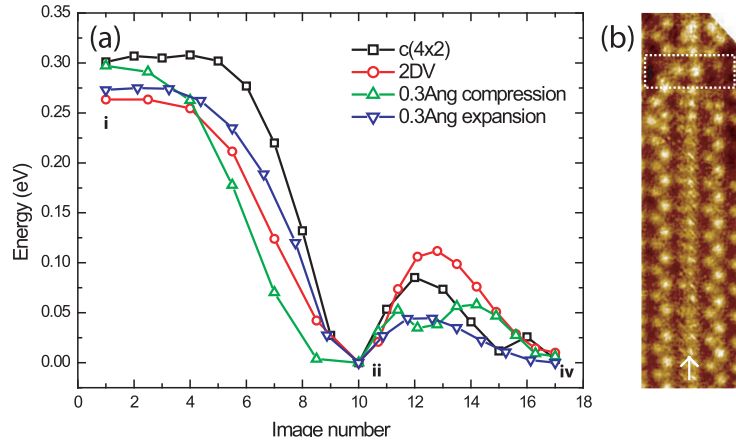


Figure 5.14: Comparison of perfect  $c(4\times 2)$  surface energy band (black open squares) with defective surface energy bands for a 2DV (red open circles), subsurface compression defect (green open triangles) and a subsurface expansion defect (blue open upsidedown triangles). All bands were calculated at the threshold height for flipping. Curves are shifted to match at position (ii) for easy comparison.

introducing strain into the system. The NEB band at the threshold flipping point was then recalculated obtaining the results shown in 5.14. In this case *both* the extension and compressive defect *reduce* the barrier for the *phason pair* transition to 45 meV and 60 meV respectively. Although the barrier still remains, it has shown a remarkable reduction of 50%. The choice of 0.3 Å was largely artificial, and actually corresponds to a relatively small surface response of 0.1 Å, which is of order, or often smaller than, reported surface responses due to defects (0.1Å- 0.8Å) [173,174]. The calculations are, however, extremely computationally expensive and require over a week of computation across 120 CPU's, rendering a more systematic investigation impracticable at best.

An extensive theoretical investigation into the manipulation of Si(100) dimers has been presented to model the experimental system as well as is reasonably computationally possible. We have seen in our NEB simulations of the pristine surface that the energy barrier required for transition to a *phason pair* configuration causes the *phason pair* to be inaccessible at 5K, even within the presence of a strongly in-

teracting silicon tip cluster. To investigate the influence of defective surfaces a 2DV, and other artificial defects, were introduced which were found to significantly modify the minimum energy pathway for transition. Therefore, we have to conclude that certain surface defects *must* play a crucial role in reaching the *phason pair* configuration. Thus far, however, we have not definitively proved that defects are responsible for the experimental observations. It is possible that the DFT simulations simply do not fully encompass the Si(100) system, perhaps failing to address the long range effects due to stress caused by the buckling. Another interesting possibility, due to the low temperatures and small barriers involved, may be the emergence of quantum mechanical tunnelling. Although the silicon dimer has a relatively large mass, quantum effects have previously been observed for objects as large as CO [175].

## Chapter 6

# Tip engineering with hydrogen terminated probes

Over the last decade our understanding of the mechanisms involved in dynamic force microscopy (DFM) processes has evolved significantly. We are now reaching the end of an era of discovery and moving into a period where the focus has shifted to mastering every aspect of the experimental system. In fact, some of the the most exciting recent contributions to this field [28, 29, 55] focus on solving the last major hurdle in NC-AFM, the unknown structure of the tip apex.

In this chapter I discuss a series of *ab initio* simulations illustrating that the ability to achieve atomic manipulation depends on the precise orientation of the dangling bond(s) at the tip apex and their charge density with respect to those of surface atoms. Using the Si(100)-  $c(4 \times 2)$  surface and a hydrogen passivated tip as a prototype system, we demonstrate that it is possible to select tip apices capable of performing atomic manipulation tasks which are unachievable using another choice of apex. Building on these simulated predictions, NC-AFM experiments are conducted on the hydrogen terminated Si(100) surface where we regularly identify stable chemically unreactive tip apex structures, confirmed by DFT simulations. It

is shown that the passivated tips regularly produce consistent high-resolution images of both the  $(2 \times 1)$  surface and some of its defects. The experimental results are discussed within the context of the prototype simulations to determine whether it is possible to controllably and reversibly engineer both chemically reactive and passivated tips within a single experiment. The results presented in this chapter have been published in *Phys. Rev. B* **85**, 235305 (2012) and *Appl. Phys. Lett.* **100**, 233120 (2012). All theoretical calculations and experimental data described in this chapter were obtained by the author unless otherwise stated.

## 6.1 Role of orbital overlap in atomic manipulation

Atomic manipulation at the single atom level using dynamic force microscopy (DFM) is becoming routine [20, 21, 23, 27], allowing extraordinary experiments to be realised on surfaces inaccessible by scanning tunnelling microscopy (STM), or in systems where DFM greatly assists single atom precision. Nonetheless, due to the complex interaction between the scanning probe apex and surface atoms, atomic manipulation DFM remains fraught with difficulties and experimental unknowns. A major challenge in scanning probe microscopy (SPM), especially DFM, is to elucidate the exact nature and role of the tip-sample interaction, not only in the formation of image contrast, but, critically, during atomic manipulation.

On a given surface, a wide variety of stable image contrasts [51, 170] can be observed, and have been attributed to different tip apex structures possessing dangling bonds of varying spatial extent and electronic charge density. Just how tip structure then affects atomic manipulation has, however, thus far attracted little attention. Although Freitas and Merkle have carried out a comprehensive theoretical study of the tip types necessary to carry out fundamental mechanosynthetic [176] reactions (i.e. atomic precision chemistry driven by mechanical force) on diamond surfaces [177], their simulated tip apices are rather complex and will necessitate

challenging advances in controlling the chemistry of scanning probes. We focus here on simple prototypical systems and methods which are readily accessible by current experimental SPM methods.

Although it has been shown that a single tip can drive an exchange reaction between two atomic species at room temperature [20], such a process may not always be thermodynamically or kinetically viable. In the absence of an exchange reaction, the preference of an atom to bond to the probing tip or surface will be critical to extend the technique of DFM manipulation to arbitrary systems, and will be determined by the outermost tip orbital(s). Here we describe calculations predicting that different tip types, modelled using small silicon tip clusters, undergo very different responses during atomic manipulation experiments due to the alignment, and the electronic charge density, of the atomic orbitals at the tip apex with respect to those of surface atoms. We use a test system comprised of a Si(100) -  $c(4 \times 2)$  surface and a hydrogen terminated silicon tip cluster and attempt to deposit(extract) an atom onto(from) a surface. We observe that different classes of tip are only able to perform one of these manipulation steps, i.e. no single tip type considered here is capable of *both* atomic extraction *and* deposition. We illustrate how it may be possible to distinguish tip types via comparison of a line sequence of force-distance ( $F(z)$ ) measurements.

The example model we choose is the manipulation of the Si(100) surface. In the previous chapter it was shown that, at 5K the individual surface dimers can be manipulated from one buckled configuration to another [178,179]. Depending on the specific tip apex structure chosen for  $F(z)$  simulations, however, we noticed strong variations in the amount of hysteresis present between the approach and retract curves. In the next section we show how these variations can be exploited to gain insights into the structure of the tip apex which could, in principle, be applied to, and direct a real experiment. This system allows us to characterise the apex in

an environment where atomic manipulation is entirely non-destructive, involving no removal of atoms or bond breaking, leaving the tip unaffected after manipulation. Si(100) also provides an ideal system for investigation of atomic manipulation in the form of the hydrogen-terminated Si(100):H surface [106].

### 6.1.1 A method for characterising tip structure

To represent the Si(100) and Si(100):H surfaces a 6-layer silicon slab model was used. A terminating hydrogen layer on the lower side of the slab was added and kept fixed along with the bottom two layers of silicon to simulate the missing bulk. The two tip structures used to simulate force distance measurements ( $F(z)$ ) are depicted in Figure 6.1. We study two different types of silicon tip cluster. First, we use a symmetric, and relatively structurally stiff cluster based on an H3 Si(111) -  $(7 \times 7)$  adatom feature (see section 4.4). As an alternative we consider an asymmetric dimer-terminated cluster orientated in the (100) direction. Both tips have been shown to provide accurate models of experimental AFM tip apices [40, 41, 51–53]. Electron density plots in Figure 6.1 show that the H3 apex represents an atomically rigid, symmetric tip termination with a single diffuse dangling bond pointing normal to the plane of the tip. The dimer tip is instead comprised of a less confined structure containing an angled and lower charge density apex dangling bond which can be aligned to a greater or lesser extent with the surface Si(100) dimer, as shown in Figure 6.1(c), depending on its orientation. We note that although the charge distribution at the apex dimer atoms is qualitatively similar to previous work [52], our relaxed geometry suggests charge is transferred in the opposite direction - *away* from the apex. We attribute this to the use of the GGA, as opposed to the local density approximation, and a larger basis set producing a subtly wider tip apex.

$F(z)$  measurements have particular potential in obtaining information about the structure and symmetry of the tip apex. The effect of orbital alignment between the

tip and surface is examined via three apex terminations: the H3 tip pointing normal to the surface plane, and two rotations of the dimer tip oriented 180° relative to each other. These terminations are depicted in Figure 6.1(d). Critically, both tip and surface dangling bonds can protrude at an angle relative to the surface normal. This inherent symmetry between tip and surface leads to a very strong alignment or misalignment of the orbitals between the dimerised tip apex and surface dimer, depending on tip orientation, allowing simple examination of the role this plays in manipulation. To accomplish this, the tip is positioned such that its outermost apex atom is placed directly over the lower atom of the surface dimer, and then laterally offset in the direction between two adjacent Si(100) rows in steps of 0.5 Å (shown in Figure 6.1(e)). Simulated spectroscopy was then carried out at each position producing the calculated  $F(z)$  curves in Figure 6.2.

Plotted in Figure 6.2(a) is a row of  $F(z)$  curves each taken with the H3 tip apex

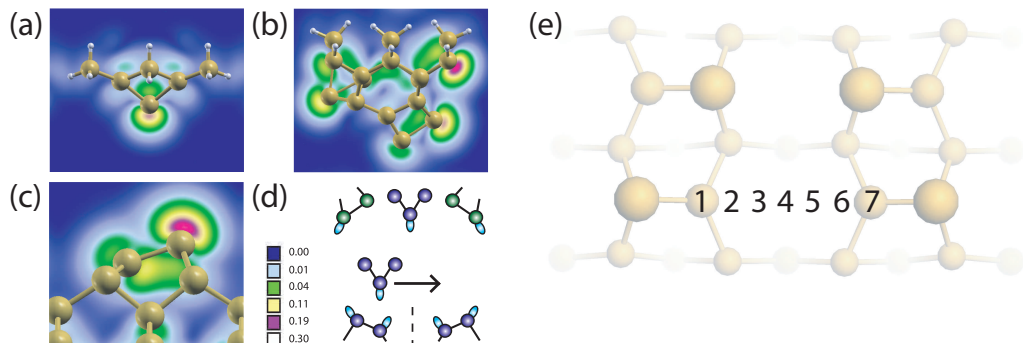


Figure 6.1: Ball-and-stick models of the H3 and dimer apex tips shown with a Si(100) surface dimer overlaid onto the calculated electronic charge density. (a) The H3 tip dangling bond is orientated parallel to the surface normal, whereas in (b) the dimer tip orbital is canted at an angle to the surface normal. The dimer tip can align or misalign with a surface Si(100) dimer (shown in (c)) depending on its orientation, and thus two extremes can be considered as distinct tips. The scheme of simulations is shown in (d). Each of the three tips are laterally displaced between two dimers (e) prior to simulating  $F(z)$  measurements. Partial electron density plots are calculated from the states within the range 0-1 eV below the Fermi energy and plotted on a square root scale to aid clear visualisation of the dangling bonds

laterally offset from the lower dimer atom as shown in the diagrams. Only the left four curves needed to be simulated, between the lower dimer atom and the centre of the row. The additional curves on the right of 6.2(a) are the same as on its left and are shown purely to highlight the differences between the H3 and the dimer tip. A steep vertical part in the approach curves as well as the force hysteresis are clear signs of a successful surface dimer flip induced by the AFM tip. Due to the symmetry of the H3 tip, rotation about the normal axis produces no change in the  $F(z)$  curves. Rotation of the dimer apex (Figure 6.2(b)) relative to the surface dimer, however, results in distinct variation in the observed hysteresis. In the case where the dimer tip is aligned with the surface dimer (left hand side), hysteresis in the  $F(z)$  curves is seen to increase in magnitude as the tip is offset from the lower dimer atom until the point where the tip no longer comes close enough to the surface dimer to form a strong interaction (i.e.  $\sim 2.9\text{\AA}$ - centre point between rows). The misaligned tip (right hand side) demonstrates a continuous reduction in hysteresis, however, more rapidly reaching a point where surface dimer manipulation no longer occurs. Therefore the asymmetry of the tip structure can be directly observed in the simulated  $F(z)$  curves.

Although a large number of detailed calculations were required to obtain these results (including data not shown between  $0\text{\AA}$  and  $2\text{\AA}$ ) the observed trends are actually very simple. On buckled surfaces such as Ge(100) and Si(100) this protocol could be experimentally implemented by taking a line of  $\Delta f(z)$  spectroscopy measurements between lower dimer atoms on adjacent  $c(4 \times 2)$  rows. Once the manipulation has taken place, and provided that the process remains deterministic, the dimer could then be flipped back into its original configuration [180] and the line spectra continued. The lower dimer atoms from adjacent rows can be used as convenient markers to check the symmetry of the  $\Delta f(z)$  curves, or more usefully,  $F(z)$  curves extracted from the frequency shift measurement. *If distinct markers are used in this way, ex-*

perimental knowledge about the exact tip apex atomic position is not required as this will not affect trends in the observed hysteresis. The same is true regarding knowledge of the orientation of a dimer type tip. Provided that the tip is not aligned 90° relative to the surface dimers in adjacent rows (removing its asymmetry), some trend in the  $F(z)$  curves should always be observed, identifying the structure as different from the symmetric H3 tip. Information about the symmetry of the AFM tip apex can therefore be obtained, and hence yield a general classification of the tip structure present. If the desired tip type has not been identified, then the typical [20] trial and error approach of tip modification must be pursued. At each stage characterisation of the tip can be made until the desired termination is obtained. It is also possible that automated probe optimisation methods [181] could help facilitate this process.

In Figure 6.3 (a) and (b) total electron density plots are shown for two primary orientations (aligned and misaligned) of the dimer apex when laterally offset by 2.5Å and positioned in  $z$  at the closest point of approach in the  $F(z)$  curves. Despite positioning the apex atom in exactly the same location prior to spectroscopy, we observe that the aligned tip interacts strongly enough to manipulate the surface dimer whereas a misaligned tip does not. This variation at 2.5Å lateral offset is likely a direct consequence of the unfavourable orientation of the tip, effectively increasing the distance between dangling bonds of the apex and lower dimer atoms such that the interaction is too weak to instigate manipulation. The differences in hysteresis can also be attributed to changes in how favourably the tip is aligned with the surface dimer. For the case of the tip orbital aligned parallel to that of the surface (Figure 6.2(b) left hand side), the tip-surface bond forms in a location which is already favourable to the creation of a strong bond. In the case of the misaligned tip (Figure 6.2(b) right hand side) the opposite is true, and the bond made will be considerably weaker. This procedure could in principle be extended to any situation where a dangling bond protrudes at an angle to the surface plane

normal, such as natural surface reconstructions (e.g. buckled surfaces), surface defects, vacancies or deposited atoms/molecules. Even in the absence of hysteresis from atomic manipulation, purely tip dependent hysteresis [54] could be studied in its place.

### 6.1.2 Predicting methods for vertical manipulation

To examine a wider range of atomic manipulation events we also considered the extraction/deposition of a single H atom, enabling an analysis of atomic manipulation involving a competition between a reactive tip and surface. We performed simu-

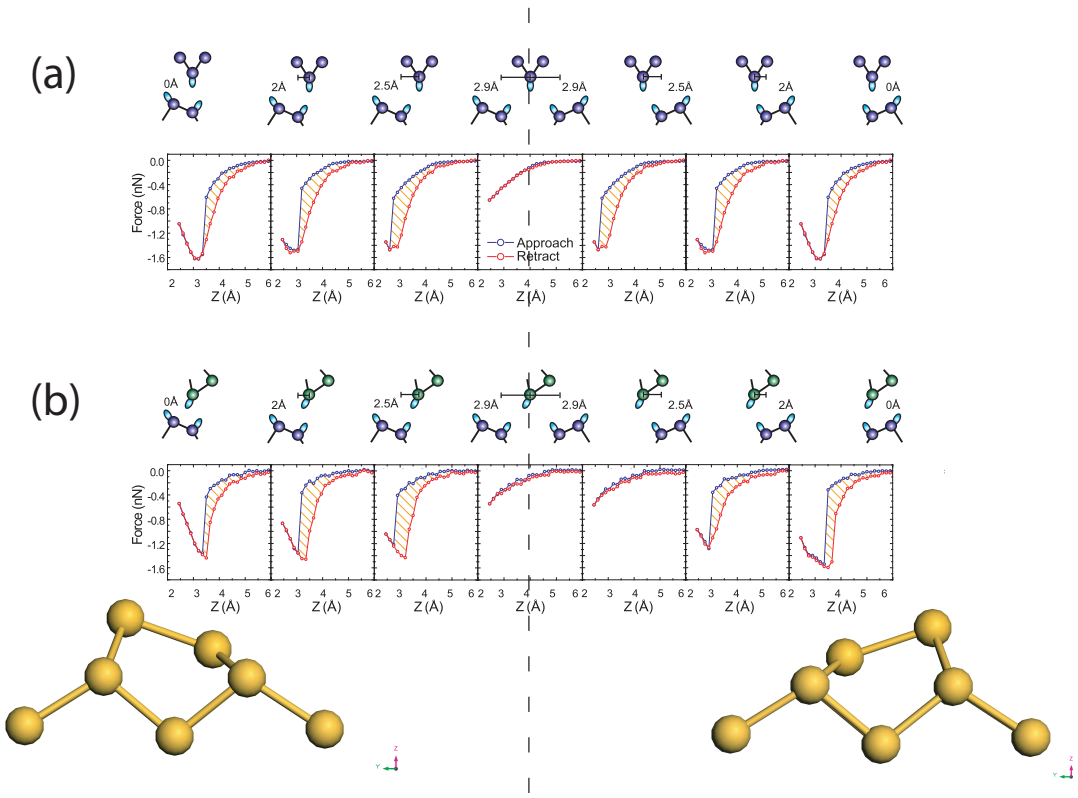


Figure 6.2: Effect of laterally positioning tips with directionally-dependent dangling bond terminations. The (a) H<sub>3</sub> and two rotated dimer tips ((b) aligned (left hand side) and misaligned (right hand side)) are positioned directly above a lower dimer atom, then displaced in steps of 0.5 Å. Clear variations in hysteresis are observed for the dimer tip when aligned or misaligned with a surface dimer.

lated force spectroscopy with the hydrogen-passivated H3 and dimer tips positioned (centred and laterally offset) above an upper Si(100) surface dimer atom. Figure 6.4 displays the calculated  $F(z)$  curves for the (a) H3 and, (b) dimer tips along with before (c,e) and after (d,f) ball and stick snap shots, at positions (a,(i)) and (b,(iii)) on approach and retract. The simulations reveal that the two tip types generate different outcomes of manipulation: the H3 apex retains the bonded hydrogen atom, despite being driven far enough into the surface to *push* a dimer into its alternative configuration, whereas the dimer apex relinquishes its hydrogen, passivating the surface. Interestingly, in this case, the orientation of the dimer tip has no effect on the success of manipulation. Therefore, if the suggested tip characterisation method was implemented, the particular orientation of the tip with respect to the surface does not need to be known, only general information regarding the tip symmetry would be required. The ability to *push* a Si(100) dimer into its alternative configuration appears to be made possible only with a strongly bound, passivated tip such as the H passivated H3 apex. Any tip type with a reactive apex would remain strongly bound to the surface dimer after approach, “pulling” it back up into its original position upon retraction of the tip as discussed in the previous chapter.

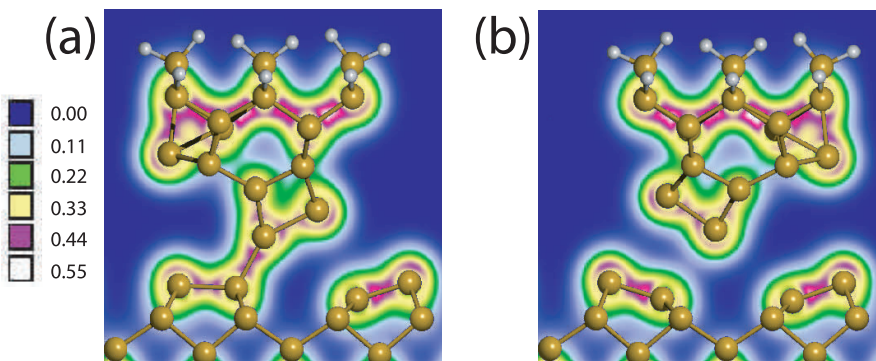


Figure 6.3: Total electron density plots corresponding to the force curves obtained with aligned and misaligned orientations of the dimer apex at 2.5 Å separation. The plots demonstrate the absence of bonding for one rotation of the tip relative to the other.

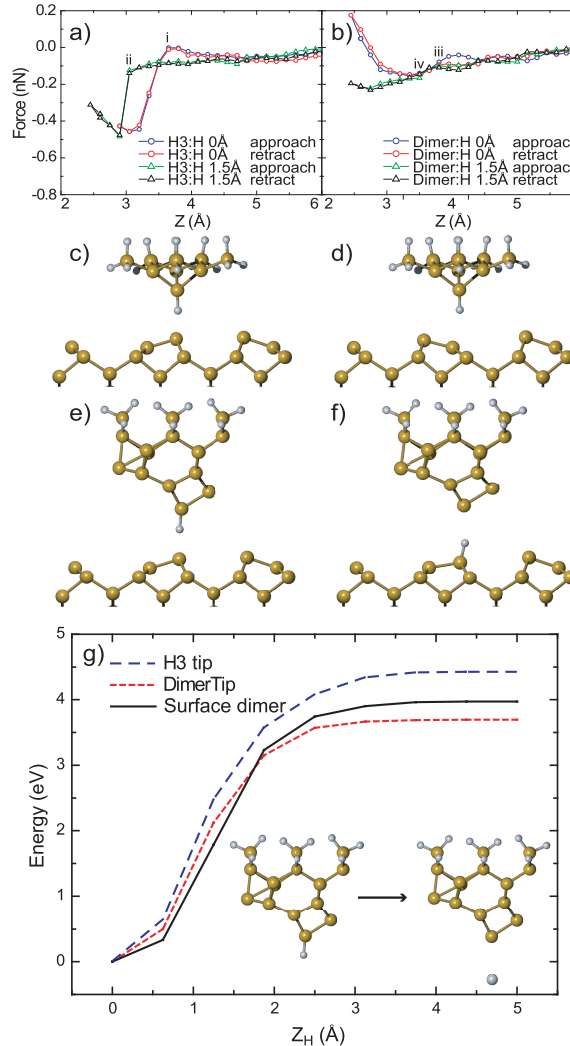


Figure 6.4: Atomic deposition(extraction) dependence on tip type. The H3 and dimerised tip structures have their apex dangling bond terminated with hydrogen to simulate the simplest possible atom deposition(extraction) experiment. Calculated force curves are shown for an (a) H3 and (b) dimer tip at two different lateral positions corresponding to 0 Å and 1.5 Å offset. Snap shots at 0 Å offset show H3(c,d)(dimer(e,f)) tip at point i(iii) on the force curve during approach and retract illustrating that the tip has retained(deposited) the hydrogen. In (g) we show the minimum energy pathway for removing a hydrogen atom from the surface upper dimer atom and from each tip type to a position of  $Z_H=5\text{ \AA}$  away as shown in the inset. The  $Z_H$  scale represents the displacement of the hydrogen from its equilibrium bonding position.

Although the local electronic surface structure will differ, parallels can be drawn between the hydrogen-terminated H<sub>3</sub> tip and a fully hydrogen-passivated Si(100) surface. If the strength of interaction between the H<sub>3</sub> tip and hydrogen is strong enough to prevent passivation of a clean Si(100) surface, it may be reasonable to expect that a clean H<sub>3</sub> tip could then be strong enough to extract a single hydrogen from a fully passivated Si(100):H surface. Such a manipulation would be unachievable using a dimer class tip under the same conditions. This highlights the possible difficulty in performing vertical manipulation with DFM in some systems. In the absence of probabilistic processes allowing both atom deposition(extraction) with the same tip, experiments in systems with chemically dissimilar species may not be possible with standard methods alone.

A nudged elastic band (NEB) method was implemented to calculate the minimum energy pathway for desorption of the hydrogen atom. The pathway is simple and intuitive, such that the barrier calculated by the NEB calculation is equivalent to the adsorption energy of the H atom. As shown in Figure 6.4(g), hydrogen is more strongly bound to the H<sub>3</sub> tip than the surface, and more weakly bound to the dimerised tip. This result supports our observation that once the simulated tip structure is positioned at small tip-sample separations upon retraction, the atom undergoing manipulation remains bonded to the structure with the highest binding energy. We therefore conclude that the type of atomic manipulation that can be performed is determined by the reactivity of the tip apex with the target atom, relative to the surface.

In the case of the H<sub>3</sub> cluster, we observe a significantly more crystalline structure in which the atoms are more closely packed allowing a greater amount of charge density to build at the apex dangling bond orbital compared to the more structurally diffuse dimer cluster. This observation is made for the electron density plots shown in Figure 6.1, and for alternative dimer-like terminated clusters discussed in the

next chapter. It is possible that crystalline tip apices will share this as a common feature. Therefore, a protocol that elucidates the symmetry of the tip (as a crystalline symmetric tip, or a less crystalline asymmetric tip) may in fact be able to generally categorise the apex as one which may or may not be able to compete with the surface reactivity.

The lateral positioning of the tips in this case had no significant influence on the success of manipulation. The  $F(z)$  curves (shown in Figure 6.4(a,b) for 0Å and 1.5Å lateral offset) demonstrated broadly the same behaviour, and were simply offset in  $z$  by an amount corresponding to the larger core-core distance between tip and surface atom (for the dimer tip, a large positive increase in force is driven by the interaction becoming strongly repulsive at small tip-sample separations). For the Si(100) system we have considered, the differences in binding energy are too large to be affected by lateral positioning of the simulated AFM tip. It may be possible, however, that in other systems the energy balance may be more subtle, allowing back and forth manipulation to be realised using a lateral offsetting technique.

The  $F(z)$  curves corresponding to the H3 tip contain an expected jump in measured force when the hydrogen atom is forced to bond to both the tip and surface (i,ii in Figure 6.4(a)). This is coupled with a lack of hysteresis confirming no permanent change to the tip has taken place. Conversely, in the case of the dimer tip there is no such sudden change in force when the hydrogen atom is transferred (iii,iv in Figure 6.4(b)) and, remarkably, no hysteresis. This unexpected behaviour appears to originate from a lack of major structural rearrangement of the tip and surface following transfer of the atom. As shown in Figure 6.4(e,f) very little change in the geometry of the tip and surface is observed, therefore it is perhaps unsurprising that the calculated forces are similar upon retract. Additionally, surface modifications also appear to have minimal effect on the  $F(z)$  curves.

The results presented here demonstrate that it is possible to obtain distinct

classes of tip apex, for a purely silicon tip, which enable specific atomic manipulation processes, while precluding others. With the correct protocol, in principle it may be possible to select tip “tools” configured for particular classes of manipulation event. In particular this is illustrated with two model tip structures able to either deposit or extract hydrogen from a Si(100):H surface, a process which may be extended to atomic/molecular manipulation on a wide variety of surfaces. We demonstrate how a tip can be characterised and selected via examination of  $F(z)$  measurements taken at different lateral positions during certain manipulation events. The results of our study suggest that even tips comprised of a single material, in our case silicon, can produce varied outcomes during attempted manipulation depending on its structure. In a real experimental system, it is also likely that contaminants may be present which could introduce chemically different species into the tip apex. Thus, depending on the sample surface and tip material in use, a large number of tip terminations may be possible further modifying the interactions present during manipulation [50].

## 6.2 Tip engineering on Si(100):H

To examine the possibilities of tip engineering, and to assess the tractability of the simulated predictions in the previous section, experiments were performed on the Si(100):H surface. Whereas in the previous section calculations were performed with a silicon/hydrogen terminated tip and a clean reactive surface, the experiments, in principle, are the reverse system, made up from a hydrogen terminated surface and a silicon tip apex. In actual fact the initial experiments were carried out concurrently with the simulations described in the previous section and not as a consequence of them. It was promptly recognised, however, that the simulated results were pertinent to the experimental observations and assisted in their explanation. Moreover, once the experimental system was understood, it became clear that the Si(100):H surface

could offer an ideal system to trial tip engineering experiments which attempt to switch between chemically reactive and unreactive tip apices, similar to the hydrogen transfer simulations in the previous section.

The remainder of this chapter will focus on NC-AFM experiments carried out on Si(100):H in which we identify chemically passivated tip structures. The chapter will finish by describing short experiments carried out on dangling bond and split-dimer surface defects before discussing tip depassivation. This section contains published results from *Appl. Phys. Lett.* **100**, 233120 (2012).

### 6.2.1 AFM observations on the Si(100):H surface

The Si(100):H surface is a fascinating system to study atomic scale silicon electronics. In recent years experimental STM techniques have approached a level where we can now reliably and reproducibly fabricate atomic structures with single atom precision [118, 119, 134]. The initial remit for our experiments on Si(100):H was to investigate the feasibility of individual atom-by-atom H desorption using an AFM as shown in Figure 6.5(a-d). The mechanism for H desorption in AFM must originate from different interactions than for the STM. Whereas in STM quanta of energy are imparted to the Si-H bond, causing it to break, in AFM, desorption is only likely to take place via direct removal of the H due to strong chemical bonding to the AFM tip apex. Elegant studies over the last decade (see section 2.3.6) have already demonstrated the importance of tip structure for both imaging and manipulation experiments. Moreover, the simulated results described in the previous section highlight that in a silicon-hydrogen system, even the crystal structure at the tip apex can have a ‘yes or no’ impact on the success of manipulation. Therefore a reliable understanding of the AFM tip is essential to attempt desorption experiments in AFM.

A large number of STM experiments have been carried out on the Si(100):H (2 ×

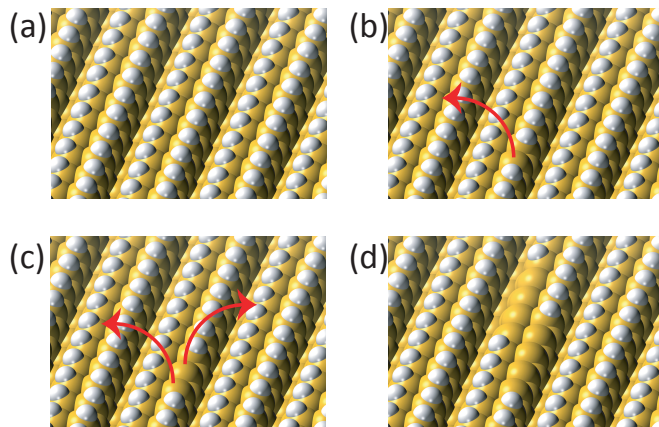


Figure 6.5: Ball-and-stick models of the Si(100) - (2 × 1) surface demonstrating individual hydrogen atom extraction from the clean surface (a). The initial remit of the project was to remove surface hydrogen atoms one-by-one (b),(c) to create larger structures with atomic precision (d), and importantly, without stray undesired desorption from the surrounding area.

1) surface, however as highlighted in section 4.3, the same surface has been subject to a very limited number of AFM studies, in fact only a single image of the (2 × 1) has been published prior to this investigation. As such very little is known about AFM interactions on Si(100):H and the typical tip structures present. Therefore, prior to complicated manipulation experiments, we require a better understanding of the tip-surface interaction. In particular, we need to test an important assumption typically made for silicon systems, namely that the tip becomes terminated with a reactive silicon cluster, which in principle, represents the only class of tip that would be capable of the proposed AFM desorption experiments.

Measurements were taken with a Createc GmbH LT STM-AFM system with Nanonis control electronics and software. qPlus sensors with tungsten tips (resonant frequency in the 17-21 kHz range,  $Q = 3000\text{-}9000$  at 77 K) were used for both the STM and the AFM experiments. A series of constant current images are shown in Figure 6.6, demonstrating typical image contrasts obtained on the (2 × 1) passivated surface. Figure 6.6(a) shows large scale images of the clean Si(100) (negative and

positive biases) and the Si(100):H - (2 × 1) surfaces (positive bias) demonstrating typical defect densities from our preparation. On the Si(100) surface we typically observe defect densities within the region of 0.1% - 1% made up from mostly dimer vacancies, and sometimes surface adsorbates as shown in this particular image. After hydrogen passivation, however, we observe a significant increase, largely due to additional surface adsorbates and dangling bond clusters arising from the imperfectly clean gas line and higher background pressure during cracker operation. The most regularly observed STM contrasts during our investigations are shown in Figure 6.6 (b) and (c) representing empty and filled states tunnelling respectively. The majority of investigations were performed by applying a positive sample bias in which we most often observe individual hydrogen atom resolution. The images shown in Figure 6.6(b) represent the most commonly observed types of ‘good’ contrast observed at positive biases, where we can at least resolve the individual dimers. Shown are a combination of contrasts demonstrating clear atomic or dimer resolution, in many cases we observe asymmetries in the dimers as shown in the second and forth images. In Figure 6.6(c) are a series of negative bias images, which in the authors experience are generally more difficult to interpret than for positive biases. In the majority of filled states images the row structure becomes more prominent, rather than the individual hydrogen atoms. It should be clear that a number of distinct image types are possible in STM which, although varying with applied sample biases and current setpoint, are most often observed after changes in the tip structure.

When performing AFM measurements on the Si(100):H surface it is prudent to initially select a suitable region in constant current operation. Even at 77K thermal drift can affect measurements in AFM. Worse still can be piezoelectric creep introduced from the three scan tubes present in the beetle head design. A typical AFM image, taken over a region of 3x3nm can take between 20-30 minutes to complete, de-

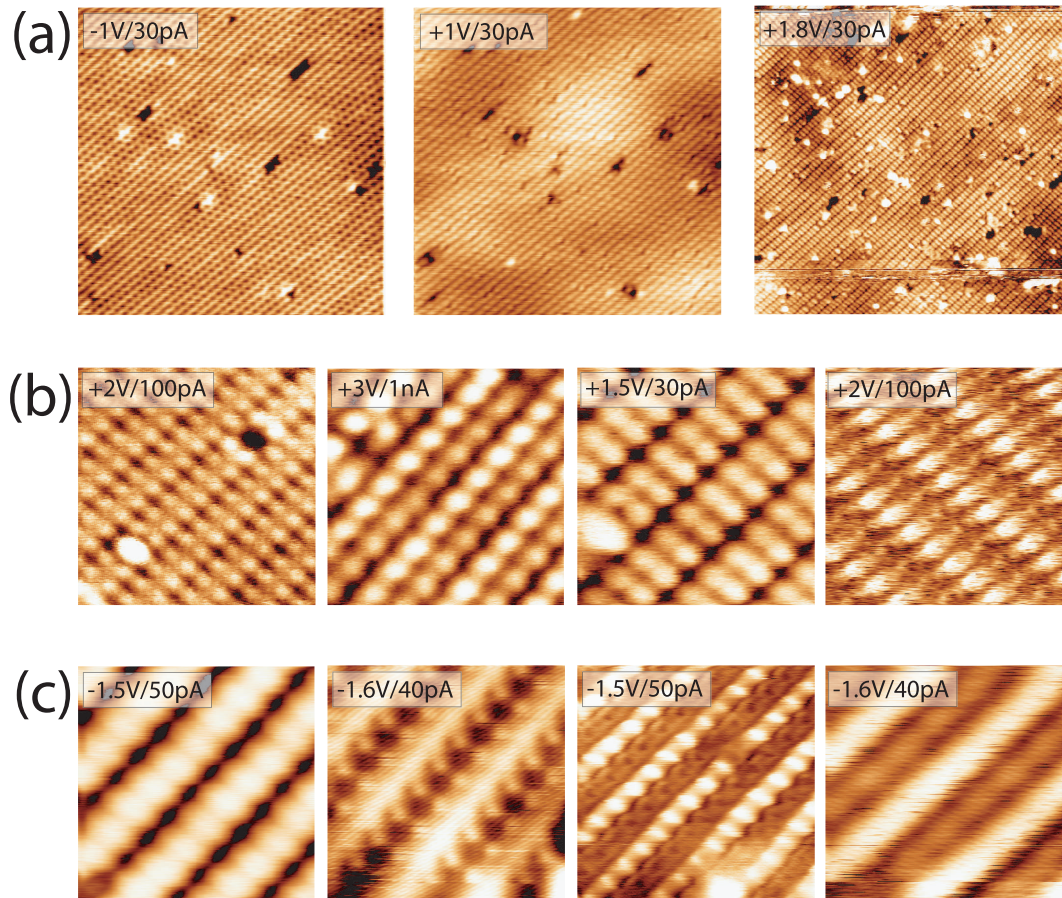


Figure 6.6: STM images of clean and hydrogen passivated Si(100). (a)  $30\text{nm}^2$  images of Si(100) taken at negative and positive sample biases respectively, shown with a positive bias image of Si(100):H illustrating typical defect densities on the two surfaces. (b) Empty and (c) filled states images of Si(100):H -  $(2 \times 1)$  depicting the most commonly observed image types, including atomic, dimer, and row resolutions. Parameters shown with images.

pending on the feedback requirements to maintain a low noise level<sup>1</sup>. Consequently the scan area can easily drift onto undesirable regions a few nanometres outside of the initial scan window. To reduce the problem, preliminary constant current imaging was often continued for several scans, up to an hour, while piezoelectric creep stabilised. To minimise thermal drift we used the atom-tracking technique, which tracks the position of a target atom for a number of minutes, thus directly measuring the the thermal drift before applying a linear correction to the x y and z piezo directions. This not only helps to answer the question “what am I looking at?”, by directly comparing the AFM to the previous STM image, but helps avoid the large adsorbate clusters which can severely damage the tip apex.

In Figure 6.7 a series of constant  $\Delta f$  topography images are shown (b-d) taken directly after a constant current filled states image (a). The typical procedure for the transition between STM and AFM involves pulling the tip away from the surface by 1nm, reducing the applied bias voltage to 0V, then switching the active feedback and slowly increasing the  $\Delta f$  setpoint until atomic resolution is achieved. Figure 6.7(b) shows an initial AFM image demonstrating atomic-scale corrugations at very low  $\Delta f$  setpoint directly after the transition. Analysing this image alone, it is easy to interpret the bright rectangular features as the surface dimers, particularly if the defect in the lower left corner of the images is used as a marker. Subsequent increases in  $\Delta f$  setpoint(Figure 6.7(c),(d)), however, tell a different story and we observe a reduction in the size of the bright features, and the appearance of prominent dark suppressions appearing as pairs. Upon closer inspection one can notice that the corner defect in fact lies exactly between rows of the dark suppressions, indicating that the dark features correspond to the surface dimers of the Si(100):H surface.

To confirm the observations in Figure 6.7 we simultaneously obtained both AFM and STM data enabling *direct* comparison between well understood current obser-

---

<sup>1</sup>It is possible to observe images demonstrating particularly high atomic corrugations. In this case noise in the AFM signal is less noticeable and the scan speed/gains can be increased.

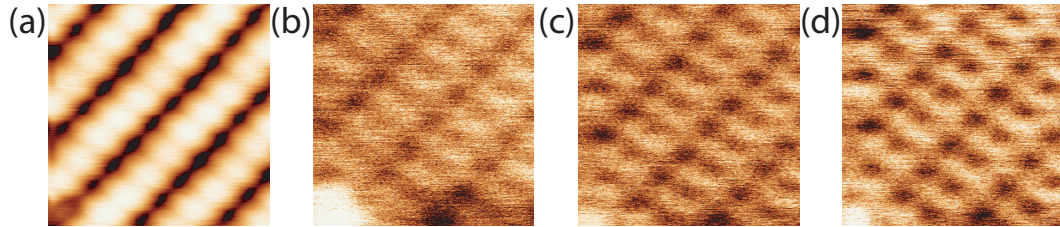


Figure 6.7: Constant  $\Delta f$  images taken at increasing setpoint. (a) Previous constant current image taken with parameters -1.5V/50pA. (b) Subsequent low setpoint (larger tip-sample separation) constant  $\Delta f$  image taken at -13.20Hz setpoint. Subsequent images taken with setpoints of (c) -13.50Hz and (d) -13.80Hz. Amplitude of oscillation,  $a_0=400\text{pm}$ .

vations and the apparently inverted AFM topography. Simultaneous measurements are relatively easy to carry out with the qPlus AFM setup and simply require the application of a bias voltage during normal AFM operation. Although, in principle, the tunnel current and frequency shift signals are well decoupled on the Createc system, it may still be possible to observe cross-talk between the two signals [167]. Moreover recent work has highlighted the presence of physical interactions originating from applied bias voltages, the so called “Phantom force” [182, 183]. Consequently care was always taken to first obtain AFM images at 0V applied bias, such that a basic comparison could be made between constant  $\Delta f$  images attained with and without applied bias. In addition, bias voltages were maintained at a level such that the measured tunnelling current remained in the tens of pA range [180].

An example of simultaneously acquired  $\Delta f$  and current data is shown in Figure 6.8(a) and (b) respectively. The same inverted contrast as noted for Figure 6.7 is present for the AFM data shown in (a), however, in this case we can directly observe the positions of the simultaneously acquired tunnel current maxima shown in (b). Superimposed onto the two images is the ball-and-stick model for the (2 × 1) surface clearly demonstrating that the bright maxima in the tunnel current image, known to correspond to the positions of the hydrogen atoms, line up perfectly with the dark suppressions in the constant  $\Delta f$  image.

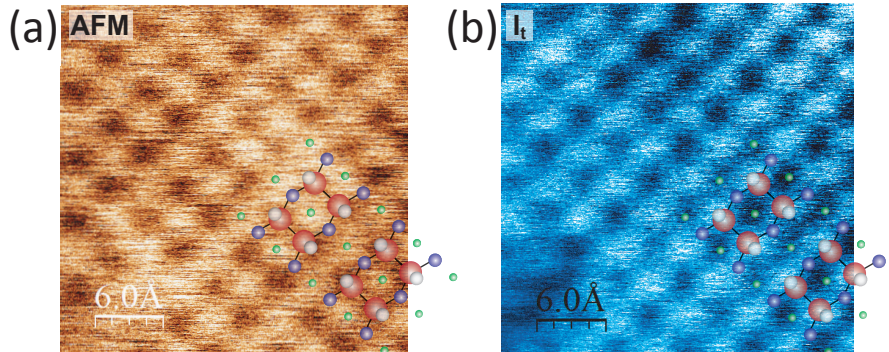


Figure 6.8: Tunnel current data obtained simultaneously during acquisition of a constant  $\Delta f$  AFM image. (a) Constant  $\Delta f$  AFM topography image, taken with an oscillation amplitude of 400pm and -36.5Hz setpoint with a +1.2V applied bias. (b) Simultaneously acquired tunnel current data showing bright protrusions corresponding to positions of H atoms.

In actual fact, prior to obtaining the simultaneous data, it was already possible to attribute the dark suppressions to the H atomic positions with some degree of confidence due to the extremely reproducible image resolution we obtain. In many of our images we clearly observe the dark features as dimer pairs arranged in rows, corresponding to the row direction observed in STM. Moreover, in several of our images dimer vacancy (DV) defects were clearly observed indicating the position of the dimer rows (see next section).

### 6.2.2 Identifying passivated tip structures

One of the most puzzling aspects of the AFM images obtained on Si(100):H is the extremely reproducible contrast observed throughout almost every image obtained thus far. In fact we have only observed one set of data which significantly diverges from our typical observations which I will return to at the end of this section. Displayed in Figure 6.9 are a selection of constant  $\Delta f$  topography images obtained from the clean Si(100) surface (a)(data courtesy of Adam Sweetman [170]) and the Si(100):H sample (b). The results for the clean Si(100) surface clearly show a

diverse variety of contrasts, in which atomic resolution (corresponding to buckled or symmetric dimers) is present in each image. In contrast, the results obtained on the passivated surface, taken across multiple experiments with multiple tip apices, all share very similar features in which each dimer appears as two dark suppressions, often joined to form a ‘peanut’ shape across the whole dimer. Although the level of noise present across the images shown in Figure 6.9(b) varies, there is very little difference in the overall form of the features from image to image. This is in contrast to the bright protrusions normally observed on semiconductor surfaces, due to the attractive chemical interaction between tip and surface atoms. This suggests that a particular atomic configuration is routinely cultivated at the tip apex.

The dark features observed suggest that rather than an attractive interaction, the tip in fact experiences a repulsive interaction as it scans over the hydrogen atoms. This is possible because the *total* force felt by the tip remains attractive due to the long range contributions, therefore the overall frequency shift remains negative. To elucidate the contrast mechanism on Si(100):H,  $\Delta f$  spectroscopy measurements were performed in a manner similar to the on/off method explained in Section 2.3.4 and 4.8.1. Whereas the Si(111) -  $(7 \times 7)$  surface contains the corner hole feature to act as a null site, thus allowing the short-range extraction of force, no such feature exists for Si(100) surfaces. Therefore a ‘best alternative’ approach was adopted, in which we take measurements above the H atom, and in the site between rows most distant from the other surface atoms as shown in Figure 6.10. Although this approach will not provide perfect extraction of the short-range interactions, it is possible to compare the results with DFT  $F(z)$  simulations carried out in the same locations.

Figure 6.10 shows an example of experimentally obtained data presented in the same format as the data obtained on Si(111) - $(7 \times 7)$  (shown in Figure 4.16 in section 4.8.1). It should be immediately obvious that rather than the typical in-

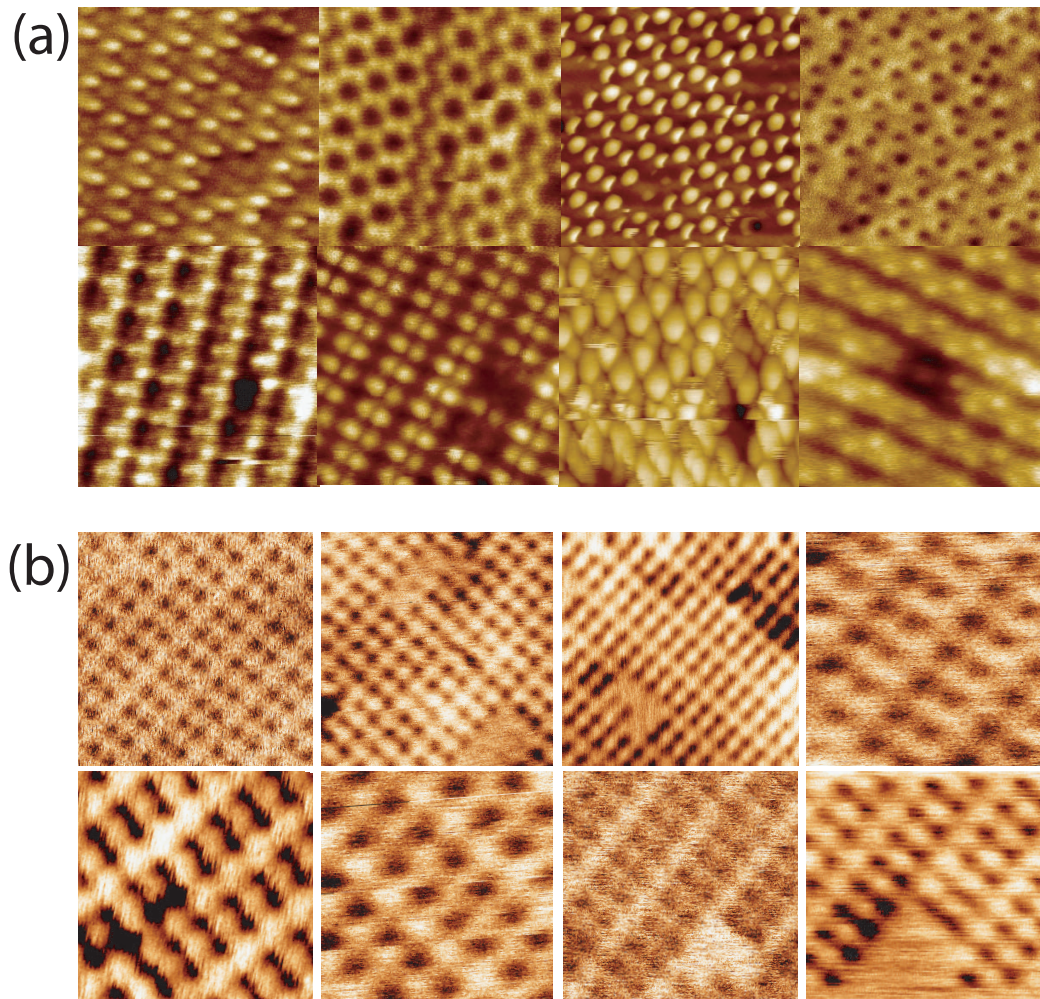


Figure 6.9: Collage of constant  $\Delta f$  topography images taken at '0V' applied sample bias on both the (a) clean Si(100) surface and (b) the passivated Si(100):H surface. There are clear differences in the number of observed image contrasts across experiments, suggesting that we regularly obtain the same AFM tip apex in Si(100):H studies. Data shown in (a) courtesy of Adam Sweetman [170]. Top centre images in (b) courtesy of Peter Sharp.

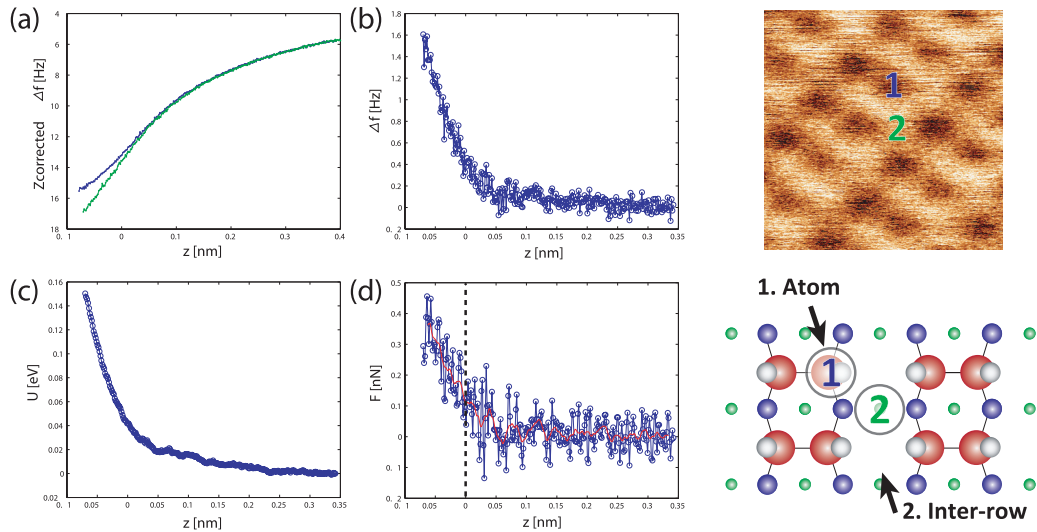


Figure 6.10: Calculation of experimental  $F(z)$  difference curve with the on/off method. (a)  $\Delta f$  measurements taken over a surface hydrogen atom (blue - position 1) and between dimer rows (green - position 2). (b) Short-range  $\Delta f$  following subtraction of 2 from 1. (c) Interaction potential  $U(z)$  calculated from (b) via the Sader-Jarvis method. (d)  $F(z)$  calculated as the derivative of (c), blue curve (open circles) corresponds to a direct numerical differentiation, whereas the superimposed solid red curve is obtained by a 5 point average differentiation, significantly reducing noise without compromising the physical interpretation. Dashed line marks tip-sample separation during image acquisition.

teraction potential we normally expect, consisting of a strong negative increase in force, corresponding to attractive chemical bonding between atoms, followed by a rapid positive increase in force due to Pauli repulsion, on Si(100):H we apparently observe no attractive interaction, but immediately enter the repulsive regime. The force data in Figure 6.10(d) is obtained via differentiation of the energy curve in (c). The blue data with open circles in (d) is a direct differentiation of (c) and therefore contains significant noise; the solid red curve superimposed on the same plot is data obtained from a five point average differentiation, thus reducing the noise from the numerical differentiation. Both data plots are included to highlight the absence of an attractive well in  $F(z)$ , demonstrating that this does not originate from the averaged differentiation technique.

The apparent absence of any attractive interaction during spectroscopy is a puzzling result. To understand the tip-sample interaction responsible for such an observation it is necessary to make a comparison with DFT simulations. Prior to our AFM experiments we first prepare the scanning tip in STM, coercing the tip into a state which provides stable feedback and high-resolution images. Consequently the tips are regularly indented into the surface or subjected to brief voltage pulses until the desired STM image quality is obtained. As such experiments typically assume that a significant amount of surface material contaminates the scanning tip apex. Therefore simulated tip structures are designed to contain those same materials, attempting to reflect the real tip termination. Although contaminants can include oxides, carbon, and dopant atoms from the sample, we initially attempted to describe the tip apex as a pure silicon tip, or a hydrogen passivated tip, which are obviously abundant materials in the Si(100):H system. This choice of tip structure was motivated by the simulated findings in the previous section, which showed a dramatic reduction in attractive tip-sample forces with hydrogen passivated tip structures.

$F(z)$  measurements were simulated in the same two locations that experimental  $\Delta f$  spectra were taken, before subtracting the two measurements thus calculating the force difference. In principle this approach removes any experimental assumptions, such as long range fitting methods might introduce, enabling a direct comparison between theory and experiment. Plotted in (a) and (b) are the two simulated force curves corresponding to a tip positioned above a surface hydrogen atom (1 - blue filled squares) and positioned between rows (2 - red filled triangles), along with the simulated (green filled circles) and experimentally (black open circles) calculated force difference, for the (a) silicon and (b) hydrogen passivated tip structures respectively.

In Figure 6.11(a), we can clearly observe that the silicon terminated tip interacts

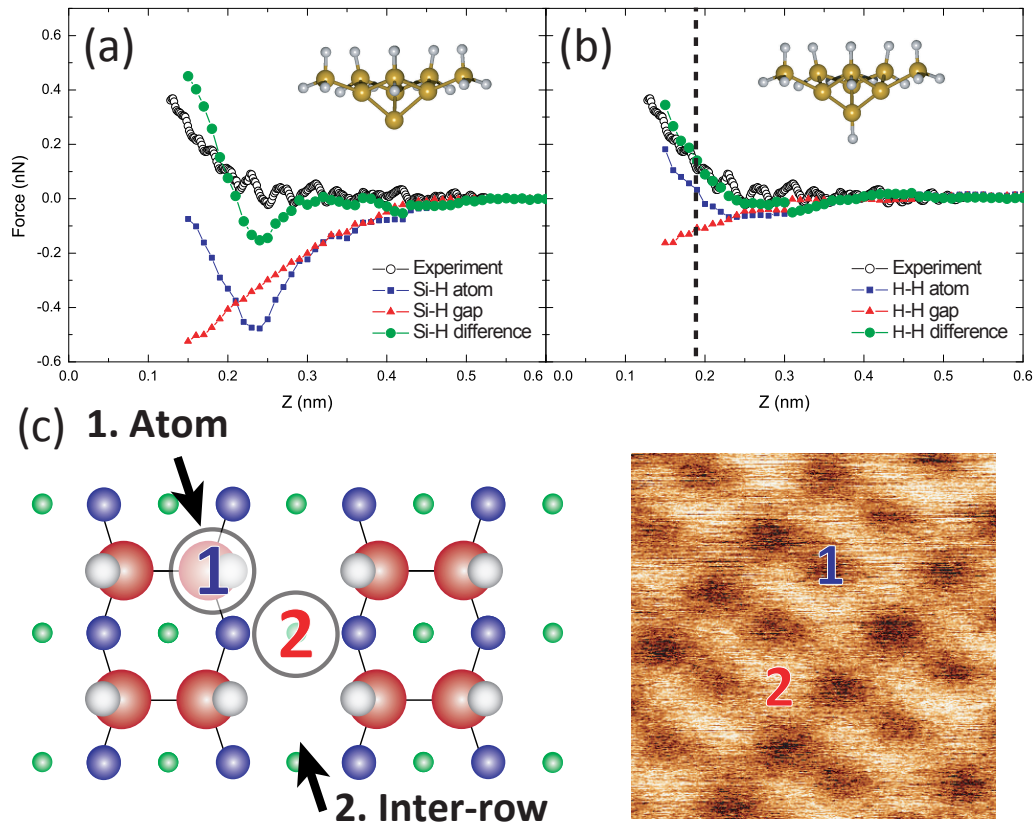


Figure 6.11: Comparison of DFT simulated and experimental force-difference data with (a) a reactive silicon terminated cluster and (b) an unreactive hydrogen terminated silicon cluster. (c) Illustration of the on/off positions used to take both experimental and DFT measurements. Blue filled squares correspond to location 1 above a hydrogen atom, red filled triangles correspond to location 2 between rows. Green filled circles represent simulated force-difference data and black open circles experimental force-difference data. Dashed line in (b) marks tip-sample separation during experimental image acquisition.

strongly with the surface in both locations, an attractive force of up to -0.55nN is calculated between the AFM tip and Si(100):H surface. Even after calculation of the force difference, a significant attractive force of  $\sim$ -0.15nN is still present, which is sufficiently above the noise level to be observed experimentally. In contrast, for the hydrogen passivated tip cluster we observe a significantly suppressed attractive interaction, producing a calculated force difference demonstrating extremely strong agreement with the experimental observations. In fact the  $F(z)$  difference curves only diverge in two locations; very close to the surface, deep into the repulsive regime, and in the region between 0.2-0.35nm where we observe a slightly larger attractive interaction in the DFT data. The first point can be answered quite easily. In the simulation we use a very small tip cluster, in which only five atoms are free to move and respond to tip-surface induced deformation. Therefore, when the tip is very close to the surface, where a large repulsive force is felt, the apex is unable to elastically deform to the same extent as the real experimental tip. Thus the apex will remain closer to the surface than a real tip might, resulting in a sharper force increase. The second point is slightly more challenging to address, and once again highlights the apparent absence of an attractive interaction in the experimental data. The simulated  $F(z)$  curve taken over a hydrogen atom clearly includes a small attractive component, and although the calculated force difference leads to a significant reduction in its appearance, it is not completely suppressed suggesting that it should be possible to observe an attractive interaction experimentally. Even considering the small apparent discrepancies between the simulated and experimental data, there is still extremely good agreement, and as such we strongly believe that our scanning tips regularly become hydrogen passivated at the apex, leading to the reproducible inverted-contrast observations shown in Figure 6.9(b).

### 6.2.3 Direct observation of atomic scale dispersion interaction?

The data presented in the previous two figures correspond to 1D measurements of  $\Delta f$  taken along the  $z$  axis. Although, as has been described, we can ascertain a huge amount of information from these simple measurements, it is possible to go several steps further and build up a complete 3D map of interactions between the tip and surface by taking multiple spectroscopy measurements across a 2D surface grid. The major benefit of grid-spectroscopy measurements is the ability to obtain data with sub-Ångstrom resolution in x,y *and* z directions. Therefore detailed information can be obtained along any plane relative to the surface. Grid-spectroscopy is particularly well suited for microscopes operating at  $\sim$ 5K temperatures where the thermal drift rates are small enough for such a time consuming measurement. Grid-spectroscopy measurements in AFM can typically take several hours, depending on the integration times and the data density required, therefore a low rate of drift is essential. At liquid nitrogen and room temperatures the thermal drift rate needs to be precisely corrected for. Measurements on the Createc system were taken at 77K using the atom-tracking facility present in the Nanonis software to minimise drift. Grid-spectroscopy measurements could only be carried out if the scanning tip had moved less than 10nm for several hours, and only if at least 12 hours had passed since the last coarse piezo movement, at which point non-linear creep was minimised.

To build up a 3D data set the tip is taken out of active feedback and is either scanned laterally in x-y, reducing z after each constant height scan [184], to build up several slices of data forming the 3D matrix, or alternatively  $F(z)$  spectra can be taken at each point across a 2D grid aligned parallel to the surface. For the data presented in this thesis the grid-spectroscopy method is applied which eliminates any possible data contamination due to drift between constant height scans. Slices of data at particular tip-sample separations can then be extracted from the larger

3D data set, corresponding to constant height images. It is important to note that the atomic contrast observed in constant height images is inverted with respect to constant  $\Delta f$  images. Therefore hydrogen atoms appear as bright features in the constant height mode.

Several slices through the 3D data set are shown in Figure 6.12 taken at different tip-sample separations using the same tip which produced the images shown in Figure 6.7 and the data shown in Figures 6.11 and 6.10. The tip-sample separation is defined relative to the setpoint required to take the image in Figure 6.7(d).

At large tip-sample separations (a) no atomic contrast is found in  $\Delta f$ . At very small tip-sample separations (e), well into the repulsive regime, strong bright protrusions are observed, consistent with our observations in constant  $\Delta f$  feedback. At intermediate distances, however, the surface dimers are apparently observed as very weak suppressions just above the noise level of the system. The dimers begin to appear as suppressions at tip-sample distances of around +123.6 pm (b), appearing most clearly in (c) at  $z = 71.26$  pm. Upon continued approach the contrast vanishes (d) until the tip comes very close to the surface where most of our images are taken (e). The position of one atom is marked with a red cross to show the alignment between images. Although the noise level is very high it is still possible to observe darker features in the locations of the surface dimers (the transition is particularly clear when viewed as a video, which has been made available online [192]). The relative positions of the  $\Delta f$  slices are marked on the experimental  $F(z)$  curve reproduced in Figure 6.12(f). It is interesting to note that the images in (b) and (c), which display the dimers as dark suppressions, lie in what should be the attractive region of the interaction curve. This suggests that an attractive interaction *is* in fact observed experimentally, however, the interaction is so weak, that it is only slightly larger than our  $\Delta f$  noise level making it almost impossible to detect in a single 1D  $F(z)$  curve. When viewed alongside a larger number of data points however, the

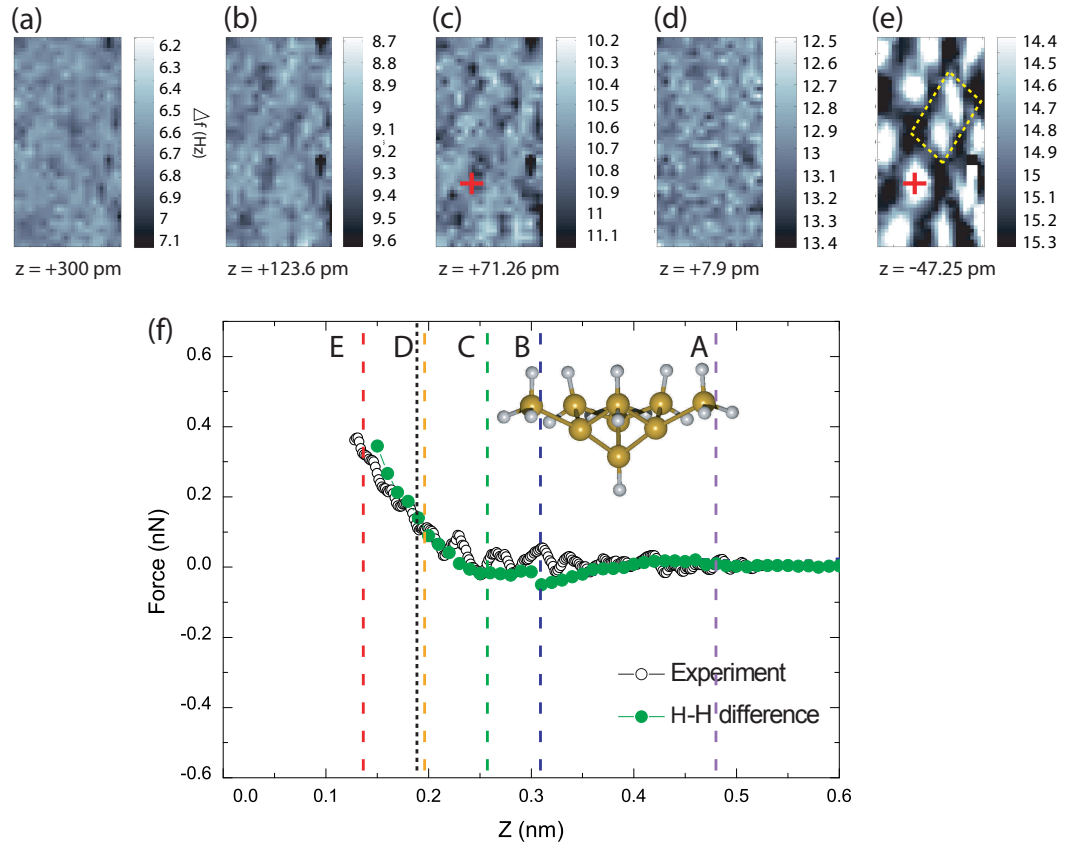


Figure 6.12: Constant height  $\Delta f$  slices extracted from a 3D grid spectroscopy measurement at decreasing tip-sample distances. (a) At large tip-sample separations only noise is observed. At intermediate distances (b),(c) weak dark suppressions appear corresponding to attractive interactions. (d) As the tip moves closer to the surface we transition from attractive to repulsive interactions dominating image contrast. (e) Repulsive interaction observed very close to the surface. (f) Experimental and DFT simulated force difference curve shown with dashed lines indicating the tip-sample separation for each constant height image e.g. (a) corresponds to dashed line A. Dotted black line represents  $z=0\text{nm}$  for experimental measurements.

small variations in noise across the surface become clearly visible. At  $z = +7.9$  pm (d) a transition is observed between the attractive and repulsive regimes where once again atomic contrast is not present.

Two horizontal slices clearly illustrating the repulsive and attractive image regimes are shown in Figure 6.13(a) and (b) respectively, displayed with a vertical slice, taken along two dimers (c). Solid black lines are superimposed onto the vertical slice in (c) representing the locations of the surface hydrogen atoms. At very small tip-sample separations we can see that the frequency shift becomes less negative (repulsive interaction) above the hydrogen atom sites (light and dark blue region), however, at slightly larger tip-sample distances, around the yellow region of the figure we can see that the hydrogen atoms correspond to increases in frequency shift (attractive interaction) for all but the third dimer from the left, which appears to be laterally offset. The transition between attractive and repulsive interactions with hydrogen terminated tips was in fact predicted to occur theoretically [185] at tip-sample separations which correspond surprisingly well to our simulated and experimental data. Moreover the 3D measurements solve the one remaining discrepancy between our simulated and experimental  $F(z)$  curves which were previously interpreted not to show an attractive interaction.

At the beginning of this section it was noted that we have only ever observed conventional strongly attractive atomic resolution contrast in one experimental session. During an experiment in which the inverted contrast was obtained, a spontaneous tip change occurred which reversed the contrast so that the H atoms appear as maxima rather than minima (in constant  $\Delta f$  feedback). Figure 6.14 shows three images obtained after the tip change demonstrating non-inverted contrast. In Figure 6.14(a) and (b) two images are shown in which only the dimers are observed, after increasing the  $\Delta f$  setpoint in (a), the individual hydrogen atoms are resolved (c). This particular data set is provided courtesy of Peter Sharp. The observation of bright features

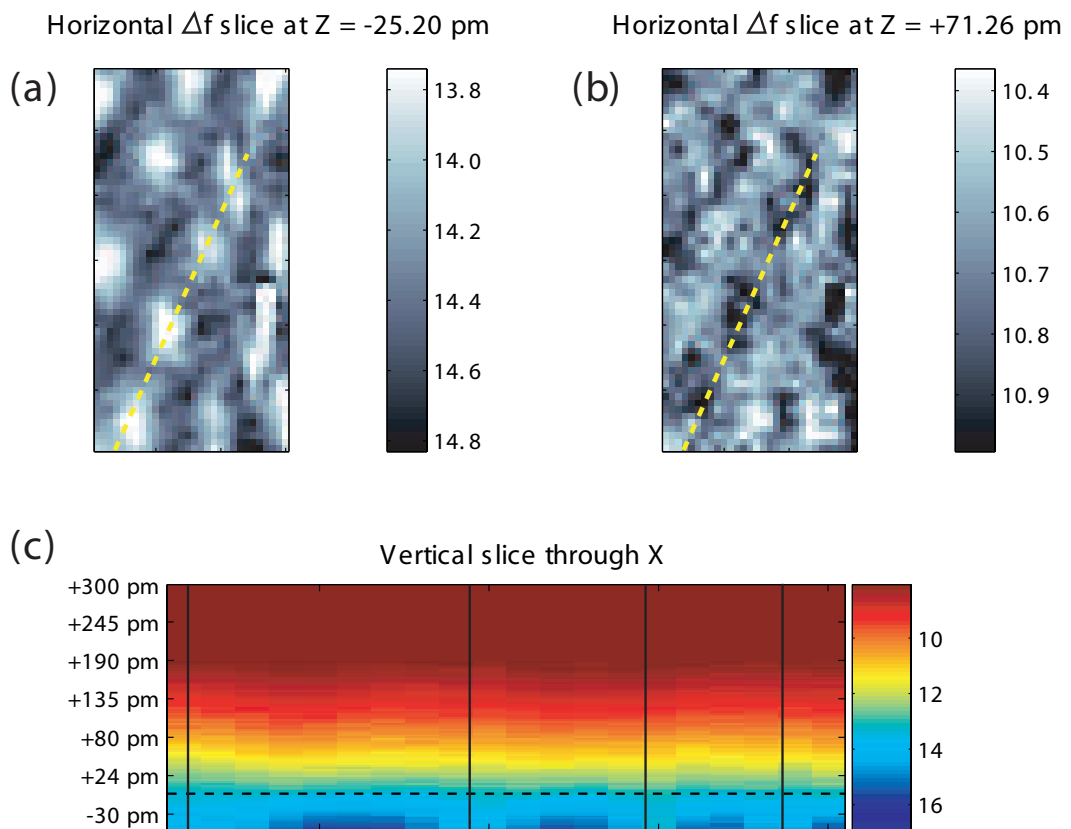


Figure 6.13: Constant height  $\Delta f$  ‘slices’ with (a) repulsive and (b) attractive image contrasts are shown with a vertical  $\Delta f$  slice through X in (c). The vertical slice was taken through the region marked by a yellow dashed line in (a) and (b). The dashed line in (c) corresponds to  $z=0\text{nm}$ , i.e. the tip-sample separation for the image shown in Figure 6.7(d). The solid black lines in (c) represent the hydrogen positions in (a).

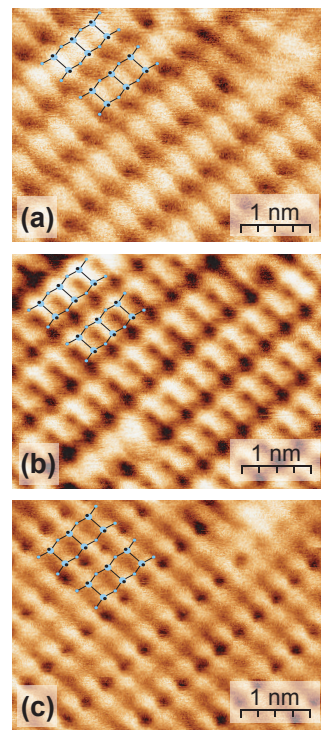


Figure 6.14:  $\Delta f$  feedback images taken with a tip demonstrating conventional “non-inverted” contrast. Dimers now appear as protrusions (a), (b). (c) At higher set-points the individual H atoms are resolved . Images (a)-(c) acquired with  $\Delta f=-27.1\text{Hz}$ , -23 Hz, and -30 Hz, respectively; oscillation amplitude=300 pm for all images. Data courtesy of Peter Sharp

corresponding to each atom is typical of Si-Si systems [170, 178]. If we consider the simulated DFT  $F(z)$  curves in Figure 6.11(a), then in principle a reactive silicon tip apex should provide the conventional contrast shown in Figure 6.14. We should stress, however, that these images were only obtained following a tip change from an inverted type contrast. Unfortunately experimental  $F(z)$  spectroscopy was not possible in this case due to tip instabilities returning the tip back to an inverted imaging state.

#### 6.2.4 Surface defects: Tip engineering and defect determination

The results presented in the previous subsections strongly support the identification of our scanning probe apices as hydrogen terminated. In every AFM image taken immediately following STM, our tips *always* produced inverted contrast images, indicative of a hydrogen passivated tip. Therefore it appears that the hydrogen passivated Si(100) surface routinely cultivates passivated tip structures in *both* STM and AFM modes of operation. In AFM it is well known that it is the outermost tip apex atom which dominates contrast formation and atomic manipulation. Therefore, although we reproducibly observe a single contrast in AFM, the larger tip apex structure may produce the variations observed in STM imaging.

In the previous section, in which I discussed the role of tip structure in atomic manipulation, one of the major findings suggested that specific tip types are required to perform certain manipulation tasks. The initial remit for our AFM experiments on Si(100):H was to investigate whether it is possible to desorb individual hydrogen atoms via chemical force alone. To achieve this goal a reactive tip apex is almost certainly necessary in order to overcome the Si-H surface bond strength. Consequently, our characterisation suggests that we are unable to desorb surface hydrogen without modification of the naturally passivated tip structure (see Figure 6.15(a)). Ideally, we require a situation which enables controlled depassivation of the tip apex as shown in Figure 6.15(b), producing images similar to those shown in Figure 6.14. This might be achievable, for instance, via transfer of the tip hydrogen to a surface dangling bond feature. In principle, our reactive tip might then be able to remove a hydrogen from the Si(100):H surface (Figure 6.15(c)), but only if the bond formed between the *tip* and hydrogen is strong enough to overcome that between the *surface* and hydrogen. This presents the first problem. The second problem arises if we then assume that the reactive tip succeeds in removing a hydrogen from the surface. If successful then the tip will return to the original state of being hydrogen

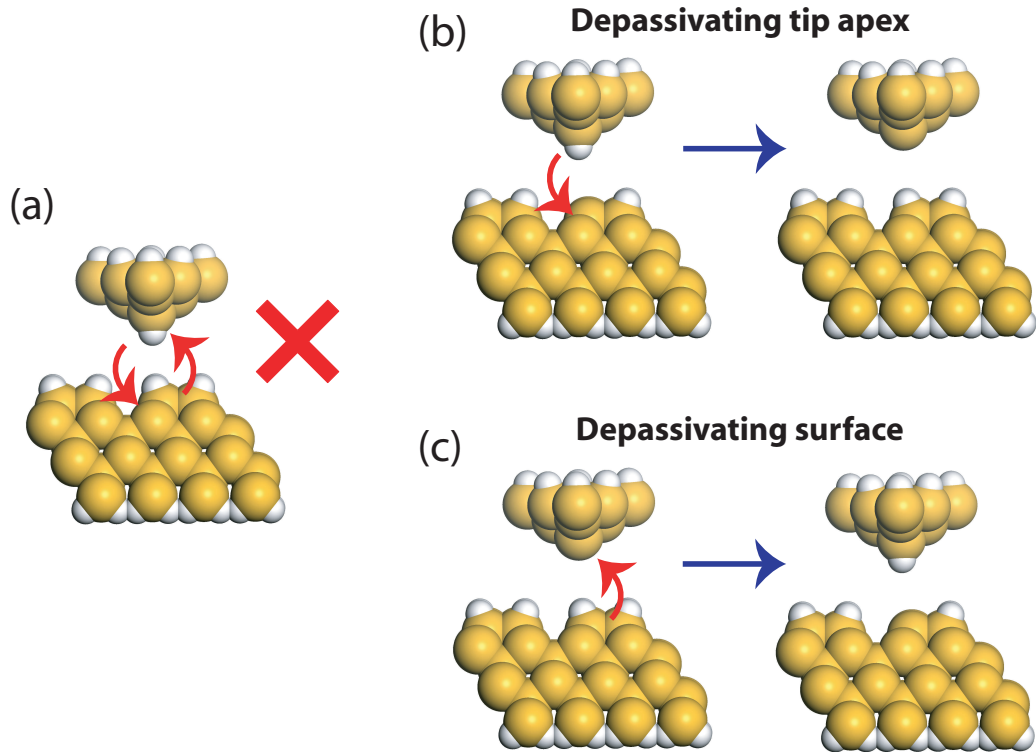


Figure 6.15: Schematics of AFM manipulation on Si(100):H. (a) Hydrogen tip - hydrogen surface, manipulation unable to take place. (b) Hydrogen tip - silicon surface, possible system for depassivating tip apex. (c) Silicon tip - hydrogen surface, possible system for depassivating surface.

passivated. Thus we once again require removal of the passivating hydrogen before surface desorption can continue.

The first problem arises from the theoretical simulations described in the beginning of this chapter. In that work it was discovered that only apices demonstrating particular features were able to transfer a tip-adsorbed hydrogen atom to the surface, or from the surface to the tip. Therefore, even if it is possible to obtain a reactive tip, only certain structures may be able to instigate surface desorption. The second problem is more critical. At low temperatures the type of manipulation described should be completely deterministic, as it relies on a competition between  $\text{Si}_{tip}\text{-H}$  and  $\text{Si}_{surface}\text{-H}$  bond energy. If the tip Si-H bond is weak enough that the hydrogen

is transferred to the surface, then it is also weak enough that it will be unable to compete with the surface Si-H bond, thus failing to instigate removal of surface hydrogen. Therefore it would seem that we cannot *both* de-passivate a tip whilst *also* using it for surface desorption. Consequently, unless more complicated modifications to the system are made (e.g. depositing material to form regions of more reactive surface, to act as a ‘rubbish dump’ for tip adsorbed hydrogen) reproducible surface desorption in AFM could be challenging, at best.

In fact, according to the simulations shown in Figure 6.11, when the surface is completely passivated, we find that even with a reactive H<sub>3</sub> apex, we are unable to remove surface hydrogen, suggesting that a completely passivated surface forms a stronger bond with the hydrogen than the tip. Although these results put the possibility of surface desorption into further doubt, it does suggest that tip de-passivation should be possible with a large number of apex structures.

### Dangling bond defects

We have seen that operating in the repulsive regime leads to reproducible, high-resolution images due to our well defined tip structure. It may be possible that our imaging mechanism is similar to the sub-molecular resolution obtained with CO terminated tips [28, 55]. As such, controllable tip de-passivation would offer an interesting opportunity to engineer our tips between a high-resolution, unreactive state, and unpassivated reactive configurations capable of manipulation (such as adsorbed atoms/molecules). To examine this possibility we attempted to image the reactive dangling bond features present on the Si(100):H - (2 × 1) surface.

In section 4.3.1 I discussed the presence of varied defect types on Si(100):H (also see Figure 6.6) which can be observed as bright features, similar to dangling bonds. To confidently identify DB features, constant current images were taken using bias voltages between 2 and 2.2 V such that dark depletion areas are clearly visible, a

distinct marker of DB defects [121, 122]. In Figure 6.16 we identify one such DB defect situated close to a single dimer vacancy (a). Constant  $\Delta f$  images were then acquired with (b) and without (c) an applied sample bias allowing simultaneous measurement of  $\Delta f$  and  $I_t$  (blue images).

Comparing our experimental and simulated results for reactive and unreactive tips on Si(100):H<sup>2</sup>, we find that our tip-sample separation is around 2.5-3.5Å and 1.5-2Å for Si-H and H-H interactions respectively, therefore the range for the reactive interaction is ~1-2Å more than for Si(100):H. The DB feature originates from an unpassivated silicon ~1.45Å below the hydrogen layer, therefore from this crude approximation, we expect to observe a small variation in  $\Delta f$  due to the DB in our images, corresponding to a bright feature in topography. This is clearly observed in the 0V AFM image shown in Figure 6.16(c), where the DB appears as a bright feature directly above the dimer vacancy. Although the DB appears as a bright feature, its magnitude is no greater than that for the DV. We attribute this to the suppression of the DB relative to the surface hydrogen layer, therefore both the DB and the DV appear less repulsive than the surrounding hydrogen atoms.

Upon application of a +1.2V sample bias, however, we observe the DB to appear as a dark suppression rather than the expected bright protrusion. Line profiles are shown below the topographic and  $I_t$  images illustrating the alignment of the tunnel current and AFM features. Cross-talk effects, both instrumental and physical, are well known to occur during simultaneous acquisition of force and  $I_t$  data. The typical interpretation requires a large tunnelling current to be present, however, in our measurements  $I_{t_{max}}$  is in the 10-20pA range, well below the magnitudes typically observed to cause interference. On highly doped n-type samples, such as the ones used in our experiments, it has been suggested that tunnelling electrons can enter the dangling bond orbital, increasing its charge state (see section 4.3.1 and

---

<sup>2</sup>If experimental  $F(z)$  spectra can be compared and aligned with simulated data, the tip-sample separation can be inferred from the simulated geometry.

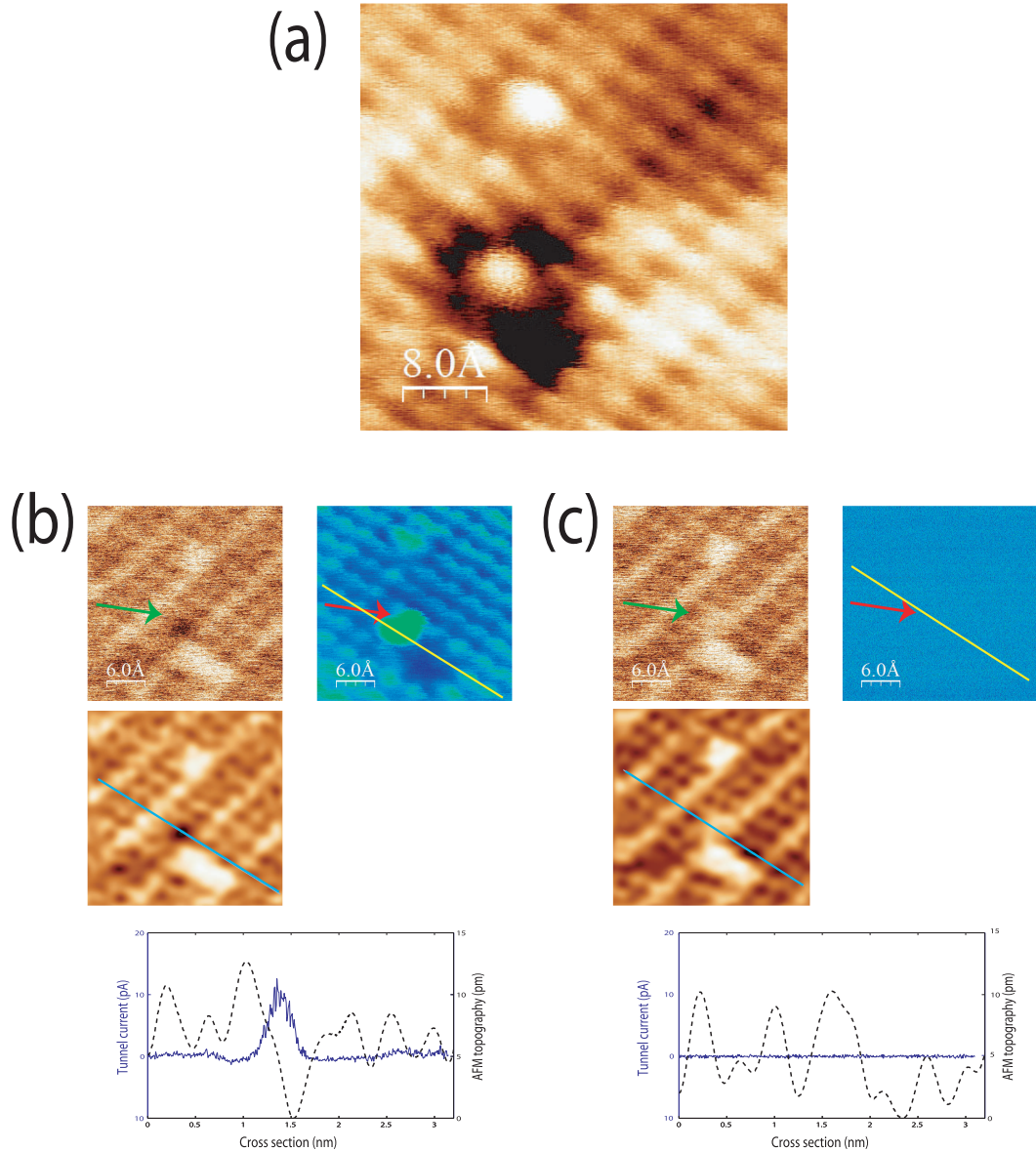


Figure 6.16: STM and AFM images of a DB defect. (a) Constant current image of the DB feature surrounded by a dark depletion region (acquired with +2V/100pA). Constant  $\Delta f$  AFM images taken (b) with and (c) without an applied sample bias of +1.2 V. (b) and (c) show constant  $\Delta f$  topography images with simultaneously acquired tunnel current. Below are low pass filtered constant  $\Delta f$  topography images with  $\Delta f$  and  $I_t$  line profiles, taken in the positions marked by solid lines. In (b) the  $\Delta f$  and  $I_t$  are slightly offset. Therefore, line profiles are taken in offset positions such that they both line up over equivalent dimers.

[122]. Such a mechanism, however, should lead to a stronger attractive interaction between the tip and DB feature and not the decrease observed in our experimental data. We therefore, as yet, have no conclusive explanation for these observations. Unfortunately, due to tip instabilities,  $\Delta f(z)$  data suitable for analysis was not obtained for the DB feature. The limited number of measurements that were taken, however, failed to instigate any modification of the tip apex. To properly examine whether it is possible to engineer the state of the AFM apex further experiments are required, in which a wider variety of tip structures can be tested.

### **Split-dimer defect**

In principle, the well defined nature of the AFM tip apex is perfect for characterisation of surface features, including surface defects. The high-resolution obtained from our AFM measurements can examine in detail some of the surface features observed on Si(100):H. Specifically we examined the split-dimer features often observed on the  $(2 \times 1)$  reconstruction. Thus far the split-dimer defect has remained a mystery, with experiments failing to agree on its structure (see section 4.3.). In principle AFM maps out the ‘true’ atomic structure of the surface, therefore it should be possible to directly observe the structure of the split-dimer defect. In Figure 6.17 AFM images of a split-dimer defect are shown following high resolution STM. Throughout our investigations we consistently found the split-dimer defect to appear ‘invisible’ in AFM. As shown in Figure 6.17(a), however, using the dimer vacancy defect as a marker, and after careful drift correction of our images, we find that the split dimer defect appears almost identical to a normal surface dimer, but with a slightly larger spacing between dark suppressions as shown in Figure 6.17(c).

A number of explanations for the split-dimer defect have previously been put forward, including clusters [112] and dihydride structures [114]. Our data, and the image in Figure 6.17(a) suggests that the split-dimer defect, at the surface layer,

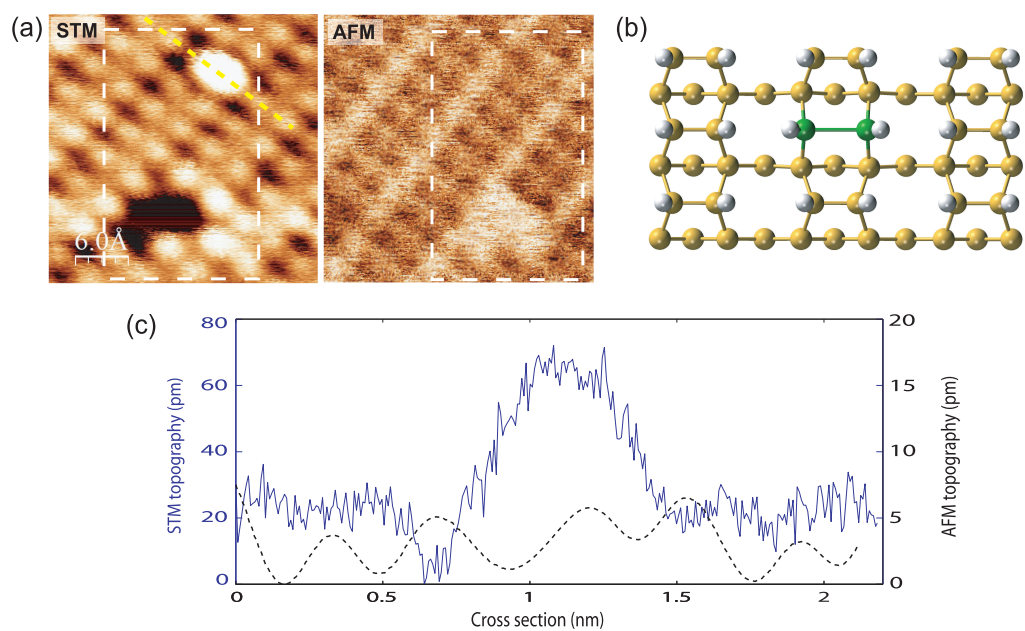


Figure 6.17: (a) Before and after STM and AFM images of a split-dimer defect shown with a dimer vacancy acting as a convenient marker. The split-dimer, marked with an arrow, appears as a slightly wider features, very similar to the surrounding surface dimers. Measurement of atomic separations suggest that the split-dimer may originate from a contamination increasing the bond length of the dimer. (c) Line profiles of STM and AFM topography taken across the split-dimer defect.

consists of singly passivated atoms, very similar to the surrounding hydrogen terminated dimers. It is expected that with the passivated tip termination, dihydride, and more complicated adsorbate structures should be easily distinguishable from the monohydride ( $2 \times 1$ ). This result is supported by the investigation from Bellec *et al.* [112] which showed that dihydride structures could not explain the split-dimer, as they had already convincingly attributed dihydride structures to another defect. On average, in this particular image, we calculate the atom-atom spacing along a single dimer to be  $0.33 \pm 0.02$  nm, whereas the split-dimer distance is measured to be  $0.44 \pm 0.02$  nm, over three standard deviations larger than the normal dimers. Therefore we measure a 30% increase in the distance between hydrogen atoms. If parallels are drawn between the split-dimer defect and the Si-Si bond length in a normal surface dimers( $\sim 2.43$  Å), the increased separation corresponds to a bond length of  $\sim 3.24$  Å. It is therefore suggested that the split-dimer feature might possibly originate from subsurface defects, such as a non-silicon dimer (Figure 6.17(b)), perhaps introduced during the preparation of our surfaces. Alternatively, a subsurface defect may be present that introduces strain directly beneath a Si-Si dimer, extending the bond length and affecting the local density of states. To conclusively rule out dihydride or other multi-atom structures, however, experiments first need to be carried out on the ( $3 \times 1$ ) reconstruction to characterise their appearance.

Throughout this chapter we have repeatedly demonstrated the critically important role that tip structure plays in both image acquisition and atomic manipulation in AFM. We conclude that passivated tip structures dominate on the Si(100):H surface and that a complicated competition between tip and surface reactivity determines the potential for manipulation. We suggest that it may be possible to engineer the tip, switching from an unreactive to reactive state by exploiting surface dangling bond defects. This could potentially allow a controllable selection of tip-tools to obtain both very high-resolution image acquisition and chemical manip-

ulation. In principle, the well defined passivated tip apex is ideal for characterisation of surface defects. The preliminary results shown at the end of this chapter suggest that novel information can be obtained regarding the thus far unknown structure of the split-dimer defect.

## Chapter 7

# Analysing tip structure and molecular functionalisation

In chapter 5 I described a series of experiments conducted on the Si(100) surface, in which we examined mechanical ‘dimer flipping’ with an AFM probe, concentrating on the manipulation of the surface dimers. In that chapter I explored both the effect of the scanning probe, and extensively investigated the role of surface defects on manipulation. The following chapter focussed on the AFM tip structure, and examined methods to engineer the tip apex within a silicon-hydrogen environment.

In this chapter I continue to examine AFM tip processes with *ab initio* simulations. Characterisation of the AFM probe is approached from two perspectives: first, I examine the stability of silicon tip clusters and simulate typical methods to improve their structure, alternatively the unknown tip structure can be replaced entirely with one that is well defined via functionalisation of the AFM probe with a C<sub>60</sub> molecule. Molecular functionalisation of the AFM probe not only allows us to avoid the uncertainties associated with unknown silicon tip structures, but also allows exciting experiments to be carried out which reveal the submolecular structure of the C<sub>60</sub> molecule. The work relating to on-tip C<sub>60</sub> molecules has been published

in *Phys. Rev. Lett.*, **108**, 268302 (2012). All simulated results were obtained by the author. The experimental C<sub>60</sub> results were obtained by others, and are highlighted where appropriate.

## 7.1 Structural development of silicon tip apices

In the first half of this chapter we examine the stability of silicon tip apices and find that some structures (even in small, simple tips) are unstable when used for manipulation. Moreover we observe that unstable structures can be revealed from characteristic hysteretic behaviour present in calculated  $F(z)$  data. To examine the structural evolution of the tip within a low temperature DFM experiment, we simulated repeated tip-surface indentation until the tip structure converged to a stable termination and the characteristic hysteretic behaviour was no longer observed.

The structures considered in this study, and the characterisation process are illustrated in Figure 7.1. The three tip structures considered, and a ball-and-stick model of the Si(100)-c(4×2) surface are shown in (a). We once again consider the H<sub>3</sub> and dimerised silicon tip clusters. The dimerised tip, however, can be modified by removing a stabilising atom from one side which we label a D<sub>2</sub> tip (a). Although the apex structure is not significantly altered, removal of the stabilising atom leads to a noticeable increase in structural rearrangements during simulated spectroscopy. In the previous chapter, I suggested that  $F(z)$  measurements can be used to characterise tip structure via examination of the energy dissipation during dimer manipulation. A similar method is implemented in this work to assess the evolving structure of tip D<sub>2</sub>. Rather than laterally offsetting the tip between dimer rows, however, the tips are rotated through 360° around the surface normal axis, either positioned above the down atom, or up atom of a surface dimer.  $F(z)$  measurements are then calculated at four tip-surface alignments (see Figure 7.1(b)). This procedure is used not only as a theoretical assessment of tip stability, but also highlights that the rotational

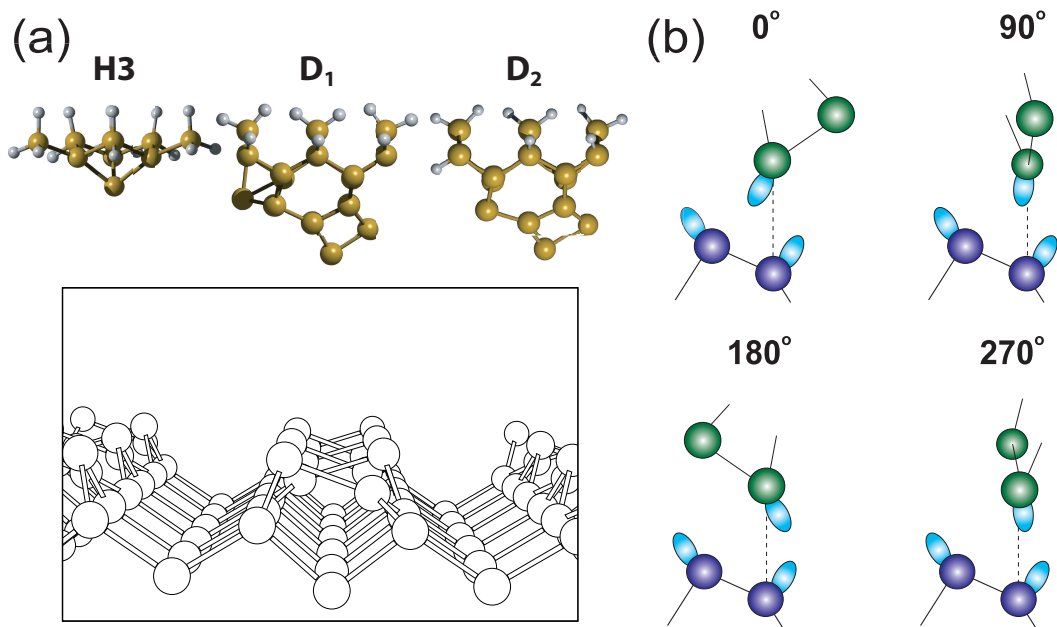


Figure 7.1: The three tip structures considered are a structurally rigid ‘H3’ termination, and two dimer terminated tips shown in (a). D<sub>1</sub> is relaxed with an additional stabilising atom as compared to D<sub>2</sub>. (b)  $F(z)$  measurements are calculated for four rotations of the tips with respect to the surface dimers. Note that due to the symmetry of the surface 90° and 270° are the same, but are still calculated independently.

alignment of the tip relative to the surface, in some cases, can dramatically affect the chances of major structural rearrangement.

Tip orientation is rarely considered in theoretical work because of the high computational cost of running multiple simulations. Therefore results are generally only presented for tip structures at a single position, even though modifying the tip-surface alignment can also strongly affect calculated  $F(z)$  curves and the hysteresis pathways followed by the tip and surface structures. For instance, the bulk like rear structure of tip apices are almost always aligned parallel to the surface for convenience when designing the tip structure. There is no reason to expect, however, that the experimental tip apex will follow the same rules. Therefore it is clear that our theoretical simulations are constrained by the huge number of possible orientations

a single tip apex can adopt relative to *any* surface, even surfaces with perfectly symmetric dangling bond protrusions. We demonstrate that even when varying just a single rotational degree of freedom, the difference in tip-surface interactions are as significant as for a completely different tip structure.

Interestingly, we observe that the structurally ‘weak’ D<sub>2</sub> tip, prior to development, demonstrates significant hysteresis in  $F(z)$  measurements taken over rigid surface sites, such as the up surface dimer, indicating a significant level of tip dominated energy dissipation. Although similar observations have previously been reported [54], the study required large and complicated tip structures to represent the experimental scanning probe. In the current work only small apices are considered, to enable a complete DFT treatment of the system. Therefore it would seem that even in very small structures, tip-dependent hysteresis can occur, further confirming the likelihood that tip structure can play a dominant role in many experimental dissipation observations.

### 7.1.1 Energy dissipation in small apex clusters

Presented in Figure 7.2 are simulated  $F(z)$  curves taken with the H3 (a) and D<sub>1</sub> (b) tips positioned above the up (green and black triangles) and down (red and blue circles) atoms of a surface Si(100) dimer.

Even though the tip-surface alignment of the D<sub>1</sub> apex varies upon rotation around the surface normal axis, its structure is very stable and we observe minimal variation in the simulated  $F(z)$  curves. A small deviation is calculated only when the tip is rotated to the position we define as 180 ° (see Figure 7.1(b)), where *both* of the atoms within the tip and surface dimers are able to interact with each other. More interesting behaviour arises when we carry out the same simulations with the D<sub>2</sub> apex shown in Figure 7.3. In this case a significant increase in energy dissipation (over a single cycle) is calculated for the down atom position of the tip

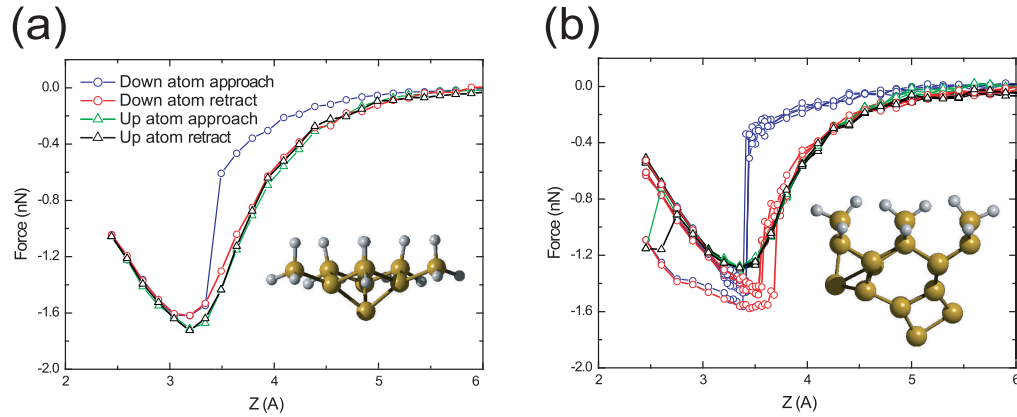


Figure 7.2: Simulated  $F(z)$  curves for the (a) H3 and (b) D<sub>1</sub> tip structures taken above the up (green and black triangles) and down (red and blue circles) atoms of a surface Si(100) dimer. These tips show very little variation upon rotation around the surface normal axis. The H3 tip contains a symmetric apex and does not produce variation when rotated, therefore only a single rotation is shown.

(red and blue circles) amounting to an average 74% increase, from 0.39eV to 0.68 eV relative to the more stable D<sub>1</sub> cluster. The increase in hysteresis corresponds to additional tip deformations throughout the simulated  $F(z)$  measurement. For the D<sub>2</sub> tip, even though a significant level of dissipation is observed in the down atom position(a typical indicator of dimer manipulation [178, 179]), the dimer, part way through the flipping process, in fact returns to its original state. This is noticeable as a sharp decrease in force during the retract curve. For successful manipulation, the target down atom of the dimer must be ‘pulled’ high enough such that the up and down atoms trade places, switching the dimer buckling angle. The tip-dimer interaction for the D<sub>2</sub> tip, therefore, is not quite sufficient to pull the down atom high enough to instigate manipulation.

Particularly interesting observations are made when the D<sub>2</sub> tip is positioned above the structurally rigid up atom of the Si(100) dimer. Even though the surface atom remains mostly stationary throughout the  $F(z)$  measurement, a significant level of energy dissipation is calculated, amounting to 0.17 eV over a single cycle.

The calculated  $F(z)$  curves taken above the up Si(100) dimer atom are shown in Figure 7.3 (approach - green triangles, retract - black triangles). Ball-and-stick snap shots, at the positions marked in Figure 7.3(b), are shown in (d-f) within and after the region of hysteresis. Although the surface dimer remains in the same position, it is clear that the D<sub>2</sub> tip undergoes significant deformation, pulling the apex downwards into a narrower shape. The geometry shown in Figure 7.3(f) is taken at the same  $z$  position as (d), during retraction from the surface. From the calculated geometries we can see that the tip structure in (d) and (f) differ, thus modifying the tip-surface interaction leading to the observed hysteresis. This theoretical result, is extremely similar to experimental observations on the Si(100) surface which recorded dissipation of up to 0.5 eV/cycle [170] for a tip demonstrating “dimer-tip” type atomic resolution [186, 187].

This result has significant implications for understanding the origin of experimental dissipation observations. Unlike the hysteresis observed for the down atom position (occurring over the single oscillation cycle when dimer manipulation takes place), *all* oscillation cycles where the point of closest approach falls below 3.5 Å will demonstrate hysteresis. Thus tip-dependent dissipation, with the D<sub>2</sub> tip, should be noticeable on *any* surface. It has already been established that tip-dependent dissipation is a ubiquitous mechanism [54]. That study, however, required large structures to better model the complicated experimental tip termination. Here we show that even very simple, small tip clusters can cause a significant level of dissipation.

### 7.1.2 Enhancing tip stability via surface indentation

Examination of the tip geometries in our simulations suggest that the increase in  $F(z)$  hysteresis is driven by significant structural rearrangement. The weakly bound configuration of the D<sub>2</sub> tip provides alternative structural pathways during approach

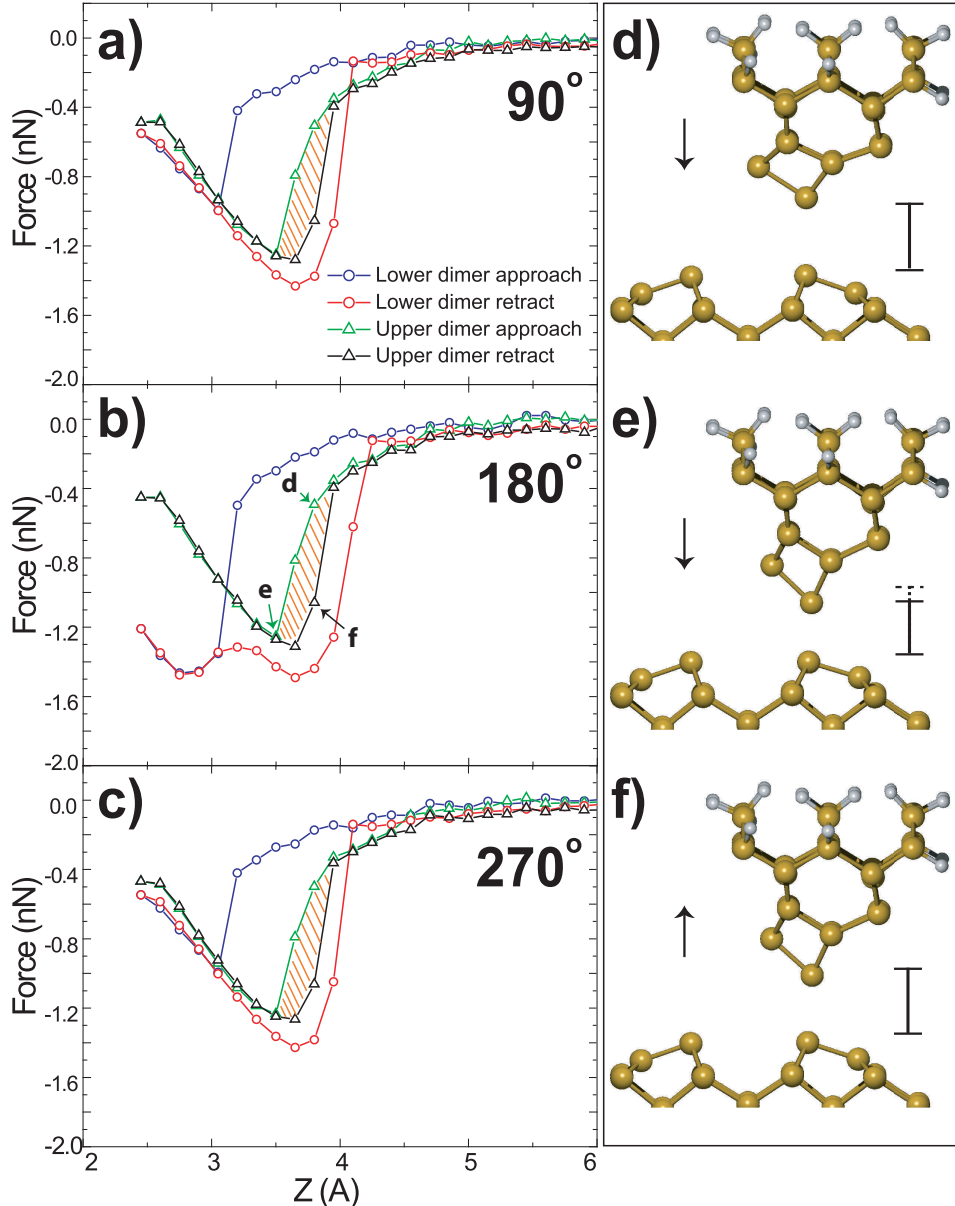


Figure 7.3: Simulated  $F(z)$  curves for the  $D_2$  tip at rotations (a)  $90^\circ$  (b)  $180^\circ$  and (c)  $270^\circ$ . Energy dissipation is significantly increased, and critically is also observed for the up atom site. Ball-and-stick snap shots are shown (d) within and (e) after the region of hysteresis shown in (b) during tip approach. (f) shows a ball-and-stick snap shot during retract at the same position as (d), illustrating the alternative structural pathway taken by the tip, thus causing the observed hysteresis.

and retract. Clusters demonstrating greater stability do not allow the atomic rearrangements required for the additional hysteresis. Therefore, in some instances, the presence of tip-hysteresis may act as an identifier for potentially unstable configurations. In Figure 7.4 we show one such instance, where the D<sub>2</sub> tip, although stable for the simulations in the previous figure, undergoes major structural rearrangement when aligned at ‘0 °’. The calculated  $F(z)$  curve at this position is shown in Figure 7.4(a), in which two sharp jumps in force are present during retraction of the tip. Shown in (b-e) are geometries illustrating the major stages of tip rearrangement. Initially the tip configuration is as shown in (b), then the D<sub>2</sub> tip forms a strong bond with the Si(100) surface dimer in (c), resulting in similar deformations to those already shown in Figure 7.3. Upon retraction of the tip, however, the strong surface bond introduces significant strain to the tip structure, developing it into a much sharper configuration relative to the initial D<sub>2</sub> apex. Partial electron density maps, highlighting the dangling bond orbitals, are shown for the original D<sub>2</sub> tip (f) and the sharpened structure (g) which we term D<sub>2a</sub>. Simple examination of the electron density plot reveals that the tip structure maintains a single prominent dangling bond orbital at its apex, which in principle should produce atomic resolution.

Experimentally, during  $\Delta f(z)$  measurements or tip indentations carried out specifically to modify the apex, the scanning tip is constantly oscillating at a rate of kHz, often with an amplitude larger than the silicon interaction potential. Therefore, as the average  $z$  position is ramped towards the sample, the tip will undergo multiple cycles of approach and retract. As a result, any structural development of the tip apex must occur over multiple approach-retract cycles, until a stable configuration is obtained that no longer reconstructs. To properly reflect this process, DFT  $F(z)$  calculations were continued using the D<sub>2a</sub> tip without any modification of the system. Upon continuation we observe two further stages of structural development until a final stable configuration is reached. We term these two tips D<sub>2b</sub> and D<sub>2c</sub>.

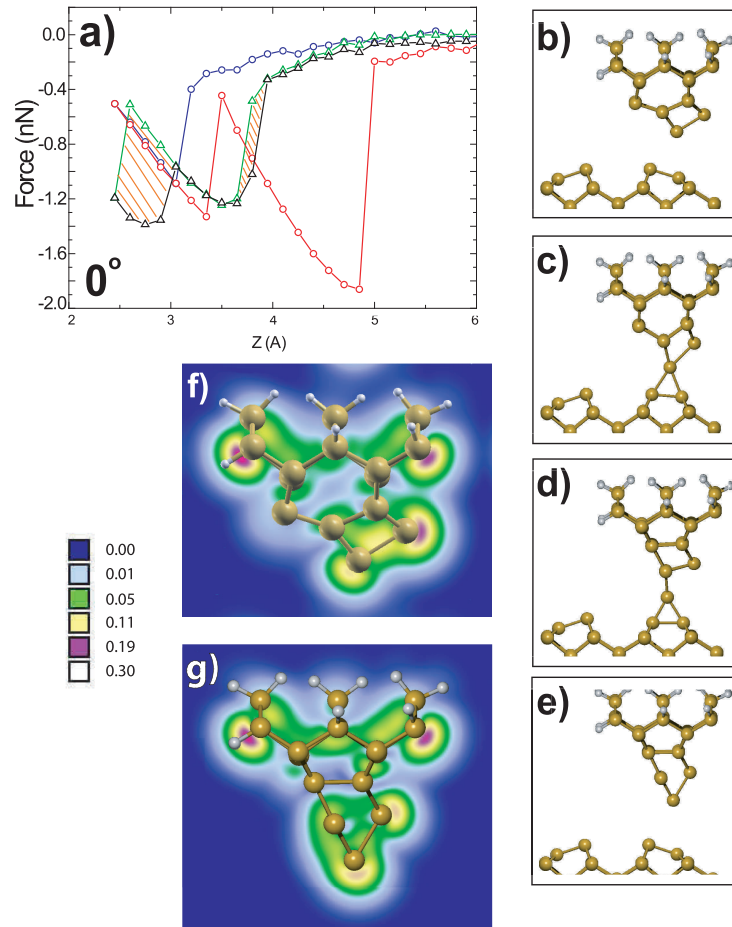


Figure 7.4: Structural development via tip indentation. (a) Calculated  $F(z)$  approach and retract curves for the  $D_2$  tip at ‘ $0^\circ$ ’ positioned above down (red and blue circles) and up (green and black triangles) surface dimer atoms. Calculation positioned above down atom leads to structural rearrangement of the tip, noticed as a discontinuities in the retract curve at  $\sim 3.5\text{\AA}$  and  $\sim 5\text{\AA}$ . Ball-and-stick model in (b) depicts starting configuration of tip during approach, followed by the major stages in tip rearrangement during retract (c-e). Electron density plots of (f) initial and (g) final tip ( $D_{2a}$ ) configurations.

and show the respective  $F(z)$  curves leading to their development in Figure 7.5.

For the  $D_{2a}$  to  $D_{2b}$  transition shown in Figure 7.5(a), a significant number of atomic rearrangements occur, visible as rapid variations in the retract curve. In fact, the tip not only undergoes significant rearrangement, but actually deposits an atom onto the Si(100) surface. Material deposition is commonly observed during experimental imaging and spectroscopy, sometimes leading to improvements in image resolution, or often leading to instabilities and deterioration of image quality. The partial electron density plot in (b) illustrates the apex dangling bond structure of tip  $D_{2b}$ , which appears to protrude at a large angle relative to the surface normal. This structure would likely lead to a complicated tip-surface interaction [170].

To test the stability of the  $D_{2b}$  tip a further calculation was carried out, just as for the  $D_{2a}$  structure, resulting in the  $F(z)$  curve shown in Figure 7.5(c). For the  $D_{2b}$  to  $D_{2c}$  transition, extreme features are observed both in the approach and retract sections of the calculated  $F(z)$  due to the complicated interaction between the tip and the newly deposited silicon adatom. Although the  $F(z)$  data suggests a complicated rearrangement of the tip structure, most of the features actually originate from movement of the surface adatom. The  $D_{2c}$  tip structure is shown in Figure 7.5(d) and (e) displayed from two perpendicular perspectives. This final tip configuration is found to be stable upon continued spectroscopy, suggesting that the tip apex is fully structurally developed. Interestingly, we find that the stable tip terminates in a dimer like structure, with each terminating atom located at very similar  $z$  positions. Each ‘dimer’ atom is associated with a dangling bond protruding in the  $-z$  direction, angled away from one another as shown in Figure 7.5(e). The cluster appears to be more crystalline than its predecessors, perhaps explaining the dimer termination due to the (100) orientation of the base structure. It is interesting to note that a dimer terminated tip such as this might be able to produce double-lobed surface features, doubling effects, or even fail to produce a well separated,

understandable signal altogether. Such observations would depend on the surface under study, and the separation of the surface atoms which can be a particularly challenging problem when obtaining atomic resolution [188].

The simulated results in this section provide interesting insights into the atomic rearrangements taking place during well known, and commonly observed experimental processes. We examined the role that alternative structural pathways play during spectroscopy measurements, which might lead to tip dominated dissipation observations, similar to previous suggestions [54]. Critically, however, our observations are made using the small, simple tip clusters required for a full DFT treatment of the system, rather than the larger, more complicated, structures that must exist experimentally. Therefore, if dissipation can be observed for clusters of this size, it is very reasonable to expect that the same processes can occur in much larger experimental systems, suggesting that tip structure could play a dominant role in many experimental dissipation observations.

We also show that tip apices demonstrating hysteretic behaviour may be inherently unstable during  $F(z)$  measurements, or soft tip indentations, leading to major structural redevelopment of the tip apex. In our specific example, we show that a tip which may appear to be structurally stable at certain orientations with respect to the surface, might interact completely differently at another position. We suggest, therefore, that examination of tip orientation may be just as valuable as testing entirely new structures when making experimental comparisons. We expect that these results might apply not only for rotation around the  $z$  axis (as studied here) but also the  $x$  and  $y$  axes not considered in this study. We also propose a method for developing tip structures, similar to experimental approaches, via repeated soft indentation into the surface until alternative stable structures are obtained. Such an approach might be particularly useful to build up a library of theoretical tip structures, which could assist the interpretation of experimental observations [170].

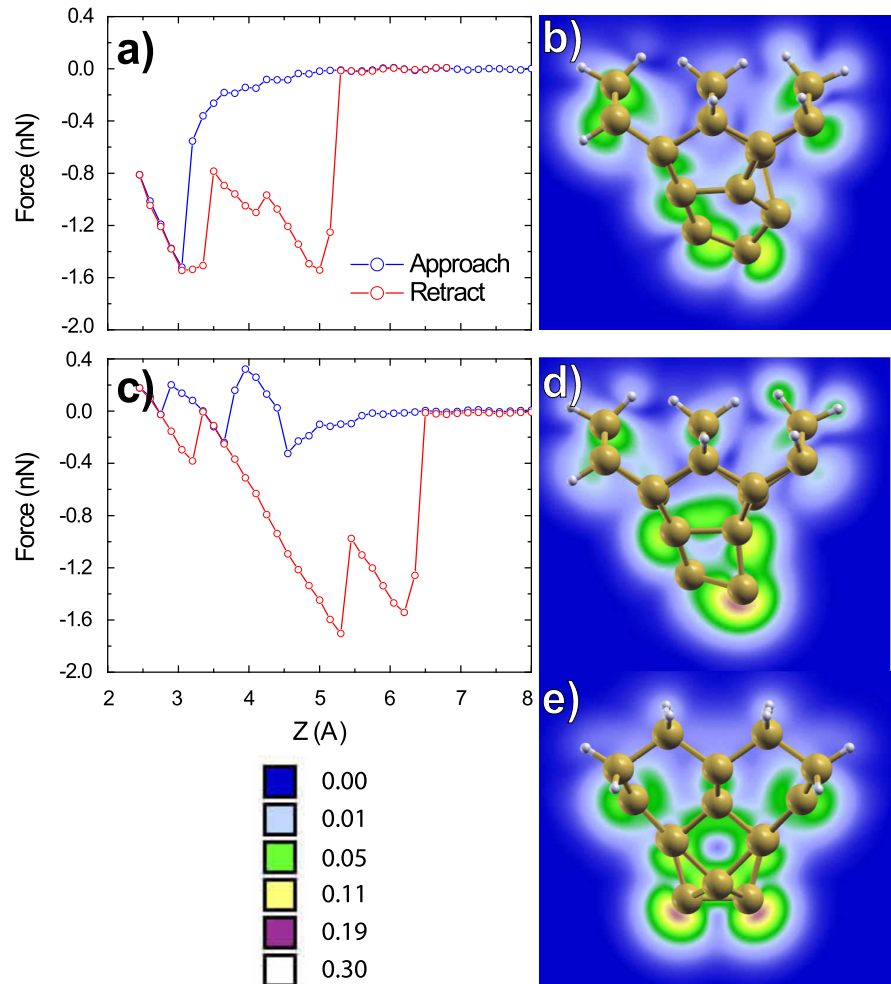


Figure 7.5: Continued development of tip D<sub>2a</sub> via repeated tip indentations. (a) Calculated  $F(z)$  curve and (b) final tip configuration following indentation of the tip structure shown in Figure 7.4(g) leading to tip D<sub>2b</sub>. (c) Indentation of tip D<sub>2b</sub> results in further modification noticeable as a series of sharp discontinuities in calculated  $F(z)$  prior to reaching a final, stable double tip shown from two perspectives in (d-e).

## 7.2 Molecular C<sub>60</sub> tip functionalisation

In the previous section I continued to discuss the structure of tip apices typically found in silicon systems. The main motivation of the work was to investigate the structure and stability of silicon tip clusters with DFT, in a way that could be linked to experimental observations. The more our DFT theory can be linked to experiment, the better our understanding will be of the otherwise unknown tip structure. In Chapter 6 we considered the Si(100):H system where we discovered a naturally occurring hydrogen passivated tip structure. The H-terminated tip appeared to be extremely reproducible, thus allowing us to confidently characterise our tip structure and design experiments to exploit its passivated nature. In this section I discuss the approach of molecular-tip-functionalisation, pioneered by Gross *et al.* [28, 55] using CO, Cl and pentacene terminated tips and Schull *et al.* [150] with C<sub>60</sub> molecules.

The major benefit provided by tip-functionalisation is the huge reduction in uncertainty associated with the tip structure, i.e. we know that we have a molecule terminating our tip. This procedure opens up the possibility for unique experiments that can only be carried out by picking up the molecule. In our case, we functionalise our tips with C<sub>60</sub> molecules deposited onto the Si(111)-(7×7) surface. By exploiting the ‘reverse imaging’ technique, pioneered by Giessibl *et al.* [25, 29, 189], we are able to deduce the orientation of the C<sub>60</sub> molecule on our tip with respect to the surface, attaining sub-molecular resolution in the *attractive regime*. In the following section I give a brief review of the experimental AFM results (obtained by Adam Sweetman, Andrew Stannard, Philip Moriarty and Cristina Chiutu), before describing in more detail *ab initio* DFT calculations aimed at understanding the origin for the sub-molecular resolution. All results presented in this section have been published in *Phys. Rev. Lett.*, **108**, 268302 (2012).

### 7.2.1 Sub-molecular resolution in the attractive regime

Experiments were performed on the Si(111)-(7 × 7) surface, using a sub-mono layer coverage of C<sub>60</sub> molecules. The low surface coverage of C<sub>60</sub> enabled careful examination of the tip-adsorbed molecule in clean surface regions, without uncontrolled interference from other fullerenes. A single molecule could be transferred to the tip in a number of ways, including with  $I(z)$  or  $\Delta f(z)$  spectroscopy taken directly above a molecule, or more commonly by crashing into the molecule during high-speed, low feedback (and high current) STM imaging. Upon transfer of the molecule, clear discontinuities are observed in the image, often followed by a distinct change in contrast relating to the C<sub>60</sub> tip structure.

Once the molecule has been picked up by the tip, depending on its orientation, the apparent shape of the (7 × 7) adatoms are observed to change in constant current operation. The STM resolution observed is related to the molecular orbital structure of the C<sub>60</sub>, and does not provide direct atomic resolution of the molecule (although its orientation can be inferred from theoretical simulations [190]). In the constant  $\Delta f$  mode of operation, however, we appeared to directly observe the sub-molecular atomic structure of the C<sub>60</sub> molecule. The Si(111)-(7 × 7) adatoms can be thought of as an array of inverted tips, able to image the C<sub>60</sub> molecule attached to the scanning tip. The relatively large separation, and narrow spatial extent of the Si(111)-(7 × 7) adatoms can thus be exploited to “reverse image” [25, 29, 189] the tip state (Figure 7.6(a)).

Two example images, taken at 0V applied bias in constant  $\Delta f$  operation are shown in Figure 7.6 where we can clearly observe a double lobe (b) and pentagon-lobed (c) structure, repeated for each adatom of the surface unit cell. Due to the five-fold symmetry of the pentagon structure, and the appearance of the preceding STM images (not shown), it is extremely likely that these features originate from the pentagonal face of the C<sub>60</sub> molecule. Interestingly, some of the lobes appear

to be brighter than others, suggesting a ‘tilt’ of the tip-adsorbed molecule relative to the surface. The unique appearance of the surface adatoms makes it difficult to attribute other reasonable structures, such as a silicon- or contaminant-terminated tip, to the observed resolution. An alternative image contrast is the double lobe structure shown in (b). Due to the symmetry of the lobes we suggest that these observations originate from a single C-C or C=C bond pointing downwards towards the surface. Although we cannot discern whether the contrast originates from a C-C or C=C bond from the FM-AFM data alone, comparison of the preceding dynamic STM data(unless the resolution spontaneously appeared during FM-AFM imaging) with theoretical calculations can be used.

From the experimental data, we are extremely confident that the observed FM-AFM resolution originates from tip-adsorbed C<sub>60</sub> molecules. The origin of the intramolecular atomic contrast is, however, not immediately clear. To understand the origins of the resolution we obtain, experimental  $F(z)$  measurements were carried out and compared with detailed DFT simulations.

### 7.2.2 Modelling the C<sub>60</sub>-Si(111)-(7 × 7) system with DFT

Describing the combined Si(111)-(7 × 7) surface and on-tip C<sub>60</sub> system is computationally challenging due to the large size of both the unit cell and the C<sub>60</sub> molecule. The very many possible bonding configurations of the C<sub>60</sub> to the AFM tip also presents a significant problem. To simplify the theoretical system some approximations were made (following a number of checks to ensure that the results were not strongly affected). First, the AFM tip was considered to be a single isolated C<sub>60</sub> molecule. In a real experimental system the C<sub>60</sub> will be bonded to the scanning probe in some way that may perturb the cage structure. In our case this “back-bonding” could be either to a tungsten, or most likely silicon coated, tip (or even to a larger C<sub>60</sub> cluster formed at the apex of the probe). Modelling the many possible config-

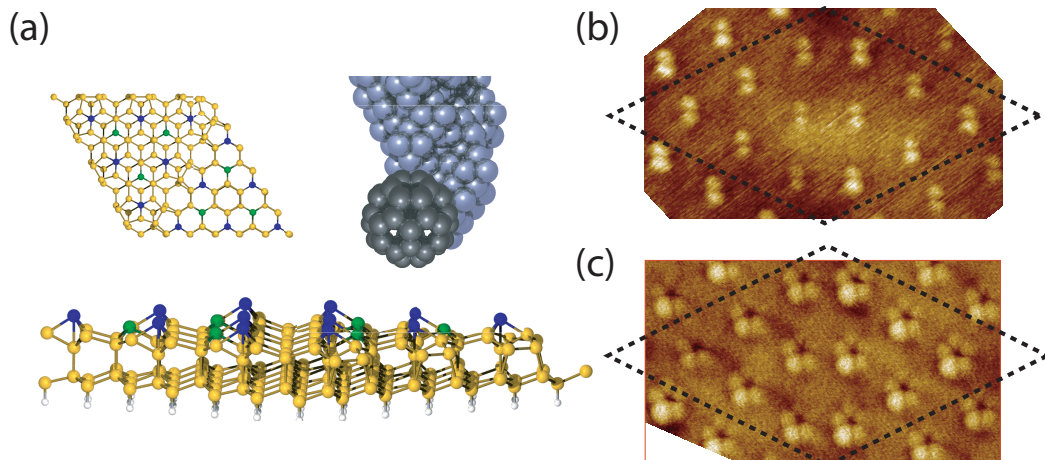


Figure 7.6: Sub-molecular resolution of C<sub>60</sub> in the attractive regime. The scheme of experiments is shown in (a), in which a tip-adsorbed C<sub>60</sub> molecule is used to scan the Si(111)-(7 × 7) surface in constant  $\Delta f$  feedback. The localised spatial extent of the surface dangling bond images the molecular structure of the C<sub>60</sub> molecule revealing (b) double lobe and (c) pentagon lobe structures thought to correspond to a single C-C bond, and the pentagon face of the molecule. Features appear as bright maxima, suggesting chemical bond formation. (b) Data acquired with  $a_0=2\text{\AA}$  and a  $\Delta f$  setpoint of -46 Hz and (c) with  $a_0=2\text{\AA}$  and  $\Delta f= -22.3$  Hz. Experimental images courtesy of Philip Moriarty and Andrew Stannard.

urations available would be very computationally expensive due to the large size of the parameter space that must be explored. However, the precise bonding configuration at the “base” of the tip-adsorbed C<sub>60</sub> molecule is unlikely to strongly affect the fundamental interactions and imaging mechanism giving rise to sub-molecular contrast in FM-AFM. This supposition is supported by the calculations described below.

To model the adsorption of the C<sub>60</sub> molecule on an AFM tip and to simulate  $F(z)$  measurements for the different possible orientations of the molecule, some portion of the C<sub>60</sub> molecule must be constrained. We chose three primary orientations for study: pentagon-face-down, hexagon-face-down and double-bond-down. For the pentagon-down orientation, the rear pentagon atoms of the C<sub>60</sub> molecule were fixed. For the hexagon-down orientation the atoms corresponding to the hexagon on the opposite side of the cage are fixed. For the double bond-down orientation the two hexagons surrounding double bond located on the opposite side of the cage are constrained. This offers a greater degree of flexibility of the C<sub>60</sub> cage than more stringent constraints (discussed later) might.

In order to model the Si(111)-7x7 surface the full 7x7 reconstruction was simulated using a 3-layer slab [143]. Hydrogen atoms were used to terminate the silicon bonds on the lower side of the slab, which were kept fixed, along with the bottom layer of silicon, to simulate the missing bulk. This provides the minimum slab thickness to accurately describe the dimer-adatom-stacking fault model thus producing a system of 309 atoms (Figure 7.7(a)). Even with implementation of the fast SIESTA atomic orbital code the calculation of such a large system requires a great deal of computing time. To explore the multiple orientations of the C<sub>60</sub> on-tip molecules and their interaction with the surface on a practical time-scale, an approximation to the Si(111)-7x7 adatom was made. This is the small ten-atom H3 silicon cluster shown in Figure 7.7(b), as already described in previous chapters. The cluster

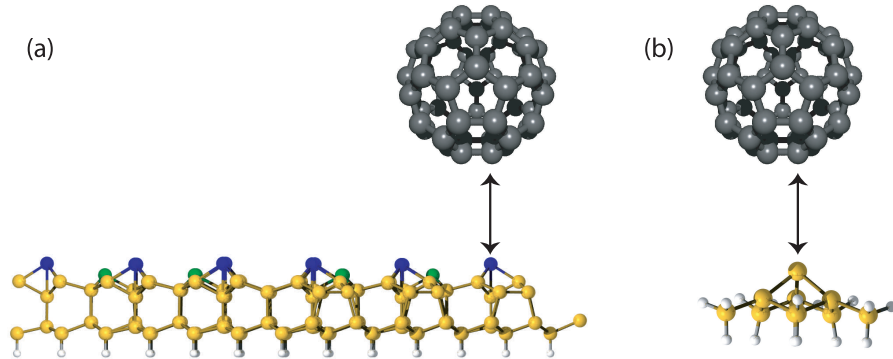


Figure 7.7: Simulated systems considered in the DFT study. (a) A complete Si(111)-(7×7) unit cell three silicon layers thick. The adatoms of the cell are shown in blue, and the rest atoms in green for clarity. (b) The silicon H3 cluster used to approximate an adatom of the Si(111)-(7×7) surface.

is made up of ten silicon atoms in a similar local configuration to the 7x7 adatom structure and have previously been used to model a 7x7 adatom [40,41]. The bottom layer of the silicon cluster is constrained, along with a passivating layer of hydrogens, to act as the fixed bulk. This leaves four silicon atoms free to relax, simulating a surface adatom.

Similar to the convention applied during the previous chapters, it is important to note that for all simulated  $F(z)$  spectra the vertical distance  $z$  is defined as the distance between the surface plane measured by the vertical position of the surface adatom and the target C<sub>60</sub> atom for spectroscopy prior to relaxation (surface molecule distance,  $D_{SM}$ ). Thus, at close C<sub>60</sub>-surface separations where deformations take place within the molecule, the vertical distance  $D_{SM}$  will be different to the C-Si atomic separation.

### 7.2.3 Origin of sub-molecular C<sub>60</sub> resolution

To obtain simulated  $F(z)$  curves, a C<sub>60</sub> molecule representing the AFM tip apex was initially positioned at a vertical distance of 7 Å above the approximated Si(111) adatom surface. The C<sub>60</sub> was positioned such that the different faces of the molecule

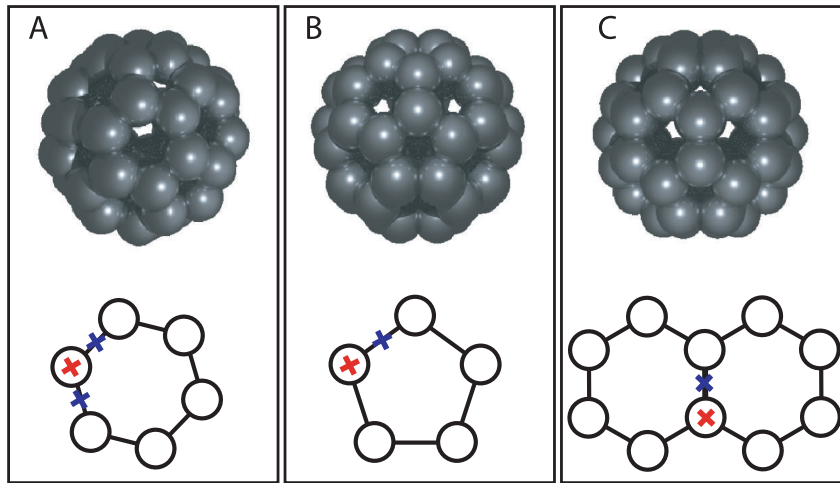


Figure 7.8: Diagram depicting the different orientations of the C<sub>60</sub> molecule considered in our DFT calculations. (a) The hexagonal face of the C<sub>60</sub> molecule prone to the surface, where spectra were taken directly positioned over a carbon atom (**HA**), a C-C single bond(**HB**<sub>s</sub>), and a C=C double bond(**HB**<sub>d</sub>); (b) The pentagonal face of the C<sub>60</sub> molecule prone to the surface, where spectra were taken centred over a carbon atom (**PA**) and directly over a C-C single bond(**PB**); and (c) a C=C double bond-prone orientation where spectra were also taken over the carbon atom(**DA**), and C=C double bond(**DB**). This orientation is additionally considered in order to observe how deformations within the C<sub>60</sub> cage might differ.

were aligned with the surface plane in different orientations such as hexagon-down(a), pentagon-down(b) or double bond-down(c). These different faces are shown in Figure 7.8. The adatom of the silicon cluster was then either centred directly beneath a C<sub>60</sub> atom, or between atoms such that it is centred on a bond, and was done so for each orientation of the molecule, diagrams are shown in Figure 7.8 along with an explanation of our site-labelling. The tip was then moved in quasi-static steps approaching the surface to just beyond the force turning point, and then retracted in the same way. At each step the geometry of the system was optimised until the forces on the non-fixed surface and tip atoms were no larger than 0.01eV/Å. At each point the vertical forces acting on the fixed C<sub>60</sub> atoms were summed up to give the total force acting on the simulated tip.

From the experimental data alone it is unclear which interactions are responsible

for the image formation in the zero bias nc-AFM mode of operation. As previously mentioned, the sub-molecular contrast appears as bright protrusions in the constant  $\Delta f$  images, consistent with a weak attractive interaction. Taking the pentagon-down orientation as an example, examination of the five lobed structure produced by an on-tip C<sub>60</sub> reveals that the lobe spacing ( $\sim 180 \pm 20$  pm) is somewhat larger than either the single or double bond length within a C<sub>60</sub> molecule. Without insights from theory it is thus not necessarily clear whether it is a process of C-C bond breaking and C-Si bond formation, or a weak interaction with the carbon atoms/bonds with the reactive Si(111)-(7x7) surface that produces such striking patterns.

To elucidate the contrast formation mechanism responsible for the atomic resolution experimental FM-AFM images, site-specific  $F(z)$  spectroscopy was simulated out using the SIESTA DFT code and compared to experimental spectra. To check that the smaller cluster properly modelled the Si(111)-(7 × 7) surface, test  $F(z)$  measurements were taken using a C<sub>60</sub> PA tip on both the simplified adatom structure and also the corner adatoms on both the faulted and unfaulted sides of the full 7x7 surface. As can be seen in Figure 7.9, the simulated  $F(z)$  curves agree very well until a turnaround in force is seen. As would be expected for the larger and more responsive surface, the maximum attractive force is slightly lower, indicating that the larger slab is more easily able to distribute strain induced by the close proximity of the C<sub>60</sub> molecule. From this comparison we determine that the smaller silicon cluster well reproduces the essential attributes of an adatom of the full 7x7 reconstruction, particularly in the weakly interacting regime corresponding to our FM-AFM imaging conditions, and is consequently used for all other DFT spectroscopic calculations in this section.

A comparison between the simulated and experimental  $F(z)$  data is shown in Figure 7.10(a). During this experiment, in which bright pentagonally arranged features were observed,  $\Delta f(z)$  data were acquired above one of the pentagon lobes(see

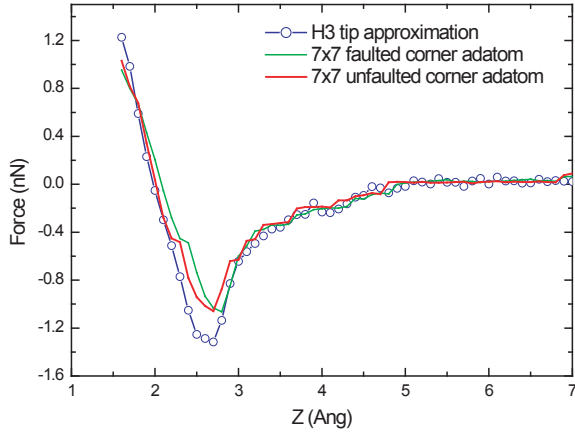


Figure 7.9: A comparison of  $F(z)$  spectra for a  $C_{60}$  molecule with one of its pentagon faces prone to the surface interacting with the adatom on the simple silicon cluster (open circles), and the faulted/unfaulted corner adatoms of the full  $7 \times 7$  unit cell (red and green lines). In each case, spectra were acquired for an adatom placed directly below a carbon atom in a pentagonal face of the  $C_{60}$  molecule(PA). Good agreement can be seen between the spectra for the simple silicon cluster model of an adatom and the full ( $7 \times 7$ ) unit cell, although the former overestimates the peak attractive force.

inset to Figure 7.10(a)), and the corner hole site on the Si(111)-(7  $\times$  7) surface. Using the on/off technique and the Sader-Jarvis method, the short range contribution to force was extracted and is shown as black open circles in Figure 7.10(a). Simulated  $F(z)$  data were then calculated for the PA (red dotted line) and PB (blue dashed line) arrangements to help ascertain the origin of the experimental force interaction. We clearly find, that for each position of the pentagon relative to the surface adatom, a significant interaction is observed matching extremely well with the extracted experimental data.

To understand why the two simulated force curves are so similar, we examined the system geometries and produced electron density difference plots to visualise the positions, and spatial extent, of any Si-C bonds formed. Density difference plots are obtained by calculating the total electron density before, and after electronic relaxation. Thus the difference between the two is the difference in electron density due

to the interaction between molecules. In this case the density difference plots reveal the locations of density depletion and excess relating to the formation of chemical bonding. Figure 7.10(b) depicts one of the density difference plots, calculated at the position marked with a red arrow in (a) along the PA curve. From this it is clear that the force interaction originates from weak chemical bonding between the carbon and silicon atoms within the C<sub>60</sub> cage and the surface adatom. Regardless of whether the C<sub>60</sub> is positioned in the PA or PB position we always observe C-Si bond formation. The reason for the similarities between the PA and PB  $F(z)$  data originates from a sudden shift in the C<sub>60</sub> geometry, shown in Figure 7.10(c) in which the C<sub>60</sub> cage distorts in order to allow the C-Si bond to form. Therefore the PB  $F(z)$  curve, at tip-sample separations below  $\sim 2.7\text{\AA}$  corresponds to a PA-like geometry.

Sharp transitions in  $F(z)$ , similar to those found for the PB simulated data, are also observed experimentally (see Figure 7.10(a)). In the simulated system, we apply constraints to some of the atomic positions within the C<sub>60</sub> cage, to act as an approximation for the bond formed with the AFM tip, and to enable calculation of forces. In the experimental system, it is likely that many more complicated adsorption geometries exist, perhaps giving the C<sub>60</sub> molecule a greater degree of freedom, allowing for more extreme snap-to-contact like events. To examine this possibility we carried out further simulations for the other orientations of the molecule, whilst also testing the effect of constraining different numbers of C atoms.

#### 7.2.4 C<sub>60</sub> stability and bond evolution

$F(z)$  measurements were simulated above a silicon adatom with three different orientations of a C<sub>60</sub> molecule, pentagon down, hexagon down and C=C double bond down as described in the previous section. For each orientation,  $F(z)$  measurements were simulated centred on either a C atom or centred on a C-C/C=C bond. For the case of the hexagon-down orientation this required spectra to be taken over both

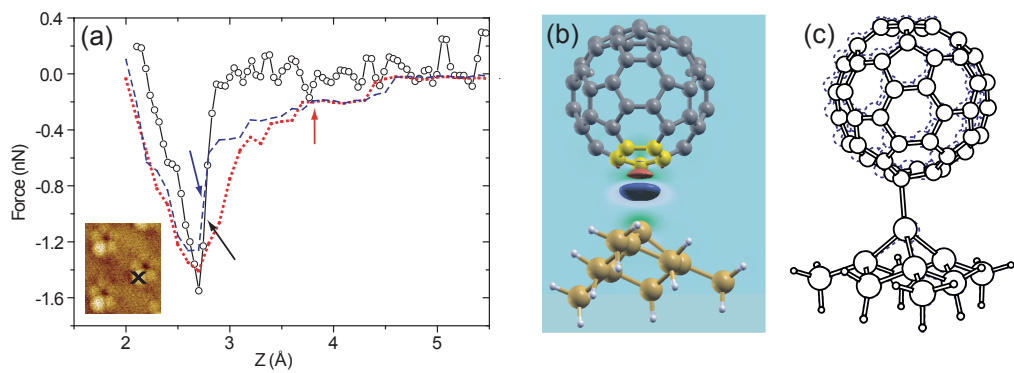


Figure 7.10: Measuring and calculating the chemical force responsible for submolecular atomic contrast. (a) Comparison of experimental (open black circles) and simulated  $F(z)$  data. Simulations were carried out for PA (red dotted line) and PB (blue dashed line) positions of the molecule. Blue and black arrows highlight jump-to-contact events in the experimental and PB data. Inset image shows location of experimental spectra. (b) Electron density difference plot showing the C-Si bond at a tip-sample separation of 3.8 Å (red arrow). The red contours represent a charge density difference of  $-0.005 \text{ \AA}^3$  (density depletion) and the blue contours a difference of  $+0.005 \text{ \AA}^3$  (density excess). (c) Ball-and-stick representation of the distortion of the  $\text{C}_{60}$  cage induced by bond formation. Dashed lines before, and solid lines after, the transition marked by the blue arrow in (a).

bond types. The calculated  $F(z)$  curves for each orientation are shown in Figure 7.11 (retract curves are omitted for clarity). For calculations carried out with the pentagon-down orientation, a stronger force interaction is observed when a C atom, rather than a C-C bond, is located directly above the silicon adatom. This strongly suggests that at a given negative  $\Delta f$  setpoint, the force interaction is strongest between the C atoms and Si adatom during scanning and that it is this attractive interaction which produces the bright features observed in experiment, for all orientations.

Repeated simulations for the hexagon-down and double bond-down orientations yield a very similar picture of the  $C_{60}$ -adatom interaction: the strongest interaction is observed when a C atom, rather than a bond between C atoms, is located above an adatom. In particular, within the weakly interacting region of the calculated  $F(z)$  curves, at any given tip-sample separation the force is always slightly greater for spectra over a carbon atom as compared to spectra over the bonds.

At closer distances, however, there are sudden jumps in the over-bond spectra causing the  $F(z)$  curves for different sites on the  $C_{60}$  molecule to match very closely below a certain threshold tip-sample separation. These jumps correspond to a sudden jump to contact between the surface silicon adatom and a carbon atom within the  $C_{60}$  cage, despite the silicon adatom being initially positioned directly over a C-C bond. This in turn strongly supports the proposal that an interaction with the carbon atoms of a  $C_{60}$  molecule is favourable in producing the force interaction responsible for FM-AFM image contrast. This observation also suggests that sub-molecular imaging with an on-tip  $C_{60}$  can only be achieved within a relatively small force interaction window in the attractive regime, between the point where the  $F(z)$  curves diverge and where a jump to contact occurs. The instabilities that a sudden jump to contact may cause could explain the difficulty in observing certain orientations of the  $C_{60}$  in experiment, such as hexagon down. Simulations of

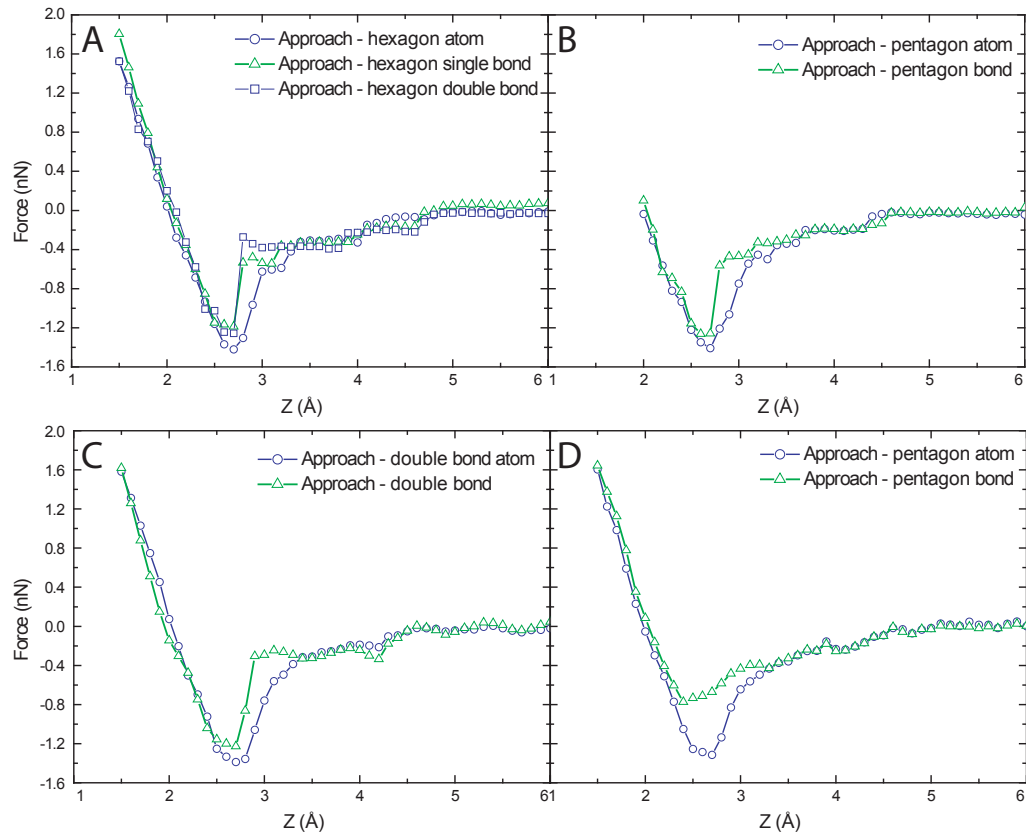


Figure 7.11: Calculated  $F(z)$  approach curves for three different orientations of the  $C_{60}$  molecule: (a) hexagon-down; (b) pentagon-down, and (c) double-bond-down, taken at the sites shown in Figure 7.8. (d) Simulations for the pentagon-down case were carried out with much tighter constraints on the atoms on the opposite side of the  $C_{60}$  cage - the rear pentagon and its surrounding hexagon atoms were all constrained. Retract data are omitted for clarity in each figure in this case but follow very similar profiles to each approach curve.

the pentagon-down orientation carried out with more restrictive constraints - where not only the opposite pentagon but its surrounding hexagon atoms are constrained (Figure 7.11(d)) - show a much less pronounced jump to contact. This is a direct consequence of the C<sub>60</sub> cages inability to distort to the same extent as observed for less rigorous constraints.

It is possible to provide more direct information on the interaction between a Si adatom and the C<sub>60</sub> molecule by examination of the evolution of the electronic charge density distribution. Figure 7.12 shows charge density difference plots for various C<sub>60</sub>-surface positions along the  $F(z)$  curve calculated for the pentagon down orientation of the C<sub>60</sub> molecule in the PA configuration. The formation of a chemical bond between the two structures can clearly be observed starting at a  $D_{SM}$  of 4.4Å(c), shown in Figure 7.12 down to a  $D_{SM}$  of 3Å(j). As depicted in Figure 7.12, the region of density difference is spatially localised to a position between the surface adatom and the pentagon atom of the C<sub>60</sub>. Selected C<sub>60</sub>-surface separations are shown to illustrate how the formed chemical bond becomes stronger up to a point where it is then no longer localised to a single carbon atom (g-j), but covers a much larger spatial extent including the surrounding C-C bonds of the pentagon down face. To highlight the evolution of the chemical bond, additional contours are superimposed onto the density difference images, the red contours represent a charge difference of  $-0.005\text{\AA}^{-3}$  (density depletion) and the blue contours a difference of  $+0.005\text{\AA}^{-3}$  (density excess).

The evolution of the chemical bond formation shown in Figure 7.12 suggests that only within a small window of C<sub>60</sub>-surface separation will a localised chemical bond be formed capable of producing lobe structure resolution as observed experimentally. If the C<sub>60</sub>-surface distance was decreased further then the chemical bond formed would cover an increasingly large spatial region merging the individual lobes into a larger structure. Such an interaction could even so great that the C<sub>60</sub> would no

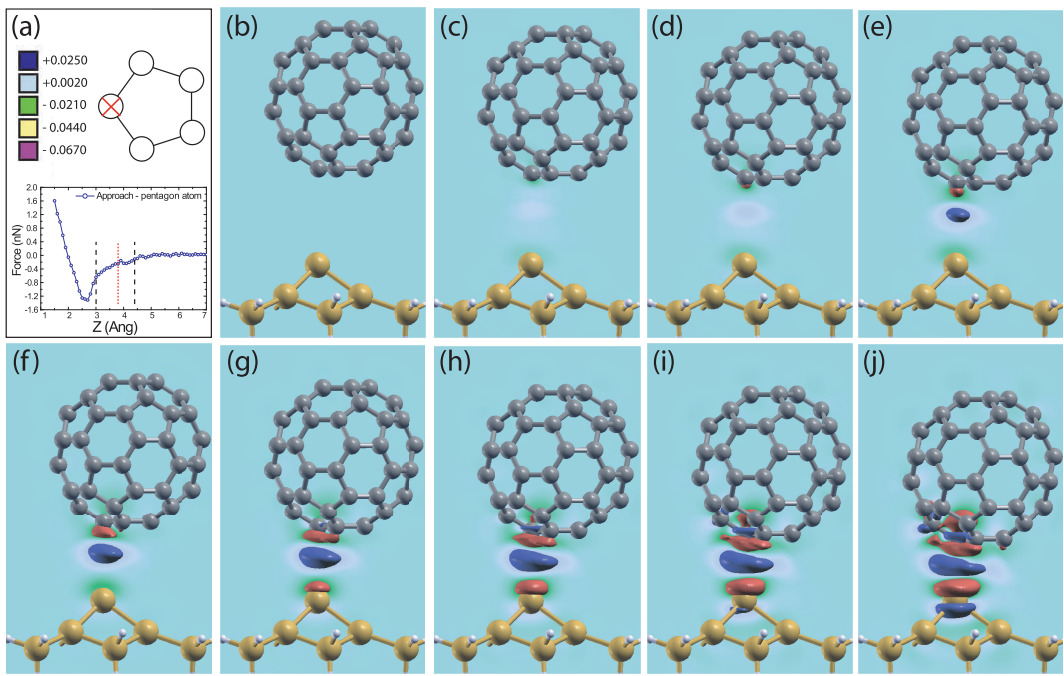


Figure 7.12: Evolution of the chemical interaction between C<sub>60</sub> and a silicon adatom. Density difference plots are shown for the PA configuration. A weak chemical bond is observed to form at a C<sub>60</sub>-surface separation of 4.4 Å in (c) and increases in strength up until a separation of 3 Å in (j). Additional contours are superimposed onto the density difference images. The red contours represent a charge difference of -0.005 Å<sup>3</sup> (density depletion) and the blue contours a difference of +0.005 Å<sup>3</sup> (density excess). The graph in (a) shows the range of tip-sample separations (black lines) spanned by the density difference plots in (b)-(j). The red line represents the tip-sample separation for the density difference plot shown in Figure 7.10.

longer be stable and begin to shift and rotate on the tip apex.

We can therefore conclude, with a strong degree of confidence, that by functionalising the tip with a C<sub>60</sub> molecule, we are able to obtain atomic resolution submolecular information about the C<sub>60</sub> cage from FM-AFM measurements. For the first time, attractive regime submolecular resolution of the individual atoms within the C<sub>60</sub> molecule, made possible only with the inverted imaging technique, has been obtained. From our detailed simulations we are able to attribute the experimental results to the formation of weak chemical bonds between the C<sub>60</sub> carbon atoms and the silicon adatoms of the (7 × 7) surface. We find that atomic resolution is only

possible within a small window of weak chemical interaction, stronger interactions may lead to a loss of submolecular resolution, and more importantly, tip instabilities originating from the movement or deformation of the C<sub>60</sub> cage.

Functionalising the scanning probe in this way dramatically reduces the uncertainty regarding the AFM tip structure, one of the major issues associated with FM-AFM measurements. We are not only able to state with confidence that our tip apex consists of a C<sub>60</sub> molecule, but can also discern its orientation, and even the tilt of the molecule with respect to the surface (for instance with the pentagon down orientation). It has already been shown by Gross *et al.* that molecular functionalisation can open up unique experimental opportunities, such as sub-molecular resolution imaging. Although this approach cannot completely solve our need for a well defined tip, for instance chemically reactive tips are desirable in many instances, it does offer an interesting opportunity to study molecular interactions. For instance, the interaction between two CO molecules [191] (one on the tip and another on the surface), and also two C<sub>60</sub> molecules [190] can be measured, making possible the direct measurement of molecular pair potentials.

# Chapter 8

## Conclusions

Interactions between atoms and molecules are ubiquitous in nature. The atomic force microscope offers the unique ability to directly probe these interactions, thus enabling us to obtain interesting information about a range of surface phenomena. The AFM is a scanning probe technique and as such relies on an interaction between the surface and tip. When operated at the atomic scale, these interactions take place between the individual atoms at the tip apex and the surface. The specific nature of the tip apex, therefore, is critical to understanding and directing experiments with an AFM, such as many of the experiments described in Section 1.

Throughout this thesis I have examined the effects of tip structure in AFM imaging and manipulation experiments, focussed on semiconductor surfaces. To understand the observations made for Si(100), Si(100):H and the Si(111)-(7x7)-C<sub>60</sub> systems, *ab initio* DFT simulations, or a combination of modelling and experiment, were conducted. In each chapter the critical nature of the AFM tip termination, and the interaction it has with the surface, has repeatedly become the focus of discussion. We have found that identification of the tip apex, and the role it plays during an experiment, is essential to understand surface processes and tip-sample interactions. Based on the success of the combined experimental and simulated results described

in this thesis several methods are proposed to help characterise and modify silicon tip structures, thus enabling specific experiments to take place and generally reducing the uncertainty often surrounding the tip apex.

In Chapter 5 experiments were carried out to determine whether individual dimers on the Si(100) surface could be mechanically switched between different configurations. In order to understand the experimental results, and explain the mechanisms underpinning the dimer flipping process, detailed DFT simulations were conducted to examine the energy balance of ideal and defective surfaces, with or without the presence of an AFM tip. We found that whilst we could reproduce the experimentally observed  $F(z)$  curves using simulated reactive silicon tip clusters, understanding the potential energy surface was significantly more complicated. A detailed NEB investigation showed that whilst tip-induced variation of the PES played a significant role in instigating the initial stages of dimer flipping, it could not explain the complete process leading to formation of phason-pair structures. To answer that question, it was necessary to also consider the effect of surface defects. We found that, due to induced strain, defects significantly affected the barrier heights for transition, thus suggesting a possible pathway for manipulation.

The following chapters moved on to focus more on the AFM tip structure. In Chapter 6 I considered hydrogen-silicon systems, and examined methods to identify tip structures both theoretically and experimentally. A series of *ab initio* DFT calculations showed that, in some cases, the success of atomic manipulation can critically depend on the specific structure present at the tip apex. An experimental method was suggested to characterise tips, rooted in simulated observations, which could characterise tip structures capable of performing specific manipulation tasks. Building on these simulated predictions, the results of NC-AFM experiments carried out on the hydrogen terminated Si(100) surface were described. We found that on the the Si(100):H surface we regularly cultivated chemically passivated, hy-

drogen terminated, tip apices which led to distinct ‘inverted’ image contrasts in our constant  $\Delta f$  images. With a combined DFT and AFM investigation, we were able to identify the specific termination present in our experiments and reported the existence of a weak attractive interaction, due to short-range dispersion forces, between our tip and sample. A robust characterisation allows us to design specific NC-AFM experiments tailored to the properties of the tip apex. To demonstrate this I discussed the possibility of engineering the tip structure between reactive and unreactive states, via surface dangling bond (DB) features, and presented some preliminary experiments in which we attempted to image the chemically reactive DB sites. Our passivated tip structure enables stable imaging within the Pauli repulsion regime, sharing similarities with the ground breaking experiments performed in IBM Zurich [28, 55]. To investigate whether we could obtain ultra-high resolution with our AFM tips, we attempted to image the split-dimer defect, hoping to determine its structure once and for all. In the future we hope to pursue the possibilities for sub-molecular imaging in our passivated system.

In Chapter 7 this thesis returned to reactive silicon systems to study tip processes and relate them to experimental observations. We found significant dissipation originating from the alternative structural pathways taken by the tip apex atoms during  $F(z)$  measurements with a simple silicon cluster. Additionally, we simulated structural development of a silicon tip cluster. These processes provide interesting information regarding tip stability, and commonly observed experimental behaviour. Finally, I finished by describing a series of experiments in which we functionalised the AFM probe with a  $C_{60}$  molecule, essentially eliminating the problem of unknown tip structure. We found that by exploiting an ‘inverse imaging’ technique, we could obtain intra-molecular atomic resolution of the  $C_{60}$  molecule. The image mechanism was found to originate from weak chemical bond formation between the reactive silicon surface and the individual carbon atoms of the  $C_{60}$  cage.

The results described in this thesis enhanced our understanding of a number of experimental processes. Furthermore, they have pointed the way towards a number of future experiments. Our characterisation of the AFM tip in hydrogen-passivated systems suggests that we may be able to obtain ultra-high resolution images of surface and molecular structures. To conclude our investigation of the split dimer defects, many more experiments need to be carried out to properly characterise their appearance and properly determine the origin of the increased hydrogen spacing. To rule out more complicated structures it is necessary to test our passivated tip apex on the other reconstructions of Si(100):H, in particular, the dihydride structures found on the (3x1) reconstruction. Dihydride features are known to consist of two closely separated hydrogen atoms. Consequently, if we are able to resolve the individual atoms with AFM, we will know that dihydride, or any other complicated structures, cannot be responsible for the split dimer defect. Perhaps more interestingly, rather than examining defects, surface adsorbed molecules can be studied. The passivated tip structure opens up the interesting possibility of obtaining submolecular resolution without intentional modification of the tip apex.

Additionally I discussed the possibility of engineering the tip between reactive and unreactive states. To pursue this further a large sample of experiments need to be carried out which attempt to transfer the tip adsorbed hydrogen to the surface, via a dangling bond. The simulations described in Chapter 6 revealed that whilst such an experiment is possible, there is a strong dependence on the exact configuration of the tip apex. Therefore, to properly conclude whether tip engineering on Si(100):H is experimentally possible, numerous attempts are required, such that a sufficiently large tip parameter space is explored.

The NC-AFM is now reaching the end of a period of discovery. As it moves into a period of mastery, the focus is shifting more and more to how we can control every aspect of the experimental system. As we improve the technique, and develop

ever more exciting opportunities to investigate the atomic world, understanding, and controlling the tip apex, will undoubtedly remain the central focus of many experiments yet to come.

*Bibliography*

---

# Bibliography

- [1] E. Drexler, *Engines of Creation: The Coming Era of Nanotechnology* (Anchor, 1987).
- [2] R. E. Smalley, Scientific American **285**, 76 (2001).
- [3] K. Eric Drexler *et al.*, available at <http://www.imm.org/SciAmDebate2/smallley.html> (2003).
- [4] R. Baum, Chemical and Engineering News **81**, 37 (2003).
- [5] G. Binnig, Applied Physics Letters **40**, 178 (1982).
- [6] G. Binnig, H. Rohrer, C. Gerber, and E. Weibel, Physical Review Letters **49**, 57 (1982).
- [7] G. Binnig, H. Rohrer, C. Gerber, and E. Weibel, Physical Review Letters **50**, 120 (1983).
- [8] Gerd Binnig, Nobel lecture: Scanning tunneling microscopy from birth to adolescence, [http://www.nobelprize.org/nobel\\_prizes/physics/laureates/1986/binnig-lecture.html#](http://www.nobelprize.org/nobel_prizes/physics/laureates/1986/binnig-lecture.html#), link available September 2012.
- [9] D. M. Eigler, C. P. Lutz, and W. E. Rudge, Nature **352**, 600 (1991).
- [10] D. M. Eigler and E. K. Schweizer, Nature **344**, 524526 (1990).
- [11] M. F. Crommie, C. P. Lutz, and D. M. Eigler, Science **262**, 218 (1993).
- [12] J. J. Boland and J. S. Villarrubia, Science **248**, 838 (1990).
- [13] T. A. Jung, R. R. Schlittler, J. K. Gimzewski, H. Tang, and C. Joachim, Science **271**, 181 (1996).
- [14] S.-W. Hla, L. Bartels, G. Meyer, and K.-H. Rieder, Physical Review Letters **85**, 2777 (2000).
- [15] J. Repp, G. Meyer, S. M. Stojkovi, A. Gourdon, and C. Joachim, Physical Review Letters **94**, 026803 (2005).
- [16] K. K. Gomes, W. Mar, W. Ko, F. Guinea, and H. C. Manoharan, Nature **483**, 306 (2012).
- [17] G. Binnig, C. F. Quate, and C. Gerber, Physical Review Letters **56**, 930 (1986).
- [18] Y. Sugimoto *et al.*, Physical Review B **81**, 245322 (2010).
- [19] Y. Sugimoto *et al.*, Nat Mater **4**, 156159 (2005).
- [20] Y. Sugimoto *et al.*, Science **322**, 413417 (2008).

## Bibliography

---

- [21] M. Ternes, C. P. Lutz, C. F. Hirjibehedin, F. J. Giessibl, and A. J. Heinrich, *Science* **319**, 10661069 (2008).
- [22] N. Oyabu, Y. Sugimoto, M. Abe, s. Custance, and S. Morita, *Nanotechnology* **16**, S112 (2005).
- [23] N. Oyabu, s. Custance, I. Yi, Y. Sugawara, and S. Morita, *Physical Review Letters* **90**, 176102 (2003).
- [24] F. J. Giessibl, *Science* **267**, 68 71 (1995).
- [25] F. J. Giessibl, *Science* **289**, 422 (2000).
- [26] Y. Sugimoto *et al.*, *Nature* **446**, 6467 (2007).
- [27] Y. Sugimoto *et al.*, *Physical Review Letters* **98**, 106104 (2007).
- [28] L. Gross, F. Mohn, N. Moll, P. Liljeroth, and G. Meyer, *Science* **325**, 1110 (2009).
- [29] J. Welker and F. J. Giessibl, *Science* **336**, 444 (2012).
- [30] J. A. Stroscio and W. J. Kaiser, editors, *Scanning Tunneling Microscopy*, New edition ed. (Academic Press Inc, 1994).
- [31] J. N. Israelachvili, *Intermolecular And Surface Forces* (Academic Press, 2010).
- [32] M. Guggisberg *et al.*, *Physical Review B* **61**, 11151 (2000).
- [33] Y. Li *et al.*, *Physical Review Letters* **96** (2006).
- [34] L. Pizzagalli and A. Baratoff, *Physical Review B* **68**, 115427 (2003).
- [35] M. A. Lantz, *Science* **291**, 2580 (2001).
- [36] K. Takayanagi, Y. Tanishiro, M. Takahashi, and S. Takahashi, *Journal of Vacuum Science & Technology A: Vacuum, Surfaces, and Films* **3**, 1502 (1985).
- [37] J. Pethica and W. Oliver, *Physica Scripta* **T19A**, 61 (1987).
- [38] S. Kitamura and M. Iwatsuki, *Japanese Journal of Applied Physics* **34**, L145 (1995).
- [39] T. R. Albrecht, P. Grutter, D. Horne, and D. Rugar, *Journal of Applied Physics* **69**, 668 (1991).
- [40] R. Perez, M. C. Payne, I. Stich, and K. Terakura, *Physical Review Letters* **78**, 678681 (1997).
- [41] R. Perez, I. Stich, M. C. Payne, and K. Terakura, *Physical Review B* **58**, 1083510849 (1998).
- [42] P. Dieska, I. Stich, and R. Perez, *Nanotechnology* **15**, S55 (2004).
- [43] J. Tobik, I. Stich, R. Perez, and K. Terakura, *Physical Review B* **60**, 11639 (1999).
- [44] P. Dieska, I. Stich, and R. Perez, *Physical Review Letters* **91**, 216401 (2003).
- [45] A. S. Foster *et al.*, *Physical Review Letters* **92**, 036101 (2004).
- [46] A. S. Foster, C. Barth, A. L. Shluger, and M. Reichling, *Physical Review Letters* **86**, 2373 (2001).
- [47] Y. Sugawara, M. Ohta, H. Ueyama, and S. Morita, *Science* **270**, 1646 (1995).

## Bibliography

---

- [48] A. Schwarz, W. Allers, U. Schwarz, and R. Wiesendanger, Applied Surface Science **140**, 293 (1999).
- [49] M. Ondracek *et al.*, Physical Review Letters **106**, 176101 (2011).
- [50] A. Campbellov *et al.*, Nanotechnology **22**, 295710 (2011).
- [51] N. Oyabu *et al.*, Physical Review Letters **96**, 106101 (2006).
- [52] P. Pou *et al.*, Nanotechnology **20**, 264015 (2009).
- [53] R. Bechstein *et al.*, Nanotechnology **20**, 505703 (2009).
- [54] S. Ghasemi *et al.*, Physical Review Letters **100** (2008).
- [55] L. Gross *et al.*, Nature Chemistry **2**, 821 (2010).
- [56] F. Mohn *et al.*, Physical Review Letters **105**, 266102 (2010).
- [57] L. Bartels *et al.*, Physical Review Letters **80**, 2004 (1998).
- [58] F. Giessibl, Japanese Journal of Applied Physics Part 1-Regular Papers Short Notes & Review Papers **33**, 3726 (1994).
- [59] F. Giessibl and B. Trafas, Review of Scientific Instruments **65**, 1923 (1994).
- [60] J. E. Sader and S. P. Jarvis, Applied Physics Letters **84**, 1801 (2004).
- [61] F. J. Giessibl, Physical Review B **56**, 16010 (1997).
- [62] R. O. Jones and O. Gunnarsson, Reviews of Modern Physics **61**, 689 (1989).
- [63] R. M. Martin, *Electronic Structure: Basic Theory and Practical Methods* (Cambridge University Press, Cambridge, 2004).
- [64] R. G. Parr and W. Yang, *Density-Functional Theory of Atoms and Molecules* (Oxford University Press, New York, 1989).
- [65] F. Jensen, *Introduction to Computational Chemistry* (John Wiley & Sons, Chichester, 1999).
- [66] M. Born and R. Oppenheimer, Annalen Der Physik **84**, 04570484 (1927).
- [67] P. Hohenberg and W. Kohn, Physical Review B **136**, B864 (1964).
- [68] L. H. Thomas, Mathematical Proceedings of the Cambridge Philosophical Society **23**, 542548 (1927).
- [69] E. Fermi, Rend. Accad. Naz. Lincei **6**, 602 (1927).
- [70] P. A. M. Dirac, Mathematical Proceedings of the Cambridge Philosophical Society **26**, 376 (1930).
- [71] W. Kohn and L. Sham, Physical Review **140**, 1133 (1965).
- [72] D. M. Ceperley and B. J. Alder, Physical Review Letters **45**, 566 (1980).
- [73] J. P. Perdew, K. Burke, and M. Ernzerhof, Physical Review Letters **77**, 3865 (1996).
- [74] J. M. Soler *et al.*, Journal of Physics-Condensed Matter **14**, 27452779 (2002).
- [75] D. Hamann, M. Schluter, and C. Chiang, Physical Review Letters **43**, 1494 (1979).
- [76] R. P. Feynman, Physical Review **56**, 340 (1939).

## Bibliography

---

- [77] L. Kantorovich, *Quantum Theory of the Solid State: An Introductionn* (Springer, 2004).
- [78] P. Ordejon, E. Artacho, and J. M. Soler, Physical Review B **53**, 10441 (1996).
- [79] L. Kantorovich and C. Hobbs, Physical Review B **73**, 245420 (2006).
- [80] R. E. Schlier and H. E. Farnsworth, The Journal of Chemical Physics **30**, 917 (1959).
- [81] D. J. Chadi, Physical Review Letters **43**, 43 (1979).
- [82] K. Inoue, Y. Morikawa, K. Terakura, and M. Nakayama, Physical Review B **49**, 14774 (1994).
- [83] J. P. LaFemina, Surface Science Reports **16**, 137260 (1992).
- [84] R. M. Tromp, R. J. Hamers, and J. E. Demuth, Physical Review Letters **55**, 1303 (1985).
- [85] R. Wolkow, Physical Review Letters **68**, 2636 (1992).
- [86] C.-C. Fu, M. Weissmann, and A. Sal, Surface Science **494**, 119 (2001).
- [87] J. Ihm, D. H. Lee, J. D. Joannopoulos, and J. J. Xiong, Physical Review Letters **51**, 1872 (1983).
- [88] T. Tabata, T. Aruga, and Y. Murata, Surface Science **179**, L63 (1987).
- [89] K. Hata, Y. Sainoo, and H. Shigekawa, Physical Review Letters **86**, 3084 (2001).
- [90] R. J. Hamers, R. M. Tromp, and J. E. Demuth, Physical Review B **34**, 5343 (1986).
- [91] Y. Kondo, T. Amakusa, M. Iwatsuki, and H. Tokumoto, Surface Science **453**, L318 (2000).
- [92] T. Yokoyama and K. Takayanagi, Physical Review B **61**, R5078 (2000).
- [93] T. Mitsui and K. Takayanagi, Physical Review B **62**, R16251 (2000).
- [94] M. Matsumoto, K. Fukutani, and T. Okano, Physical review letters **90**, 106103 (2003).
- [95] M. Ono *et al.*, Physical Review B **67** (2003).
- [96] K. Sagisaka, D. Fujita, and G. Kido, Physical Review Letters **91**, 146103 (2003).
- [97] K. Sagisaka and D. Fujita, Physical Review B **71**, 245319 (2005).
- [98] K. Sagisaka, D. Fujita, G. Kido, and N. Koguchi, Surface Science **566**, Part **2**, 767 (2004).
- [99] K. Yokoyama, T. Ochi, A. Yoshimoto, Y. Sugawara, and S. Morita, Japanese Journal of Applied Physics Part 2-Letters **39**, L113 (2000).
- [100] S. Morita and Y. Sugawara, Japanese Journal of Applied Physics **41**, 4857 (2002).
- [101] D. Sawada *et al.*, Japanese Journal of Applied Physics **47**, 6085 (2008).
- [102] T. Uozumi, Y. Tomiyoshi, N. Suehira, Y. Sugawara, and S. Morita, Applied Surface Science **188**, 279 (2002).
- [103] J. Wang, T. A. Arias, and J. D. Joannopoulos, Physical Review B **47**, 10497 (1993).
- [104] Y. Sainoo *et al.*, Japanese Journal of Applied Physics **38**, 3833 (1999).

## Bibliography

---

- [105] A. Sweetman, S. Gangopadhyay, R. Danza, N. Berdunov, and P. Moriarty, Applied Physics Letters **95**, 063112 (2009).
- [106] J. Boland, Advances in Physics **42**, 129 (1993).
- [107] Y. J. Chabal and K. Raghavachari, Physical Review Letters **54**, 1055 (1985).
- [108] J. J. Boland, Physical Review Letters **65**, 3325 (1990).
- [109] T. Sakurai and H. D. Hagstrum, Physical Review B **14**, 1593 (1976).
- [110] J. J. Boland, Surface Science **261**, 17 (1992).
- [111] E. J. Buehler and J. J. Boland, Surface Science **425**, L363 (1999).
- [112] A. Bellec, D. Riedel, G. Dujardin, N. Rompotis, and L. N. Kantorovich, Physical Review B **78**, 165302 (2008).
- [113] M. Fujimori, S. Heike, Y. Suwa, and T. Hashizume, Japanese Journal of Applied Physics **42**, L1387 (2003).
- [114] J. L. OBrien *et al.*, Physical Review B **64**, 161401 (2001).
- [115] A. Mayne, D. Riedel, G. Comtet, and G. Dujardin, Progress in Surface Science **81**, 151 (2006).
- [116] G. P. Lopinski, D. D. M. Wayner, and R. A. Wolkow, Nature **406**, 48 (2000).
- [117] S. R. Schofield *et al.*, Physical Review Letters **91**, 136104 (2003).
- [118] B. Weber *et al.*, Science **335**, 64 (2012).
- [119] M. Fuechsle *et al.*, Nature Nanotechnology **7**, 242 (2012).
- [120] X. Tong and R. A. Wolkow, Surface Science **600**, L199 (2006).
- [121] J. L. Pitters, L. Livadaru, M. B. Haider, and R. A. Wolkow, The Journal of Chemical Physics **134**, 064712 (2011).
- [122] L. Livadaru, J. Pitters, M. Taucer, and R. A. Wolkow, Physical Review B **84**, 205416 (2011).
- [123] J. W. Lyding, T.-C. Shen, J. S. Hubacek, J. R. Tucker, and G. C. Abeln, Applied Physics Letters **64**, 2010 (1994).
- [124] J. J. Boland, Surface Science **244**, 1 (1991).
- [125] R. S. Becker, G. S. Higashi, Y. J. Chabal, and A. J. Becker, Physical Review Letters **65**, 1917 (1990).
- [126] T. C. Shen *et al.*, Science **268**, 1590 (1995).
- [127] S. Ciraci, R. Butz, E. M. Oellig, and H. Wagner, Physical Review B **30**, 711 (1984).
- [128] L. Soukiassian, A. J. Mayne, M. Carbone, and G. Dujardin, Surface Science **528**, 121 (2003).
- [129] L. Soukiassian, A. J. Mayne, M. Carbone, and G. Dujardin, Physical Review B **68**, 035303 (2003).
- [130] K. Stokbro *et al.*, Physical Review Letters **80**, 2618 (1998).
- [131] T. Hitosugi *et al.*, Physical Review Letters **82**, 4034 (1999).

## Bibliography

---

- [132] J. N. Randall *et al.*, Journal of Vacuum Science & Technology B: Microelectronics and Nanometer Structures **27**, 2764 (2009).
- [133] A. Bellec *et al.*, Physical Review Letters **105** (2010).
- [134] S. Chen, H. Xu, K. E. J. Goh, L. Liu, and J. N. Randall, Nanotechnology **23**, 275301 (2012).
- [135] K. Takayanagi, Y. Tanishiro, S. Takahashi, and M. Takahashi, Surface Science **164**, 367 (1985).
- [136] J. S. Villarrubia and J. J. Boland, Physical Review Letters **63**, 306 (1989).
- [137] S. D. Solares *et al.*, Langmuir **21**, 12404 (2005).
- [138] K. Hata, T. Kimura, S. Ozawa, and H. Shigekawa, Journal of Vacuum Science & Technology A **18**, 1933 (2000).
- [139] L. Sanchez, R. Otero, J. M. Gallego, R. Miranda, and N. Martin, Chemical Reviews **109**, 2081 (2009).
- [140] D. Bonifazi, O. Enger, and F. Diederich, Chemical Society Reviews **36**, 390 (2007).
- [141] P. J. Moriarty, Surface Science Reports **65**, 175 (2010).
- [142] S. Gangopadhyay *et al.*, Surface Science **603**, 2896 (2009), ei.
- [143] R. Rurali, R. Cuadrado, and J. I. Cerd, Physical Review B **81**, 075419 (2010).
- [144] P. H. Beton, A. W. Dunn, and P. Moriarty, Applied Physics Letters **67**, 1075 (1995).
- [145] P. Beton, A. Dunn, and P. Moriarty, Surface Science **361****362**, 878 (1996).
- [146] P. Moriarty, Y. Ma, M. Upward, and P. Beton, Surface Science **407**, 27 (1998).
- [147] D. Keeling, M. Humphry, P. Moriarty, and P. Beton, Chemical Physics Letters **366**, 300 (2002).
- [148] N. Martsinovich and L. Kantorovich, Nanotechnology **19**, 235702 (2008).
- [149] N. Martsinovich and L. Kantorovich, Physical Review B **77**, 205412 (2008).
- [150] G. Schull, T. Frederiksen, M. Brandbyge, and R. Berndt, Physical Review Letters **103**, 206803 (2009).
- [151] G. Schull, T. Frederiksen, A. Arnau, D. Sanchez-Portal, and R. Berndt, Nature Nanotechnology **6**, 23 (2011).
- [152] R. Pawlak, S. Kawai, S. Fremy, T. Glatzel, and E. Meyer, ACS Nano **5**, 6349 (2011).
- [153] K. Kobayashi, H. Yamada, T. Horiuchi, and K. Matsushige, Applied Surface Science **140**, 281 (1999).
- [154] K. Kobayashi, H. Yamada, T. Horiuchi, and K. Matsushige, Applied Surface Science **157**, 228 (2000).
- [155] J. M. Mativetsky, S. A. Burke, R. Hoffmann, Y. Sun, and P. Grutter, Nanotechnology **15**, S40 (2004).
- [156] F. Loske, P. Rahe, and A. Khnle, Nanotechnology **20**, 264010 (2009).
- [157] F. Loske *et al.*, Nanotechnology **20**, 065606 (2009).

## Bibliography

---

- [158] C. Hobbs and L. Kantorovich, Surface Science **600**, 551 (2006).
- [159] S. Mizuno, T. Shirasawa, Y. Shiraishi, and H. Tochihara, Physical Review B **69**, 241306 (2004).
- [160] G. Henkelman, G. Jhannesson, and H. Jnsson, Methods for finding saddle points and minimum energy paths, in *Theoretical Methods in Condensed Phase Chemistry*, edited by S. D. Schwartz, , Progress in Theoretical Chemistry and Physics Vol. 5, pp. 269–302, Springer Netherlands, 2002.
- [161] H. Jonsson, G. Mills, and K. W. Jacobsen, *Nudged Elastic Band Method for Finding Minimum Energy Paths of Transitions* (, 385).
- [162] G. Henkelman and H. Jnsson, The Journal of Chemical Physics **113**, 9978 (2000).
- [163] D. Sheppard, R. Terrell, and G. Henkelman, Journal of Chemical Physics **128**, 134106 (2008).
- [164] G. Henkelman, B. P. Uberuaga, and H. Jnsson, The Journal of Chemical Physics **113**, 9901 (2000).
- [165] G. H. Simon, M. Heyde, and H.-P. Rust, Nanotechnology **18**, 255503 (2007).
- [166] F. J. Giessibl and H. Bielefeldt, Physical Review B **61**, 9968 (2000).
- [167] Z. Majzik *et al.*, Beilstein Journal of Nanotechnology **3**, 249 (2012).
- [168] G. Meyer, Review of Scientific Instruments **67**, 2960 (1996).
- [169] F. J. Giessibl, Applied Physics Letters **76**, 1470 (2000).
- [170] A. Sweetman, S. Jarvis, R. Danza, and P. Moriarty, Beilstein Journal of Nanotechnology **3**, 25 (2012).
- [171] G. S. Hwang, Surface Science **465**, L789 (2000).
- [172] S. Yoshida *et al.*, Japanese Journal of Applied Physics **41**, 5017 (2002).
- [173] Y. Naitoh, Y. J. Li, H. Nomura, M. Kageshima, and Y. Sugawara, Journal of the Physical Society of Japan **79**, 013601 (2010).
- [174] S. Morita, R. Wiesendanger, and E. Meyer, *Noncontact Atomic Force Microscopy* (Springer, 2002).
- [175] A. J. Heinrich, C. P. Lutz, J. A. Gupta, and D. M. Eigler, Science **298**, 13811387 (2002).
- [176] K. E. Drexler, *Nanosystems: Molecular Machinery, Manufacturing and Computation* (John Wiley & Sons, 1992).
- [177] R. A. Freitas and R. C. Merkle, Journal of Computational and Theoretical Nanoscience **5**, 760 (2008).
- [178] A. Sweetman *et al.*, Physical Review Letters **106**, 136101 (2011).
- [179] A. Sweetman *et al.*, Physical Review B **84**, 085426 (2011).
- [180] A. Sweetman, R. Danza, S. Gangopadhyay, and P. Moriarty, Journal of Physics: Condensed Matter **24**, 084009 (2012).
- [181] R. A. J. Woolley, J. Stirling, A. Radocea, N. Krasnogor, and P. Moriarty, Applied Physics Letters **98**, 253104 (2011).

## *Bibliography*

---

- [182] A. Weymouth, T. Wutscher, J. Welker, T. Hofmann, and F. Giessibl, Physical Review Letters **106** (2011).
- [183] T. Wutscher, A. J. Weymouth, and F. J. Giessibl, Physical Review B **85**, 195426 (2012).
- [184] M. Z. Baykara, T. C. Schwendemann, E. I. Altman, and U. D. Schwarz, Advanced Materials **22**, 2838 (2010).
- [185] N. Miura and M. Tsukada, Japanese Journal of Applied Physics **41**, 306 (2002).
- [186] Y. Sugimoto *et al.*, Physical Review B **73**, 205329 (2006).
- [187] Y. Naitoh, Y. Kinoshita, Y. Jun Li, M. Kageshima, and Y. Sugawara, Nanotechnology **20**, 264011 (2009).
- [188] F. J. Giessibl, Reviews of Modern Physics **75**, 949 (2003).
- [189] S. Hembacher, F. J. Giessibl, and J. Mannhart, Science **305**, 380 (2004).
- [190] C. Chiutu *et al.*, Physical Review Letters **108**, 268302 (2012).
- [191] Z. Sun, M. P. Boneschanscher, I. Swart, D. Vanmaekelbergh, and P. Liljeroth, Physical Review Letters **106**, 046104 (2011).
- [192] File is playable from a web browser and should not require download. Available at [https://www.dropbox.com/s/kny14tvfadqujcf/Si100H\\_movie.wmv](https://www.dropbox.com/s/kny14tvfadqujcf/Si100H_movie.wmv).